THE UNIVERSITY OF MANCHESTER

PHD THESIS

X-ray Microscopy of Particulate Matter in Automotive Filters

Author:
Matthew P. JONES

Supervisor:
Dr. David EASTWOOD,
Prof. Sarah HAIGH,
Prof. Chris HARDACRE

A thesis submitted to the University of Manchester for the degree of Doctor of Philosophy in the

Department of Materials, School of Natural Sciences, Faculty of Science and Engineering

2022

Blank Page.

Contents

43,346 Words

List of Figures

List of Tables

Blank Page.

Abstract

Matthew P. JONES

X-ray Microscopy of Particulate Matter in Automotive Filters

It is important to develop technologies for clean and fuel efficient combustion engines. Particulate filters mitigate Particulate Matter (PM) pollution by filtering PM from exhaust gas. Over the operational lifetime of a particulate filter, PM, such as soot and ash, will build up on filter surfaces and in filter pores. These effect performance in myriad ways. In this project we develop quantitative X-ray microscopy techniques for the study of these processes. During this project we imaged particulate deposits in automotive filters using time lapse X-ray Computed Tomography (XCT), X-ray Ptychotomography (XPT) and other methods. Time lapse XCT was used to resolve deposits as they built up in the pores and surfaces of the filter overtime. This required building a bespoke aerosol flow rig and data processing pipeline. From this method we were able to extract useful quantitative data about the filtration. For example, we were able to plot the channel scale deposition profiles of soot-like nanopowder deposited in the deep bed and on the wall of a particulate filter. In the future this method could be used to validate models of soot filtration in particulate filters. In this project we also demonstrate XPT as a high resolution 3D non-destructive imaging technique for the study of ash. This allows us to make new insights into the micro-structure and evolution of automotive ash, which has an important effect on the in-use performance of these filters. For example, we were able to quantify the internal porosity of ash particles and found a positive correlation between particle size and internal porosity.

Blank Page.

Declaration

I, Matthew P. JONES, declare that this thesis titled,**"X-ray Microscopy of Particulate Matter in Automotive Filters"** and the work presented in it are my own. I confirm that no portion of the work referred to in the thesis has been submitted in support of an application for another degree or qualification of this or any other university or other institute of learning

Blank Page.

Copyright

I, Matthew P. JONES, agree with the following copyright statements:

- The author of this thesis (including any appendices and/or schedules to this thesis) owns certain copyright or related rights in it (the "Copyright") and they have given the University of Manchester certain rights to use such Copyright, including for administrative purposes.
- Copies of this thesis, either in full or in extracts and whether in hard or electronic copy, may be made only in accordance with the Copyright, Designs and Patents Act 1988 (as amended) and regulations issued under it or, where appropriate, in accordance with licensing agreements which the University has from time to time. This page must form part of any such copies made.
- The ownership of certain Copyright, patents, designs, trademarks and other intellectual property (the "Intellectual Property") and any reproductions of copyright works in the thesis, for example graphs and tables ("Reproductions"), which may be described in this thesis, may not be owned by the author and may be owned by third parties. Such Intellectual Property and Reproductions cannot and must not be made available for use without the prior written permission of the owner(s) of the relevant Intellectual Property and/or Reproductions.
- Further information on the conditions under which disclosure, publication and commercialisation of this thesis, the Copyright and any Intellectual Property and/or Reproductions described in it may take place is available in the University IP Policy, in any relevant Thesis restriction declarations deposited in the University Library, the University Library's regulations and in the University's policy on Presentation of Theses.

Blank Page.

Acknowledgements

First of all, I would like to thank my supervisory team at the University of Manchester; Dr. David Eastwood, Prof. Sarah Haigh, and Prof. Chris Hardacre.

Special thanks to David for your support and guidance. I always felt encouraged after our talks. You went above and beyond, particularly during beamtimes, where your expertise was indispensable. I learned a lot. I hope we can stay in contact and that this isn't the last time we work together.

I would also like to thank everyone at Johnson Matthey who were involved, particularly Dr. Andrew York, Dr. Gareth Hatton, and Dr. Timothy Hyde. Your input was consistently helpful and encouraging. I always felt that the industrial relevance of this project was a key element and I hope that this work continues to have an impact at Johnson Matthey. My sincerest thanks.

I would also like to acknowledge everyone at the University of Manchester at Harwell and I-13 for your support and expertise. Special thanks to Sarah Batts for always helping with my admin disasters and to Dr. Fabien Leonard for your technical support.

Thanks also to Dr. June Callison and Dr. Josie Goodall from the Catalysis Hub for supporting my aerosol experiments. I know these were not the typical experiments carried out at the hub, so your support in helping me to pursue these safely was invaluable. Thanks also to my fellow Catalysis Hub PhD students, especially Antonio and Monik. I think this would have been impossible without having comrades to struggle alongside.

To Karen, thank you for always taking the time to listen and providing much needed distractions from my studies when things got hard.

Finally, to my parents. If I listed all the ways you've supported me this thesis would be far too long. So I am not going to. Just know I feel so privileged to be your son, and that none of this would have been remotely possible without you being you. Words are not enough.

List of Terms

ABS	**A**crylonitrile **B**utadiene **S**tyrene
AS	**A**mmonium **S**ulphate
BEV	**B**attery **E**lectric **V**ehicle
CCD	**C**harge **C**oupled **D**evice (Sensor)
CCN	**C**onvolutional **N**eural **N**etwork
CFD	**C**omputed **F**luid **D**ynamics
CMOS	**C**omplementary **M**etal **O**xide **S**emiconductor
COVID 19	Pandemic of **Co**rona**vi**rus **D**isease in 20**19**
CPU	**C**entral **P**rocessing **U**nit
CT	**C**omputed **T**omography
DNA	**D**eoxyribo**N**ucleic **A**cid
DPF	**D**iesel **P**articulate **F**ilter
EDX	**E**nergy **D**ispersive **X**-ray Spectroscopy
FBP	**F**iltered **B**ack **P**rojection algorithm
FDK	**F**eldkamp, **D**avis, **K**ress algorithm
FIB	**F**ocused **I**on **B**eam Milling
FOV	**F**ield **O**f **V**iew
FVM	**F**inite **V**olume **M**ethod
GDI	**G**asoline **D**irect **I**njection
GPF	**G**asoline **P**articulate **F**ilter
HEPA	**H**igh **E**fficiency **P**article **A**ir Filter
HVAC	**H**eating, **V**entilation, **A**ir **C**onditioning
IARC	**I**nternational **A**gency for **R**esearch on **C**ancer
ICE	**I**nternal **C**ombustion **E**ngine

ID	**I**nsertion **D**evice
LB	**L**attice **B**oltzmann
Micro-CT	**Micro** X-ray **C**omputed **T**omography
ML	**M**achine **L**earning
MIP	**M**ercury **I**ntrusion **P**orosimetry
NLM	**N**on **L**ocal **M**eans
NO_x	**N**itrous **O**xides
OEM	**O**riginal **E**quipment **M**anufacturer
PFI	**P**ort **F**uel **I**njection
PGM	**P**latinum **G**roup **M**etals
PM	**P**articulate **M**atter
PM10	**P**articulate **M**atter smaller than **10** μm
PM2.5	**P**articulate **M**atter smaller than **2.5** μm
PPE	**P**ersonal **P**rotective **E**quipment
REV	**R**epresentative **E**lementary **V**olume
ROI	**R**egion **O**f **I**nterest
SART	**S**imultaneous **A**lgebraic **R**econstruction algorithm
SIRT	**S**imultaneous **I**terative **R**econstruction algorithm
SCR	**S**elective **C**atalytic **R**eduction
SCRF	**S**elective **C**atalystic **R**eduction **F**ilter
SDG	**S**ustainable **D**evelopment **G**oal
SD	**S**tandard **D**eviation
SEM	**S**canning **E**lectron **M**icroscopy
SMPS	**S**canning **M**obility **P**article **S**izer
TEM	**T**ransmission **E**lectron **M**icroscope
TXM	**T**ransmission **X**-ray **M**icroscope
WHO	**W**orld **H**ealth **O**rganisation
XCT	**X**-ray **C**omputed **T**omography
XPT	**X**-ray **P**tycho**T**omography
XRF	**X**-**R**ay **F**luorescence
ZDDP	**Z**inc **D**ialkyl**D**ithio**P**hosphate

ZNP	**Z**inc **N**ano**P**articles

Blank Page.

Chapter 1

Introduction

1.1 Motivation

Pollution of the environment with suspended particulate matter (PM) from the combustion of fossil fuels is endemic to both historic and modern industry. Taking London as a historical case study shows that as early as 1273 the loss of woodland around London caused the purchase of cheap inefficient 'sea coal' in place of firewood. Complaints from noblemen about the degradation of the air quality from the coal smoke led to King Edward I prohibiting the burning of coal in London. Although poorly enforced, at least one person was put to death for this offense in around 1300 (Jacobson, 2012). Almost 500 years later the industrial revolution began in Britain with many of the innovations required for industrialisation being of British invention. As a result, by the middle of the 19th century Britain was the world's leading commercial nation. In 1873 an unusually thick and persistent smog directly caused at least 268 deaths in London (Jacobson, 2012). Gradually, from the 1890s, electrification, the use of gas fires and the relocation of heavy industry from the city centre, eased the local environmental burden. However, the smog problem reappeared in post war London when 'The Great Smog' of 1952 drove the city to a standstill due to unnavigable visibility over a four day period. It is now estimated that 12,000 people perished and 100,000 faced serious illness due to the anthropogenic environmental disaster (Jacobson, 2012). In response the British government lead by Sir Anthony Eden passed the Clean Air Act of 1956, a world first. The legislation contains sections on the "Prohibition of Dark Smoke from Chimneys", the "Requirement that new furnaces shall be as far as Practicable Smokeless" and the

FIGURE 1.1: Great Smog of London, 1952: Photograph taken during the Great Smog. Authorities had to take action due to poor visibility, as shown in this image. Image Source: Keystone—Hulton Archive/Getty Images.

"Requirement that new furnaces shall be fitted with a plant to arrest grit and dust". This legislation is often seen as an important milestone for modern environmental legislation and emission control in the UK (HMGOV, 1956).

Smog disasters on the scale of 'The Great Smog' have stopped in 21st century London, however a better understanding of the long term health effects of PM pollution has been developed, and indeed, contemporary public health in London is still damaged by PM. The primary emission source nowadays is internal combustion engine emissions from goods vehicles, trucks, buses, commercial vehicles and passenger cars. In London it has been estimated that the total mortality effect of anthropogenic PM2.5 in 2010 was 52,630 life-years lost, equivalent to 3,537 deaths at typical ages and, 88,113 life-years lost, equivalent to 5,879 deaths at typical ages due to long term exposure to NO_2 (Walton et al., 2015).

Switching to a global perspective we can see that the issue of automotive pollution is ubiquitous in industrialised societies. As such, the UN Sustainable Development Goal (SDG) 11.6, 'to reduce the adverse per capita environmental impact of cities', uses urban PM levels as an indicator. PM is defined as microscopic particles of solid/liquid matter suspended in exhaust or in the atmosphere. Different types of PM are grouped by size; PM10 is less than 10 μm in diameter, PM2.5 is less than

2.5 μm and Ultrafines are less than 100 nm. In 2021, 97.3% of the global population breathed air below the World Health Organization's air quality guidelines value for PM (Greenstone, Hasenkopf, and Lee, 2022). The guidelines state that annual average concentrations of PM2.5 should not exceed 5 $\mu g/m^3$, while 24-hour average exposures should not exceed 15 $\mu g/m^3$ for more than 3 - 4 days per year (WHO, 2021). Furthermore, this issue is not being resolved, more than half of the world population experienced an increase in PM2.5 from 2010 to 2016 (UN, 2017) and despite the economic downturn during COVID19 pollution levels remained steady (Greenstone, Hasenkopf, and Lee, 2022).

These high PM levels have a negative health effect. There is 50% penetration beyond the larynx with an aerodynamic diameter of 10 μm, and 50% penetration into the respirable fraction at an aerodynamic diameter of 4 μm (Brown et al., 2013). When PM penetrates beyond the larynx it can travel deep into the lungs, permanently mutate DNA and lead to increased risk of lung cancer and respiratory conditions. Furthermore, respirable PM, particularly ultrafines, are likely to be absorbed into the blood stream, increasing the risk of cardiovascular conditions and heart attacks (Brown et al., 2013). Raaschou-Nielsen et al., 2013, conducted a study of 312,944 people in nine European countries and showed that for every increase of 10 $\mu g/m^3$ in PM10, the lung cancer rate rose by 22%. The more penetrative PM2.5 showed a 36% rise over the same increase. The IARC and WHO have both classed suspended PM as a Group 1 'known' carcinogen (IARC, 2012).

Battery Electric Vehicles (BEV) are a potential long term solution to anthropogenic PM pollution from vehicles as the drivetrain emits no PM. However, there are significant barriers to quickly scaling the number of BEVs in the vehicle fleet, even in developed nations. These include but are not limited to; supply chain uncertainty, lack of charging infrastructure, and relatively higher upfront costs (Olivetti et al., 2017; Berkeley, Jarvis, and Jones, 2018). In order to facilitate this transition governments have set target dates to phase out internal combustion engine (ICE) vehicles in the next 15 - 20 years as they seek to manage a transition to BEVs (Berkeley, Jarvis, and Jones, 2018). However, ambient PM2.5 is currently the greatest risk to global health when measured by life expectancy loss; PM pollution reduces average life

FIGURE 1.2: Modern Smog in New Delhi, 2018: Photograph showing modern air pollution in New Delhi. Image Source: Associated Free Press.

expectancy globally by 2.2 years, first-hand cigarette smoke by 1.9 years, alcohol use by 8 months, HIV/AIDS by 4 months, malaria by 3 months, and conflict and terrorism by 9 days (Lelieveld et al., 2020; Greenstone, Hasenkopf, and Lee, 2022). This demonstrates the importance of developing cleaner internal combustion before alternative powertrains are phased-in in-order to protect global health.

Awareness of these health issues has lead to increasingly stringent regulations limiting emissions from ICEs. The most recent regulations in the form of Euro 5/6 (2009/2014) have increased fuel efficiency regulations whilst also imposing PM regulations on gasoline vehicles. Gasoline Direct Injection (GDI) engines now offer a favourable trade-off to manufacturers between fuel efficiency and emissions. Less pumping loss, more precise fuel volume and timing control, higher compression ratios, more charge cooling and higher combustion efficiency, all improve fuel efficiency compared to port fuel injection (PFI) gasoline vehicles (Alkidas, 2007). Furthermore, GDI emit less NOx and PM compared to diesel engines, thus requiring less costly aftertreament systems (O'Driscoll et al., 2018). However, GDI emits higher PM emission compared to PFI, due to fuel impingement on the piston and cylinder walls, incomplete fuel evaporation, and the inhomogeneity of the air fuel mixture (Amirante et al., 2017; O'Driscoll et al., 2018). Thus GDI often requires a particulate filter to comply with Euro 6 PM regulations.

Structurally particulate filters are 'wall flow filters' with channels that run parallel

to exhaust gas flow, channels are blocked alternately at the inlet then outlet of neighbouring channels in a 'honeycomb' monolith. The blocked channel ends force the exhaust gas to flow through the connected pores in the walls of the filter, from an inlet channel to an outlet channel, filtering out particles. Overtime these deposited particles effect the performance of the filter. Understanding these processes on the particle, pore and channel scale is an ongoing area of research. In this thesis we apply x-ray microscopy to this area of study.

1.2 Thesis Outline

This thesis aims to provide comprehensive information on applications of X-ray microscopy in automotive filtration and is organised as follows:

- **Chapter 2**, *Scientific Background and Literature Review;* This chapter includes a review of XCT, the XCT experimental workflow and applications of XCT in Materials Science. We also review other microscopy techniques used in this project (X-ray Ptychotomography & Scanning Electron Microscopy). We then review the literature concerning automotive exhaust filters.

- **Chapter 3**, *Experimental;* This chapter presents detailed methods of the succeeding results chapters.

- **Chapter 4**, *4D In-Situ Microscopy of Aerosol Filtration in a Wall Flow Filter (Jones et al., 2020)*. In this chapter we correlated data from backpressure readings to changes in the porous microstructure of a particulate filter by resolving pore scale deposition with XCT. This was the first time that deep bed filtration had been studied this way.

- **Chapter 5**, *Multiscale Time Resolved Microscopy of Aerosol Filtration in GPFs.* We demonstrated the capability of the time lapse filter imaging technique to bridge the length scales between pore scale imaging and channel scale imaging of these devices.

- **Chapter 6**, *X-ray Ptychotomography and XRF-CT of Automotive Ash.* In this chapter results are presented on high resolution 3D microscopy of ash agglomerates. From these micrographs we are able to determine internal porosity, external porosity, and particle size distribution of ash. We also correlate the XPT to chemical fluorescence data.
- **Chapter 7**, Conclusions.

Chapter 2

Scientific Background and Literature Review

In section 2.1 we provide the scientific background behind x-ray computed tomography (XCT) and the workflow typically used by the experimentalist to extract meaningful results from the technique. In section 2.2 we review applications of XCT in Materials Science, specifically looking at applications of time lapse x-ray computed tomography. In section 2.3 and 2.4 we discuss x-ray ptychography and scanning electron microscopy repectively. Finally, in section 2.5 we provide a review of the study of automotive wall flow filters.

2.1 X-ray Computed Tomography

2.1.1 X-ray Imaging

X-ray microscopy can trace it's origins to the work of Wilhelm Röntgen who in 1895 produced and detected electromagnetic radiation in the wavelength range now referred to as X-rays. Röntgen, whilst working with cathode ray tubes, had noticed that a piece of cardboard covered in a fluorescent material, that had been placed away from the cathode ray discharge tube, would fluoresce despite the discharge tube being covered in cardboard to prevent light escaping (Nusslin, 2020). He quickly convinced himself that the fluorescence was caused by an invisible radiation that could penetrate the cardboard covering, as well as thin sheets of metal. That the "x radiation" (x referring to the unknown nature of the radiation) propagated in a straight line. That the source of the radiation was the point where the cathode ray

FIGURE 2.1: A Radiograph of Anna Bertha Ludwig's Hand. The first medical radiograph. Source: Wikipedia Commons.

struck the glass of the discharge tube and that metal targets produced even stronger rays. That the absorption of "x radiation" depended on the density and thickness of the materials the radiation passed through and that every material when subjected to the radiation emitted secondary radiation (Nusslin, 2020). These discoveries lay the ground work for X-ray microscopy as a discipline and allowed Röntgen to take the first medical radiograph with a photographic plate, see Figure 2.1, an image of his wife Anna Bertha's hand. Röntgen's dicovery won the inaugural Nobel Prize in Physics in 1901.

X-ray imaging has advanced in the proceeding 120 years. For example, it could take days for Röntgen to create a single radiograph, this was largely due to difficulty developing effective vacuums (Nusslin, 2020). By comparison modern users of synchrotron light sources are able to image with sufficient time resolution to observe the rapidly changing structure of fluids during cavitation with ultra-high speed imaging by acquiring radiographs from 500 ns pulses (Zhang et al., 2020). Furthermore, the resolution of modern x-ray imaging has been extended into the micro-scale and nano-scale at both laboratory and synchrotron x-ray sources. For example, XM-1 at the Advanced Light Source in Berkeley, California, has achieved 15nm spatial resolution with Fresnel zone plates (Chao et al., 2005). Whilst laboratory sources, such as the commercially available Zeiss Xradia 810 Ultra, are able to achieve spatial resolutions of 50nm. However, the underlying physical principles for the interaction of x-rays with matter still hold today as they did in 1895, these are discussed in the next section.

2.1.2 Attenuation Theory

As x-rays travel through matter they can interact with the constituent atoms and attenuate. Thus, by placing a detector downstream of the sample we can form a 2D shadow image of the sample, i.e. a radiograph. As can be seen in Figure 2.1, the high density bone and metal ring, black in the radiograph, are resolved because the x-rays are absorbed by the dense matter and do not reach the photographic plate behind Anna's hand. In contrast the soft tissues appear gray, and the surrounding air appears white as x-rays more easily pass through lower density materials. The Lambert-Beer law describes the attenuation of a beam interacting with matter. For the case of a monochromatic beam traveling through a homogenous material:

$$I = I_0 e^{-\mu x} \tag{2.1}$$

Where I is the attenuated intensity after the X-rays pass through the object of thickness x, I_0 is the original X-ray intensity, and μ is the attenuation coefficient of the material, which is defined as:

$$\mu(x) = \sum_{i=1}^{N} \sigma_i n_i(x) \tag{2.2}$$

Where N is the number of species in the homogeneous material, where σ_i is the attenuation cross section of the i^{th} species, and n_i is the number density of i^{th} species atoms in x thickness of material. Thus, from Equation 2.1 we can see that I is related to the density of the material. However, actually determining the σ_i term is more complex. It can be estimated as the total of different cross section contributions caused by specific x-ray matter interactions, such as:

$$\sigma_i = \tau_{pe} + \sigma_R + \sigma_C + k_n + k_e \tag{2.3}$$

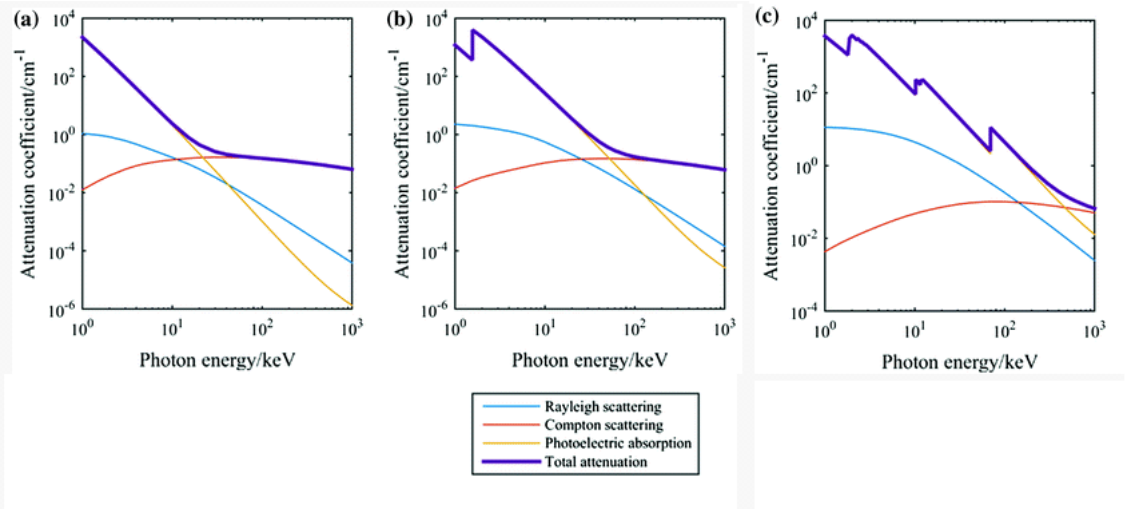

FIGURE 2.2: Plots of attenuation coefficients, μ, for **a** carbon, **b** aluminium and **c** tungsten, against photon energy, E, showing contributions to the total attenuation value. Values of attenuation coefficients were obtained from the National Institute of Standards and Technology (NIST) online database. Source: Thompson and Leach, 2017.

Where τ_{pe} is the contribution of the photoelectric effect to the attenuation cross section, σ_R is the Rayleigh scattering contribution, σ_C is the Compton scattering contribution, and $k_n + k_e$ is the electron-positron pair production contribution. The magnitude of these effects change depending on the atomic number, Z, see Table 2.1, and the energy of the photon beam, E, see Figure 2.2. As shown in figure 2.2 the attenuation profiles are dominated by the photoelectric contribution in electron dense metals such as tungsten, and at energies below 10 keV and 12 keV in carbon and aluminium respectively. Above these energies Compton scattering dominates. Figure 2.2 also shows that as photon energies increase one can observe 'jumps' in the photoelectric contribution to μ. This is because at these energies the x-ray photons have enough energy to overcome the work function of electrons in certain electron shells, exciting the electrons to a higher state and attenuating the photon. For aluminium in figure 2.2.b the 'jump' is due to the aluminium k-edge. This energy (1.55 keV) is just above the binding energy of the k-shell electrons in aluminium, hence removing the electron from the atom. Famously, the observation that electrons are not excited by light below a critical energy, or work function, lead to Albert Einstein's famous postulation about the quantum nature of light in the last paper he published in his legendary 'Annus Mirabilis' (Einstein, 1905).

TABLE 2.1: Shows different physical mechanisms for the interaction of X-rays and matter. The top row lists x-ray matter interaction types and the left column lists interaction sites. For each specific interaction it's cross-section contribution to σ_{tot}, see Equation 2.3, is stated in terms of atomic number, Z. Source: Adapted from Hubbel, 1969.

	Absorption	**Elastic Scattering**	**Inelastic Scattering**	**Multi-photon effects**
Atomic Electrons	Photoelectric effect, $\tau \sim Z^4$ or $\tau \sim Z^{5\star}$	Rayleigh Scattering, $\sigma_R \sim Z^2$	Compton Scattering, $\sigma_C \sim Z$	Two-photon Compton scattering, $\sigma_{CC} \sim Z$
Nucleons	Photonuclear reactions, $\sigma_{ph.n} \sim Z(E \geq 10MeV)$			
Electric Field of Nucleus	Electron-Positron Pair Production, $k_n \sim Z^2(E \geq 1.02MeV)$			
Electric Field of Electrons	Electron-Positron Pair Production, $k_e \sim Z(E \geq 2.04MeV)$			

In equation 2.1 we gave the monochromatic form of the Lambert-Beer law. However, the case of a monochromatic beam and homogenous material is rare in real world applications of x-ray microscopy. Below in Equation 2.5 is the Lambert-Beer law modified for a polychromatic x-ray beam and a heterogeneous material:

$$I(L) = \int_0^{E_{max}} I_0(E).e^{-\int_0^L \mu(x).dx}.dE \tag{2.4}$$

Where I is the intensity of the beam, and E is the energy distribution of the beam. Where L, the distance through which the beam travelled in the material, is a line integral along which the attenuation coefficient μ changes with x (a point in space along L). Since attenuation is also proportional to energy this is an important distinction to make, as seen later, the choice of mean spectrum energy is important in applications of x-ray imaging.

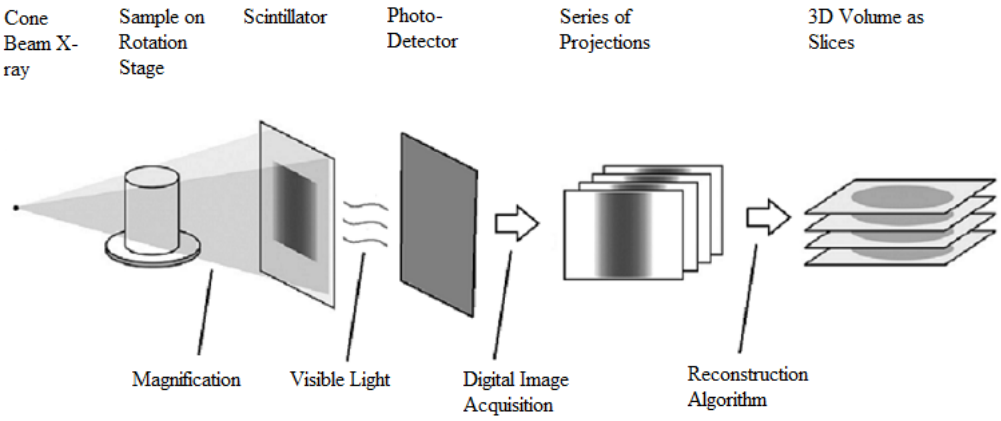

FIGURE 2.3: Schematic of the process of acquiring 3D images with XCT from a cone beam laboratory x-ray source; from the imaging set-up, to acquisition of projections, and reconstruction into a 3D volume. Source: Adapted from Landis and Keane, 2010.

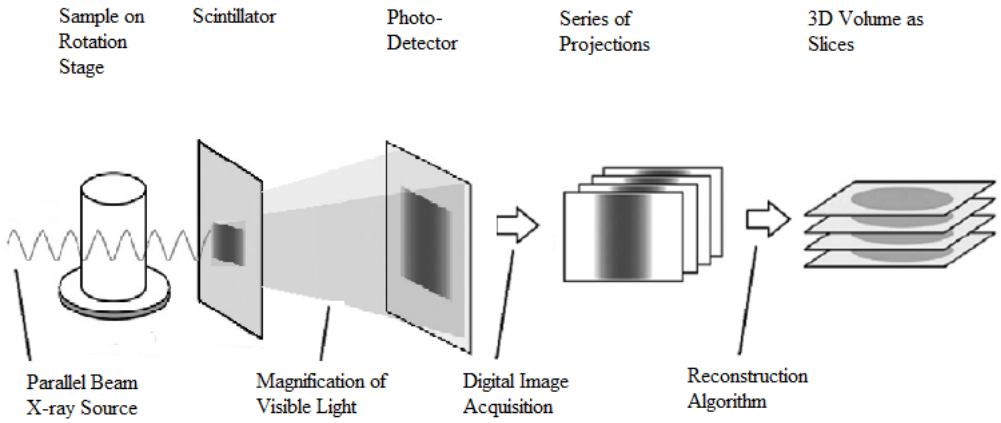

FIGURE 2.4: Schematic of the process of aquiring 3D images with XCT from a parallel beam synchrotron x-ray source; from the imaging set-up, to acquisition of projections, and reconstruction into a 3D volume. Source: Adapted from Landis and Keane, 2010.

2.1.3 X-ray Computed Tomography Fundamentals

X-ray Computed Tomography (XCT) is a non-destructive volume imaging technique that acquires 'projections', x-ray radiographs taken from a range of angles, that can be reconstructed by a computer algorithm into a 3D image. The technique was first developed for medical imaging by Hounsfield and Cormack, who won the Nobel prize in physiology in 1979. By considering attenuation theory, section 2.1.2, we can see that tomograms are fundamentally 3D maps of x-ray absorption. In figure 2.3 we illustrate a cone beam set-up which is common in lab-based sources, however recent models often have different beam geometries. For example the Xradia Ultra is a transmission x-ray microscope (TXM) that focuses the x-rays onto the sample position. Generally, in lab-based sources, a three-dimensional digital volume of a sample is produced by XCT by the steps shown in Figure 2.3. First a polychromatic x-ray beam passes through the object, the signal is enlarged through geometric magnification due to the 'cone' shaped beam and is converted to visible light at the scintillator. The detector captures the visible light and converts it into electrical signals, which are then saved in memory. This information is then read as one 2D image, i.e. a radiograph. In attenuation contrast set-ups each pixel in the radiograph can be thought of as a measure of the intensity, I, see Equation 2.5, of the beam at the detector position after travelling through the sample. In order to improve this measure, imaging artefacts caused by a false image on the x-ray detector (a baseline charge in certain pixels of the detector independent of photons striking it) are removed by flat field correction. Projections are captured at different angles by the same process as the sample rotates. The projections are then reconstructed into a 3D image by a computer algorithm.

Alternatively at synchrotron sources a parallel beam set-up is usually used, see Figure 2.4. In this case a parallel beam illuminates the sample and is converted to visible light at the scintillator. The visible light is then magnified through an objective lens where it then illuminates the detector. The remainder of the process is similar to that for a cone beam set-up. The use of synchrotron radiation can have many advantages for XCT experiments, mostly due to its superior brilliance. A brief and generalised summary of the advantages and disadvantages of laboratory vs. synchrotron XCT

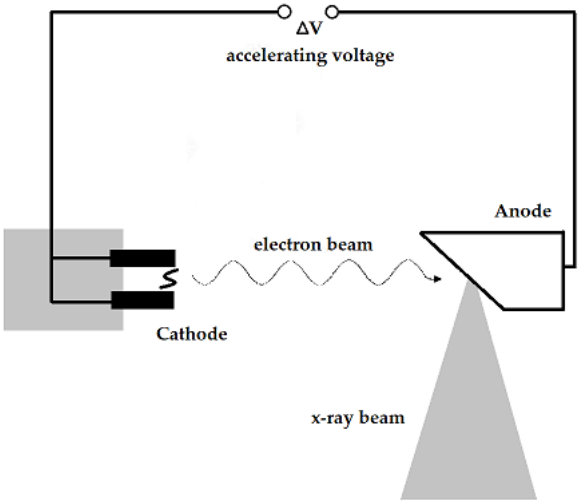

FIGURE 2.5: A schematic of the operating principle of an x-ray tube.

is presented below in table 2.2.

2.1.4 X-ray Sources

There are two common ways to generate x-rays for XCT experiments. First is the x-ray tube, found in most laboratory XCT machines. An x-ray tube consists of a anode and cathode in an enclosed evacuated enclosure. The cathode, which is usually made of tungsten, is heated by the joule effect until enough energy has been input to overcome the work function of the metal and liberate electrons from the tungsten filament of the cathode (Thompson and Leach, 2017). A voltage across the anode/cathode then causes these liberated electrons to accelerate towards the anode. The accelerated electrons will then interact with the matter of the anode, often made of molybdenum or tungsten (Thompson and Leach, 2017), although many other targets are available. The high speed electrons then interact with the matter and produce x-rays which escape from the surface of the target anode, forming a cone beam of x-rays, as shown in figure 2.5. X-rays are produced from three electron - matter interaction events (Thompson and Leach, 2017):

1. The electrons are decelerated by the nucleus of an atom, this deceleration will emit an x-ray photon with energy proportional to the momentum lost by the electron. This is termed 'bremsstrahlung' radiation (from the Germen words for breaking and radiation). Typically, one electron will emit several photons

TABLE 2.2: A generalised comparison of the advantages and disadvantages of Laboratory XCT and Synchrotron XCT.

Laboratory XCT	**Synchrotron XCT**
Resolutions from 100 μm to 50 nm. Easier to image samples of different sizes due to the cone beam. Sample sizes from 300 mm to 50 μm. Magnification determined from cone beam geometry.	Resolutions from 20 μm to 30 nm. The smaller parallel beam illuminates small area, thus sample size is limited by beam size. Sample sizes from 50 mm to 20 μm. Magnification determined by objective lenses after the scintillators.
Acquisitions from minutes to many hours. Therefore well suited to longer timescale experiments such as (slow) fluid drainage in tight rock samples.	High flux, high brightness enabling up to 20 tomograms per second. Therefore ideal for fast experiments.
Limited number of machines are capable of phase contrast. Broader spectrum at higher energies mean high contrast systems are preferable.	Excellent phase contrast, no beam hardening (with monochromatic beam), high signal to noise (greater flux). Therefore ideally suited to low contrast systems, such as soft tissue samples.
The sample needs to be very close to the source to achieve high resolutions making the accommodation of rigs around the region of interest problematic.	Typically appropriate for in-situ experiment as the rigs can easily fit in the hutch without compromising magnification due to beam geometry. Large source to sample and sample to detector working distances.
Easy access to large number of commercially available machines. Ideal for routine scanning in metrology and quality assurance.	Limited access to a few bespoke beamlines worldwide. Only appropriate for one off experiments where lab-CT is insufficient.

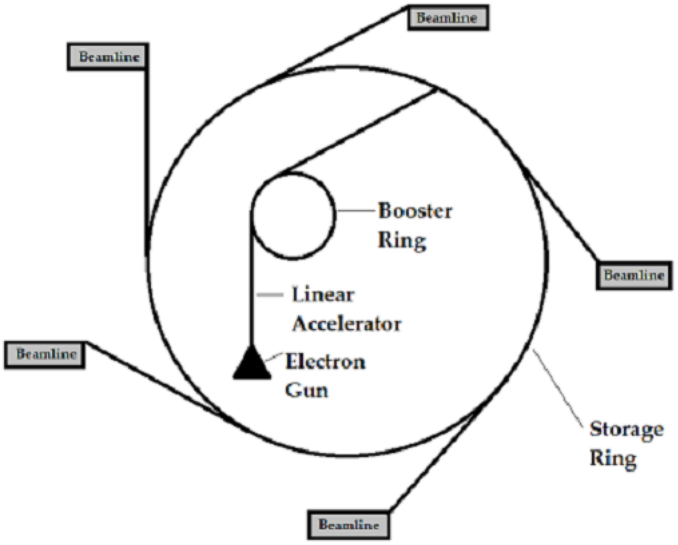

FIGURE 2.6: A schematic of the layout of a synchrotron. N.B. electrons do not in reality travel in a true circle, rather a polygon due to bending magnets and insertion devices that direct the path of the electrons.

in a series of decelerations. This cascade of decelerations creates a continuous spectrum of x-rays and constitutes the majority of x-rays in a typical x-ray tube spectrum.

2. Characteristic x-rays are emitted when an electron 'knocks out' an electron from an orbital of an atom. An electron from an outer orbital will then fill this vacancy, in doing so it loses energy, emitted in the form of a x-ray photon with a characteristic energy.

3. The electron directly collides with the nucleus of the atom, all the energy of the collision is transferred to a high energy bremsstrahlung photon. This is a low probability event.

The second method is using synchrotron radiation. A simplified schematic of a synchrotron is shown in figure 2.6. It consists of an electron gun which fires electrons into a linear accelerator. The line accelerator accelerates the electrons to high (relativistic) speeds into the booster ring which in turn 'tops-up' the electron beam in the storage ring (Willmott, 2019). A 3rd generation synchrotron can typically store a beam of a 1 - 8 GeV (Bilderback, Elleaume, and Weckert, 2005). A vacuum is maintained to prevent electrons scattering from air molecules and magnets maintain the

motion of the electrons around the synchrotron (Willmott, 2019). Tangential from the storage ring are beamlines, at the end of which are beamline endstations where synchrotron users can perform different experiments depending on the radiation developed at any given beamline around the ring. X-rays are developed by bending magnets or Insertion Devices (ID), installed at the opening of each beamline (Willmott, 2019).

Bending Magnets (Willmott, 2019): Synchrotrons consist of a series of straight sections with bending magnets directing the electron beam into each section. At each bending magnet the beam accelerates in a transverse direction with respect to the path of the beam, induced by the Lorentz Forces applied to electrons as they travel through the magnetic field. Acceleration of charged particles emits electromagnetic radiation, as discussed in regard to 'bremsstralung' radiation above. This radiation propagates along a beamline where it can be used in a beamline endstation by users.

Insertion Devices (ID) (Willmott, 2019): There are two types of ID, wigglers and undulators. Both operate by a mechanically analogous method. Effectively, the ID can be considered as a series of bending magnets at a straight section of the ring that are concatenated such that a alternating magnetic field is created which directs the electron beam along a sinusoidal path. The construction of the ID consists of two banks of alternating permanent or electro-magnets set directly opposite each over such that north pole is opposite south pole, followed by south pole opposite north pole, et cetera. The associated acceleration of travelling this path causes the particles to emit synchrotron radiation. At undulators the radiation from each bend in the trajectory constructively interfere with one another. The effect of this is to form one or multiple spectral peaks. These peaks are called harmonic peaks. Moreover, the beam is highly collimated and has high spectral brightness. On the other hand, wrigglers create a broad continuous spectrum of collimated (but less so) bright radiation without harmonic peaks.

2.1.5 Signal Detection

Once x-rays have been generated and propagated through the sample volume, the resultant signal, which contains information on the structure of interest, must be detected. Solid state x-ray detectors, and solid state scintillators coupled to CCD/CMOS detectors, have effectively entirely replaced gas ionisation detectors in modern applications of XCT (Thompson and Leach, 2017). Indeed, advances in detector technology have been a boon to 4D XCT experiments as increased temporal resolution requires detectors with good quantum efficiency. As already described above, the detector will consist of a paired scintillator and a photodetector, and in the case of parallel beam set-ups an objective between them for magnifying the visible light signal from the scintillator. Scintillators fluoresce light through the process of scintillation and ideally do so rapidly with a high light yield (Leo, 1994). Scintillator materials used in XCT applications are usually inorganic single crystals or transparent ceramics. The structure of this material will determine the quantum efficiency of the scintillator at a particular energy, some examples for x-rays include; sodium iodide doped with caesium (single crystal), zinc sulphide (single crystal), and Lutetium Aluminium Garnet (LuAG, both as single crystal and transparent ceramic) (Leo, 1994; Thompson and Leach, 2017; Fuchs, Kachelriess, and Kalender, 2000; Li et al., 2017; Yanagida and Fujimoto, 2014).

During scintillation the incident x-rays will interact with the matter of the scintillator by exciting electrons from the valance band of the scintillator crystal into the conduction band, thereby creating a loosely bound electron-hole pair (Leo, 1994). The electron-hole pair will then drift through the lattice until it reaches an inhomogeneity site induced by a dopant or impurity. Here the inhomogeneity has electron bands in the 'forbidden' region between the valence and conduction bands of the scintillator crystal, thereby allowing the electron to rapidly de-excite, hence emitting light (Leo, 1994). The dopants are chosen so that the wavelength is in the visible light range (Leo, 1994). Other less rapid scintillation mechanisms will also occur due to meta-stable states in the material (Leo, 1994). The scintillation light is then directed to a photodetector, often a photomultiplier tube (Leo, 1994; Thompson and Leach, 2017). Here the incident light will release electrons on the photocathode via

the photoelectric effect. The electrons will then cascade through a series of dynodes held at different potentials in order to create a robust output signal (Thompson and Leach, 2017).

The quality of a XCT detector is determined by characteristics such as; detector efficiency, light yield, energy resolution, dynamic range and temporal characteristics such as stability (ability to respond consistently after prolonged irradiation), response time and after-glow (Thompson and Leach, 2017). Detector efficiency is determined by a composite of quantum efficiency, i.e. the ratio of absorbed x-rays to those contributing to the output signal, and fill factor, i.e. the ratio of x-ray sensitive area to non-detecting area (Thompson and Leach, 2017). For example, solid state detectors are very advantageous compared to xenon gas ionisation detectors due to their higher quantum efficiency due to their higher z, see Section 2.1.2 (on attenuation theory). Moreover, they are much denser, hence they have much higher volume specific photon yields. Response time is the ability of the detector to detect an event and then recover to detect a second independent event, it is determined by the speed of the scintillation mechanism described above (Leo, 1994), and can be slowed by issues such as after-glow (where the previous image erroneously persists on the detector) causing detector 'pile-up' due to slower secondary scintillation events(Thompson and Leach, 2017; Li et al., 2017). For example, in the case of LuAg transparent ceramic scintillator from Li et al., 2017, it was found that the fast component of the scintillation response occurred at 59 ns whilst the slower response occurred at 620 ns.

2.1.6 Reconstruction

Once the projections have been acquired by the detector they can be 'reconstructed' into a 3D model of the sample using a computer algorithm. As discussed in section 2.1.2, the x-rays are attenuated according to the Lambert-Beer law. This states that the intensity value, I, of every pixel at the detector position is a function of the attenuation coefficient, μ, and the path, L, of the x-rays. The line integral, ρ_L, of a x-ray

traveling through a sample along the line L can be written as:

$$\rho_L = ln(I_0/I) = \int_0^L \mu(x)dx \tag{2.5}$$

This is the same line integral as the exponent in Equation 2.5. Every voxel's attenuation coefficient, μ_i, contributes to the total attenuation as the beam travels along the path L. Thus, every pixel in a projection describes the line integral of the distribution of attenuation coefficients along L. We can now see that the problem reconstruction solves is to assign a value of μ to discrete volumes of space from ρ_L values, where ρ_L is calculated from the pixel intensity values of the projections, for a range of orientations of L corresponding to different angular positions as the sample rotates (Landis and Keane, 2010).

There are a many types of reconstruction algorithms. The most commonly applied methods are analytical techniques such as Filtered Back Projection (FBP) algorithms and the Feldkamp, Davis & Kress (FDK) algorithm (Thompson and Leach, 2017). Descriptions of how such backprojection algorithms work can be found in Grangeat, 1991 & Hsieh et al., 2013. Typically back projection algorithms quickly come to good solutions if the quality of the data is high. That is if there are enough projections (see Nyquist criterion, equation 2.8) and good signal-to-noise (Coban et al., 2015). However, Coban et al., 2015, demonstrate how analytical techniques perform poorly as the number of projections is reduced. Iterative algebraic methods such as Conjugate Gradient Least Squares and Simultaneous Algebraic Reconstruction Technique (SART) often output higher quality results when reconstructing challenging datasets (Coban et al., 2015; Jørgensen et al., 2021).

2.1.7 Artefacts

Many factors can determine the fidelity of a reconstructed image with respect to real structure. Negative factors will cause artefacts in the reconstructed image. Examples of artefacts include beam hardening artefacts, ring artefacts, and motion artefacts (Davis and Elliott, 2006). These are shown in figure 2.7. Beam hardening occurs because low energy, or 'soft', x-rays are attenuated more readily than high energy x-rays. As a result, as x-rays travel along a path through a material the beam will be

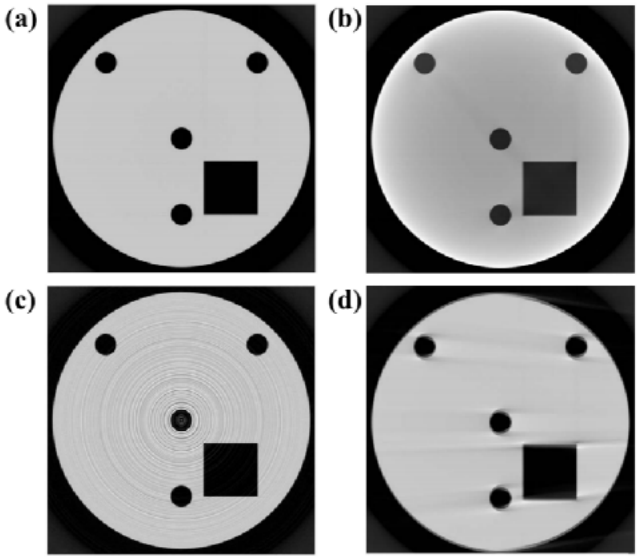

FIGURE 2.7: Typical artefacts in a cylindrical sample with geometric voids; (a) high fidelity reconstruction, (b) beam hardening artefacts, (c) ring artefacts, (d) motion artefacts. Source: Davis and Elliott, 2006.

constituted of a larger fraction of higher energy photons at positions further along the path compared to the original beam. Therefore, at a position b, further along the line path, the μ value from the reconstruction appears lower compared to position a, at the beginning of the line path (Ahmed and Song, 2018). Due to the rotation of the sample during the acquisition this leads to a cupping artefact where pixels appear brighter at the edges of the image compared to the centre (Davis and Elliott, 2006), see figure 2.7.b. Ring artefacts are caused when a pixel in the detector is defective or poorly calibrated. As the sample rotates this pixel will trace a ring in the reconstructed image (Vo, Atwood, and Drakopoulos, 2018), see figure 2.7.c. Motion artefacts are caused by unwanted motion of the sample during the acquisition of the tomogram and will result in double edges and streaking (Davis and Elliott, 2006), see figure 2.7.d. In general these artefacts should be reduced by steps taken during acquisition, for example; filtering the beam to reduce beam hardening (Ahmed and Song, 2018), carefully calibrating the detector before imaging to reduce ring artefacts, and improving the stability of the sample during acquisition in the case of motion artefacts. Moreover, in many cases specific image post-processing algorithms exist in order to reduce the effect of artefacts (Dremel et al., 2014; Ahmed and Song, 2018; Vo, Atwood, and Drakopoulos, 2018).

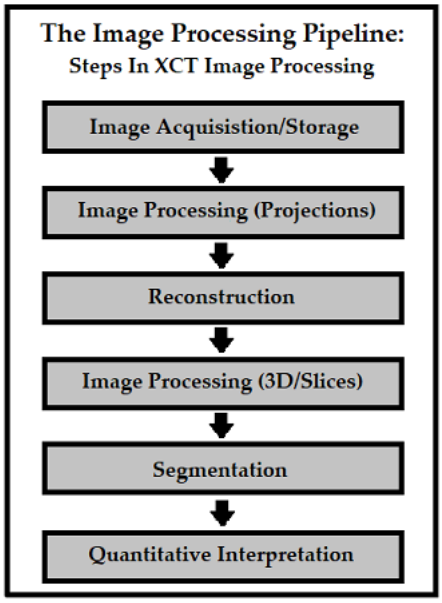

FIGURE 2.8: Typical image processing steps

2.1.8 Image Processing

Projections and reconstructed 3D images or slices are saved as digital images. In absorption contrast XCT the images will have one colour channel. This means each pixel can be represented by a single element in a array rather than, for example, three elements in a three channel Red-Green-Blue (RGB) image, and is typically rendered in grayscale. The intensity of each pixel is described by a binary number. For example, in an 8-bit image (where bit depth = 8) each pixel is described by an 8-bit binary number from 0 to 11111111 (255 in decimal). Therefore, each pixel in a 8-bit single channel image array can have 256 possible values (shades of gray if rendered in grayscale). Understanding this, we can calculate the size of an image:

$$size = X \times Y \times Z \times (2^k)^C \tag{2.6}$$

Where X, Y, Z is the length of the x, y, z axis in pixels, where k is the bit depth, and where C is the number of colour channels. Clearly, for a 2D image we can simply make $Z = 1$ and for a 4D image (3D + Time) we can add another axis, T, to equation 2.6, where T is the number of time points in a 4D data set composed of images of equal size and bit depth.

Image Processing, Projections: One of the key aspects to image processing for XCT is eventually being able to quantitatively interpret the data. A typical workflow to get to this point is illustrated in figure 2.8. It is useful to develop a programmatic data processing pipeline so that the steps leading to quantitative results are well documented, repeatable and modifiable. For this reason, for complex data pipelines, it is often best practice to use scriptable languages like python and Matlab so that each step is well documented rather than analysis being spread out on disperse software packages. That being said, software packages like Avizo™ and IPSDK™ make it relatively simple to track each step in a pipeline, however the onus is still on the practitioner to keep accurate up-to-date documentation detailing each step of a workflow. Finally, python has a active community that creates a number of powerful open-source tools for image processing. Open-source software makes workflows verifiable and repeatable for everyone, without having to pay for expensive industrial or academic software licenses.

Once the projections are saved as digital images they should be enhanced by removing artefacts. A key step in most XCT workflows is to apply dark-flat-field correction. This is a necessary step due to degradation of the detector and variations in the beam overtime, for example; charging, dust and scratches can build up on the detector overtime leading to ring artefacts, and beam inhomogeneity can occur during beam top-up. By normalising each projection with a flat field image and a dark field image, as in equation 2.7, such artefacts can be significantly reduced. A flat field image is an image taken under the same conditions (spectrum, magnification, filtering etc.) as the projection but with sample removed from the field of view. A dark field image is acquired whilst the beam is off, and can be considered the detectors baseline image. The normalised projection, N, is calculated as so:

$$N = \frac{P - D}{F - D} \tag{2.7}$$

Where P is the original projection, D is the dark field image and F is the flat field image.

Other corrections are also applied at this step in the workflow, that is, to projections, sinograms or during the reconstruction. An example is distortion correction, often in parallel beam set-ups the optics after the sample position distort the beam so that photon paths are no longer parallel to each over. This has the effect of applying radial stretching ('barrel' like distortion), or compression ('pin-cushion' like distortion), to parts of the image (Vo, Atwood, and Drakopoulos, 2015). Distortion correction from Vo, Atwood, and Drakopoulos, 2015 solves this rapidly in sinogram space based on work from the Diamond Light Source I12 beamline. Moreover, ring removal correction is applied in sinogram space since rings will appear as straight lines across a sinogram, these are easily removed with convolutional image filters (Vo, Atwood, and Drakopoulos, 2018).

Beam hardening correction can also be applied at this stage, a typical method would be based on polynomial correction, a linearisation method. As discussed above beam hardening is the result of non-linearity of the attenuation coefficient, μ, with respect to line path length due to μ's energy dependence. However, if for a range of path lengths, the spectrum and the materials μ value is known it is possible to calculate the intensity at each point along the line path. Therefore, by fitting a polynomial function to the data points, a correction function can be obtained for a single material only, and the projections can then be reconstructed using FBP (Dremel et al., 2014; Ahmed and Song, 2018). This is a simple, fast and effective beam hardening correction method, however it is limited in it's application to single material systems. A range of other such linearisation methods exist that attempt to reconcile issues with multi-material systems, such as algorithms from Man et al., 2001, Brabant et al., 2012 and Segel et al., 1987 to name a few. Linearisation methods remain the most used in practical applications of industrial CT (Ahmed and Song, 2018).

Image Processing, 3D images & Slices: Once the projections are processed and reconstructed the next step is to process the resulting 3D images, or slices, so that they can be easily segmented. This will initially include steps such as cropping (reduces X, Y, Z in Eqn. 2.6) and converting to a lower bit depth (reduce k in Eqn. 2.6) so that processing and segmentation tasks are less computationally intensive due to the size of the image.

Global denoising filters are often applied. Global filters work by convolving a kernel through the entire image with the aim of reducing noise in the image. Noise can be considered random fluctuations in the intensity values of pixels. Denoising is particularly important with a view to segmentation because if the noise range overlaps with a threshold then some noise will be erroneously included in the segmentation. Two local convolutional global denoising filters that are commonly applied are the local mean filter and the Gaussian filter (Heinzl, Amirkhanov, and Kastner, 2018). The local mean filter is the most basic and operates by moving a kernel of a predefined size, often a square much smaller than the image, through the image pixel by pixel. The mean intensity within the kernel is calculated and output as the smoothed value of the pixel. Different applications of the local mean filter are shown in figure 2.9 where we varied the kernel size using python's scikit-image module (Walt et al., 2014). The figure shows how as the kernel size is increased the intensity of the smoothing/blurring effect increases. The gaussian filter works similarly. However, the values are weighted by a gaussian distribution such that pixels near the pixel of interest are favoured compared to those at the edge of the kernel, further away from the pixel of interest.

Figure 2.9 shows the blurring effect of local filters, this is problematic for XCT image processing as it will blur edges in the image. Sharp edges are important for creating accurate segmentations of the interfaces of phases of interest. Edge-preserving filters, such as the non local mean (NLM) filter, are therefore useful tools in image processing. NLM filtering replaces the value of the pixel of interest by the weighted mean of pixel values in small patches centred on other pixels distributed through the whole image, with the mean calculated so that pixels that have patches with similar grey level neighbourhoods to the current patch centred on the pixel of interest are weighted favourably (Buades, Coll, and Morel, 2005). In practical applications, particularly in XCT where NLM is applied to large images, the quadratic relationship between computational complexity and number of pixels can be limiting. In these cases the algorithms will often reduce the area from which patches are taken, from the whole image to a smaller subsection around the pixel of interest, as well as taking other measures to reduce computation (Karnati, Uliyar, and Dey, 2009). In figure

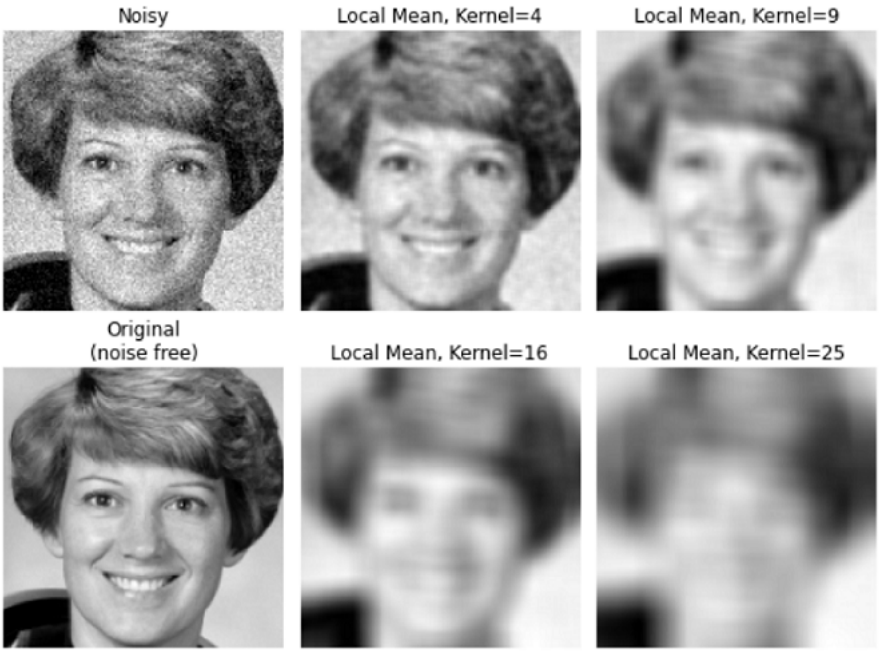

FIGURE 2.9: The effect of local mean smoothing on a noisy image of astronaut Eileen Collins. Four different square kernels were used, with edge lengths of 4, 9, 16, & 25 pixels.

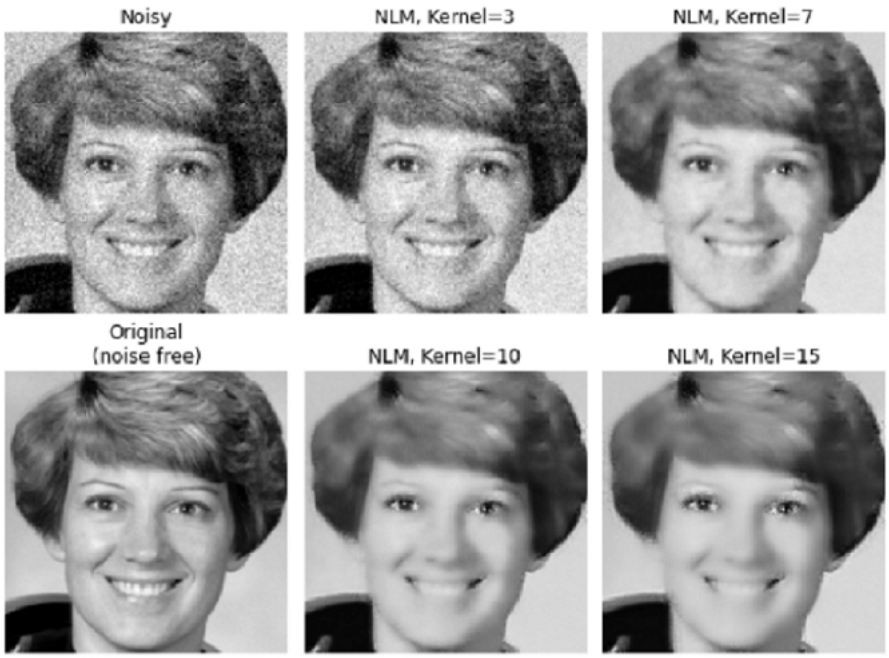

FIGURE 2.10: The effect of non local mean smoothing on a noisy image of astronaut Eileen Collins. Four different square kernels were used, with edge lengths of 3, 7, 10, & 15 pixels within a search area of 40×40 pixels.

2.10 we show the effect of applying NLM smoothing to a noisy image with varying patch (a.k.a. kernel) sizes using scikit-image (Walt et al., 2014). Comparing figure 2.9 & 2.10 one can clearly see the comparatively good edge-preserving properties of the NLM example.

Segmentation: Once the images have been sufficiently enhanced, the next step in the data analysis pipeline (fig 2.8) is to segment the image. The aim of segmentation methods is to select the pixels in an image which represent a particular region or phase of interest, and then to assign these a particular pixel intensity in the output image. Typically the phase of interest will be assigned an intensity equal to 1, with all other (background) pixels being assigned 0, thereby creating a simple binary image or boolean array. This can be repeated for each segment in the original image, eventually combining the set of binary images as so: $Segmented\ Image = 1^{*}Binary_1 + 2^{*}Binary_2\ \ ...\ \ + n^{*}Binary_n$. With each segment being assigned pixel intensities of 1, 2, 3 etc. and the unassigned background having an intensity of 0, in a single fully segmented image. Segmentation is necessary for quantification of the volume fraction of phases of interest, voids, pores, inclusions or fibres (Heinzl, Amirkhanov, and Kastner, 2018). Furthermore, the segmentation result is needed for further calculations such as the computation of lengths, diameters, or shape factors in metrology applications (Heinzl, Amirkhanov, and Kastner, 2018).

The most fundamental segmentation techniques are the global histogram or threshold based techniques. These are useful when it is possible to segment the entire image based on the grayscale ranges of the phases of interest. For the case of segmenting bimodal histograms into a binary image that separates a phase of interest from the background, several methods exist. In an ideal case where the bimodal histogram has two clear peaks and a trough, see figure 2.11, simple methods such as simply choosing the low point between the two peaks or choosing the mid-point between the two peaks (ISO_{50} method) can be effective. A classic and widely used method is Otsu's method (Otsu, 1979). Otsu, 1979, selects an optimal threshold via the discriminant criterion; that is, by maximizing the discriminant measure, .i.e. the measure of separability of resultant classes in gray levels. Otsu's method is quite

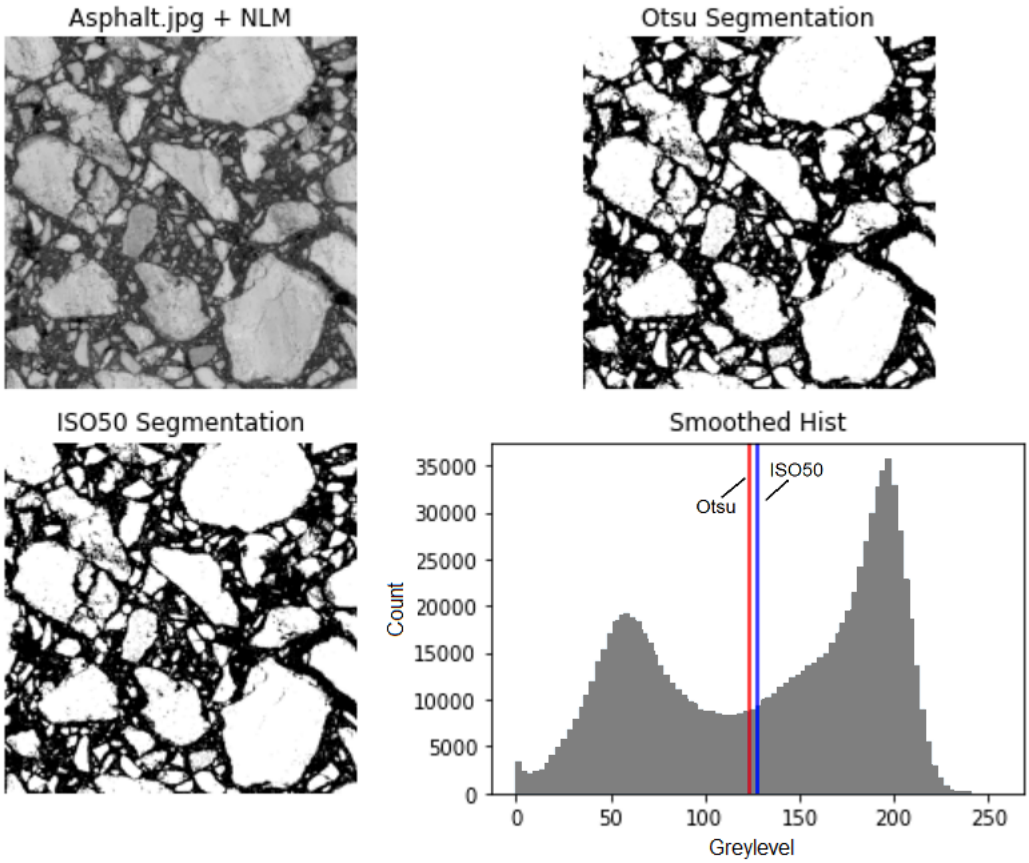

FIGURE 2.11: The application of global threshold based segmentation using scikit image (Walt et al., 2014), to a macrophotography image of asphalt.

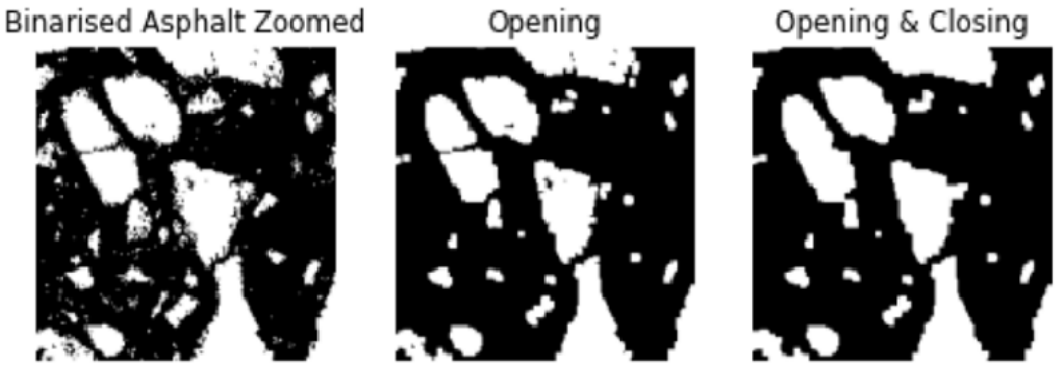

FIGURE 2.12: The application of binary opening and closing to a magnified binary image of asphalt. Binarisation was performed via Otsu's method as in figure 2.11 and zoomed into a 200×200 pixel area. Binary opening and closing was performed with a 4×4 square kernel.

robust and works even where there is no clear bimodal histogram, due to, for example, the trough low-point being obscured by noise or one of the peaks being much smaller than the other. Local thresholding methods are also a useful technique, here the threshold is adjusted for each voxel depending on its surrounding grey level neighbourhood (Heinzl, Amirkhanov, and Kastner, 2018).

Alternative effective techniques for segmentation include the watershed method, such as that provided by openCV (Bradski, 2000). The watershed method is named after the geological concept of a line that separates neighbouring catchment or drainage basins in a landscape. The watershed algorithm will assign the height of pixels based on their intensity so that bright pixels are considered high points in a topological map of the image. The local minima (like valleys in a landscape) are then flood filled by different labels (different coloured water). As the water level rises, the different labels would start to merge, this is prevented by building 'barriers' to prevent label mixing. Eventually all the labels have reached the same topological height as the local maxima (peaks). Where the different labels met (the barriers) is the watershed that divides neighbouring catchment basins. This is a useful technique when neighbouring areas with continuous and similar grey levels need to be separated. Areas of research where this may be useful include separating pores, particles and cells that share edges in a micrograph.

Once the segmentation has been applied it is frequently necessary to remove noise

from the segmentation. If there is sufficient noise in the original image this can easily lead to noise in the segmentation. Morphological operations provide a powerful tool to further improve the fidelity of a segmentation. The two most common are binary erosion and binary dilation. The first removes, or 'erodes', pixels from all edges of a binary segment by a structuring element and the second achieves the opposite effect. Performing erosion followed by dilation successively with the same element is called a 'binary opening', this will remove all binary noise from the image smaller than the structuring element. The opposite, a 'binary closing', a dilation followed by erosion, will remove all binary holes in the image smaller than the structuring element. An example of this process is shown in figure 2.12 using scikit image (Walt et al., 2014). Once a clean segmentation has been achieved one completes the experiment by extracting useful quantitative information from the binary images depending on the objectives of the experiment.

2.2 Time Resolved XCT in Materials Science

In this project we use time resolved XCT to study filter materials. In this section we discuss key experimental considerations when using time resolved 4D XCT methods in Materials Science, with case examples.

XCT was originally exclusively a medical diagnostic tool however it soon became an important technique in a range of disciplines. Geo-scientists use XCT to quantify the internal structure of rocks in order to understand the porosity, grain structure and fluid flows within them (Cnudde and Boone, 2013; Kyle and Ketcham, 2015; Tang et al., 2019), forensic science has analysed tool marks on bone in order to determine likely cause of injury (Alsop et al., 2021; Baiker-Sørensen et al., 2020; Rutty et al., 2013), and cultrual heritage and natural history specimens can be probed and conserved with digital twins using XCT (Albertin et al., 2019; Wilson et al., 2017). Materials scientists are concerned with the effect of microstructure on the performance of engineering materials and often make use of XCT. Some areas of research in materials science that often make use of XCT include; metrology of additively manufactured parts, corrosion, and fibre analysis in polymer composites, to name a few (du Plessis, Yadroitsava, and Yadroitsev, 2020; Wu et al., 2019; Garcea, Wang, and Withers, 2018). In materials science time resolved, time lapse, temporal, or 4D (3D + time) XCT experiments are required when we need to investigate how internal structures and volumes change with time, examples include; crack propagation in mechanical testing (Gudla et al., 2020), fluid transport in porous materials (Dobson et al., 2016), and lithiation in batteries during cycling (Paz-Garcia et al., 2016).

2.2.1 Acquisition Parameters for Time Lapse XCT.

There are a number of factors that will effect the quality of the time lapse data acquired during such an experiment. These will include typical parameters considered during XCT acquisition; voltage, power, spot size, magnification, filtering, number of projections and other parameters (Zwanenburg, Williams, and Warnett, 2021). However, in the case of time lapse XCT it is usually critical to consider the trade-off of these parameters with respect to image quality and acquisition time. Furthermore

acquisition parameters exist that are unique to time lapse experiments. Important parameters and their implications for time lapse data are described below:

- *Synchrotron vs. Laboratory XCT.* As previously discussed, see Table 2.2, synchrotron sources offer excellent brightness and the beamline hutch offers plenty of room for setting up in-situ rigs. This brightness means that high flux at low x-ray energies can be developed for fast imaging of low contrast systems. Similarly enough flux can be developed to achieve fast imaging with monochromatic beams (Dobson et al., 2016). However, due to high demand at synchrotron sources beamtime can be difficult to obtain, particularly for longer experiments (> 1 week). Furthermore, synchrotron is not ideal for large samples as the FOV is limited in size by the diameter of the beam. Laboratory XCT often offers a viable alternative for time resolved experiments but is comparitevely more limited by the trade off of acquisition speed and resolution due to lower flux (Vavřík et al., 2017; Yang et al., 2015).

- *Magnification.* In parallel beam set-ups the choice of objective lens directly determines the magnification, and consequently pixel size, of the image. In general, assuming all other factors remain constant, as magnification increases less flux will be incident on the objectives FOV, thus requiring longer acquisition times for good signal-to-noise ratio.

  In cone beam laboratory set-ups magnification is determined by the ratio of source-to-detector distance and source-to-object distance. Thus, to optimise magnification and minimise pixel size it is beneficial to put the sample as close to the x-ray source as possible. Optimising acquisition time requires that the entire beam illuminates the ROI, thus optimising flux. However, the ROI is often too small to optimise the latter, meaning longer acquisition times are needed for good signal-to-noise at high magnifications. Furthermore, these experiments often require specific sample environments or test rigs that create the conditions necessary for in-situ or in-operando experiments. These set-ups need to be able to rotate so that projections can be acquired from multiple angles for tomographic reconstruction. The environments and rigs often take

up significant room around the ROI in the laboratory machine, thereby limiting the source-to-object distance, thereby lowering maximum magnification allowed by the set-up and further increasing acquisition times at high magnifications.

- *Spectrum.* The choice of beam energy is important for both lab and synchrotron applications, controlled by installation of optical components (mirrors, filters, monochromators) and the spectrum developed from the ID gap at synchrotron sources, and the accelerating voltage in lab sources. Higher maximum energy will result in more penetrating x-rays that may be needed for highly attenuating samples. High maximum energies can also lower acquisition time as more x-rays reach the detector, however with detriment to contrast and increased beam hardening artefacts if unfiltered. High energy can also create more scattering and zinger artefacts. Filtering can be used to remove unwanted low energy x-rays to make a more penetrating beam with a high mean energy that prevents beam hardening artefacts. However, including a filter will lower the total flux and therefore increase acquisition time. Lower beam energy is preferred for low contrast systems. However, higher mean energy is usually needed from lab sources in order to develop enough flux, particularly in the case of fast time resolved XCT, this can make imaging low contrast samples more challenging.

- *Beam flux.* At synchroton sources the choice of a white beam, pink beam, or a broader distribution of beam energies compared to a monochromatic beam will decrease acquisition times, due to higher beam fluxes at the ROI, but can introduce more artefacts and noise from beam hardening and scattering effects. These can lower the image quality and spatial resolution.
  Higher beam fluxes are achieved in lab sources by increasing the current (and therefore power assuming voltage is constant). This will have the knock-on effect of increasing the spot size and lowering image quality due to the Penumbra effect (Zwanenburg, Williams, and Warnett, 2021). Flux can be further maximised by removing filters, once again with a trade-off with respect to image quality.

- *Exposure Time.* Exposure time is proportional to the flux that reaches the detector per projection, greater exposure results in brighter projections, better signal-to-noise, but longer acquisition times. When trying to maximise speed and image quality simultaneously it is important to find the minimum exposure that results in acceptable image quality within the aims of the experiment.

- *Number of Projections.* Under sampling with fewer projections will directly favour time resolution at the detriment of image quality (Villarraga-Gómez and Smith, 2020; Zwanenburg, Williams, and Warnett, 2021). The theoretical minimum number of projections for a faithful reconstruction is found using the Nyquist sampling criterion (Herman., 1980), stated below.

$$N = \frac{\pi}{2} d \tag{2.8}$$

  Where N is the minimum number of projections and d is the diameter of the detector in pixels. Although undersmapling with respect to the Nyquist sampling criterion will have a negative effect on image quality, Villarraga-Gómez and Smith, 2020, found it will not neccesarily effect accuracy for dimensional analysis. Once agian finding the minimum number of projections that results in acceptable image quality within the aims of the experiment is important.

- *In-situ Test Rig & Sample Environment Design.* Time lapse in-situ experiments often require rigs or environments to produce the experimental conditions understudy. It is important to try to optimise sample design, and sample environment or test rig design, to optimise the flux that can reach the ROI. This means using materials that are more x-ray transparent and using as little material as possible along the beam path to prevent attenuation. In the case of lab CT the rig or environment should be designed such that the sample can be placed as close to the source as possible (if high magnification is required).

- *Rotation Stage Operation.* Continuous rotation of the stage whilst projections are procured over a $0.1 - 0.5^{\circ}$ arc in a 'fly scan' will increase acquisition speed by a factor of approximately 1.7 times compared to stopping rotation for each projection (Zwanenburg, Williams, and Warnett, 2021). Furthermore, for fast

tomogram acquisition rates, the time between fly scans should be minimised by using a rotation stage that can rotate continuously, or, for stages with limited degrees of freedom, by making sure that acquisition occurs from $0^\circ \rightarrow 180^\circ$ and from $180^\circ \rightarrow 0^\circ$. This reduces time spent waiting for the stage to return to the 'starting' position of the subsequent scan.

- *Dark and Flat Field Imaging*. Time between scans can be reduced by procuring fewer dark and flat field images. Often a set of dark and flat field images is procured for every tomogram. This means moving the sample out of the beam for acquisition of the dark and flat field images and then moving the sample back for the next tomogram. By reducing the number of dark and flat fields acquired the acquisition time can be reduced. However, if significant detector charging or damage occurs between dark-flat field acquisitions image quality will be worse.

2.2.2 Literature Examples of Time Resolved XCT in Materials Science

One of the fields of materials research which requires fast time resolved XCT imaging is mechanical testing. In these experiments it is often desired to image internal cracks as they propagate through the material. For example, Gudla et al., 2020 study environment induced cracking (EIC) of an aluminium alloy that has been pre-exposed to a corrosive environment for 250 hrs. The in-situ experiment was performed in humid air (50–70 %) by fitting a tensile test rig (Deben CT5000) with wet sponges at its base. In this case study synchrotron XCT was performed whilst the sample was strained at the Diamond Light Source I13-2 imaging beamline. A CMOS detector (PCO Edge 5.5) coupled with $4\times$ magnification through the objective gave $1.6\mu m^3$ voxels. Each tomogram was reconstructed from 1200 projections with each projection having an exposure time of 0.035 seconds, thus it took 90 seconds to acquire each tomogram. Gudla et al., 2020 performed the experiment both continuously, where the sample was strained at a constant displacement rate and tomograms were acquired at regular intervals, and using a stepped method, where the sample would be strained incrementally and then 'held' (i.e. strain rate is kept as close to 0 as possible) whilst the tomogram is acquired. During this experiment

20+ tomograms were acquired per sample.

Synchrotron radiation is typically needed for this type of time resolved study. Firstly, the high brilliance of synchrotron radiation is required to illuminate the sample with enough flux to obtain sufficient signal to noise with short exposure times, 0.035 seconds, to resolve small $5\mu m$ depth cracks in a dense metallic sample. As discussed above, high flux through the ROI is very important when trying to optimise both time and spatial resolution. Secondly, it is advantageous to have a parallel beam set-up, rather than a cone beam set-up, for experiments with mechanical testing rigs or large sample environments. This is due to the geometric limitations inherent with the cone beam set-up, i.e. the practitioner wants to place the region of interest as close as possible to the cone beam source to maximise magnification. However, test rigs often prevent the sample from being placed as close to the source as would be ideal. Parallel beam set-ups at synchrotron sources circumvent this issue by using an objective lens after the scintillator, see Figure 2.4. In general synchrotron beamline hutches offer more space for straight-forward installation of rigs and environments compared to typical lab sources.

Another area of materials engineering research that widely utilises time resolved synchrotron XCT is the study of fluid transport in porous media. In these experiments the porous material is placed in a flow cell and fluids are injected through the cell. Transport of fluids in porous media is critical in applications as diverse as the transport of ions in redox flow batteries, soil permeability, and carbon sequestration in geological reservoirs (Tariq et al., 2018; Ferreira, Archilha, and Pires, 2022; Giammar et al., 2018). A case example of this comes from Dobson et al., 2016, who study flow in a gravel bed. Dobson et al., 2016, use cylindrical perspex flow cells of 6 and 25mm internal diameter filled with sandstone gravel. This created a pore matrix inside the cell with pore diameters of $10 - 150\mu m$. A 6M solution of $KI_{(aq)}$ was flowed at $40 - 100\mu L/s$ through the cell during the experiment. Using this set-up at the JEEP I12 beamline, Dobson et al. were able to demonstrate 'ultra-fast' (up to 0.05s per tomogram) time resolved imaging of flow, see Figure 2.13, this required optimising the imaging set-up. A Vision Research Phantom Miro™ 310 M camera was used for the experiment, this can capture upto 5000 fps. The fastest acquisition

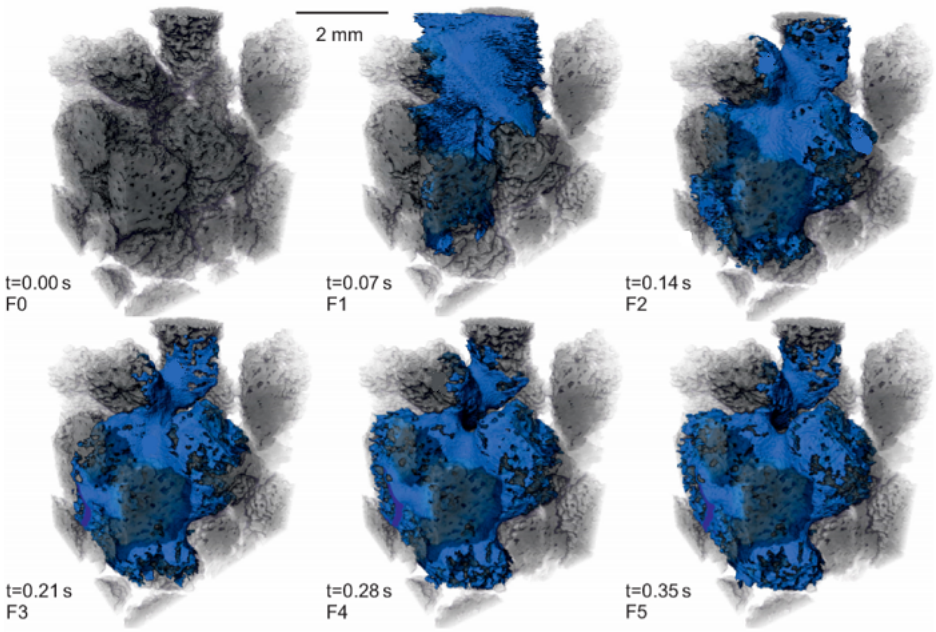

FIGURE 2.13: The first six frames from Dobson et al. showing the wetting of the sandstone gravel. The pore scale structure changed rapidly at the start of the wetting. Tomograms were acquired at a rate of 14 Hz (0.07s per tomogram). This region is a small $3.5mm \times 3.5mm \times 2.0mm$ subvolume. Source: Dobson et al., 2016.

rate of $20Hz$ (0.05s per tomogram) was determined by the top speed of the rotation stage. In order to acquire tomograms at this rate the data was deliberately under sampled such that only 250 projections were acquired per tomogram with projection exposure times of $200\mu s$ in the lower magnification ($3.8\mu m$ pixels) for the larger flow cell, and 550 projections with exposures of $90\mu s$ in the higher magnification ($2.5\mu m$ pixels) for the smaller flow cell. Different magnifications were used so that the different internal diameters of the cells fitted within the field of view. Dobson et al. tested both white beam and monochromatic beam (selectable energy range from 53 - 150 kV) for their experiment and found that although white beam could reduce scan times by 30 - 40% and produce negligible beam hardening, it produced worse contrast between low density phases, more x-ray scattering, and more noise (Dobson et al., 2016). Thus, the monochromatic beam was used.

We have now looked at cases of fast time resolved synchrotron XCT experiments with sub-second time steps (Dobson et al., 2016), and longer time steps in the order of 1 minute (Gudla et al., 2020). However, time resolved 4D experiments often do

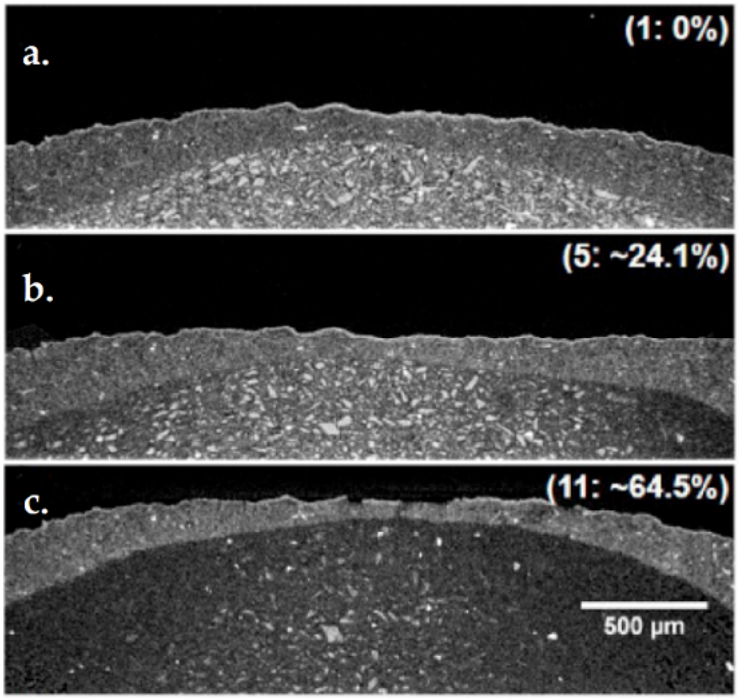

FIGURE 2.14: 16-bit grayscale tomogram vetical slices of (a) the first frame from the experiment of Paz-Garcia et al. (2016) at 0% lithiation, (b) the fifth frame at $\sim$ 24.1% lithiation, (c) the last frame (eleventh) at $\sim$ 64.5% lithiation. Source: Dobson et al., 2016.

not necessarily require fast imaging methods. For example, in applications where the material of interest can be easily cycled through evolutions and then can easily be stopped from evolving during the image acquisition, or when the the time scale of evolution process is slow. An example of the former is the discharge of battery materials. Paz-Garcia et al., 2016 study the degradation of silicon based anode materials that could be a potential candidate to replace graphite materials in Li-ion batteries. However, the lithiation and delithiation of material that occurs during use is associated with large deformations due to volume changes. XCT, being an inherently volumetric technique, is a useful tool for analysing this process (Paz-Garcia et al., 2016).

Figure 2.14 shows the microstructural changes in a Li-ion cell with a theroretical capacity of $\sim 7.45 mAh$ as it was discharged at $25 \mu A$ (Paz-Garcia et al., 2016). Discharge was performed in 10 steps, the first being for 10 h. The electrode was lithiated to 3.36%. The remainder of the discharges were 20 h long. The cell was lithiated by

$\sim$ 6.72% each time. XCT was performed using commercially available laboratory-CT apparatus, specifically the Xradia Versa MicroXCT-520 (Paz-Garcia et al., 2016). This used a duel magnification approach that is a combination of a typical cone beam and parallel beam set-up, see Figures 2.3 & 2.4. Essentially, a more columnated cone beam shape is developed than in conventional laboratory-XCT, and this is incident on an objective lens. Paz-Garcia et al. place the sample 15mm from both the source and detector and use a 4$\times$ objective lens, this produced 1.7μm pixels using a 30s exposure at a tube voltage of 45kV. In figure 2.14 the top layer with the darkest grayscale values is the Li metal. The intermediate layer is the glass fibre separator, and the bottom layer shows Si particles and lithiated silicon ($Li_{3.75}Si$). Paz-Garcia et al. showed with their 4D XCT experiment that the lithiation caused significant expansion in the Si-based electrode. At 64.5% lithiation the electrode is $\sim$ 3$\times$ the volume of the initial state. This was caused by the expansion of active particles (this was also accompanied by a drop in attenuation) (Paz-Garcia et al., 2016).

In summary, 4D XCT is powerful technique for observing volumetric change with time. 4D XCT has diverse applications that cover many time and length scales, from the fast sub-second imaging of porous flow (Dobson et al., 2016) and observing rapid microstructural changes in combustion processes (Parker et al., 2021), to slower processes such as discharging a battery over many hours (Paz-Garcia et al., 2016). In each case the key consideration is the trade-off between temporal and spatial resolutions, with faster experiments having to sacrifice spatial resolution and vice versa. As a result, although lab CT is useful for long experiments, this method is most optimised with synchrotron radiation due to the brilliance of synchrotron x-ray beams. Further considerations arise from the large sample environments and test rigs often required for these experiments, and the choice between 'stepped' and continuous scanning methods.

2.3 X-ray Ptychography

N.B. CDI and Ptychography is applied in EM and OM, however here we are referring to the x-ray methods unless stated otherwise.

The Abbe diffraction limit describes the resolution limit of an idealised optical system.

$$d = \frac{\lambda}{2n\sin(\theta)} \tag{2.9}$$

Where λ is wavelength, n is the refractive index of the objective/medium, and θ is the maximal half angle of the cone of light that can be accepted by the objective. The $n\sin\theta$ term is called the numerical aperture. For transmission x-ray and transmission electron microscopes the numerical aperture rather than λ determines the maximum achievable resolution of the technique in practice (Guizar-Sicairos and Thibault, 2021). Because of this, moving forward, the upper limit for spatial resolution in x-ray microscopy is determined by improving the manufacturing tolerances of Fresnel zone plates (Pfeiffer, 2018). In order to work around this technological bottleneck in x-ray microscopy lensless techniques have been developed; Coherent Diffraction Imaging (CDI) and Ptychography.

The basic conception of these lensless techniques is to replace a physical lens with an algorithmic 'lens' that reconstructs a real space image of the sample from the reciprocal space diffraction patterns at the detector. In order to create such diffraction patterns spatially and temporally coherent light is required to produce discernible interference patterns. Furthermore, coherence is required so that enough *a priori* information is available for later reconstructions. In theory this allows for wavelength-limited resolution (Pfeiffer, 2018). However, reconstructing an image from a diffraction pattern is problematic, this is because the detector only resolves the amplitude of the signal not the phase. This is the 'phase problem' (Pfeiffer, 2018; Guizar-Sicairos and Thibault, 2021).

Modern ptychography developed from CDI. In CDI reconstruction and phase retrieval is achieved using a Hybrid Input-Output algorithm that iteratively reconstructs the object from the magnitude of its Fourier transform and iteratively applies constraints in real and reciprocal space. This CDI reconstruction algorithm was developed by Miao et al., 1999, and based of work from Fienup, 1978. Faulkner and Rodenburg, 2004, demonstrated that ptychographic reconstructions could be obtained with a similar iterative phase retrieval method from CDI. This was termed

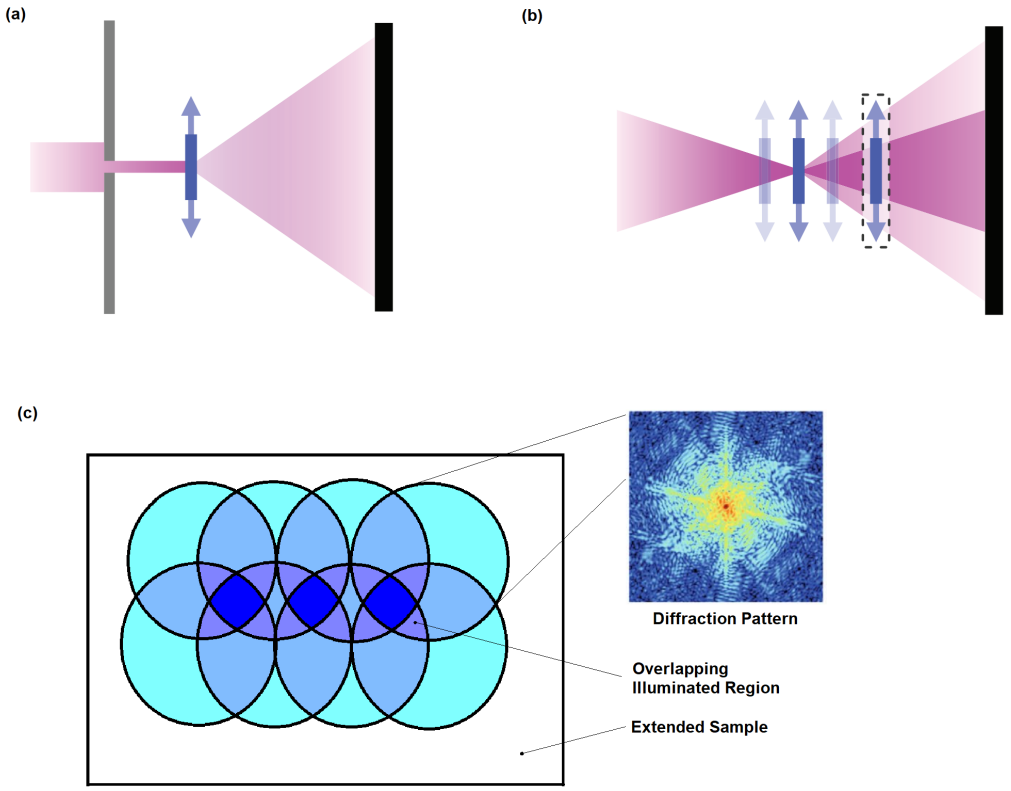

FIGURE 2.15: (a) A simple ptychography set-up; aperture shapes the beam onto the sample so that far field diffraction patterns can be obtained whilst the probe scans across the sample. (b) Pre-focused ptychography set-up; due to recent algorithms that reconstruct the illumination function a pre-focued beam can be used. (c) When the probe is scanned across the sample the illuminated regions overlap, here we have 50% overlap in vertical and horizontal directions. (a), (b) adapted from Guizar-Sicairos and Thibault, 2021.

the Ptychographic Iterative Engine (PIE). Iterative reconstruction brought ptychography into it's modern form.

In ptychography experiments coherent far-field diffraction patterns are obtained by scanning a spatially bound probe through the object such that diffraction patterns overlap significantly, see figure 2.15. In fact ptychography can be seen as a scanning version of CDI, however, unlike CDI, ptychography uses a probe that has both significant spatial structure and spectrum (Guizar-Sicairos and Thibault, 2021). Ptychography has a number of advantages compared to CDI, firstly it does not require an isolated sample, as a result it is possible to scout and zoom in a large extended sample. This is because ptychographic reconstructions benefit from simultaneous

constraints from multiple diffraction patterns, meaning that other constraints, such as isolation, are not needed for reconstruction. Ptychographic reconstruction algorithms force consistency between overlapping illuminated areas during reconstruction. This provides the additional information, and the high degree of overdetermination, required to resolve ambiguities and help the phase retrieval process come to a fast and efficient convergence (Guizar-Sicairos and Thibault, 2021; Pfeiffer, 2018). Furthermore, ptychography as a technique is more robust against noise (Guizar-Sicairos and Thibault, 2021).

A review of the basic principles and algorithms relevant to ptychography, including PIE, is given in Pfeiffer, 2018. The PIE algorithm, developed by Faulkner and Rodenburg, 2004, works through all of the diffraction patterns at different scan positions one-by-one. The current best guess of the exit wave for a diffraction pattern at position r, is calculated from the multiplication of P(r), the illumination function, with O(r), the current object transmission function. The exit wave, ψ_j(r), describes the intensity and phase of the wave after interacting with the sample, is then updated so that the real measured diffraction intensities, I_j(q), replace the current best guess intensities, whilst keeping the phases from the guess (because these were lost due to the phase problem). From this updated exit wave the O(r) is recalculated in the region of the diffraction pattern. The algorithm then moves to the next region. This is repeated for all the diffraction patterns in the ptychography scan, once done a single generation of the iteration algorithm has been completed. This process is then repeated until the object function converges. Simply stated, the algorithm iteratively finds the complex O(r) values where I_j(q), the measured intensities at reciprocal space coordinate q, are equal to squared Fourier transform of the complex exit wave, ψ_j(r). ψ_j(r) itself is found from the multiplication of the complex illumination function translated by the scan position r_j, P(r - r_j), and O(r). This is mathematically expressed by the Fourier constraint in equation 2.10 below:

$$I_j(q) = |F\{\psi_j(r)\}|^2 = |F\{O(r)P(r - r_j)\}|^2 \tag{2.10}$$

Although PIE works well with optical ptychography and in simulation, issues can

arise in x-ray ptychography due to the illumination function not being accurately known *a priori* for x-rays. Improvements on PIE for x-ray ptychography also iteratively reconstruct the illumination function rather than assuming it is known (Thibault et al., 2009; Guizar-Sicairos and Fienup, 2008; Maiden and Rodenburg, 2009; Thibault and Guizar-Sicairos, 2012). This lead to an immediate improvement in image quality, furthermore, this concept meant focused X-ray beams could be used without having to model the wave-field. Although the use of focusing optics means the technique is not strictly lensless, it is important to note that the technique is not limited in resolution by this focusing optic. The resolution of the technique is much smaller than the probe diameter (Pfeiffer, 2018). The focusing optic means that the probe size can be more easily and precisely controlled. This brings us to the state-of-the-art for x-ray ptychography.

In the x-ray regime ptychography has promising applications where acquiring high-resolution images with quantifiable contrast is needed. Furthermore, by precisely rotating the sample many ptychographs can be acquired from multiple angles which can then be reconstructed into a 3D volume as with XCT. This combination of x-ray ptychography and computed tomography is often termed X-ray Ptychotomography (XPT). XPT can extend the spatial resolution of XCT into the sub 100 nm range, this is also achievable with larger fields of view than in XCT (Guizar-Sicairos and Thibault, 2021). The limiting factor to the experimentalist in regards to field of view is the reconstruction time, since, unlike in XCT, each projection has to be reconstructed. Reconstructing a well sampled ptychograph of a large field of view requires considerable computing resources and time. In XPT several such ptychographs are required at a range of angles for computed tomography, further increasing data processing requirements. Another advantage of ptychography is that the scanning probe makes ptychography set-ups synergetic with X-ray Fluorescence (XRF) experiments. In these XRF experiments a probe is scanned across the sample whilst characteristic x-rays are measured at each probe position, this can be achieved simultaneously with ptychography on the same set-up. Again, this XRF data, if procured from a range of angles, can be reconstructed into 3D to make complimentary elemental maps of the sample. These qualities have seen researchers from the materials sciences make use

of x-ray ptychography (Holler et al., 2019; Chen et al., 2013; Zhu et al., 2016).

2.4 Scanning Electron Microscopy

During EM experiments a high energy beam of electrons is directed onto a sample resulting in a number of different electron-matter interactions that can provide useful information about the sample. These phenomenon are shown in figure 2.16. SEM is concerned with detecting electrons and photons emitted from the top surface of the sample as a result of the sample interacting with the beam, these are; secondary electrons, characteristic x-rays, backscattered electrons and Auger electrons, see figure 2.16. In SEM experiments the electron beam is rastered across the surface of the sample in order to create an image. Secondary Electron (SE) imaging is carried out when high resolution imaging of the surface of a sample is required. SEs are low energy excited electrons generated from atoms in the sample due to inelastic scattering of the primary electrons. Due to their low energy they are absorbed by the bulk of the sample if they come from too deep. As a result the only SEs detected come from the surface, usually the top 5 -10 nm in metals. At very high accelerating voltages a second kind of SE is generated, these are SEs that have been formed from atoms in the sample due to inelastic scattering with backscattered electrons. These SE will lower the quality of SE image obtained. Backscattered Electrons (BSE) are generated by the elastic scattering of electrons. Due to their higher energy they come from deeper in the sample. BSEs are used to produce images that reveal information of the composition and topology of the sample.

SEM can also procure chemical information through Energy Dispersive X-ray Spectroscopy (EDX). An EDX spectrum is generated from the characteristic x-rays emitted when electrons from constituent atoms are removed by the electron beam. Removing an electron creates an electron hole. Electrons from higher energy shells then fill these holes, when they do so the energy difference is preserved by the emission of a characteristic x-ray photon with energy equal to the difference between the energies of the two shells. This energy is characteristic of specific elements. The analysis volume is hundreds of nm to several mm (vertically and horizontally), see figure 2.16. The volume is much larger compared to the spot size of the electron beam on

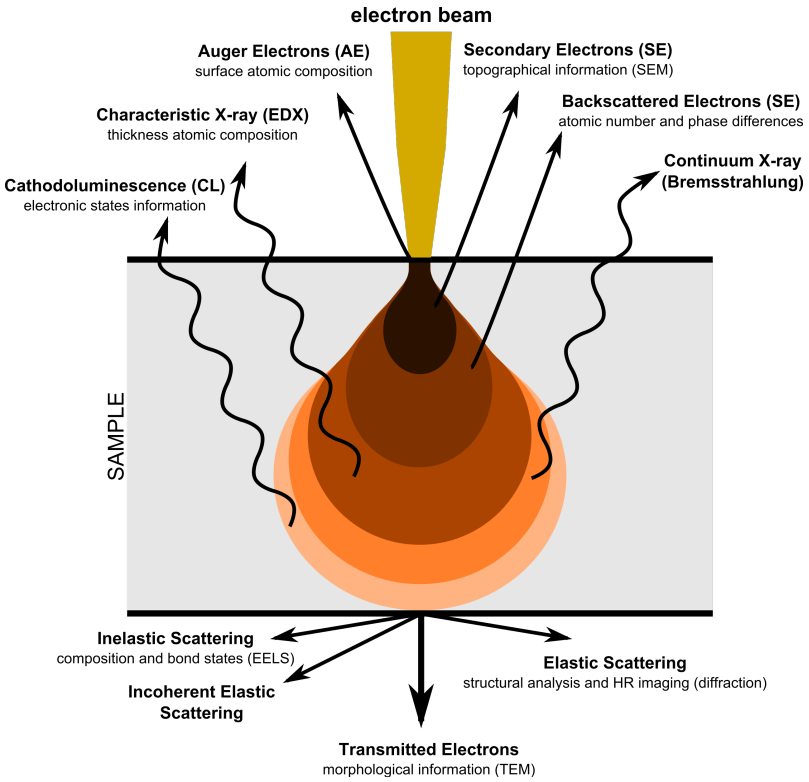

FIGURE 2.16: Schematic of phenomena resulting due to the interaction of a high energy electron beam and matter. Source; Wikicommons.

the sample and the analysis volume in SE mode. This is because the incident electrons scatter in the specimen forming a large bell shaped region. This is because, unlike in SE mode, characteristic x-rays are able escape from a greater depth where they are detected by the detector. By rastering through the sample a map of elemental distribution can be produced by this method. However, EDX has lower spatial resolution compared to SE mode imaging due to a larger escape depth. Furthermore, elemental analysis in SEM EDX is limited by low intensity peaks that are often obscured by background radiation caused by bremsstrahlung radiation and the energy resolution of the detector (approximately 125 eV with a typical silicon drift detector). This can be a useful method for qualitatively observing the elemental distribution in a sample. For ideal, flat and conductive (or coated) samples quantitative analysis of the elements present is also possible.

During this project we have used a JEOL JSM-6610LV to acquire SE images and EDX maps of particulates, ash and other filter structures, both in-situ and ex-situ. The microscope is an analytical SEM capable, in idealised conditions, of 3nm point-to-point resolution at a 30 keV accelerating voltage. The electron beam is developed from a thermionic-emission tungsten filament electron gun. Thermionic emission guns work by heating the filament (cathode) to high temperatures (approximately 2800 K) to emit thermoelectrons which are then accelerated by a potential difference between the filament cathode and anode into a electron beam with a designated energy. The brightness of the image generated from SEM is determined by the beam current, amongst other factors. The number of thermoelectrons developed by the filament partly determines the beam current. The beam then passes through a condenser lens and aperture. Beam current is modified by focusing the beam such that only a certain fraction passes through the aperture. The beam is then rastered across the sample by the scan-coils, and focused to a spot on the surface of the sample by the objective and final aperture. Interaction of the beam with the sample produces different detectable events that can be used to analyse the sample, as discussed above, see figure 2.16.

The SE detector used in this project is an Everhart-Thornley detector, see figure 2.17. The detector consists of a collector electrode that is held at 100V in order to maintain

an electric field that directs the SEs to the scintillator. The scintillator is typically coated with an Al film, once the electrons collide with this film they are accelerated to the scintillator crystal. This results in the emission of visible light, which is then amplified through a photo-multiplier tube before being detected by a camera. A number of factors will effect the resolution and quality of the image obtained from this method. As previously eluded to the beam current will determine the brightness and amount of signal because more primary electrons in the beam will result in more scattering events and hence more SEs. Similarly increasing the accelerating voltage will increase brightness and signal because higher energy primary electrons result in higher energy SEs which can escape the sample from a larger analysis volume to reach the detector. The amount signal is also dependant on the working distance (WD), which is the distance from the objective to the focus when the sample is in focus. At shorter working distance more SEs are detected. Finally, spot size will also effect the amount of signal. Spot size is the size of the focus diameter on the sample. Larger spot sizes will result in more oversampling (when analysis volumes from neighbouring points during the raster overlap) and larger beam current, therefore large spot sizes obtain more signal. However this is with detriment to resolution. Smaller spot sizes will improve the resolution of the image due to the finer probe size, allowing for the separation of small objects. Similarly, low voltages will improve resolution. This is because lower energy electrons scatter less in the sample meaning SEs are collected from a smaller volume. Finally small WD is required for high resolution imaging, this is because of the trade-off in SE imaging between spatial resolution and signal. For high resolution imaging low voltages and spot sizes are required, thus in order to acquire a quality image a small WD is needed to obtain enough signal from the ROI. However, small WD will also result in a shallower depth of field.

It is important to carefully consider sample preparation for SEM. When preparing electrically insulating materials such as the ceramic filter materials and particulate materials of this project it is important to consider the charging phenomenon. When the beam interacts with insulating materials it can leave areas charged if those areas do not form a charge balance with the primary electron beam. Charge balance is

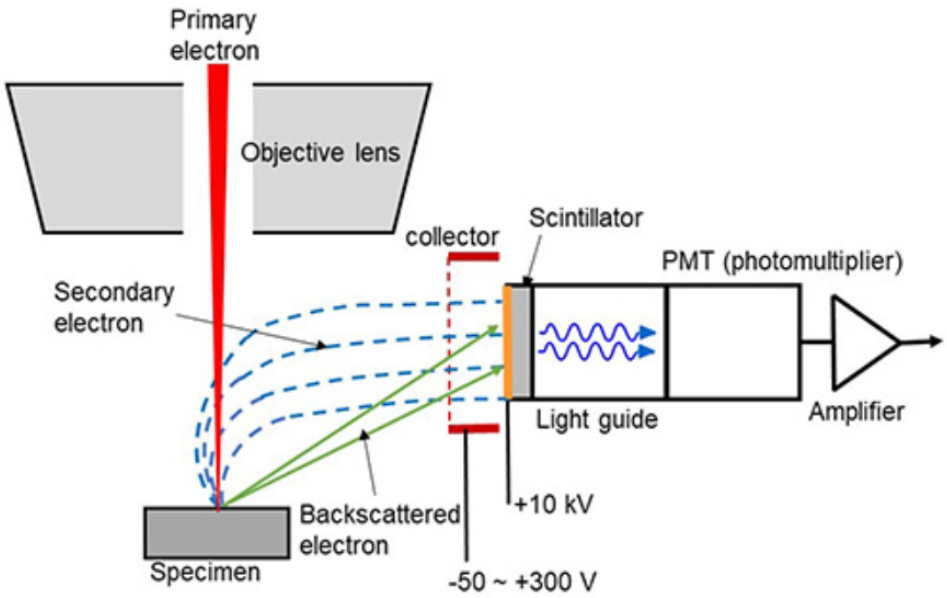

FIGURE 2.17: Schematic showing the operating principle of a Everhart-Thornley detector. Source: Jeol, 2022

observed when the sample, or ROI within the sample, emits electrons at the same rate as they gain electrons from the beam. This can be achieved by coating the insulating sample in a thin sputter-coated conductive layer. This will conduct electrons away from charged areas achieving the balance. Reducing the dwell time and lowering the accelerating voltage can also reduce charging artefacts. Finally, operating the SEM in low vacuum mode can also reduce charging artefacts, this is because the air molecules will help dissipate the charge from the surface. Charging artefacts are observed as; low topological contrast, locally anomalously bright and dark regions, image distortion and sample movement or breakage.

The EDS detector used for this project is an Oxford Instruments Xmax 80 silicon drift detector (SDD). SDDs work by creating electron-hole pairs when an x-ray collides with a Si single crystal. The energy required to create an electron-hole pair is 3.6 eV, thus a single Mn Kα (5.9 keV) characteristic x-ray generates approximately 1640 electron-hole pairs. These electrons and holes are separated across a capacitor. The potential difference across the capacitor can then be used to determine the number of electron-hole pairs developed from which the element of the characteristic x-ray can be determined. Typically larger spot size, accelerating voltages and acquisition

times are required for SEM EDX compared to SE imaging in order to obtain sufficient signal. Furthermore an overvoltage should be chosen such the the primary electrons have an energy approximately 1.7 times that of the highest energy peak to be observed, however lower voltages of 10 keV is desirable if low energy x-rays are of interest (Willis and Conner, 2003). Sample preparation should be as flat as possible and coated with metal or carbon if the sample is insulating. It it is important to choose a coating that does not overlap with elements of interest, thereby obscuring the peak.

2.5 Multi-scale and Correlative Approaches

Researchers are often looking to combine insights across multiple length scales, and to bring together different perspectives on the same region of interest, by combining multiple different methods. An example of the later is that it is very common for SEM SEI and EDX maps to be combined so that the practitioner can observe how small structures resolved in the SEI are represented in the EDX map, thereby inferring the chemical speciation of the small structures. In order to achieve this the images have to be spatially registered. This workflow whereby two techniques are combined via registration to observe the same region of interest is often termed 'correlative microscopy'. This concept was extended into 3D by Burnett et al., 2014, when studying pitting and corrosion in a stainless steel sample, terming it 'correlative tomography'. In the same work, Burnett et al. were also able to combine insights across multiple length scales using various methods with different spatial resolutions and fields of view. They started with medium resolution (3.4 μm^3 voxel size) XCT in a larger region of a steel rod that had been subjected to corrosion and pitting. This non-invasive imaging of the rod in 3D allowed the distribution of pit volumes to be measured. This was repeated in-situ for multiple cycles of corrosion and pitting. Next a high resolution XCT scan was applied (0.8 μm^3 voxel size) to observe a single pit selected from the medium resolution image. This allowed the finer structures in the pit, such as a network of corroded boundaries and surface breaching features, to be resolved. Next, by matching surface features in the high resolution XCT to those observed with SEM, Focused Ion Beam (FIB) SEM serial sectioning was

applied to a sub-volume within the volume studied by the high resolution XCT. This had 50 nm thick slices, 8.3 nm × 10.8 nm pixel size. Such high resolution imaging showed corrosion fronts that grew beneath the surface from the pit had a morphology suggestive of grain boundary corrosion (Burnett et al., 2014). Correlated EBSD was then carried out on the final FIB slice, providing crystallographic information, and scanning-TEM (STEM) and STEM EDX was also applied to this final FIB slice (Burnett et al., 2014).

Such correlative tomography workflows can provide access to a range of length scales for the same region with each preceding length scale providing context to the current region of interest. XCT can be applied at multiple scales from microscales of 100-1 μm to nanoscales of 1000-50 nm. As demonstrated by Burnett et al., 2014, FIB SEM can be incorporated into the correlated tomography workflow for $>$ 5 nm resolution and in some cases even extended as far as $>$ 0.2 nm resolution with TEM techniques. Utilising a range of techniques with different resolutions can be useful when examining how nanoscale and microscale features effect device level performance in applications such as batteries and particulate filters (Ziesche et al., 2020; Varambhia et al., 2022). In this project we have used a range of complimentary techniques (such as XCT, XPT, SEM), in order to understand particulate filters at different scales.

2.6 Filtration

Filtration as a technology for solid-fluid separation has been used throughout history, from ancient Egypt (ca. 200 BC), where inscriptions revealed its use in water purification (Tien and Brenner, 2013), through to its ubiquitous use in modern manufacturing and pollution abatement (Johnson et al., 2021; Jacobson, 2012). Indeed, it's relevance in recent years has been highlighted by increased awareness of how Particulate Matter (PM) emitted by modern automobiles is damaging public health worldwide (UN, 2017; Raaschou-Nielsen et al., 2013), and by the use of PPE respirators in healthcare settings to filter virally loaded aerosol during the ongoing COVID 19 pandemic (Du et al., 2021).

Filtration inherently occurs in an unsteady state (Tien and Brenner, 2013). During filtration particles continually accumulate in the filter. As these particles accumulate, they change the filter structure. As a result of this structural change the filter's efficiency (i.e., ability to collect particles) and the pressure drop needed to maintain steady flow across the filter also continually changes. Thus, the filter quality factor, a function of filtration efficiency and pressure drop that optimises for high efficiency and low pressure drop, also changes with time. This is stated below, where n is the filtration efficiency (fraction of particles captured by mass or number) and δP is the pressure drop across the filter.

$$Q_f = \frac{-ln(1-n)}{\Delta P} \tag{2.11}$$

Therefore, when making studies of filtration accurate models of the particle deposit concentrations and pressure gradient over time are of interest from both theoretical and practical standpoints (Tien and Brenner, 2013). This is certainly true for automotive particulate filters. High filtration efficiency in automotive filters is necessary for filtering out particles to meet tightening emission regulations. However, filtration efficiency must not come at too high a backpressure cost, if the total exhaust backpressure is too high it will prevent the cylinder from being able to blow out combustion products into the exhaust, lowering the fuel efficiency of the engine. In automotive filters ash and soot deposit in the interior pores of the filter and on the

inlet surface over time, these deposits change the porous filter structure and therefore effect the filtration efficiency and pressure drop, and thus quality factor, of the particulate filter during operation.

Deposition of the suspended particulates onto a filter can occur via six mechanisms. The relative importance of each depends on the specific conditions within the filter, such as flow rate, pore size, and particle radius. These are discussed below and illustrated in Figure 2.18:

1. **Direct Interception** - When the aerosol normal path passes within one particle radius, r_p, of the filter surface it will be intercepted, thus being deposited. In other words, any particles that travel along the same trajectory as the fluid but still impacts the collector are consider to have been directly intercepted. This process slightly favours large particles but is independent of particle velocity. See streamlines A, B in figure 2.18.

2. **Inertial Impaction** - Another key mechanism for deposition for aerosol particles with diameters greater than 1 μm is inertial impaction (Tien and Brenner, 2013). By considering an aerosol flowing over collecting body (such as a filter wall, grain, or fibre) we know intuitively both PM and gas flow move rectilinearly at a remote distance from the filter section. That is to say, in a non-disturbed flow the particle and gas trajectories are the same. However, as the aerosol approaches the collector the gas streamlines change direction. They bend around the filter section, obeying the no-slip condition at the filter surface. However, the PM, having considerable inertia, changes trajectories slower than the fluid. Their deviation from the gas streamlines will cause the particles to come within one r_p of the collector surface, thereby depositing on the filter. This mechanism favours relatively large, massive, high velocity particles. The mechanism is illustrated as the dashed line ejected from trajectory D in figure 2.18.

3. **Diffusion** - For particles $< 1\mu m$ in size without other external forces applied to them (a.k.a. electrostatic forces), Brownian diffusion is the dominant mechanism that determines the deposition rate in a filter (Tien and Brenner, 2013).

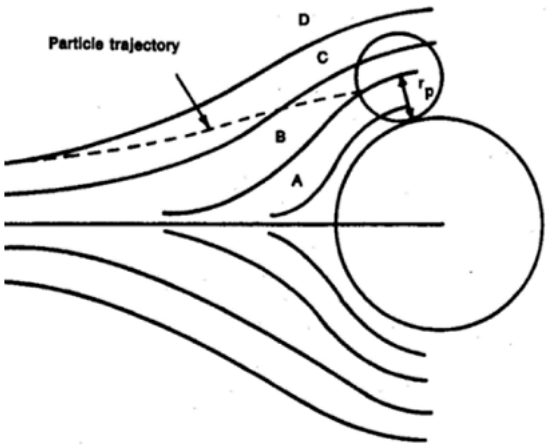

FIGURE 2.18: Filtration mechanisms for aerosol particle deposition: Particles will travel along the flow paths (solid lines) unless they have enough inertia or Brownian motion to move from these paths to new trajectories (dotted line). Particles traveling along paths A or B with $r \leq r_p$ will be intercepted by the fibre. Particles with enough momentum on paths C or D may impact the filter by inertial impact, whilst small slow particles may do so by diffusion. They do so by moving from the gas flow paths to new trajectories (dotted line). Source; Overton, 1973.

Brownian motion allows particles to cross between streamlines and thus contact the filter. This is favoured for small particles and low velocities.

4. **Electrostatic** - Aerosol particles and filters carry electric charges, forces of attraction between them may cause particles to move towards the filter and impact upon it (Tien and Brenner, 2013). Furthermore, forces of repulsion between aerosol particles with the same charge may also cause deposition.

5. **Sedimentation** - If the density of the particles in an aerosol is different from that of the gas (assumed greater), then the particles move in the direction of the gravitational force and settle out (Tien and Brenner, 2013).

6. **Sieving** - Sieving is the direct interception of a particle due to it's diameter being larger than the pore throat diameter the aerosol moves through. Just like peas in a kitchen sieve.

2.6.1 Macroscopic Description of Filtration

The macroscopic equations describe the relationships between important characteristics of a filter based on the particle conservation principle, an expression for assumed filtration rate, and mechanics for flow in porous media. In this section we work closely from Tien and Brenner, 2013, "Granular Filtration of Aerosols and Hydrosols", Chapter 2. If the reader wants more detailed derivations this text should be the first port of call.

1. Consider monodisperse particles in an aerosol flowing over a collecting surface. As the fluid flows past the collector some of the aerosol particles will travel from the fluid to the surface of the collector via the mechanism described above. For a fluid moving with a superficial velocity, u_s, along the axial direction, z, and assuming a filter with a relatively large ratio of filter diameter to pore diameter we can model the flow to be one dimensional in the direction of the superficial velocity. Therefore, from the conservation principle we can state that:

$$u_s \frac{\delta c}{\delta z} + \frac{\delta(\epsilon c)}{\delta t} + \frac{\delta \sigma}{\delta t} = 0 \tag{2.12}$$

   Where; c is the concentration of particles in the fluid, ϵ, is porosity, t, is time, and σ is specific deposit (volume of deposit per unit volume of filter). Equation 2.12 can be simplified to equation 2.13 by substituting in a corrected time term, θ, see equation 2.14:

$$u_s \frac{\delta c}{\delta z} + \frac{\delta \sigma}{\delta \theta} = 0 \tag{2.13}$$

   Where:

$$\theta = t - \int_0^z \frac{\epsilon}{u_s} dz \tag{2.14}$$

2. Now consider filtration rate, N. If we approach the problem from a volumetric view then N is given as the volume of deposit collected per unit filter volume per unit time. By introducing σ, the specific deposit (volume of deposit per unit volume of filter, a local function that changes with time), the relationship between N and σ is simply expressed as the rate of change of the specific

deposit σ with time. Moreover, it is reasonable to simply assume that the filtration rate depends on the state of the filter, which may be described by σ, and is therefore also a time dependant and local function, and that N depends on c, the concentration of particles in the fluid. Therefore, N can be stated as:

$$N = \frac{\delta\sigma}{\delta t} = N(\alpha, c, \sigma) \tag{2.15}$$

Where α is a parameter vector for the filtration process.

3. As the particles are separated from the fluid and deposit in the filter they will continuously change the filter structure, this can be described as a change in porosity as shown in equation 2.16:

$$\epsilon = \epsilon_0 - \frac{\sigma}{1 - \epsilon_d} \tag{2.16}$$

Where ϵ_0 is the initial porosity and ϵ_d is the porosity of the deposits.

4. Finally, the pressure drop, ΔP, during filtration can be obtained by integrating through the axial pressure gradient. Such as:

$$-\Delta P = -\int_0^L \frac{\delta P}{\delta z} dz \tag{2.17}$$

$$= -\frac{\delta P}{\delta z} \int_0^L G(\beta, \sigma) dz \tag{2.18}$$

Where:

$$G(\beta, \sigma) = \frac{\delta P / \delta z}{(\delta P / \delta z)_0} \tag{2.19}$$

Since in most applications the pressure drop relative to the initial clean condition is of most relevance it is useful to put pressure drop in terms of this initial term, see equation 2.19.

In summation, in most applications the dynamic behaviour of a filter can be obtained from solutions to these macroscopic equations (i.e. equations 2.13, 2.15, 2.18) with

the following initial and boundary conditions.

$$c = 0,\ \sigma = 0 \quad for \quad z \geq 0,\ \theta \leq 0 \tag{2.20}$$

$$c = c_{in} \quad at \quad z = 0,\ \theta > 0 \tag{2.21}$$

2.6.2 Wall Flow Filters

Automotive particulate filters are placed in the exhaust of modern vehicles in order to filter PM from the exhaust stream. These filters are constructed as 'wall flow filters'. Wall flow filters consist of channels that run parallel to exhaust gas flow, channels are blocked alternately at the inlet then outlet of neighbouring channels in a 'honeycomb' monolith, often made of a cordierite or SiC substrate. The blocked channel ends force the exhaust gas to flow through the connected pores in the walls of the particulate filter, from an inlet channel to an outlet channel, filtering out particles, as shown in figure 2.19. However, installing a filter increases exhaust backpressure which lowers engine fuel efficiency. Achieving acceptable filtration efficiency and backpressure is the critical optimisation problem at the heart of automotive particulate filter design.

OEMs install particulate filters in order to adhere to regulations pertaining to the amount of emissions that can be emitted from the exhaust during testing. For example, in Europe the particulate number emitted is regulated to $6 \times 10^{11}\ km^{-1}$ as of Euro 6 (Joshi, 2017). These challenging regulations have lead to historic cheating scandals when OEMs installed 'cheat devices' to output less emissions when a test cycle was detected by the onboard computer. However, this just lead to further pressure on OEMs to develop effective exhaust technology since, in the aftermath of these scandals, testing procedures moved to the 'Worldwide Light-vehicles Test Procedure' and 'Real Driving Emission' tests (Joshi, 2017). These tests are harder to beat.

These most recent regulations in the form of Euro 5/6 (2009/2014) have increased fuel efficiency regulations whilst simultaneously imposing PM regulations on gasoline vehicles. Gasoline Direct Injection (GDI) engines now offer a favourable trade-off to OEMs between fuel efficiency and emissions. Less pumping loss, more precise

fuel volume and timing control, higher compression ratios, more charge cooling and higher combustion efficiency, all improve fuel efficiency compared to port fuel injection (PFI) gasoline vehicles (Alkidas, 2007). O'Driscoll et al., 2018, find that GDI delivered approximately a 17% improvement in mileage compared to PFI. Furthermore, GDI emmits less NOx and PM compared to diesel engines, thus requiring less costly aftertreament systems (Alkidas, 2007; Amirante et al., 2017; O'Driscoll et al., 2018). O'Driscoll et al., 2018, find that GDI offers a 86 -96% reduction in NOx emissions compared to Diesel vehicles. However, GDI emits higher PM emissions compared to PFI, due to fuel impingement on the piston and cylinder walls, incomplete fuel evaporation, and the inhomogeneity of the air fuel mixture (Amirante et al., 2017). Thus GDI often requires a GPF to comply with Euro 6 PM regulations.

Gasoline Particulate Filters. A GPF is a wall flow filter. GPFs are also often coated in a catalyst washcoat, typically a three-way catalyst (uncoated filters are also used). The washcoat is applied as a slurry of particles which then dries during the manufacturing process into a solid layer, the washcoat contains; large micron sized alumina support particles, ceria and zirconia nanoparticles (which act as oxygen donors), and platinum group metal catalyst nanoparticles (Pt, Pa, Rh). The catalyst will remove harmful pollutants from the exhaust, such as nitrous oxides (NOx), carbon monoxide and unburnt hydrocarbons (HC) by catalysing: (1) The oxidation of unburnt HC to form CO2 and water, (2) The oxidation CO to CO2 and, (3) the reduction of NO to N2 and O2. Kočí et al., 2019, show that the flow through the wall in coated filters predominantly occurs at cracks in the washcoat or uncoated zones due to the washcoat having a permeability orders of magnitude lower than the porous substrate.

The PM in the exhaust deposits into the pores and onto the walls of the filter. These particles (in the GDI/GPF system) are dominated by elemental carbon, or soot, with only a small fraction of organic carbon (Maricq, Szente, and Jahr, 2012). The GDI PM is also predominantly below 100nm as shown by several studies (Harris and Maricq, 2001; Khalek, Bougher, and Jetter, 2010; Maricq et al., 2000).

Filtration in GPFs inherently occurs in an unsteady state. During filtration particles in a wall flow filter continually accumulate, as these particles accumulate they

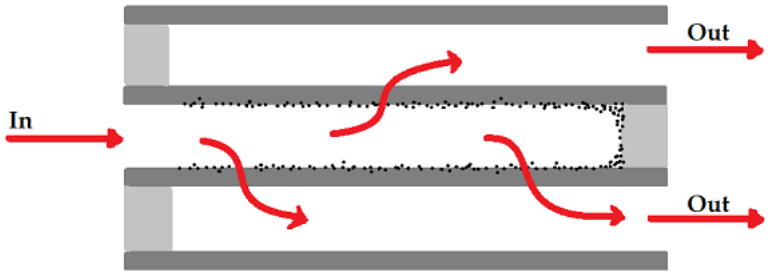

FIGURE 2.19: Illustration of the operating principle of a wall flow filter: In a wall flow filter aerosol flows into the inlet unblocked channel, flow is then forced through the porous walls of the filter into the outlet channels causing the particles to filter out of the aerosol

change the filter structure, as described by the macroscopic equations. As a result of this structural change the filter's efficiency (i.e. ability to collect particles) and the pressure drop needed to maintain steady flow across the filter also continually changes (Tien and Brenner, 2013), see equation 2.18. The dominant filtration mechanism in automotive wall flow filters is Brownian diffusion for soot particles and smaller agglomerates (< 200 nm), for larger agglomerates interception dominates, whilst gravitational settling and inertial impact are believed to have negligible effect during the 'deep bed filtration' that occurs inside the porous walls of the filter (Konstandopoulos et al., 2000; Vlachos and Konstandopoulos, 2006; Joshi and Johnson, 2018).

Initially soot particles are captured in the internal filter pores which are much larger than the particle diameters, this part of the filtration is classified as deep bed filtration. During deep bed filtration the backpressure increases rapidly as deposit builds up in the internal flow paths of the filter, see point 2 in the pressure drop curve in figure 2.21. Filtration efficiency (the fraction of particles removed from a fluid by a filter) depends on pore size, pore shape, and porosity during deep bed filtration. Typical filtration efficiency for a fresh filter is around 50 - 70%. After enough soot and PM, dependant on filtration conditions, has been loaded into the filter the PM stops depositing in the pores and starts depositing in a layer on the wall surface, this is called a 'soot cake' in the literature. Direct interception and inertial deposition are favoured during the soot cake filtration (Konstandopoulos et al., 2000). During this phase the back pressure increases linearly at a relatively slow rate compared to deep

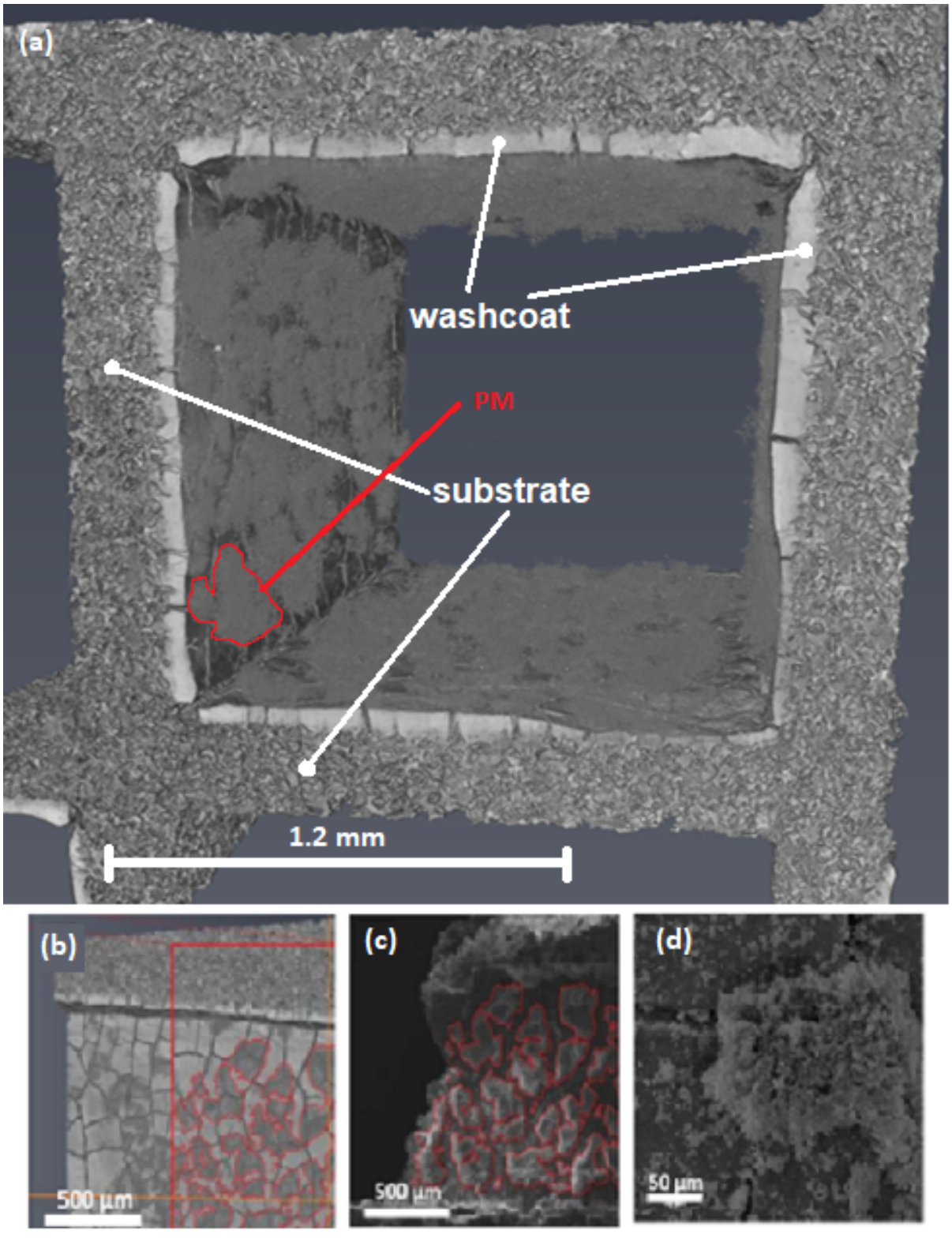

FIGURE 2.20: (a) XCT Volume Rendering of the catalysed coated inlet channel of a GPF which has been aged such that ashy PM has deposited on the surface. (b) XCT volume rendering of the wall surface, ashy PM agglomerates are outlined in red, (c) a correlated SEM image showing the same ashy PM agglomerates outlined in red, (d) higher magnification SEM image of a PM agglomerate on the wall surface.

bed filtration, see point 3 & 4 in figure 2.21. Filtration efficiency can be as high as 98% during the soot caking phase.

The porosity, mean pore size and wall thickness needs to be optimized by OEMs to provide both acceptably high filtration efficiency and low pressure drop. This needs to be done on a case by case basis for each engine/exhaust system. Small pores and low porosities will offer high filtration efficiency but with a high back-pressure penalty, whilst large pores and high porosities will result in lower filtration efficiency but lower backpressures. The pore size distribution is also a critical factor, large outliers can 'leak' aerosol through the filter material, whilst small outliers can become easily blocked during the filtration and increase backpressure. Thick walls also increase filtration efficiency with detriment to backpressure and the opposite for thin walls. Ito et al., 2015, demonstrate an increase in filtration efficiency from 78% to 86% for an increase in wall thickness from 0.22 to 0.30 mm. Broadly, porosities of 45–55% provide the best filtration performance for uncoated applications, whilst porosities of 60% are typical for washcoated GPFs (Joshi and Johnson, 2018). Mean pore size is typically 13–15 μm for bare and 15–20 μm for washcoated GPFs (Joshi and Johnson, 2018).

Once the soot cake has formed it is necessary to regenerate the soot as backpressure will continue to increase linearly with concentration of deposit, this would eventually lead to unacceptably high backpressure. In DPFs soot regeneration was achieved through the reduction NO2. However, there is little NO2 available in the GPF hence regeneration is unlikely by that route. Instead, excess oxygen and the high temperatures needed to oxidize the soot is available during fuel-cut events (e.g. decelerations). Therefore regeneration occurs through the full oxidation of soot ($C + O_2 \rightarrow CO_2$) and partial oxidation of soot ($C + \frac{1}{2}O_2 \rightarrow CO$) in uncoated filters, and the full oxidation of soot in coated filters (Joshi and Johnson, 2018). Soot regeneration is more efficient in coated filters due to oxygen donors, ceria and zirconia, in the washcoat. Furthermore, the washcoat traps heat in the GPF more effectively compared to bare GPFs.

Non-combustible ash particles also build-up in filters during use, however these cannot be regenerated. As a result the ash layer will build up in the filter until the

filter eventually needs to be cleaned. Automotive ash consists of sulphates, phosphates and other oxides of zinc, calcium, magnesium, iron and other metals (Lambert et al., 2016; Joshi and Johnson, 2018). Ash is primarily formed by burning inorganic additives in lubricating oil, but also by metal components from engine wear that are transported to the piston by the lubricating oil, and by the corrosion of the exhaust components upstream of the filter (Joshi and Johnson, 2018). The accumulation increases backpressure and therefore worsens fuel efficiency. Figure 2.20 shows a loading of 20g/l of ash deposited in the inlet of a GPF, it shows how a thick layer of ash builds up on the walls of the GPF. This is opposed to observations of DPFs, where ash predominantly formed a plug at the back of the filter (Joshi and Johnson, 2018). However, it has been well established that small amounts of ash, approximately 2-3 g/L, can improve the filtration efficiency of the GPF, whilst only slightly increasing backpressure, because the ash layer introduces a high quality filtration layer (Shao et al., 2016; Lambert et al., 2017; Hua et al., 2018). Lambert et al., 2017, demonstrated how contaminants that mimic lubricant oil ash build up in concentrations of up to 3 g/L improved filtration efficiency from 60% to 80%. Soot-loaded pressure drop is also improved with ash, Shimoda et al., 2012, show that 10–20 g of ash (at 1 g of soot loading) reduced pressure drop by 20%. This was because the ash prevented the soot from depositing in the deep bed, where it has a greater effect on backpressure.

However, ash build up also has a chemical effect on filter performance as it has been shown that species in ash can act as catalyst poisons in coated DPFs and coated GPFs (Seong et al., 2019; Moldovan et al., 2003; Twigg et al., 2004; Choi and Seong, 2016). S, Zn, P are the primary elements that contribute to catalyst poisoning. Sulphur originates from the combustion of fuel constituents that contain sulphur. Whilst Zn and P originate from Zinc dialkyldithiophosphate (ZDDP, an additive in lubricant oil) that forms ash. Analysis from Seong et al., 2019, suggests that catalyst light-off point and oxygen storage is worse in the presence of ash due to increased PGM catalyst sintering and the reaction of P & ZDDP ash components with oxygen storage species like Ceria. These will effect the coated GPFs ability to reduce gaseous emissions and regenerate soot. However, another study from Choi and Seong, 2016, shows that Ca

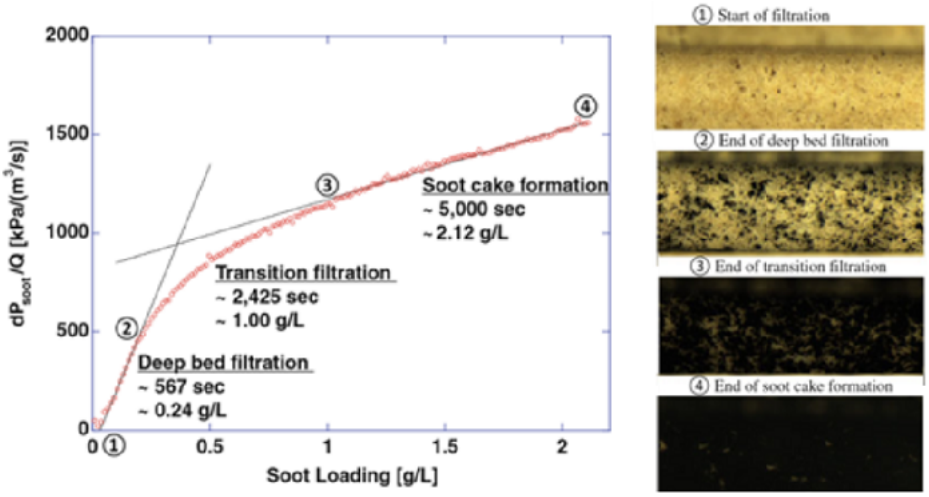

FIGURE 2.21: In-situ Optical Microscopy of Exhaust Filtration: Left, a pressure drop curve for soot loading in a bare DPF filter. Numbers 1-4 represent different stages of the filtration and each corresponds to an image of the surface of the filter (right). The Y-axis in pressure drop due to soot (dPsoot) normalised by volumetric flow through the filter (Q). The X-axis is soot loading concentration in g/L. Source: Adapted from Choi and Lee, 2013.

species in ash can enhance soot regeneration.

Finally, the recent discovery of hydrated ash species has led to further interest in GPF ash (Bagi and Kamp, 2022). Hydrated ash forms due to the humidity of the exhaust acting as water of crystallisation. Hydrated ash forms a dense crystal structure that is bonded to the GPF surface, this will contribute relatively more than dehydrated ash to backpressure and filter blocking and is difficult to remove during GPF cleaning (Bagi and Kamp, 2022). The nature of ash and how ash can effect the GPF in operation is particularly active area of research in GPF literature (Joshi and Johnson, 2018).

2.6.3 Microscopy of Particulate Filters

The transition from deep bed to soot cake formation was studied by Choi and Lee, 2013, who developed a combined desktop optical microscopy and pressure drop apparatus to observe the surface of uncoated DPF channels as soot from a 1.9L direct injection diesel engine flowed through the filter. Online pressure drop measurements were performed alongside the optical microscopy and the soot mass was weighed at the DPF inlet by a tapered element oscillating microbalance. Three sequential

stages of soot filtration where identified; (1) deep-bed filtration, (2) transitional filtration, and (3) soot cake formation, see figure 2.21 (Choi and Lee, 2013). Pressure drop curves offer important insights into the performance of filters over time, in this case in-situ optical microscopy of the surface of the filter provides insight into the structural changes that cause the curve to have its characteristic shape, see figure 2.21 above. Deep bed filtration initially causes a sharp linear rise in pressure drop and is linked by the second image to the blocking of effective 'deep bed' pores in the wall interior, shown by the darkening of pore throats on the inlet wall surface due to soot deposition, it is assumed that the interior pores are similarly blocked. In this experiment the deep bed filtration occurs when soot deposit concentrations are in the range of 0 – 0.24g/L. This then transitions to the soot cake formation where a layer of soot is deposited on the surface of the filter, causing a steady increase in the pressure drop until the filtration is ended at a soot deposit concentration of 2.12 g/L (Choi and Lee, 2013). Choi and Lee present a well-designed laboratory scale experiment with realistic soot particles developed from a 1.9L direct injection engine and with realistic operating temperature and pressure conditions (The filtration was performed under the following conditions; soot concentration $\sim$ 15.8 mg/m3, final soot mass load $\sim$ 1.8–2.1 g/L, DPF inlet temperature of 150–200 ^{o}C, mass flow rate $\sim$ 12.46 kg/h and average space velocity of $\sim$ 88,683 h^{-1}). However, the optical microscopy utilised does not resolve the extent of the soot deposit inside the filter walls.

Vlachos and Konstandopoulos, 2006; Yang et al., 2009, perform SEM EDX on these materials. Yang et al., 2009 map the position in the filter wall where the AS particles become trapped for both SiC and Cordierite DPFs, to do this they use the sulphur emission from EDX to map the deposited AS across the filter wall. Using standard aerosol test bench techniques they show that the AS initially deposits in the deep bed, increasing backpressure more than at higher loadings of AS when caking on the inlet surface dominates deposition and improves the filtration efficiency. When the filter is in its fully loaded state SEM provides a visualisation of the cake thickness

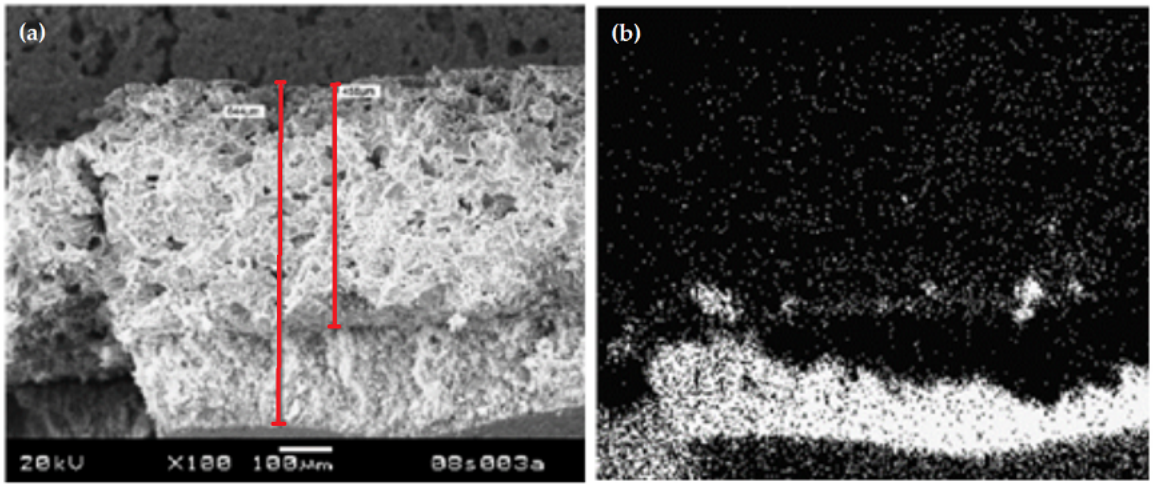

FIGURE 2.22: SEM EDX of Deep Bed Deposits in a Filter: (a) SEM micrograph cross section of the filter, the bottom part of image shows the AS cake, arrows indicate that the total AS coated wall thickness is 644µm, the substrate alone is 458µm thick. (b) EDX map of silicon fluorescence from the cordierite substrate, the FOV, scale and orientation are the same as (a). Source: Adapted from Yang et al., 2009

and the EDX map a visualisation of deep bed pore blocking, see figure 2.22. Additionally, by plotting sulphur signal vs. distance from the inlet surface an experimental estimation of AS penetration depth into the deep bed pores is found. However, EDX, without careful calibration, does not provide quantifiable information on the amount of AS in deep bed pores. Furthermore the technique can only resolve AS deposits in a small volume near the cut surface of the substrate rather than a statistically representative sample volume. The acquisition of this EDX data also seems poor as shown by the rough surface used to obtain the signal, figure 2.22. Yang et al., 2009, found 'moderate' agreement between the experimental results for penetration depth and their Lattice Boltzmann model of deep bed deposition. Model validation is important, but EDX is limited in its ability to validate models of automotive filtration. The porous ceramics used in automotive filters will present too rough a surface for EDX and resin impregnation and polishing is likely to affect the deposits under study. Furthermore, dynamic validation of deposit locations during a filtration requires in-situ imaging which is impossible with this destructive technique as it renders the sample in-operational.

Myriad studies have investigated ash particle size using SEM and light scattering techniques, see table 2.3. The particle size distribution of ash and the porosity of

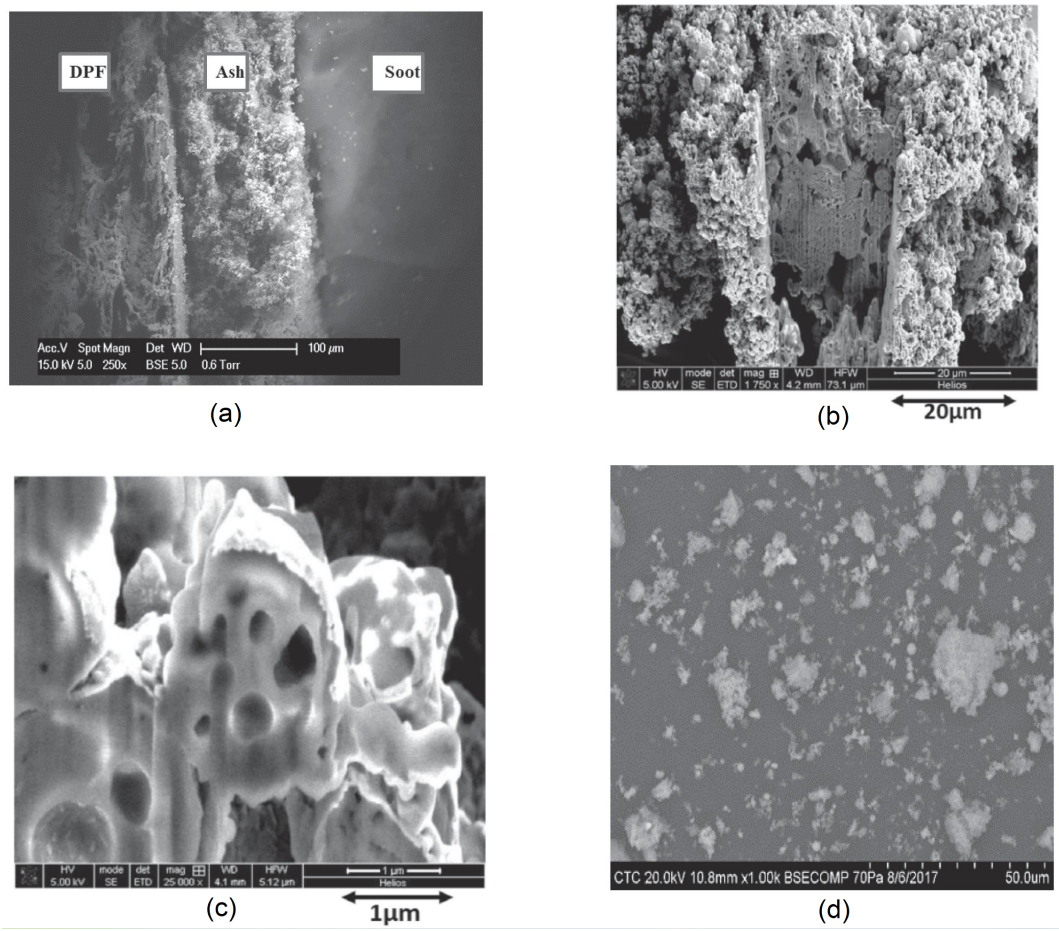

FIGURE 2.23: SEM & FIB SEM of ash; (a) in-situ SEM of a DPF with distinct ash and soot caking layers, (b) in-situ FIB SEM of an ash layer, ash particle sintering is visible since the sample was subjected to multiple high temperature regeneration events, (c) in-situ FIB SEM of an ash particle showing internal porosity, (d) ex-situ SEM of ash particles. Source; Adapted from Wang et al., 2020.

TABLE 2.3: Literature Values for ash porosity, size (mean or distribution) and permeability. Source: Adapted from Wang et al., 2020.

Source	**Porosity**	**Particle Size (μm)**	**Permeability (m^2)**
Konstandopoulos et al., 2000	-	0.5-10	$2.8\text{-}7.4\times10^{-14}$
Merkel, Cutler, and Warren, 2001	83%	0.1-0.5	-
Young et al., 2004	85%	2.4–37.6	5×10^{-12}
McGeehan et al., 2005; McGeehan et al., 2009	90%	0.1-10	-
Konstandopoulos et al., 2006	-	1	-
Sonntag and Eilts, 2016	-	0.3-30	-
Zarvalis, Lorentzou, and Konstandopoulos, 2009	-	0.5-10	$1.8\text{-}2.3\times10^{-14}$
Chiou, 2013	91-95%	0.97	-
Sappok et al., 2009	90-95%	-	$2.8\text{-}7.7\times10^{-14}$

agglomerated ash, or ash layers, are useful parameters since they are closely related to the permeability of the ash agglomerate or layer, it's filtration efficiency, and it's interaction with the catalyst (Wang et al., 2020). Figure 2.23 shows both in-situ and ex-situ SEM and FIB SEM micrographs of ash particles and layers. Typically when determining ash particle size distribution dispersed ex-situ ash is used since the particles are detached and easier to measure (Wang et al., 2020). In the studies in table 2.3 the porosity of the ash is estimated with in-situ ash packing density, which is determined gravimetrically, the typical bulk densities of the compounds that form ash (found in materials data tables), and by assuming spherical particles with size distributions equal to that determined by SEM (Sappok et al., 2009; Sappok, 2009). The packing density in this estimation is determined gravimetrically from filter plugs (where the entire filter channel is filled with ash). By cutting such a plugged section from the filter, weighing it, then removing the ash and re-weighing the cut section the in-situ packing density is determined. Using this porosity value the permeability is then calculated using the Darcy equation (Sappok et al., 2009).

The chemical components that make up ash can be found with X-ray Diffraction (XRD) and SEM & TEM EDX, see figure 2.24. From these techniques it was determined that ash contains metal oxides, metal sulphates, and phosphates. Furthermore, through SEM & TEM EDX it is possible to map the elemental distribution within ash agglomerates as shown in figure 2.24.c. From analysis such as that shown

in 2.24 it has been shown that the dominant metallic species are Ca and Zinc and elemental distribution is not homogeneous through agglomerates. The origins of ash can be roughly determined with elemental tracing techniques such as EDX:

1. Lubricant oil Ash: Ca, Zn, and Mg are metallic additives in lubricant oil whose function is to decrease friction, enhance heat transfer, inhibit corrosion and deposit detergent (Wang et al., 2020). Zn and P are anti-wear additives. Ca and Mg are typical oil detergent additives. These are by far the dominant fraction of ash, at approximately 80 - 90% (Morcfos, Ayyappan, and Harris, 2011).

2. Abrasion and corrosion-related: Fe dominates this category of ash, other elements include Cu, Al, and Cr. It has been shown that ash from corrosion increases with increasing engine speed and is much smaller than lubricant oil ash at approximately 30nm when formed under normal engine conditions (Wang et al., 2020).

3. Fuel and biodiesel fuel additives-related: Na and K are used as catalysts in the production of bio-diesel. These alkaline metals readily form ash during combustion (Wang et al., 2020).

Recent work from Varambhia et al., 2022, has examined the structure of GPF washcoats using multiscale FIB SEM and TEM. In this work a Zeiss Crossbeam 500 microscope was used to collect FIB SEM tomograms with 3nm pixel size in the XY plane and 9nm pixel size in Z (the direction of milling). Careful image preprocessing steps were applied, namely histogram matching, where each slice's histogram is matched onto each over to ensure similar intensity ranges, and the removal of curtaining artefacts. Curtaining artefacts are the result of uneven sputtering during milling and will produce alternating high-low intensity lines across the image, see 2.25.a. A Fourier followed by median filtering regime was applied to remove the curtaining, as proposed by Schwartz et al., 2019. The data was then segmented using a supervised machine learning (ML) algorithm such as random forests into background, alumina and Ceria-Zirconia phases, see figure 2.25.d. The FIB SEM data allowed Varambhia et al., 2022, to quantify the volume percent of each phase in the structure of interest, see figure 2.25.d, and to inform models of tortuosity for each phase. Varambhia et

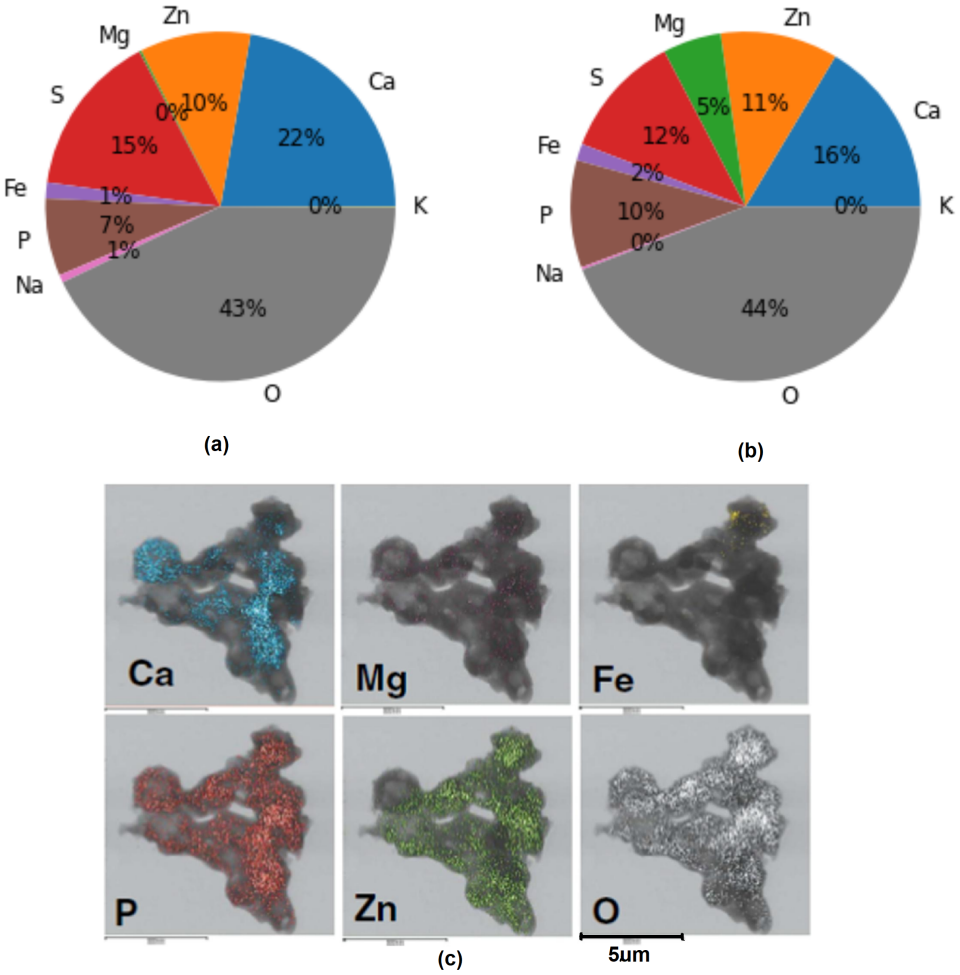

FIGURE 2.24: (a - b) Typical elemental composition of ash from two different crankcase lubricating oils from McGeehan et al., 2005 as determined by SEM EDX spectroscopy, (a) 1.5% sulphated oil, (b) 1% sulphated oil. (c) TEM EDX map of an ash agglomerate particle from Sappok and Wong, 2007. Figure 2.24.c adapted from Wang et al., 2020.

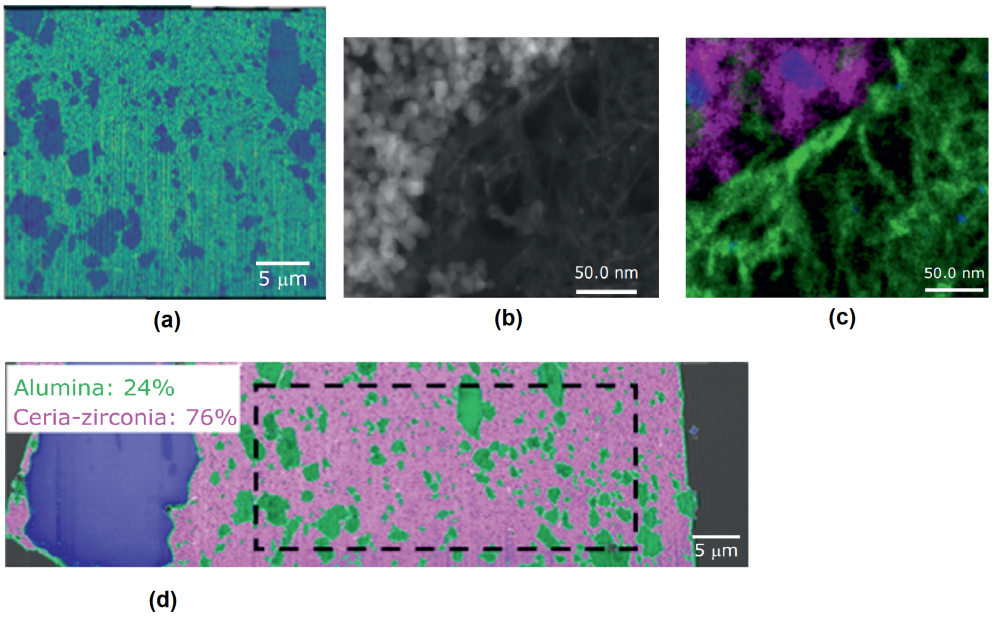

FIGURE 2.25: (a) FIB SEM of GPF washcoat with visible curtaining artefact, (b) TEM of a thin section of washcoat, ceria-zironia nanoparticles are resolved on the left, (c) TEM EDX map showing alumina in green, ceria-zirconia in magenta, and palladium in blue, (d) FIB SEM of a slice through the washcoat showing the percentage of each phase. Adapted from Varambhia et al., 2022.

al., 2022, show that the washcoat contained 24% alumina (which acts as a support material) and 76% ceria-zirconia (oxygen donors). They found the best way to perform this phase analysis is to use backscatter mode SEM, using EDX to confirm the graylevel intensity of each phase by its fluorescence, and then segmenting the image using the backscatter data, see Figure 2.25.d. An in-situ FIB lift out technique was then used and the lamella thinned until it was electron transparent for higher resolution imaging with TEM. This resolved the Ceria-Zirconia nanoparticles, whilst EDX confirmed the presence of a Pd nanoparticle within the washcoat, see figure 2.25.b-c. The size of these particles is crucial to washcoat operation as it determines the surface area available for heterogeneous catalysis and the packing density determines the permeability of the washcoat layer, which in turn determines flow of gaseous products to active sites (Varambhia et al., 2022). Again this was used to inform tortuosity models of the washcoat layer.

Varambhia et al., 2022, also used XCT to place their FIB SEM & TEM work within

the wider context of the filter channel and to better understand the microscale phenomena that are critical to coated GPF operation. XCT was acquired on a channel section cut into an area of a few square centimetres and embedded in resin for the later correlated EM work described above. A Zeiss Xradia™ 520 Versa machine was used to acquire the XCT data with 80kV acceleration voltage and 20s exposures, the pixel size was 4.74μm (Varambhia et al., 2022). Varambhia et al., 2022, develop a programmatic data processing pipeline so that the steps leading to quantitative results are well documented, repeatable and modifiable. After reconstruction the first step of their workflow was rotation and cropping. Cropping reduced the excess size of the dataset, making further computation faster. Rotation ensured that the square cross-section of the channel aligned with vertical and horizontal axes. This reduced the size of the image as it meant that horizontal and vertical cropping can be applied more efficiently. Next, histogram matching was applied to the images, this ensured all slices had similar grayscale ranges and is an important step in situations where pixel intensity varies from slice to slice in a volume (Varambhia et al., 2022). A ML segmentation algorithm was then trained and applied to the dataset in order to segment the data into substrate, catalyst and background/pore segments.

Model training was achieved within the Zeiss Zen Intellesis™ software module, whilst data preprocessing (normalisation, rotation and cropping) was scripted in python. A slice from the centre of the stack was taken for model training. This image was manually in-painted in order to assign pixels in the training image to each segment. The next step was to extract features from the original training image. Each feature extraction output an altered image of the training data with certain features having been 'extracted'. Intellesis™ offers two feature extraction options: 'Classical' mode extracts around 30 features from the training data using CPU, these probably included classical computer vision filters such as Gabor filters (edge & texture extraction), Canny edge detection (edge extraction), and smoothing filters. 'Deep Feature Extraction' mode extracts shapes and textures from the original image using the first three convolutional layers of the VGG-19 algorithm using the GPU (Varambhia et al., 2022). Each feature image was then flattened into 1D arrays and concatenated

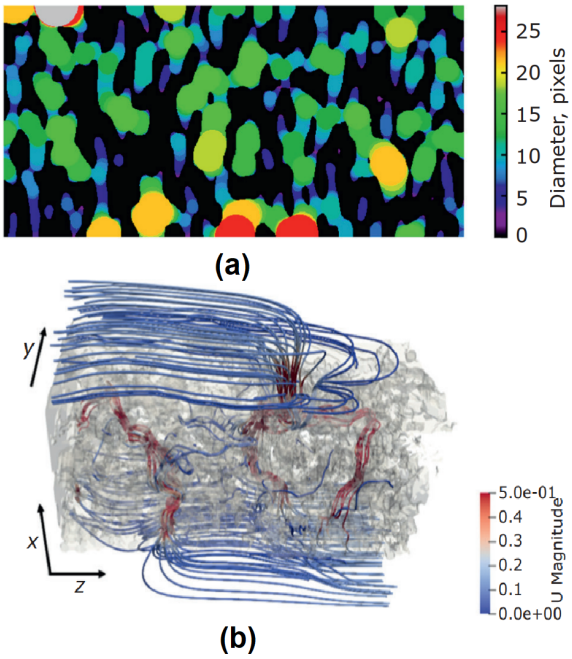

FIGURE 2.26: (a) fitting spheres to segmented XCT data of particulate filters in order separate pores and measure pore diameter distribution, (b) CFD simulations of flow streamlines through a particulate filter, data obtained from XCT. Source: Adapted from Varambhia et al., 2022.

into feature vectors. Feature vectors associate a particular pixel in the original image with the same pixel from each feature image. The feature vectors are then used as inputs into a classifier, such as the random forests classifier. Conditional random fields was then used to apply confidence intervals to the ouputs, this can be useful to avoid over fitting the data. Finally, in post-processing, Gaussian filtering and binary erosion where applied to the label image (Varambhia et al., 2022). XCT datasets of particulate filter channels are a good application for ML segmentation algorithms. The large datasets acquired by XCT, which contain many slice images of similar filter cross sections, means that training data from one slice (or a small volume) of an image stack will generalise well to the whole dataset (or to multiple datasets). Furthermore, for applications of ML segmentation where more training data is required, this data is readily available. This is particularly true in time lapse applications of XCT where large 4D datasets are acquired rapidly, producing many similar images with similar histogram ranges and noise levels.

This XCT segmentation was then used for quantifying the structure of the sample

on the length scales of 10^0 - $10^2\mu$m. Varambhia et al., 2022, demonstrated uniform pore, substrate and washcoat distribution along the length of the channel imaged with XCT. This indicates good manufacturing process control and suggests that the washcoating process can be finely controlled (Varambhia et al., 2022). Varambhia et al., 2022, suggest that with iterative testing, fast analysis & processing pipelines, and simulations, improved rational GPF designs can be achieved by fine tuning the coating process. The pore size distribution is also studied using the XCT in this study. By fitting spheres to the segmented data, see Figure 2.26, Varambhia et al., 2022, were able to estimate the pore size distribution, they report; a minimum pore diameter of 9.48 μm, mean pore diameter of 29.06 μm, and that approximately 30% of pores are larger than the mean. These large outliers can lead to lower filtration efficiency. Best practice for accurate metrology of pore size distribution with XCT is to verify pore size distribution with physical methods, such as Mercury Intrusion Porosimetry, and comparing the results as demonstrated by Václavík et al., 2017 and Gong et al., 2018a. Varambhia et al., 2022 also study the flow through the major flow channels that dictate flow through filter walls using CFD so that the major paths can be qualitatively visualised, see figure 2.26.

A number of other studies use XCT to study study the structure of particulate filters. Custer et al., 2016, Wang et al., 2020, and Price et al., 2022, use XCT to qualitatively visualise the distribution of ash on the channel and filter monolith scale. Price et al., 2022, are able to determine the distribution of different kinds of ash and their effect on backpressure on a realistic sample at the filter monolith scale. Václavík et al., 2017, Gong et al., 2018a and Nakayama et al., 2019, use XCT to measure the pore size distribution in filter wall sections using similar methods to Varambhia et al., 2022. Gong et al., 2018a, use the pore size distribution to inform a multiscale model of a GPF, whilst Nakayama et al., 2019, correlate the effect of pore size distribution on backpressure and filtration efficiency. Blažek et al., 2021, use synchrotron time lapse XCT to study the washcoating process during GPF manufacturing. They observe how washcoat shrinking and cracking depends on particle size distribution in the washcoat, they determine the effect of washcoat structures on backpressure, and they perform a statistical analysis on the washcoat distribution.

High resolution XCT has also been used to determine the permeability of ash layers (Kamp et al., 2017). In this study they use an XTEK 225 machine which has both a transmission and reflection source. The transmission source was used to image ash coating the top surface of a filter wall in-situ with a pixel size of 500 nm, whilst the reflection source was used to image the entire filer wall and ash layer with a pixel size of 1.2 μm. This data is then used in CFD simulations that implicitly solve the Navier-Stokes equation at each pixel in order to calculate permeability of the ash layer as well as the total permeability across the ash loaded filter. Kamp et al., 2017, report ash layer permeability of $5.82 \times 10^{-}14$ for a Mg-based ash layer. It seems likely that this work from Kamp et al., 2017 is still very resolution limited as many ash particles and structures are smaller than the pixel size of their XCT. For example, McGeehan et al., 2005 and McGeehan et al., 2009 show that ash particles range from 0.1 to 10 μm.

2.6.4 Image Based Modelling & Simulation of Particulate Filters

Early modelling approaches utilised 'unit-cell' models (Konstandopoulos, Skaperdas, and Masoudi, 2002), the porous filter wall is assumed to act as a group of unit cells, with each containing within it a simple geometric shape that acts as a collector of deposit (spheres for granular filters and cylinders for fibrous filters). Thus, the DPF filter is simply modelled as a granular filter, where a set of collector particles is evenly distributed in space and the ratio of collector size to the total unit cell size in each unit cell matches the macroscopic porosity of the filter. A transient filtration model is then derived by continuously re-computing the evolving unit-cell geometry due to PM deposition on each unit cells collector (Konstandopoulos, Skaperdas, and Masoudi, 2002). By applying the transient filtration unit-cell model Konstandopoulos and co-workers can calculate the amount of soot deposited as a function of superficial filtration velocity, pore size, porosity and wall thickness. The mass of PM deposited at different wall depths (or normalised wall thickness) at different loadings during deep-bed filtration can be modelled this way. This can be thought of as a idealised model based off the macroscopic equations defined above, and although a very simple model, it shows agreement with experimental SEM EDX results for deposit depth in filters with both showing a similar sharp decay in deposit

concentration with increasing wall depth. However, the lack of realistic porous microstructure in these models limits their application.

Vlachos and Konstandopoulos, 2006, have also used so-called 'digital materials' to model the micro-scale performance of DPFs from relevant 3D reconstructions of DPF pore structures. In order to create the digital materials sectioned SEM micrographs are captured from resin filled DPF substrates. Micrographs of DPFs are then reconstructed into a 3D volume using stochastic methods which reconstruct the 3D volume based on the specified statistical behaviour of correlation functions derived from the 2D micrographs (Vlachos and Konstandopoulos, 2006). These reconstructions are unreliable relative to modern XCT techniques, however at the time micro-CT with resolution high enough to resolve the porous microstructure was limited to synchrotron sources. The DPF digital materials are then used in filtration CFD models that apply the LB method for solving the 3D flow field for the first time in automotive filter literature. Suspended soot particles are treated as a separate phase with soot mass transport via convection and diffusion modelled by a suitable Euler formulation (Vlachos and Konstandopoulos, 2006). The model is run as a cyclic calculation and recalculation of flow field, particle transport and deposit shape evolution. Thus, the model simulates the extent of the deposition of soot in the deep bed and soot cake in micro-structured digital DPF materials. Vlachos and Konstandopoulos show that at the loading where the model gains 100% filtration efficiency and predicts a large drop in permeability is the same loading at which bridging between adjacent deposits occurs leading to the formation of the soot cake phase. Furthermore, by modelling the deposit distribution overtime the amount of soot under the influence of the catalyst in catalysed automotive filters can be calculated, an important factor in passive soot regeneration (Vlachos and Konstandopoulos, 2006). A number of other papers employ similar methods to this, i.e. using stochastic reconstruction of 2D micrographs, solving LB for the flow field and using Eulerian particle fields to model deposition (Stewart and Rector, 2004; Yang et al., 2009)

The last decade has seen Yamamoto and Yamauchi, 2013, Belot et al., 2020, Kamp et al., 2017 and Kočí et al., 2019, improve upon this state-of-the-art by employing micro-CT rather than stochastic reconstructions to create the filter domain for pore

scale modelling. Previously Yamamoto et al., 2006, had modelled the soot accumulation process but only very coarsely with 11µm/px XCT. More recently Yamamoto and Yamauchi, 2013, apply micro-CT to the NOx-soot regeneration process for a stationary non-transient soot deposit, Kamp et al., 2017, model the effect of ash build-up on permeability and pressure drop, and Kočí et al., 2019, model CO(g) oxidation. Plachá et al., 2020 and Belot et al., 2020 both model filtration efficiency. These studies all apply lab based micro-CT to create 3D volumes of the pore space and solve LB which allows for the calculation of the 3D distribution of local velocity and pressure on the pore scale for filter walls.

In a recent 2020 article, Plachá et al., 2020, model the filtration process. The micro-CT for this modelling is reported in a paper from the same group (Václavík et al., 2017). Václavík et al., 2017, use micro-CT and Mercury Intrusion Porosimetry (MIP) to study the pore scale of their catalysed SCRF samples before applying the technique to their CO oxidation model (Kočí et al., 2019) and filtration model (Plachá et al., 2020). Their results show that their application of the micro-CT technique, using an Xradia MicroXCT 400, does not resolve all the pores in their samples at a reported resolution of 1.14µm/px. The smallest pores in the SCR alumina washcoat are missed. However, it is important to note that non-SCR catalyst wash-coatings are much less porous than those reported on by Václavík et al. and in industrially relevant Three Way Catalyst samples the pores tend to be smaller, disconnected, and with lower overall porosity. Here they are able to segment the SCR washcoat phase from the cordierite filter phase due to the different x-ray attenuation of the two materials. They apply their micro-CT workflow to samples with different catalyst coating configurations. Thus, Kočí et al., 2019, are able to incorporate the effect of different 3D distributions of the catalyst phase on their CO-oxidation model and Plachá et al., 2020, are able to model the effect of this varying 3D distribution on the clean filtration efficiency . Placha et al. calculate the fresh filtration efficiency by first solving the velocity flow field in the microstructure of the catalytic filter wall in Open-FOAM by the LB method. Then, a Lagrangian solver is used to calculate the movement of individual soot particles in the velocity field and statistical filtration efficiency is calculated. However, the results of filtration models are not validated

by experimental observations of filtration (Plachá et al., 2020; Belot et al., 2020).

2.7 Outlook

GPFs are installed in contemporary GDI vehicles and will be installed in future GDI vehicles too. They are now the main focus of particulate filter research. GDI engines are more sensitive to backpressure changes. As a result an improved understanding of how to develop highly filtration efficient GPFs at low backpressure costs over the entire filter operational lifetime is needed. Additionally, ash effects the filter performance as it builds up as a layer on the filter wall. As a result physical properties of ash; porosity, particle size distribution, and permeability, will all directly effect the performance of the filter overtime in a way that is not well understood. Developing methods for characterising these ash properties is important for this area of particulate filter research. Finally, another important step in this research area will be to develop physics models such as those from Kočí et al., 2019, Plachá et al., 2020 and Belot et al., 2020. Working models such as these would allow OEMs to test new filter designs at specific working conditions on-chip without expensive testing. However, improved confidence in such models from experimental validation is needed to reduce the burden on testing.

In this project we have deployed a range of imaging techniques in order to better understand the research gaps mentioned above. We have used time resolved XCT with voxel size of 1.625 μm^3 to resolve how nanopowders with similar physical properties to soot deposit in the pores of particulate filters. This allowed us to observe how the microstructure of the filter deep bed changed during filtration in sections of a filter wall. This method was then extended so that the entire length of a 3 cm channel section could be imaged (by stitching together multiple tomograms). Such work can improve understanding of filtration and potentially validate physics models of filtration. Additionally, we also use XPT with correlated XRF tomography to image the fine microstructure of automotive ash with $<$ 50 nm voxels, including interior pores and particle size distribution. These images were compared to complimentary SEM EDX, and FIB SEM images of ash. XPT of ash structures allows for improved understanding of the physical properties of the ash that effects filter performance

TABLE 2.4: Table of complimentary imaging techniques as used in this project, including for each the resolution, field of view, acquisition time and samples studied.

	Resolution	**Field of View**	**Acquisition Time**	**Samples**	**Notes**
Synchrotron XCT	1.625 μm^3 voxel size	4.2 × 3.5 mm	1 - 20 mins	3 cm long 'mini channels', *see section 3.1.1*, cut from DPF, GPF, and aged GPF.	Time resolved synchrotron XCT was used in this project to study the build up of nano-particles that were flowed through operational filter samples in-situ. This was achieved with continuous imaging and flow (section 3.1.5) and also with stop-start imaging and flow (section 3.2.4).
Lab XCT	$>$ 10 μm^3 resolution	$\sim$ $6mm^2$ – $10cm^2$	20 mins - 2 hrs	Wall sections, channel sections, and monolith sections (cores) from DPF, GPF, and aged GPF.	Lab XCT was used for preliminary investigations and pre-scanning of beamtime samples. Lab XCT allowed us to observe the structure of particulate filters at a range of different scales (single walls up to monolith scale) and resolutions. Preliminary scans allowed us to check beamtime samples were not defective.
X-ray Fluorescence Tomography	0.25 – 0.5 μm^3 voxel size	25 × 13.75 μm - 50 × 25 μm	$\sim$ 10 hrs	Ash removed from aged GPF on pinhead and membrane, *see section 3.3.2*.	XRF-CT was used in a correlative workflow with XPT. Chemical imaging allowed us to resolve the chemistry of ash particles. However the method is limited by long scan times which can be costly in synchrotron beamtimes.
XPT	22.6 – 45.3 nm^3 voxel size	25 × 13.75 μm - 50 × 20 μm	1 - 2 hrs	Ash removed from aged GPF on pinhead and membrane, *see section 3.3.2*.	XPT provides 3D high resolution imaging of automotive ash at comparable resolution and field of view to FIB SEM. However, the technique is non-destructive (although the ash has to be removed from the filter).
SEM	$>$ 50 nm resolution	$\sim$ 3 μm^2 - 20 mm^2	$<$ 1 min	Wall sections from DPF, GPF, and aged GPF. Also ash removed from aged GPF on membrane samples.	SEM was used for preliminary investigation of particulate filter samples, including the aged samples because as the ash was well resolved. SEM is also complimentary to XPT in terms of resolution.
SEM EDX	35 nm pixel	36 × 27 μm	45 mins	Ash removed from aged GPF on membrane samples.	EDX was used as a complimentary method to X-ray Fluorescence Tomography.
FIB SEM (Serial Sectioning)	3 nm pixel (X, Y) and 20 nm pixel (Z)	36 × 9 × 17 μm	$\sim$ 12 hrs	Inlet surface of aged GPF wall section.	FIB SEM serial sectioning was used as a complimentary method to XPT and to verify the structure of internal pores in ash (as observed by XPT in similar samples).

in use. In table 2.4 we summarise the imaging techniques used, including for each the resolution, field of view, acquisition time and what samples the technique was applied to. The scientific background of these techniques is includes in sections 2.1 - 2.4. Details of the experimental methods used are included in the following chapter (chapter 3) and further discussion of the methods is also included in the results chapters (chapters 4, 5, 6).

Chapter 3

Experimental

Each section in this chapter links directly to the work presented in the following results chapters of the same name; section 3.1 links to chapter 4, section 3.2 links to chapter 5, and section 3.3 links to chapter 6.

3.1 4D In-situ Microscopy of Aerosol Filtration in a Wall Flow Filter

We used the pink beam modality at I13-2 to continuously image deposits of TiO2 in 4D as they built up in the pores of an automotive filter over time. We achieved this by flowing aerosol through operational filter samples and continuously rotating the samples for tomography. We studied SiC filters as a proof of concept. We present our results pertaining to a continuous in-situ experiment with an uncoated DPF in the paper Jones et al., 2020, and in Chapter 4 of this thesis. In this section we describe the experimental methods pertaining to these results.

3.1.1 Sample Preparation

Samples were cut from whole SiC DPF monoliths using a scalpel to remove a large section. This large section was then sanded down using a fine grade sand paper to a 3×3 channel cross section 3 cm long in the flow direction, see figure 3.1. The eight outer channels at the upstream end of the sample were blocked using a quick set epoxy resin, as was the inlet channel at the downstream end of the sample. This forces flow through the porous walls of the wall flow filters and is more realistic

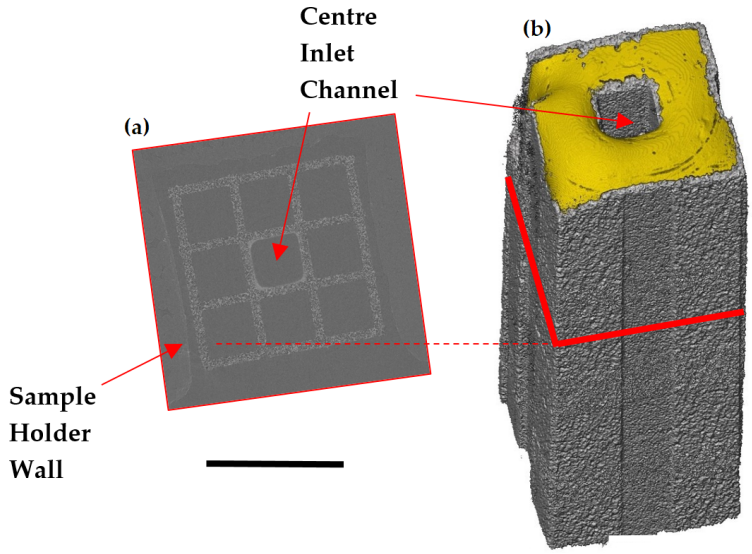

FIGURE 3.1: (a) An XCT slice and (b) a XCt volume rendering showing a typical wall flow filter sample. The samples were 2–3 cm long, with 3×3 channels, as shown in (a). Aerosol flowed into the filter through the centre channel, indicated by a red arrow, and was prevented from entering the exterior channels which were plugged with epoxy resin, shown in yellow. The central channel was blocked in the same way at the back end of the sample. Scale bar = 4 mm. Source: Jones et al., 2020

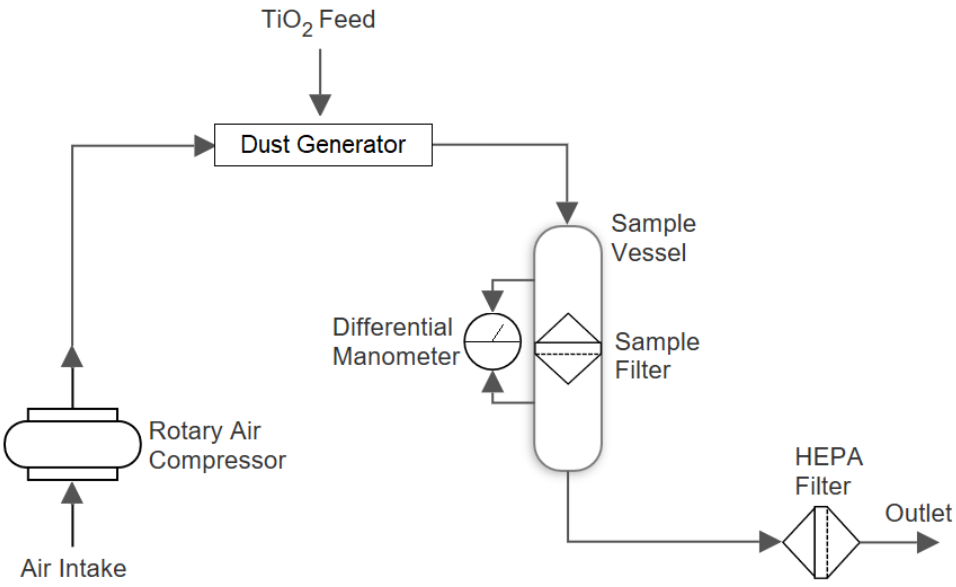

FIGURE 3.2: Schematic of the components used for the aerosol flow rig set-up at I13-2 during MG23490. Source: Jones et al., 2020.

than studying flow normal to a single filter wall (Jones et al., 2020), furthermore the extra material surrounding the inlet channel protects it from damage during sample preparation compared to removing a single filter wall (Jones et al., 2020). A rendering of a sample is shown in figure 3.1.

3.1.2 Solid Aerosol Generator (SAG 410/U)

The Topas SAG410/U was procured for this project in-order flow particles into filter samples for time-resolved in-situ imaging of particle filtration. We wanted a set-up that would allow for constant, reproducible, and adjustable powder mass flow rates. We also wanted a set-up that would be flexible and would aerosolise a range of powders of different sizes and flowabilities. The SAG410/U meets these requirements. The solid aerosol generator (SAG) consists of a rotating powder reservoir that is filled with a solid dry powder, see figure 3.3.b. During this project we have aerosolised test powders of different sizes (< 100 nm diameter to < 5μm diameter) successfully. The rotation of the reservoir prevents clumping and improved the rate at which powder travelled up the feeder, see figure 3.3.b, this is important for low flowability powders. An Archimedes screw in the feeder draws the powder from the reservoir to the top of the feeder were it is drizzled onto a rotating 'dosing ring' at the 'filling zone', see figure 3.3.b. The powder settles into a layer on top of the dosing ring and is shaped into a consistent shape. A scraper above the ring scrapes off particles above a certain height which was set by the operator. The width of the powder layer that settles on the dosing ring is determined by the width of the dosing ring used. In this way powder dose is consistent across the dosing ring's circumference. The dosing ring, which is constantly rotating during operation, transports this powder layer to the extraction site, see figure 3.3.b. Here a nozzle sucks the powder from the extraction site into the air flow, thereby aerosolising the powder. The aerosol then flows to the rest of the experimental flow rig. The flow rate through the SAG is determined by a pressure regulator, this inlet pressure must remain above 1 bar. Finally, it is possible to keep the SAG at an under-pressure. This means that the pressure inside the perspex box around the powder dosing ring and feeding mechanism is kept at a low pressure (< 1 bar), see figure 3.3.a. This means that air flows

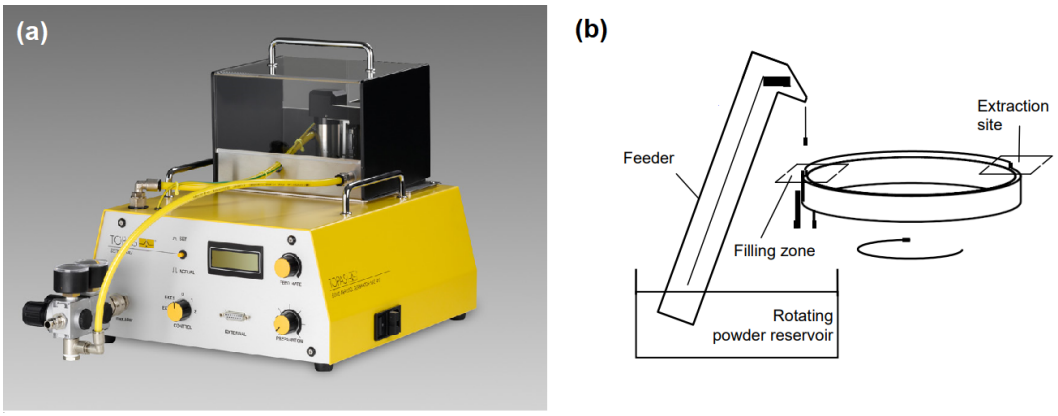

FIGURE 3.3: (a) SAG410/U Solid Aerosol Generator, (b) Schematic showing the operating principle of the SAG. Adapted from SAG410/U user manual.

from the atmosphere into the unit, rather than the other way around. This prevents contamination of the environment with powder or aerosol.

3.1.3 Aerosol Flow

A bespoke aerosol flow rig was designed and built for this experiment. A schematic of the aerosol flow rig used is shown in figure 3.2. A 5 bar head pressure was developed from an air compressor. The compressed air flowed through flexible polyurethane tubing that connected components in the aerosol flow rig. The pressure regulator at the front of the SAG was used to regulate the volumetric flow rate through the the aerosol rig. During these experiments it was important to run the SAG at an underpressure, where the pressure inside the SAG is less than the hutch environment, so that air flow from the hutch into the SAG, preventing the leakage of aerosol from the SAG into the hutch environment. The aerosol mass flow rate generated by the SAG was controlled by varying the height of powder on the dosing ring and the speed of the dosing ring. By keeping these constant and flowing aerosol into a clean HEPA filter of known mass and then re-weighing the filter the mass flow rate of the experimental set-up was determined.

The aerosol then flows to a bespoke 3D printed sample holder, shown in figure 3.4. The sample holder was printed in 5 mm thick Acrylonitrile Butadiene Styrene. The sample holder was stiff enough to avoid deflection during rotation, whilst also thin enough to minimize unnecessary beam attenuation. The sample is glued into place

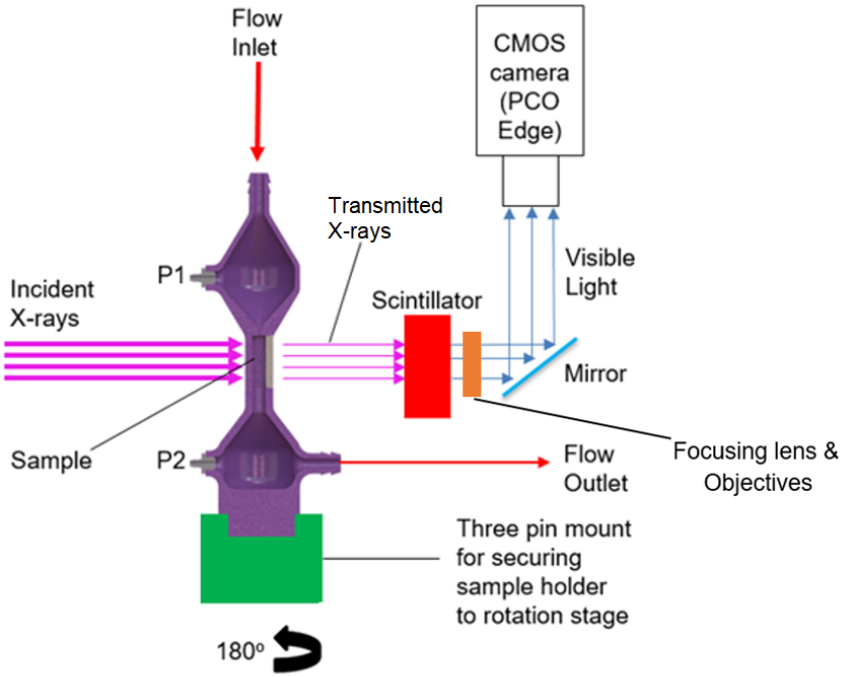

FIGURE 3.4: Diagram of the imaging set-up at I13-2. Source: Jones et al., 2020.

within the sample holder, this prevents sample movement during the experiment. The sample holder reduced in width so that a 1 mm $\times$ 1 mm opening directed flow through the central channel. The design also included outlets perpendicular to flow allowing for simultaneous pressure measurement before and after the sample position, see P1 & P2 in figure 3.4. This allowed for in-line measurement of the pressure drop through the filter during the filtration experiment. The RS PRO series manometer used had a plotting function so that the data could be saved as a spreadsheet. The manometer had an accuracy of $\pm$0.005 kPa. Finally the aerosol flows through to the HEPA filter (Pall HEPA Capsule; 99.97% 0.3 μm particle retention). The HEPA filter removes the nanoparticles from the flow in order to protect equipment in the hutch environment and to prevent inhalation of the nanoparticles.

3.1.4 Diamond I13-2 beamline

The I13-2 Diamond - Manchester Beamline was used for this experiment. I13-2 focuses on absorption and in-line phase contrast micro tomography in the 6 - 30 keV

energy range and can switch to full field microscopy with up to 50 nm spatial resolution (Rau et al., 2016). The radiation source is the 2 m long U23 undulator which produces x-rays with harmonic peaks that can be tuned depending on experimental requirements. The flux at a typical energy of 20 keV from the undulator is approximately 10^{14} ph/s at 0.1% band width, with a beam size of 400 μm × 13 μm and x-ray beam divergence of 60 μrad x 25 μrad (horizontal x vertical; all Full Width Half Maximum) (Fanis et al., 2013). The layout of the imaging branchline is shown in Figure 3.23.

Inside the first optical hutch (OH1) are the first set of shutters, slits and filters. The shutters open and close to prevent the beam reaching the endstation. The slits define the size and shape of the beam. The filters, which are made of various elements and are of variable thickness, will filter out low energy x-rays that are undesirable in many imaging experiments and reduce the heat load on more sensitive downstream components (Fanis et al., 2013). OH1 also contains a mirror to deflect the beam from its parallel coherent path, to filter harder x-rays from the beam, and to introduce a degree of focusing (Fanis et al., 2013). A second set of silts in OH2 is followed by the third pair of slits and the monochromator that are housed outside the main synchrotron ring in OH3. The monochromator narrows the bandwidth of the beam from 10^{-2} to 10^{-4} ($\Delta E/E$) (Fanis et al., 2013). By setting the double crystals of the monochromator parallel to the beam it will not effect the beam, resulting in the 'pink' beam, i.e. polychromatic, which is ideal for fast experiments (Rau et al., 2016). This pink beam spectrum will be determined by the undulators ID gap, filter, mirrors and windows. At the sample position the pink beam is $\sim$ 100 times more intense compared to the highest flux from the monochromator of approximately 10^{13} ph/s (Fanis et al., 2013). The beam then enters the experimental hutch through a 300 μm diamond window, a final set of slits, more filters, and finally a set of fast shutters (Fanis et al., 2013).

The experimental set-up in the experimental hutch is constructed on a vibration isolated table. Installed on the table is a high precision rotation stage (about 25 nm run out) for tomography and a detector stage which can be translated over a distance of 2 m for in line phase contrast (Rau et al., 2016). The scintillators and objectives are

fixed on to a revolver system so that they can easily be interchanged for multiscale imaging experiments. The different combinations of scintillators and objectives span spatial resolutions from 5 to 1 μm and field of views of $\sim 9 \times 6\ mm^2$ to $1 \times 1\ mm^2$ by using $2\times$, $4\times$ or $10\times$ objectives (Fanis et al., 2013; Rau et al., 2016). The visible light from the scintillator is reflected through a mirror through one of these objectives to either a PCO Dimax, PCO Edge or PCO 4000 camera (Fanis et al., 2013). These offer a trade off with the Dimax offering the highest acquisition rates (up to 1279 fps), the 4000 offering highest spatial resolutions, and the Edge offering intermediate qualities (Fanis et al., 2013). This data is then saved via EPICS IOC in the HDF5 file format onto Diamond Light Source central storage where it can be processed by users (Fanis et al., 2013; Bodey and Rau, 2017).

3.1.5 Imaging

The continuous workflow consisted of aerosol being flowed through the sample continuously whilst the sample was illuminated with X-rays and rotated for tomography at I13-2. For the continuous in-situ imaging the projections were acquired from the centre of the sample filter. A radiographic projection was acquired every 0.18° in an 180° fly scan (1000 projections) with exposure times of 0.01 s. Once one tomogram was acquired from $0^\circ \longrightarrow 180^\circ$ the next was immediately initialised from $180^\circ \longrightarrow 0^\circ$. We obtained flat and dark field images before and after each in-situ run (i.e. after all time steps have been acquired) rather than after each tomogram acquisition in order to reduce the time taken per projection. We utilised the 'pink beam' configuration at I13-2 with several harmonic peaks. The ID gap was set at 5 mm, and a 3.2 mm Al filter was installed before the sample to filter the beam. Thus, the spectrum reaching the sample ranged from 6 to 35 keV, the peak flux was 25 keV and the integrated photon yield was approximately 3.72×10^{12} ph/s at the sample position. The $2\times$ objective was used for this continuous workflow coupled to a $LuAg$ scintillator. This $2\times$ lens resulted in a total $4\times$ magnification with pixel size of 1.625 μm. The continuous workflow was thus able to acquire tomograms that resolved the deposits in 3D at a rate of 1 tomogram/minute. The in-situ run lasted 20 min, the run was stopped once caking layer was observed on the surface of the filter wall. The 'zeroth' scan was procured before the aerosol flow was turned

on. The first 'loaded' scan was acquired after 2 min, after which a new scan was acquired every minute. Between in-situ runs a $CdWO_3$ scintillator was used with a 1.25× objective for larger overviews of the sample. The 4× objective was also used for more detailed imaging and was coupled to a $LuAg$ scintillator. At the start of the beamtime the spectrum was optimised such that sufficient brightness and contrast was observed in the radiographs.

3.1.6 4D Data Processing

Projections were reconstructed with filtered back projection in 16 bit grayscale using the Savu platform where a distortion correction algorithm was also applied to unwarp the images (Atwood et al., 2015; Vo, Atwood, and Drakopoulos, 2015). Each volume in in-situ sequence is then cropped to 1410 × 1410 × 2110 voxels. This pixel volume represents a real volume of 2256 × 2256 × 3376 μm. The volumes were then stacked as a time sequence. Resulting in a array of dimensions 18 × 1410 × 1410 × 2110 (t, x, y, z).

In order to quantitatively interpret the dataset the volumes needed to be segmented into pore/background, filter and deposit. The volumes were first converted to 8 bit to reduce dataset size. The volumes were then smoothed with non-local means filtering. A mask was created of the filter in the 'zeroth' volume in the time series, when there has been no aerosol deposition, using a global threshold (volume > 120). This was then eroded and subsequently dilated, thereby removing noise and filling holes in the segmentation. This was then applied to the subsequent volumes in the times series to mask out the filter phase in the image. Deposit segments and background segments for each volume in the time series are then obtained through another global threshold (volume > 112). This resulted in binary volumes of the deposit segment. Noise in the segmentation was removed by smoothing and then re-segmenting the deposit segment consistently across the entire data series. These are combined for fully labelled volumes with filter, TiO_2 deposit, and background segments. This data can then be quantitatively interpreted, see chapter 4.

3.2 Multiscale Time Resolved Microscopy of Aerosol Filtration in Gasoline Particulate Filters.

We used the pink beam modality at I13-2 to image deposits of ZnO nanoparticles (ZNP) in 4D as they built up along the entire length of a sample channel and in the pores over time. We achieved this by flowing aerosol through operational filter samples, pausing flow, and then rotating the samples for tomography. We studied coated and uncoated GPFs as provided by our industrial partners Johnson Matthey. We present our results pertaining to the multi-scale time resolved experiment in Chapter 5 of this thesis. In this section we describe the experimental methods pertaining to these results. This method aimed to improve on the '4D in-situ microscopy' method described in section 3.1 by using volumetric flow rates that are equivalent to flow rates in operational conditions, improving characterisation of the aerosol developed with DMS analysis, and extending analysis to the entire sample channel.

3.2.1 Sample Preparation

Sample preparation is as described in section 3.1 but samples are removed from coated and uncoated cordierite GPF monoliths. In the case of the coated samples they were pre-scanned in a Nikon 225 lab CT machine in order to confirm the presence of a coating layer in the central channel of the filter.

3.2.2 Aerosol Flow

A bespoke aerosol flow rig was built for this experiment by updating the rig described in section 3.1. The updates are put into place to allow for improved control and measurement of volumetric flow rate at low flow. The typical volumetric flow rate used with this rig was 20 ml/min. A schematic of the aerosol flow rig used is shown in figure 3.5. A 5 bar head pressure is generated by the air compressor. The SAG operates as described in section 3.1.2 & 3.1. After the SAG, the line forks to the main line and bypass line. The bypass line is required to make sure that there is enough flow through the SAG to ensure proper suction at the extraction site so that all powder from the dosing ring is removed, ensuring a consistent aerosol mass flow rate whilst also allowing for low flow rates through the main line by splitting

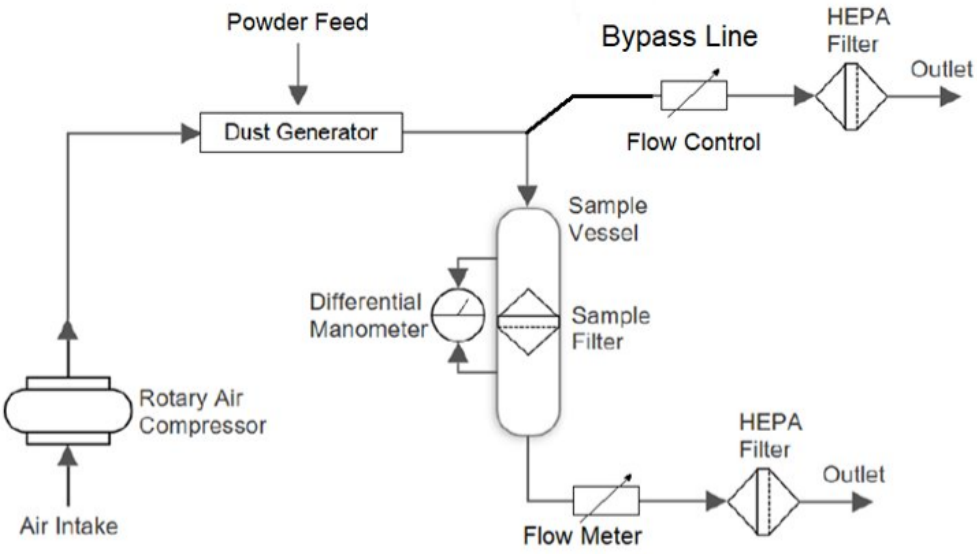

FIGURE 3.5: Schematic of the components used for the aerosol flow rig set-up at I13-2 during MG29110.

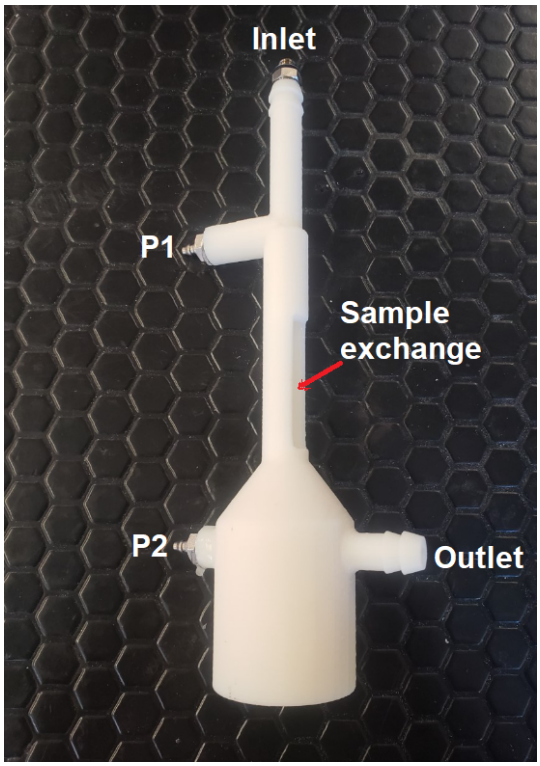

FIGURE 3.6: Photograph of the 3D printed sample holder used during MG29110.

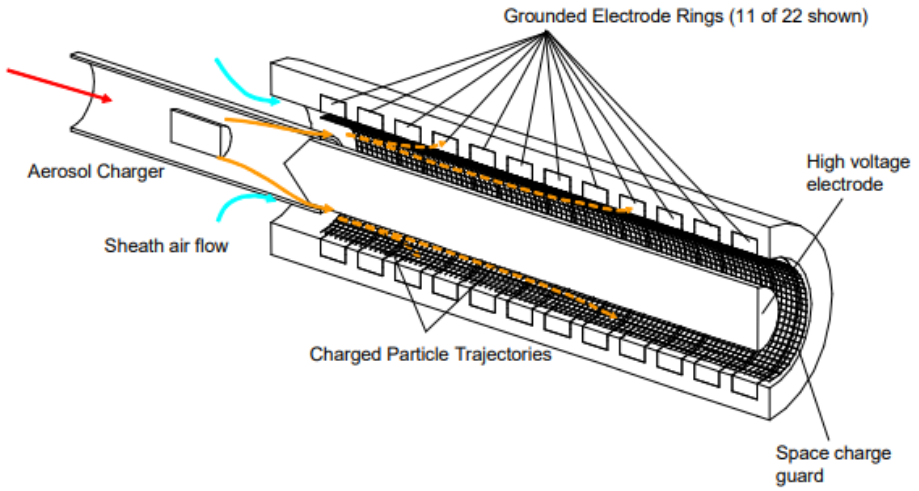

FIGURE 3.7: Schematic showing the operating principle of particle size distribution measurement in a DMS500 particle sizer. Adapted from Cambustion DMS500 user manual.

the flow. The relative amount of flow in each line is controlled by a flow controller on the bypass line. This flow controller valve can be opened and closed such that the flow meter on the main line reads the intended flow rate. Once again a HEPA filter is placed at the back of the lines to act as an exhaust filter, filtering ZNP from the aerosol in order to keep the hutch environment safe. Finally, the design of the sample holder was also updated. The dumbbell shaped sample holder, rendered in purple in figure 3.4, is replaced with a straight pipe design, see figure 3.6.

3.2.3 Aerosol Size Distribution Measurement

The DMS500 was used to measure aerodynamic diameter of the ZnO aerosol developed for in-situ time resolved imaging of filtration. The particle sizer provides a number/ aerodynamic diameter spectrum for particles between 5 nm and 1 μm. In other words it counts the number of particles in a aerosol that have aerodynamic diameters within certain binned sizes. The aerodynamic diameter of a particle is defined as that of a sphere, which has a density of 1 $g.cm^{-3}$ (unit density, equal to density of water), which settles in air at the same velocity as the particle understudy, defined below.

$$D_P = \sqrt{\frac{18\mu v_s}{\rho_0 g}} \tag{3.1}$$

Where μ is the viscosity of air, v_s is the settling velocity of the particle , ρ_0 is unit density, and g is acceleration due to gravity.

Once aerosol has been flowed into the DMS system dilution and separation steps take place before the size measurements can occur. The dilution steps reduce moisture in the aerosol and prevent further agglomeration or nucleation of the aerosol. The aerosol can be diluted to between 12:1 to 500:1, in our application a dilution of 50:1 is used. A cyclone separator then removes particles larger the 1 μm from the aerosol, this simply prevents the build-up of heavy particles at the back of the system reducing the need for maintenance. Figure 3.7 shows the operating principle of the particle size measurement. An aerosol charger that uses a fine corona wire at high voltages produces positive ions that collide with the aerosol particles thereby charging them as they flow into the classifier column, see figure 3.7. Once in the classifier column a second particle-free laminar flow of air carries the aerosol through the column, see figure 3.7, this means that the particles flow in a predictable manner. A high voltage rod in the centre of the column repels the charged particles towards the wall of the column whereupon they yield their charge to the grounded electrode rings placed along the length of the column. Their point of contact along the length of the column is a function of their charge and aerodynamic mobility. Each charge detected yields a separate particle count with time resolution of 200 ms, the ring from which the charge was detected determines which size bin the charge is counted into. Each bin is calibrated empirically to an aerodynamic particle size.

During the aerosol sizing experiment ZNP aerosol was developed by the SAG and was flowed into the DMS through identical lengths of tubing at similar humidity and temperature conditions (lab conditions) to the beamtime experiment previously performed. This is so that the ZNP aerosol size distribution and concentration measured by the DMS is a good measure for the aerosol generated during the in-situ imaging experiment performed separately (this was not an in-line measurement). This developed an aerosol concentration of 14×10^7 n/cc with an aerosol size distribution as shown in figure 3.8.

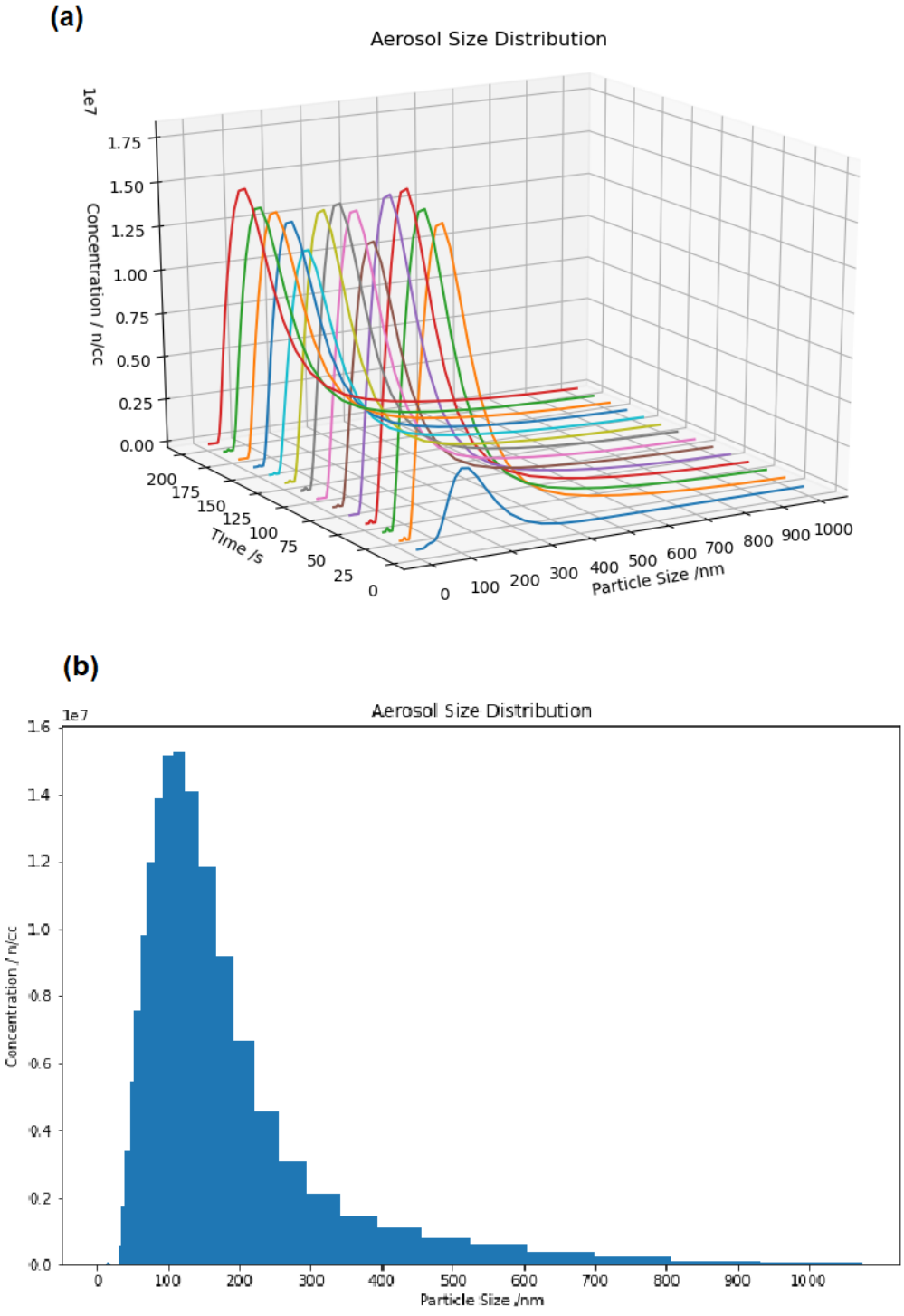

FIGURE 3.8: Aerosol Size Distribution; (a) Aerosol size distribution over 200 s of flow. The aerosol flow rig develops a consistent concentration and size distribution over test, (b) averaged distribution over the same period. The peak particle size is at 100nm

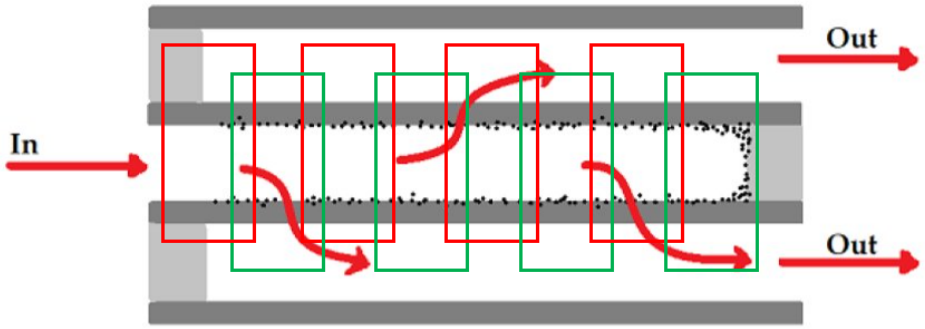

FIGURE 3.9: Schematic showing how the entire length of a GPF sample was scanned by stitching together vertically aligned ROI as shown.

3.2.4 Imaging

The imaging was performed at I13-2, the beamline is described in section 3.1.4. The multiscale and time resolved workflow consisted of aerosol being flowed through the sample at 20 ml/min, the flow being paused, and then a sequence of 8 vertically aligned tomograms that covered the entire length of the sample filter channel being acquired, see figure 3.9. These were acquired so that neighbouring tomograms overlapped by approximately 100 px. The flow would then be resumed, paused again after a set amount of time, and the vertically aligned tomograms re-acquired. This was repeated for 6 time steps. Thus a tomogram was acquired after 10 s, 20 s, 30 s, 40 s, 70 s, and 100 s of loading. Additionaly, when the sample was in a clean state (i.e. before any aerosol flow) another set of vertically aligned tomograms were acquired (0 s).

For these tomograms a radiographic projection was acquired every 0.1° in an 180° fly scan (1800 projections) with exposure times of 0.03 s. We obtained flat and dark field images before and after each set of vertically aligned tomograms. We utilised the 'pink beam' configuration at I13-2 with several harmonic peaks. The ID gap was set at 5 mm, and the Pt mirror was used, this already filtered the beam sufficiently so no extra filter was installed. Thus, the spectrum reaching the sample ranged from 6 to 29 keV, the peak flux was at 17 keV. The 2× objective was used for this continuous workflow coupled to a $LuAg$ scintillator. This 2× lens resulted in a total

4× magnification with pixel size of 1.625 μm. Data was also acquired with the 4× objective for more detailed imaging. At the start of the beamtime the spectrum was optimised such that sufficient brightness and contrast between the deposit phase and background was observed in the radiographs.

3.2.5 Multiscale & Time Lapse Image Processing

The method described in section 3.2 resulted in a large dataset that traversed length scales from the pore scale (10's of μm) to the sample length scale or channel scale (3 cm). In order to quantify the dataset it needed to be segmented into background/pore, filter, deposit, and catalyst coating (in the case of the coated samples) segments. However, due to the overlapping gray level values of the phases of interest, and low contrast between deposits and background due to the low density of the deposits (lower density due to lower flow rates compared to the section 3.1 method), this was a challenge to segment. Because of this size and complexity a robust scripted methodology was applied in order to process the images and eventually segment the dataset. This was completed using open source python packages such as numpy, scikit image, OpenCV, SimpleITK, and Tensorflow. This was achieved for a 'bare' uncoated GPF dataset as well as a 'coated' dataset. These datasets are processed in a very similar manner, where there are differences in the image processing method these are stated. The workflow is outlined in figure 3.10.

Data Reduction and Cleaning

The first steps are to reconstruct the data in Savu using the Filtered Back projection algorithm from Astra (Atwood et al., 2015). We also apply ring removal, distortion correction, and dark-flat field correction at this stage (Vo, Atwood, and Drakopoulos, 2018; Vo, Atwood, and Drakopoulos, 2015). The data is then converted into 8bit in order reduce the size of the dataset. In 8 bit each tomogram of 1470×1470×2160 (x ,y, z) has a size of 4.7 GB. Thus, each data set for a multiscale time resolved sample (which included 8 vertically aligned tomograms and 7 time steps) had a size of $4.7GB \times 8 \times 7 = 263.2$ GB.

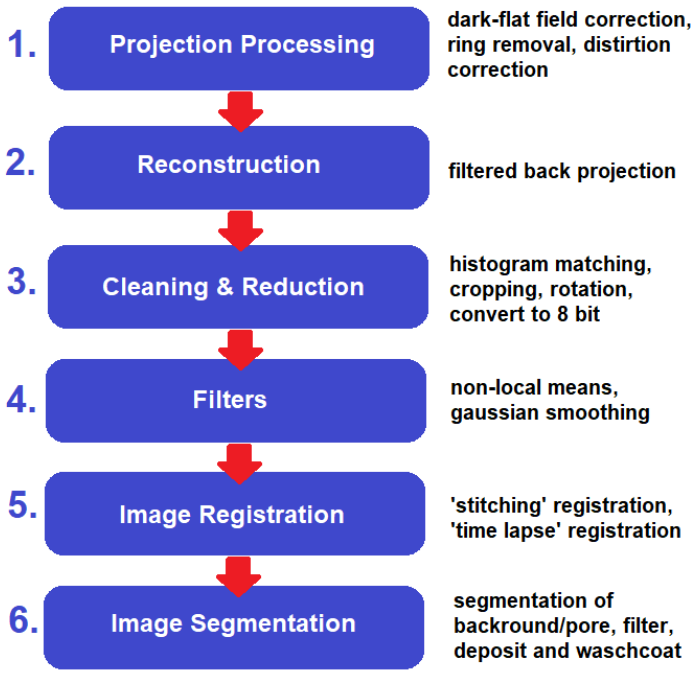

FIGURE 3.10: An outline of the workflow used to process the time lapse and multiscale data set.

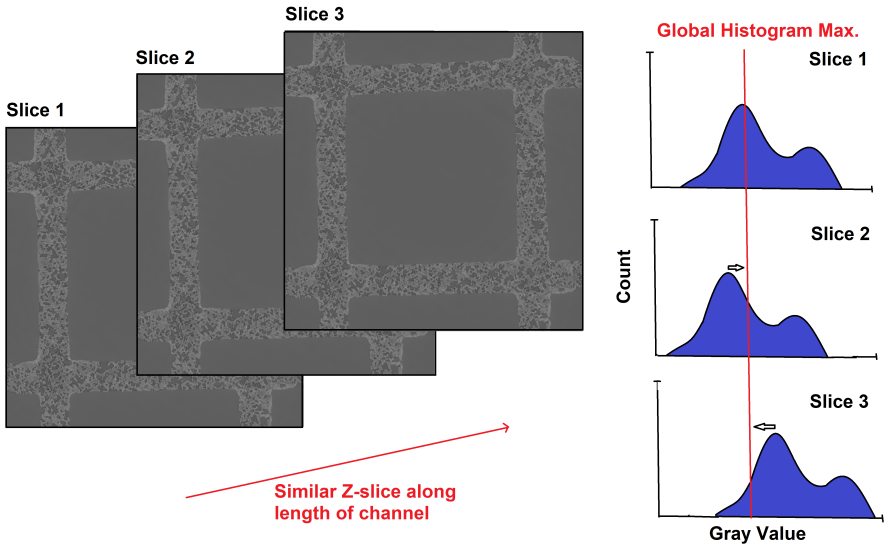

FIGURE 3.11: Schematic showing the operating principle of the histogram matching applied to the dataset; because the histogram maximum of a slice is always the background peak we can simply 'translate' the histogram so that this peak aligns with, or matches, the global average position of that peak.

We then apply histogram matching. Histogram matching was achieved by finding gray value of the global histogram maximum and matching the maximum in each slice of the dataset to the global value through histogram translation (i.e. addition or subtraction of an integer from every pixel value in a slice so that the histogram maximum in the output slice is at the same value as the global maximum value). This is only possible because of the prism-like structure of the sample, where each slice in the z-direction is of a very similar cross section and where there is a robust maximum due background pixels, see figure 3.11. Thus this method essentially makes the background values in each slice the same value. Histogram matching is an important step as it means thresholds and other pixel value sensitive processing steps can be applied consistently across the dataset.

The images, which until this point had been saved as a stack of 2D slices, were then converted into 3D tiff files of each tomogram. The images are then rotated such that the walls of the filter channels run parallel to the axes of the image. After rotation any excess space around the volume is cropped away so that each tomogram has a size of $1150 \times 1150 \times 2160$ for the bare sample dataset and $1240 \times 1240 \times 2160$ for the coated dataset.

Image Filters

The next step is to apply non-local means (NLM) smoothing to the entire dataset. This is a very resource intensive operation since NLM computation scales quadratically with increasing number of pixels. For this reason the NLM filter was applied slice-wise in parallel using multiple cores of the CPU (typically 20 cores). We use python's concurrent.futures module to launch parallel tasks of scikit image's NLM filter algorithm. However, we did not apply the filter consistently across the entire dataset. We found that noise peaked in the centre of each tomogram. This was due to detector 'browning' that occurred over time as x-rays damaged the detector. The effect of browning on noise is shown in figure 3.12. Therefore adaptive smoothing was applied to the zeroth volume by different NLM filters depending on the noise level in a region-by-region basis. Where noise was high a set of pre-defined NLM filters were applied until the SD reached an acceptable level. Where noise was low

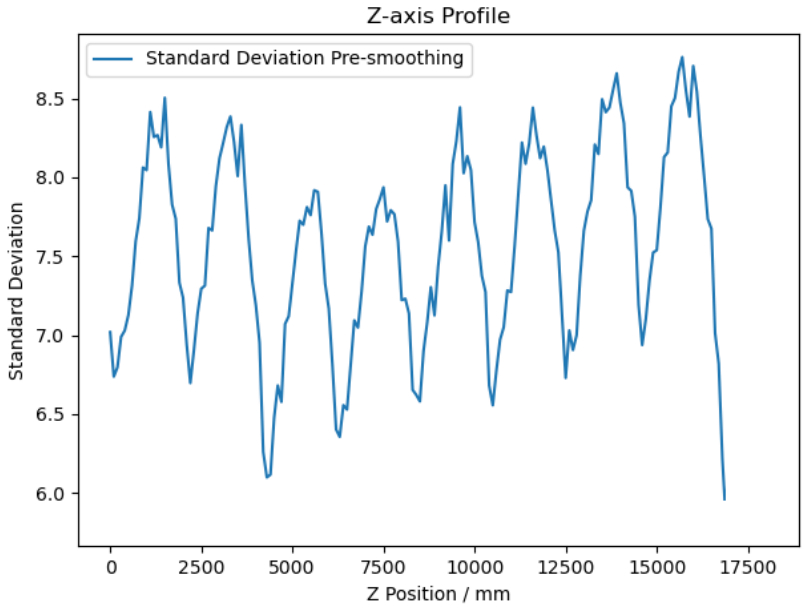

FIGURE 3.12: Standard Deviation along the entire length of a filter sample; here the peaks in standard deviation align roughly with the centre of each tomogram in the vertically aligned set of 8.

no filter, or fewer filters, were applied. After NLM smoothing of the zeroth volume we applied adaptive smoothing to the rest of the dataset (i.e. the deposit loaded volumes) by applying NLM smoothing to the deposit loaded volume until the peak signal to noise ratio (PSNR) between the equivalent zeroth volume and the deposit loaded volume no longer improved. Thereby effectively applying smoothing until the noise level in the deposit loaded volume was at a similar level as in the equivalent zeroth volume. We calculated the PSNR from a mask of the solid filter phase so that deposit in the deposit loaded volumes did not effect the PSNR calculation. It was important that the deposit loaded volumes were not over or under smoothed with respect to the zeroth volume as this lead to erroneous segmentation of pixels later in the workflow. After the adaptive NLM filtering (applied slice-by-slice) a 1D Gaussian filter was applied to smooth in the z-axis.

Image Registration

Image registration has two important roles in this workflow. The first was volume 'stitching', here we register the overlapping volumes between the eight vertically aligned tomograms onto each over so that we can create one continuous image of

FIGURE 3.13: High resolution image of a cross sectional XCT slice after the 'stitching' registration of the eight vertically aligned tomograms, resulting in a continuous volume of the sample channel. Here we show the clean (0 s loading) tomogram. Because the flow was stopped at each time step we were able to procure this set of eight tomograms with the cumulative loading time being the same in each tomogram, see section 3.2.4. Scale bar = 750 μm

the sample channel, see figure 3.13. The second is 'temporal' registration. Here we registered volumes that represent the same space but at different times of the experiment onto each other.

Volume stitching registration is applied only to the 'zeroth' tomograms, these are the tomograms acquired before any aerosol flow. The subsequent loaded tomograms are then registered onto these zeroth tomograms during the temporal registration step. Stitching in this workflow was was achieved with exhaustively optimised registrations in SimpleITK.

During registration the image that is being registered is called the 'moving image', and the image that is being registered to is the 'fixed image'. During the stitching process the 'moving image' was the tomogram further along the z-axis, i.e. further downstream, and the 'fixed image' was the tomogram above it. Exhaustive optimisation works by transforming the moving image to each point on a grid and evaluating a similarity metric at that point. A similarity metric describes the similarity of the two images, examples include mean square error and Mattes mutual information. In exhaustive optimisation the point on the grid with the best similarity metric is the optimal transformation for registering the two images.

We utilised a series of three such exhaustive optimisations each with successively finer grids to find the best 3d translation transform. The first exhaustive search was centred around the transform that superimposed the centres of the two images, in this case an identity transform, and coarsely searched a large volume for the best transform. The second was centred on the best registration found during the previous coarse optimisation and searched a finer grid of transforms. Similarly the third and final grid was centred on the best registration from the previous optimisation and had the finest search grid, defined by a step size of 1 px and a $10\times10\times10$ grid. We used the output best transform, as determined by the Mattes mutual information optimiser, as the transform that registers the two images. This transform is then applied to the moving image. We can then 'stitch together' the tomograms to make a continuous section of channel, see figure 3.13. Some efficiencies are gained by only processing the overlapping portions of both tomograms, reducing memory requirements. Furthermore, when calculating the similarity metric there is no need

to calculate it at every pixel, in fact a very small fraction of pixels suffice. We sampled only 0.02% of pixels (45000 pixels) which were sampled randomly. Thus this exhaustive optimiser based method was sufficient, since; very accurate registration was not critical to later analysis, the overlapping volumes were relatively small, and we were only required 3D translation transforms.

The temporal registration is very important to the later segmentation because the segmentation is very sensitive to registration error. For this registration the deposit loaded tomograms were the moving images and the corresponding zeroth tomograms were the fixed images. Again, the registration was achieved using SimpleITK. Similarly to the 'stitching' registration the first step was to apply a coarse exhaustive optimisation. This was centered around the transform that superimposed centres of the two images, in this case a unit transform. The metric was Mattes mutual information. Unlike in the stitching registration we also included rotations in radians in the transforms. This exhaustive optimisation was slow but it was important to find a good initial transform for the next step of the workflow so that the registration was robust and could be applied in a script to the entire dataset.

This next step was to apply a simple gradient decent optimiser. Gradient decent optimisation in image registration works by sampling the space around the initial transform by calculating the similarity metric for each point (where each point is a transform). The best transform is then selected as the new starting point and every point around that is sampled with the best point being chosen as the next point. This is repeated until the similarity metric converges at a minimum value. This is a good method for accurately finding the best registration with less computational cost compared to the exhaustive method above. However, it is important that the images are relatively well registered at the outset otherwise it is likely that the gradient decent optimiser method will 'fall' into a local minimum rather than finding the global minimum. For this reason we applied the exhaustive method beforehand in order to coarsely register the image first. By applying this workflow we found the optimal 3D Euler transform (a rigid 3D transform with rotation in radians around a fixed center with translation), using the mean squares metric. This transform was then applied to the moving image, thereby registering it onto the zeroth image. Since

the fixed image had already been transformed into a continuous channel volume during the stitching registration, this registration also aligns these moving images into a continuous set without the need to run another registration.

Filter & Deposit Segmentation

Once the the data was registered we had a data set of seven stitched together continuous filter channels (see figure 3.13), one in a clean state, referred to as the 'zeroth' volume, and six at increasing loads of deposit (10s, 20s, 30s, 40s, 70s and 100s of loading). In order to segment the data we first segment the filter and background/pore phases in the zeroth volume. A simple global threshold can be applied in order to achieve this. For the bare sample the threshold is where $volume \geq 97$, and for the coated sample, where $volume \geq 96$. We then apply binary dilation and erosion to this segmentation to smooth and fill holes in the filter segment.

We then created utility masks that helped with the remainder of the workflow. These were a 'walls' mask and a 'channel' mask, see figure 3.14. The walls mask was created by aggressively dilating and eroding the filter segmentation 2D wise with a square kernel of width 50. This was parallelised using concurrent.futures to launch parallel tasks of the scikit image erosion/dilation function. The channel mask was made by flooding the central region bound by the walls in the walls mask using the scikit image function. These are useful masks as they allowed us to select and process pixels based on their location in the image. For example, using the walls mask we can process data that lies only inside the walls by applying the inverse of the mask used in figure 3.14.b. The channel mask allowed us to select only pixels that are in the central channel, this is particularly useful for selecting on-wall deposit.

We then segmented the deposit. In order to do so the filter mask from the zeroth volume was applied to the data, see figure 3.15. Because of the registration step the zeroth filter mask would ideally mask out the filter in the subsequent deposit loaded volumes so that all the remaining high graylevel pixels belonged to the deposit segment. In figure 3.15.c we show the application of the zeroth mask to a deposit loaded volume (100s loading). However, the remaining high value pixels are from two sources, the deposit (as desired), but also from filter pixels at the edges

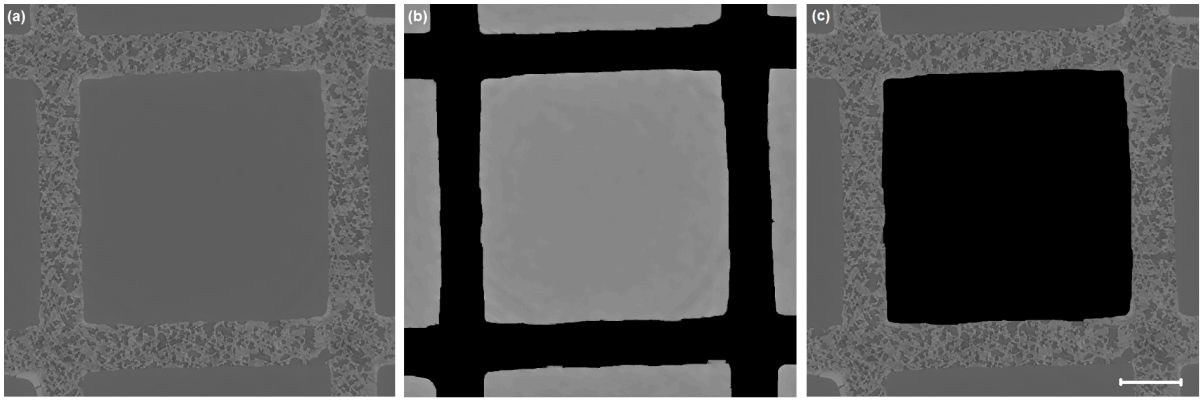

FIGURE 3.14: Utility masks used during segmentation; (a) grayscale data of a coated GPF slice, (b) the grayscale data with the 'walls' mask applied, (c) the grayscale data with the 'channel' mask applied to it. Scale bar = 300μm

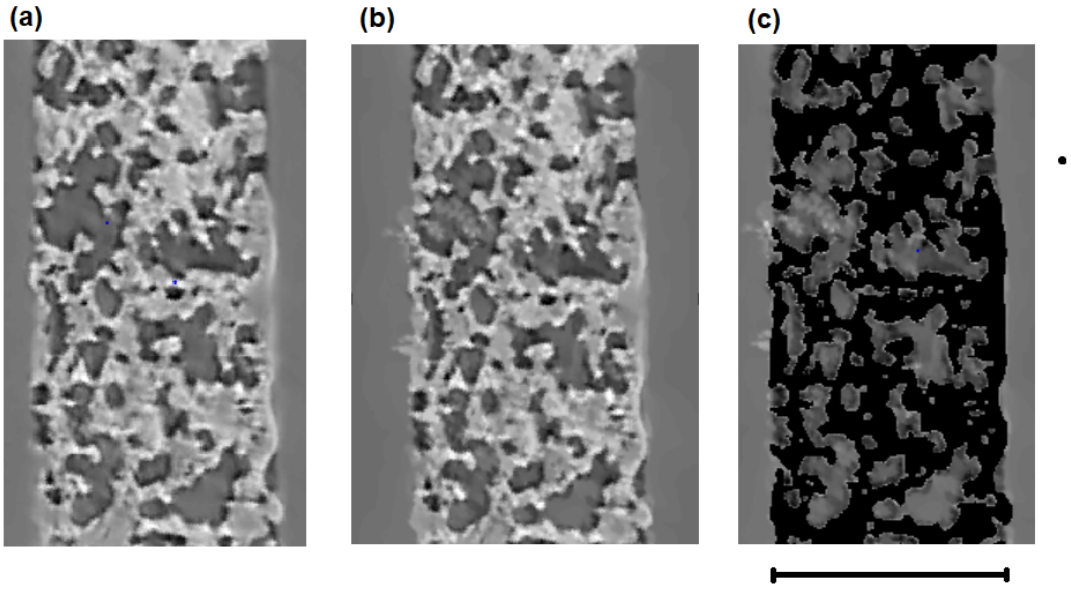

FIGURE 3.15: Applying the zeroth filter mask to deposit loaded volumes; (a) grayscale slice of the zeroth volume, (b) the same region after 100 s of loading, (c) the grayscale data with the zeroth filter mask applied to it. Scale bar = 230μm

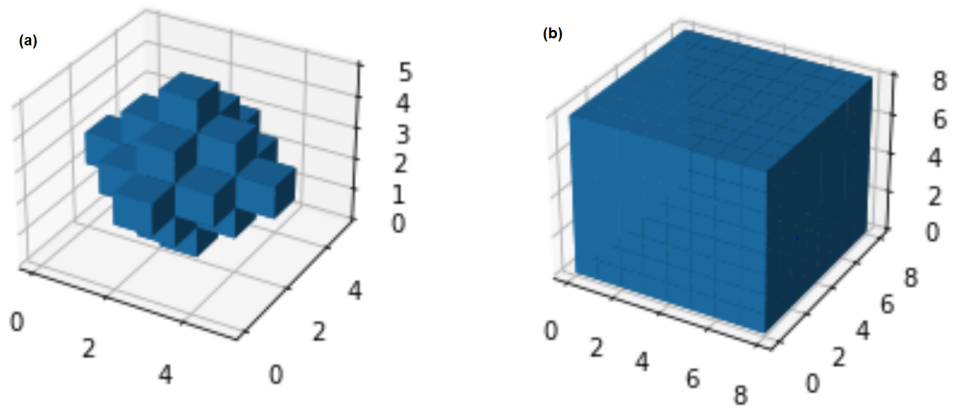

FIGURE 3.16: 3D render of the structuring elements for dilation, (a) used to dilate the filter mask, (b) used to dilate the deposit segmentation.

of the filter that are missed by the mask. These missed edge pixels were present in similar amounts even at low loads. The structuring element in figure 3.16.a was therefore used to dilate the mask. This structuring element will include any pixel that shares a face or edge with an input label pixel at a distance of 1 pixel (i.e. 18-connected at 1 pixel distance), and any pixel that shares a face at a distance of 2 pixels (6-connected at 2 pixel distance). This is done in order to remove these edge pixels from the segmentation.

The masked volume is then segmented. Pixels that were greater than or equal to the graylevel of the equivalent pixel in the zeroth volume plus eight, i.e. where $volume \geq zeroth + 8$, and also had a gray level greater than or equal to 98, i.e. where $volume \geq 98$, were included in the initial segmentation. Any connected regions of this initial segmentation that were smaller than 27 pixels were then removed from the segmentation. This is to exclude noise from the segmentation and effectively defined the resolution of the segmentation. The segmentation is then dilated by a cube of width = 9 px, see 3.16.b. This means that high graylevel pixels lying on the edge of the filter, that were excluded by the dilation of the mask, are now included in the segmentation if they were connected to a larger high gray level region. Finally, this segmentation is re-thresholded (as pixels included in the segmentation during dilation may be < 98) and the filter mask (without the dilation) is re-applied. An example of this deposit segmentation is shown in figure 3.17. This workflow is applied to all the loaded volumes.

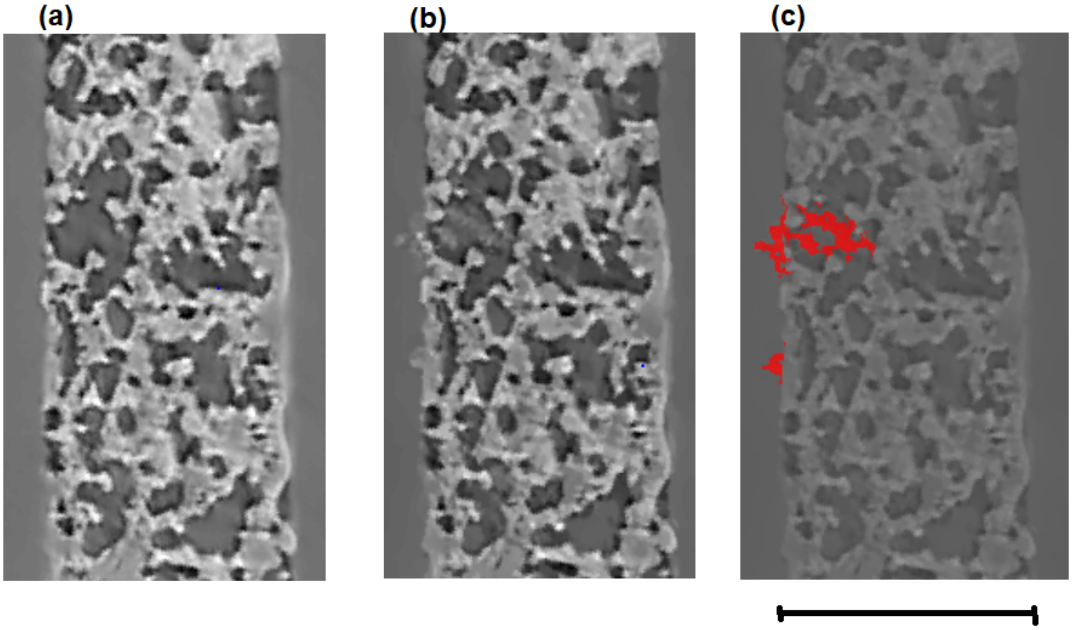

FIGURE 3.17: Result of deposit segmentation (a) grayscale slice of zeroth volume (b) grayscale slice of loaded volume (c) grayscale slice of loaded volume with deposit highlighted in red using the segmentation. Scale bar = 230 μm

Coating Segmentation

There was no consistent graylevel contrast between the catalyst coating and the filter substrate in this dataset, see figure 3.18. This makes the segmentation of the coating challenging. However, we can estimate the coating distribution by using a machine learning algorithm trained on manually segmented data. This is because machine learning algorithms can separate pixels based on image features (e.g. textures, edges, corners, gradients) at different scales of the image, thereby not solely relying on individual pixel graylevels for segmentation. A popular algorithm for semantic segmentation is the U-net algorithm developed by Ronneberger, Fischer, and Brox, 2015, primarily for biomedical image segmentation, however, it has also seen significant use across imaging applications in remote sensing, materials science and geology (Shamsolmoali et al., 2019; Ghosh et al., 2021; Liu et al., 2020). U-net is a convolutional neural network (CNN) with both maxpooling and upsampling layers with concatenation. Maxpooling is the process of reducing the size of the feature maps in each layer by a convolution that replaces the pixels in a patch with the maximum value of the patch, this effectively downsamples the feature maps so

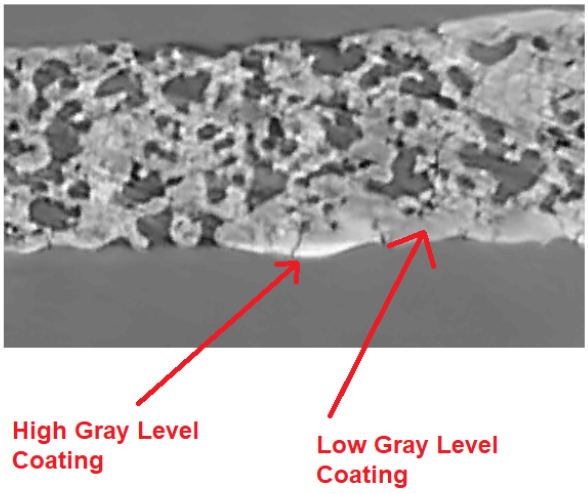

FIGURE 3.18: Cropped grayscale slice of a coated sample. The arrows point to regions that show a large range of graylevels within the coating phase. The lower graylevel coating pixels overlap with the filter substrate.

that higher level information can be extracted. Upsampling is the opposite of maxpooling. Each pixel in a feature map is replaced by a patch of pixels via nearest neighbour, hence upsampling the data. The upsampled data is then concatenated with feature maps that were not downsampled, these provide local high resolution information, whilst the upsampled data preserves the context of the higher level information achieved by downsampling. The key idea of U-net is to replace the typical contracting path of a CNN with a contracting path that is followed by a subsequent expansive path. By doing this high level, low resolution information propagates up the expansive path providing contextual information to low level, high resolution layers. This has proven beneficial for semantic segmentation.

In this workflow we have used a simple U-net to segment the catalyst coating in the coated dataset. The architecture of the U-Net we built for this workflow is shown in figure 3.19. This model was built in Keras and Tensorflow. The input was a grayscale 1240x1240 slice. Each layer in the contraction path (the left half of the symmetrical U-net architecture) has two convolutional layers, a dropout layer, and a maxpooling layers. The first layer in the contraction path had a convolutional layer that convolved 16 filters (of 3×3 kernels with) through the image, resulting in a 1240×1240×16 array of filters. Then there was a dropout layer that dropped 10%

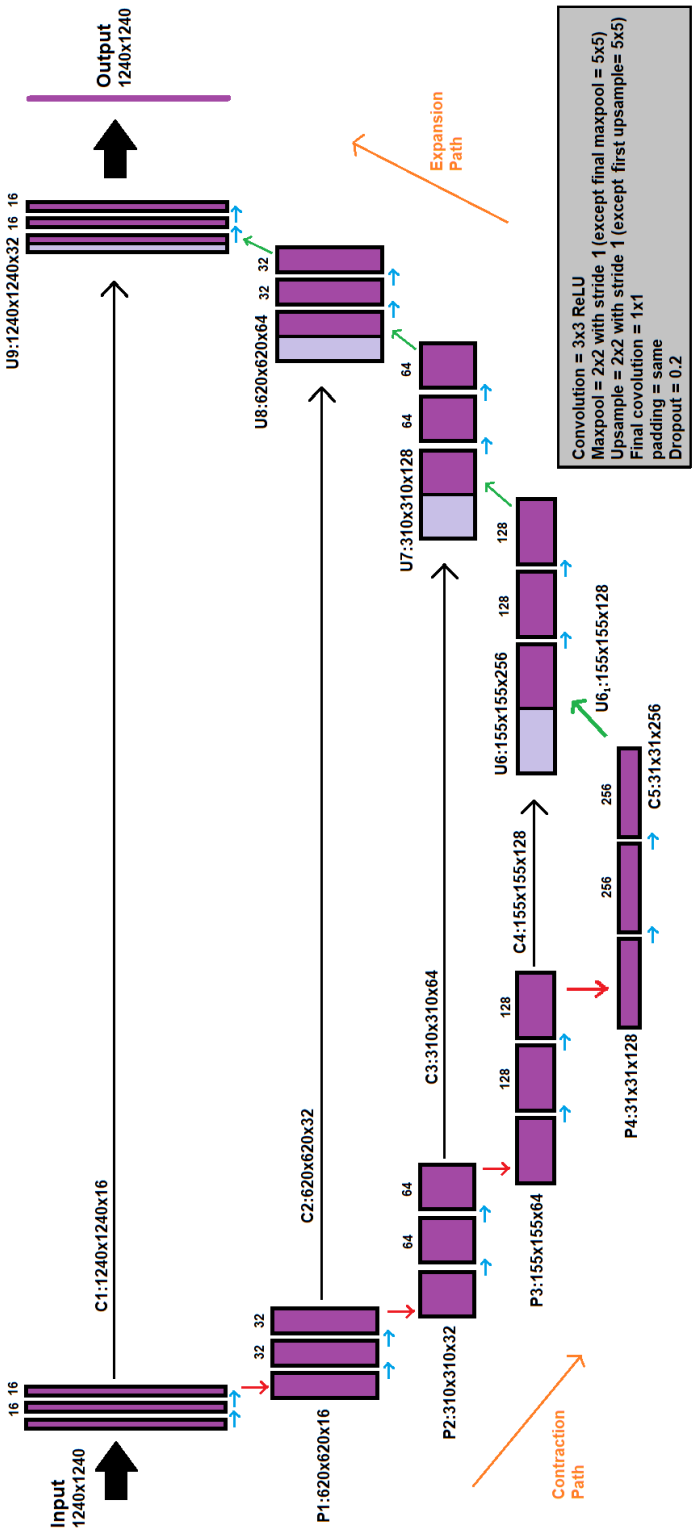

FIGURE 3.19: The U-net architecture used to segment the coating; Blue arrows show convolutional steps, red arrows are maxpooling steps and green arrows are upsampling steps. The long horizontal arrows show where the output convolutional layers were concatenated to the data in the expansion path. The concatenation steps are labelled C1, C2, C3 etc., where the dimensions of the feature map arrays are specified. Similarly, the maxpooling layers are labelled P1, P2, P3, etc., and the upsampling layers U1, U2, U3, etc.. The dimensions are also specified.

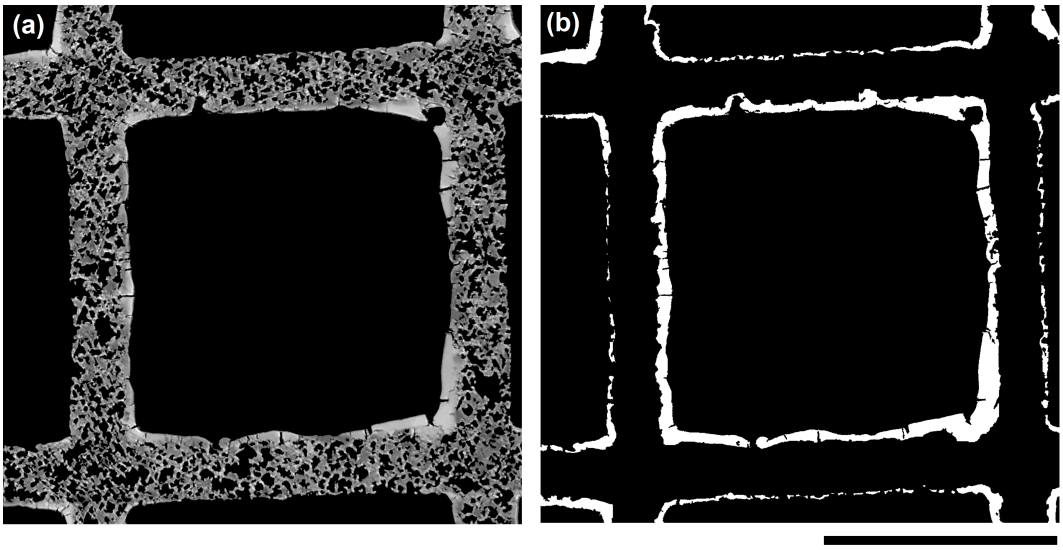

FIGURE 3.20: Training Data; (a) grayscale slice masked by the filter mask, (b) the hand labelled coating segmentation. Scale bar = 900μm

of the input values randomly during training, this prevented overfitting the data. A second convolutional layer was then applied, again resulting in a 1240×1240×16 array of filters. This was then maxpooled with a 2×2 kernel and stride of 2. Maxpooling outputs the maximum value inside the kernel as it convolves along an image, thereby downsampling it. The output of the maxpooling step, a 620×620×16 array, was then used as the input to the next layer, see 'P1' in figure 3.19. A similar process to this was then repeated three more times in the contraction path, however as we moved down the contraction path the resolution was lowered by maxpooling and the number of features increased, furthermore we used higher dropout rates for layers with high number of features. On the expansion path we have a similar architecture to the contraction path however with an extra concatenation step and upsampling instead of maxpooling. The concatenation provides local information to the upsampled layer from the contraction path of the U-net. Therefore, when moving up the expansion path the resolution increases and the number of features reduces, the reverse of the contraction path.

The training dataset consisted of 30 grayscale and hand labelled slices taken from the zeroth volume of the coated dataset. The slices were distributed along the entire length of the filter and included a range of different coating thickness. In order to

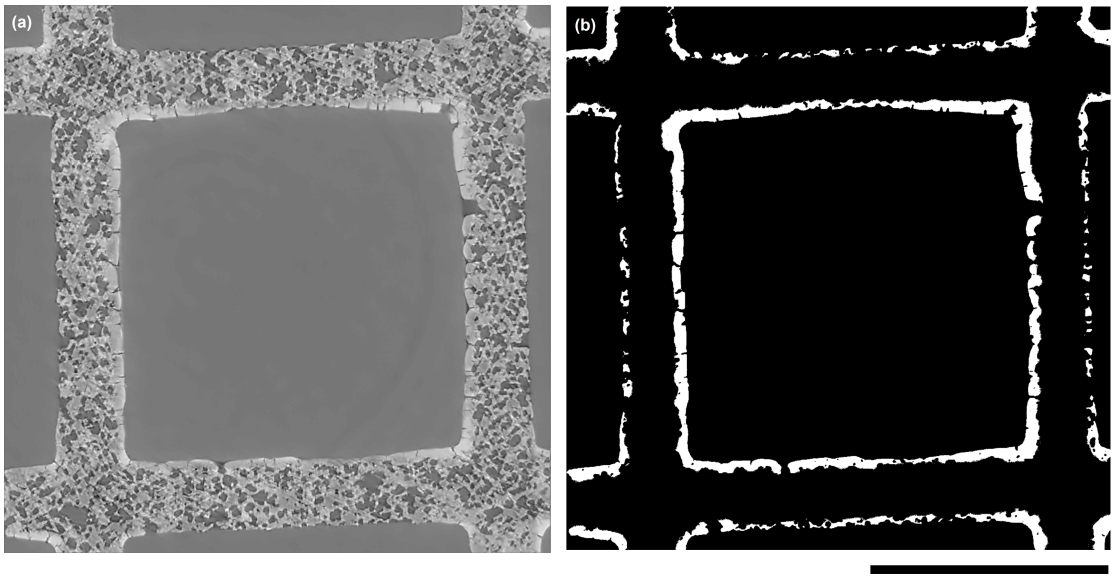

FIGURE 3.21: Model segmentation for coating; (a) grayscale slice, (b) U-net segmentation. Scale bar = 900μm

enforce consistency with the rest of the segmented data set the input images were always masked by the filter mask so that catalyst labels in the training data always came from within the filter segment. We also had a test data set that consisted of 5 similar images. These were reserved from training in order to later test the accuracy of the model on data it was not trained on. Examples of the images from these datasets are shown in figure 3.20. As a CNN the U-net model's 1,940,817 trainable parameters were trained by backpropagation using a stochastic gradient descent optimiser. Evaluation of the trained model with the test data set showed that the model had a binary cross-entropy loss = 0.174 and an accuracy = 91.1% when compared to the unseen hand labelled test data. This was acceptable accuracy for estimating the coating thickness along the walls of the filter channel. Figure 3.21 shows an example of the model's segmentation.

3.3 X-ray Ptychotomography and XRF-CT of Automotive Ash

This beamtime took place at the Diamond Light Source (DLS) I13-1 beamline. The experiment aimed to use ptychotomography (XPT) to investigate the structure of automotive ash agglomerates from pre-aged GPFs in 3D at high resolution. We also

wanted to perform correlated fluorescence tomography so that we could match elements, and by extension chemical species, to particular structures resolved by the XPT. We also used SEM and SEM EDX to validate findings.

3.3.1 Particulate Filter Ageing

The pre-aged samples were aged by our industrial partners Johnson Matthey (JM) before the start of this project. The pre-aged samples where all coated cordierite GPF monoliths. The process of accelerated ageing is supposed to mimic the ageing of real GPFs over operational lifetime in an exhaust by realistically loading the GPFs with ash. The system consisted of a furnace burner modified to burn propane, the flame was sustained by spark plugs providing continuous ignition. The burner flame was directed into the combustion chamber where an air assisted oil injection nozzle located on the cover of the combustion chamber injected lubricant oil into the chamber. The oil (zinc dialkyldithiophosphate (ZDDP) with calcium additive) was burned in the chamber releasing lubricant derived ash into the exhaust stream. A rich-lean ageing process was followed where temperature was ramped up to 950^o at 5^o per minute, once this temperature was reached it was held for 16 hours. The gas flow was such that in rich-lean conditions propane moved from 1010 ppm to 1002 ppm respectively, O2 from 0.80% to 0.27% and NO from 995 ppm to 986 ppm. H_2O was held at approximately 10% and CO was held at approximately 0.5%. The reactor moved between the different conditions so that rich conditions were held for 5 minutes then 10 s off, then 5 minutes lean. Cool down occurred under oxygenated conditions. In this experiment we used samples with 20 g/l ash loading, all these aged samples were coated GPFs.

3.3.2 Sample Preparation

This beamtime followed on from previous attempts to image the structure of these ash particle with high resolution nano-CT using ptychotomography. Previous attempts had failed due to beamline faults. This meant we could not reconstruct any ptychotomography data due to; (1) repeated failure of the rotational stage during each scan, and (2) error outputting data files causing loss of projections and

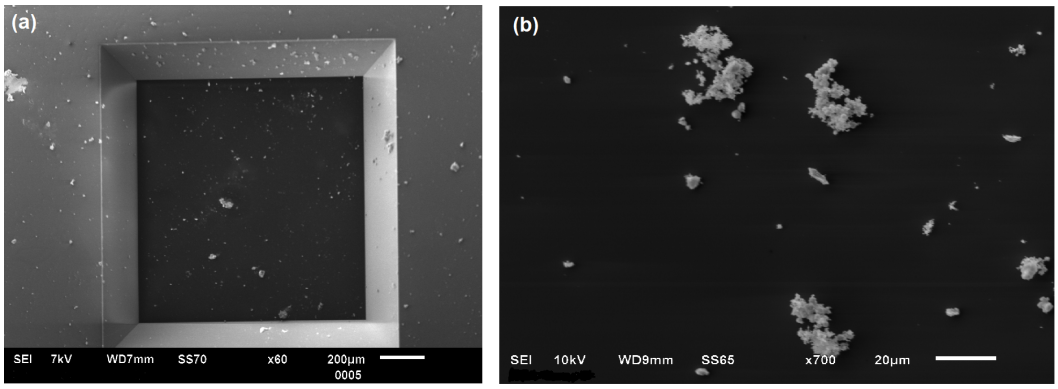

FIGURE 3.22: Overview SEM of the membrane sample loaded with ash; (a) the membrane window, (b) ash agglomerates deposited on the membrane.

data. However, we were able to learn lessons from this unsuccessful beamtime. We found the ptychography phase reconstruction was more sensitive to low transmission through the sample than we had expected (projections from this unsuccessful beamtime are presented in figure A.1). Therefore we changed our sample preparation in the following beamtime so that we no longer used ash particles adhered to the cordierite filter (this sample design was necessarily larger due to constraints in sample preparation). By doing this we expected to gain image quality but lose the ability image the entire height of an ash layer. These less attenuating samples were prepared on conductive SiN TEM membranes or on the head of wooden picks. The ash was taken from a pre-aged sample that contained 20 g/l of ash, the aging process was performed as described above in section 3.3.1. A section of GPF channel was carefully cut from the monolith using a scalpel and fine grade sandpaper. One of the walls was then removed with a scalpel to expose the ash inside the channel, effort was made to try to do so in such a way that debris from the cutting process did not contaminate the ash. To make the membrane samples the ash was gently and carefully picked up on the tip of soft tweezers and moved onto the membrane surface. The membrane was then examined with SEM to confirm the presence of ash agglomerates and to find ROI before the beamtime, see figure 3.22. For the tooth pick sample a small amount of epoxy glue was put onto the tip of the wooden pick and allowed to dry. The pick was then used to gently pick-up ash from the surface of a pre-aged GPF sample. An optical microscope was then used to confirm that the

ash pile on the toothpick formed a sharp peak. This was important for tomography because we needed to avoid self absorption from parts of the sample lying outside the FOV. The wooden pick was preferred to a metallic pin to prevent fluorescence from the pin head obscuring the XRF peaks of metallic elements of interest in the sample.

3.3.3 Diamond I13-1 beamline

In this project we have used the I13-1 beamline at Diamond Light Source (DLS) to perform XPT and XRF tomography on ex-situ automotive filter ash samples. The 250m long I13 beamline consists of independent branches, each branch has its own undulator on a shared straight section of the ring (Rau et al., 2016). I13-1, the coherence branchline, discussed here, specialises in Ptychography and CDI, whilst the I13-2 Diamond - Manchester Beamline, specialises in absorption and phase contrast XCT and full-field transmission x-ray microscopy. The length of the 250 m long I13-1 beamline is useful for coherent x-ray experiments as a large source to sample distance make the source more point-like, hence improving the coherent properties of the beam at the sample. The 3 m long I13-1 'mini-beta' layout undulator source produces 7×10^{14} Ph/s at 0.1% band width (at 8 keV) and can produce a highly coherent flux of 10^{10} Ph/s at 0.1% band width (at 8 keV), making it ideal for ptychography (Rau et al., 2011). The beam divergence is 50mrad$\times$25mrad and its minimal size is approximately 400mm$\times$13mm (horizontal$\times$vertical; all Full Width Half Maximum (FWHM)) (Rau et al., 2011).

Upstream of the beamline hutch are the front end slits, beam slits, the mirror, compound refractive lenses (CRL), two further sets of slits and the monochromator, see figure 3.23. The front end slits define the horizontal width of the beam. The mirror is used to steer the beam while shielding downstream components from radiation damage by filtering the beam, it also removes higher energy harmonics from the source (Wagner et al., 2012). The mirror can use Pt, Rh, or Si stripes depending on the energy regime required experimentally (Wagner et al., 2012; Rau et al., 2011). Downstream of the mirror is the compound refractive lens which is installed to collimate the beam. Together with the next set of slits the lens defines a secondary

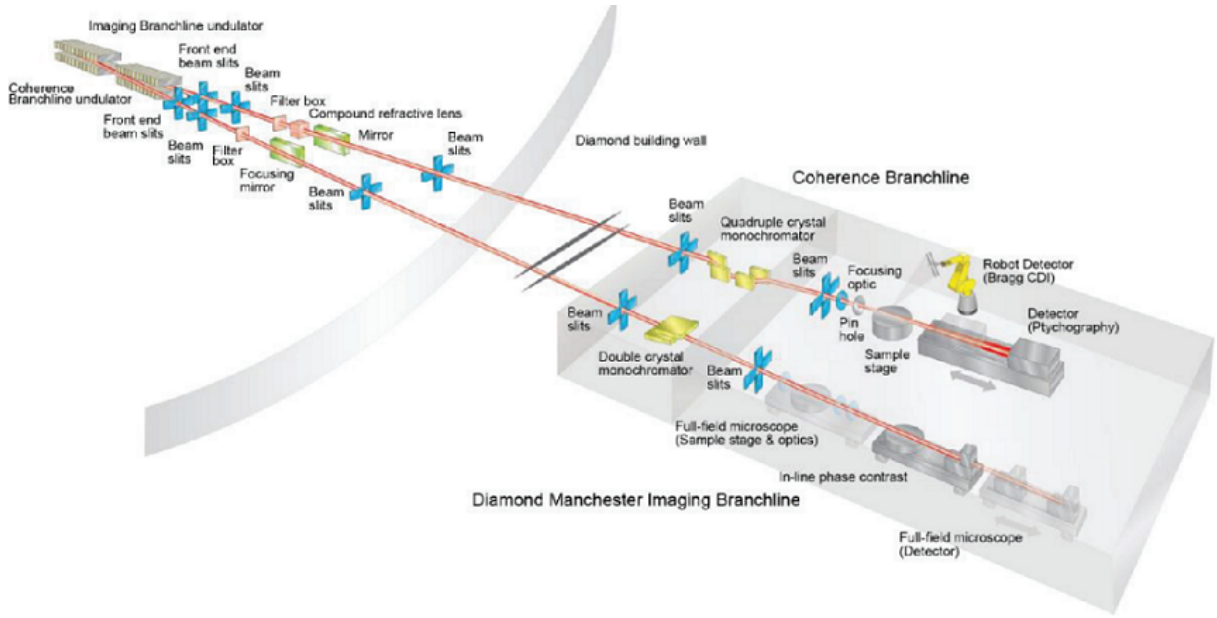

FIGURE 3.23: Schematic of the layout of the I13 beamline. Source: Rau et al., 2016

partially coherent source with adjustable horizontal and vertical coherence length (Kuppili, 2019). Before entering the beamline hutch the beam passes through the monochromator. This has a four bounce design and the choice is available between Si(111) or Si(311) crystals in order to obtain a 10^{-4} ($\Delta E/E$) bandwidth (Rau et al., 2011).

Inside the beamline hutch and before the sample position the optical components are designed to define the shape and structure of the probe on the sample. The important components are the Fresnel zone aperture, central stop, Fresnel zone plate (FZP) and the order sorting aperture (OSA). The Fresnel zone aperture acts as a simple mask that isolates the zone plate being used. The central stop attenuates the beam that would be emitted from the centre of the FZP un-diffracted, this portion of the beam would be much brighter than diffracted beam from the FZP and could saturate or damage the detector. Furthermore, scattering with air of this portion of the beam could introduce noise. The FZP acts as a lens that focuses the beam. Finally, the OSA is a pinhole aperture that removes the higher order focused x-rays emitted from the FZP by placing the OSA pinhole near the first order focus. This set-up is

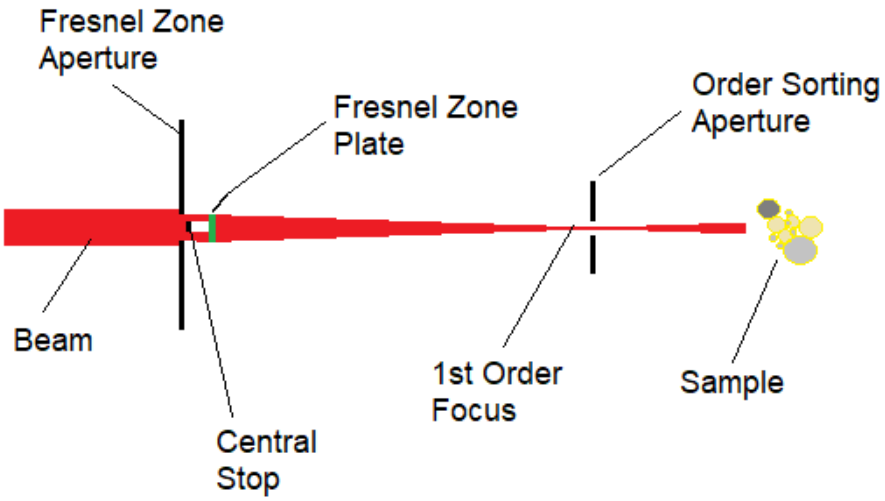

FIGURE 3.24: Schematic of pre-sample optics in the i13-1 beamline hutch

shown schematically in figure 3.24.

For XRF detection the detector is placed near the sample position at 90° . In our work a Hitachi Vortex single channel silicon drift detector is used for XRF mapping. The Vortex detector has an energy resolution of <130 eV (FWHM) at Mn Kα and an output count rate of 900 kcps is achievable. For ptychography the detector is placed downstream of the the sample position as to acquire far field diffraction patterns. A Dectris Eiger X 500k photon counting detector which has an energy range of 5 keV to 35keV was used. The detector has 75 μm pixel size, and 1030 pixel $\times$ 514 pixels, for a total active area of approximately 3000 mm^2 silicon diode array. The data from the detector is then saved via the Experimental Physics and Industrial Control System (EPICS) Input/Output Controller (IOC) so that it can be reconstructed by I13-1 in-house reconstruction workflows. For XPT the ptychographs are then reconstructed into 3D.

3.3.4 Ptychotomography (XPT)

The samples were mounted downstream of the OSA and 1st order focus, see figure 3.24. The beam from the Si 111 monochromator was monochromatic at 9.7 keV with a bandwidth $\Delta E/E = 10^{-4}$ (about 1 eV at 9.7 keV). The Si mirror was installed and the

front end slits were set a 50μm wide. The Eiger detector was used for ptychography and XPT (for more details on the I13-1 set-up see section 3.3.3).

The first step of the imaging workflow was to search through the sample to find ROI. This was achieved using the optical microscope mounted next to the sample stage at 45°. For the membrane sample we searched through the membrane until we found ash agglomerates using this optical scope, we then centred these agglomerates for ptychography. Before a XPT scan of the membrane sample we first worked out the maximum range of angles we could image over. Due to the membrane window a full 180° scan was impossible. Therefore we acquired ptychography scans near the extremes of the allowable range, increasing the range until we observed that the beam had been obstructed by the window. We then started a XPT scan over the maximum allowable range of angles. Similarly for the wooden pick mounted sample, the optical scope was used to find the ROI. The ROI was then centred for tomography, and a XPT scan was acquired over 180° of rotation.

The scan parameters used for the XPT on the membrane sample were; 100×55 (x,y) steps with 0.25 μm step size for each angle, for 500 angles acquired over 146° in a fly scan. The exposure times were 0.01 s per diffraction pattern. The scan parameters for XPT on the wooden pick sample were; 100×50 (x,y) steps with 0.5 μm step size for each angle, for 500 angles acquired over 180° in a fly scan. The exposure times was 0.01 s per diffraction pattern. The ptychograph projections were reconstructed using software developed at I13-1. These were then reconstructed into 3D using FBP for the pin head sample and SART for the membrane samples, this is because the limited range of projection angles leads to artefacts in FBP.

3.3.5 Fluorescence Tomography

Once an XPT tomogram had been acquired a correlated XRF tomogram was acquired from the same region. The same beam characteristics were used however the sample was moved further from the OSA and 1st order focus in order to reduce the probe diameter during acquisition (thereby achieving more flux through the sample). Furthermore the slits were opened to 200 μm to increase flux at the sample, which improved counts at the Vortex detector. The scan parameters used for the

XRF tomography on the membrane sample were; 100×55 (x,y) steps with 0.25 μm step size for each angle, for 70 angles acquired over 146° in a fly scan. The exposure times were 0.1 s per acquisition. The scan parameters for XPT on the wooden pick sample were; 100×40 (x,y) steps with 0.5 μm step size for each angle, for 70 angles acquired over 180° in a fly scan. The exposure times was 0.06 s per acquisition. The XRF projections were then reconstructed into tomograms using the SART algorithm without self absorption correction. The SART algorithm performed comparably better with a limited number of projections.

3.3.6 SEM EDX

To validate the XRF tomography results we also performed SEM EDX on the membrane sample studied during the beamtime. We used the JEOL JSM-6610LV at an accelerating voltage of 10 kV, at a working distance of 9 mm, with a spot size of 75 nm. We obtained each EDX map over approximately 30 minutes. For the SEM EDX validation we simply wanted a qualitative elemental map of the sample. We had hoped to image the same region with SEM as was imaged during the beamtime, however the ash on the membrane moved between the beamtime and the SEM EDX acquisition. Therefore we performed the SEM EDX on other similar ash agglomerates.

Chapter 4

4D In-situ Microscopy of Aerosol Filtration in a Wall Flow Filter

In this chapter we present results that were included in a paper from this project (Jones et al., 2020).

4.1 Introduction

Understanding the dynamic nature of wall flow filters during operation is important for manufacturers. Central to this problem is the effect of PM on filter performance as it deposits on walls and in pores overtime. Studies have used CFD methods to study how particles deposit in the 3D microstructure of filters and how these effect performance in coated and uncoated wall flow filters (Yang et al., 2009; Belot et al., 2020; Plachá et al., 2020). However, experimental validation has been limited to 2D qualitative inspection of loaded filters with optical microscopy and SEM. For example, Yang et al., 2009, use SEM EDX to map the penetration depth of laboratory generated particles into a DPF, and Choi and Lee, 2013, use in-situ optical microscopy to image the build up of soot on the surface of wall flow filters over time. However, these techniques exclude the possibility of quantitative 4D (3D + time) analysis of the porous microstructure. In this chapter we present results on 4D in-situ microscopy of aerosol filtration in a wall flow filter. This was the first time filters had been studied in this manner and acts a successful proof of concept for the method.

4.1.1 Method

A detailed description of the method is given in section 3.1. In this work we flowed a TiO_2 aerosol through operational filters sections continuously and imaged the build up of deposit in the pores of the filter whilst simultaneously measuring pressure drop across the filter. The aerosol flow apparatus consisted of a SAG410/U dust generator (described in section 3.1.2) in a flow rig that flow the TiO_2 aerosol through an intact DPF channel section. The imaging was performed at the DLS I13-2 beamline (described in section 3.1.4) such that a radiographic projection was acquired every 0.18° in an 180° fly scan (1000 projections) with exposure times of 0.01 s, thus acquiring a tomogram every 1 minute. This was repeated for 18 tomograms in a continuous time series that resolved the build of of deposit inside the filter section sample. The 2× objective was used, resulting in a total magnification of 4× and a pixel size of 1.625 μm.

4.2 Results

4.2.1 Visualisation

Figure 4.1 shows 2D segmented slices (right column) compared to grayscale slices (left column) overtime as deposit builds-up. This allows for qualitative determination of the deposit segmentation accuracy. By tracking the pore circled in red in the segmented image and comparing this region to the corresponding grayscale image we can see that that we successfully segmented regions that increased in graylevel compared to the zeroth (t = 0) image. This results in an accurate segmentation of the deposit both in the deep bed, indicated by the red circle, and the wall surface, indicated by the green arrow. The accuracy of the segmentation and the technique's inherent spatial and temporal resolution made it possible to observe pore scale filling and blocking phenomena in the micro-CT images. The pore indicated with a red circle in figure 4.1 was being filled with TiO_2 deposit during the first 12 minutes of filtration. However, the green arrow shows that at 12 minutes a deposit cake formed that blocked flow to the pore circled in red. Thus, after 12 minutes, no further deposition occurred in the pore circled in red.

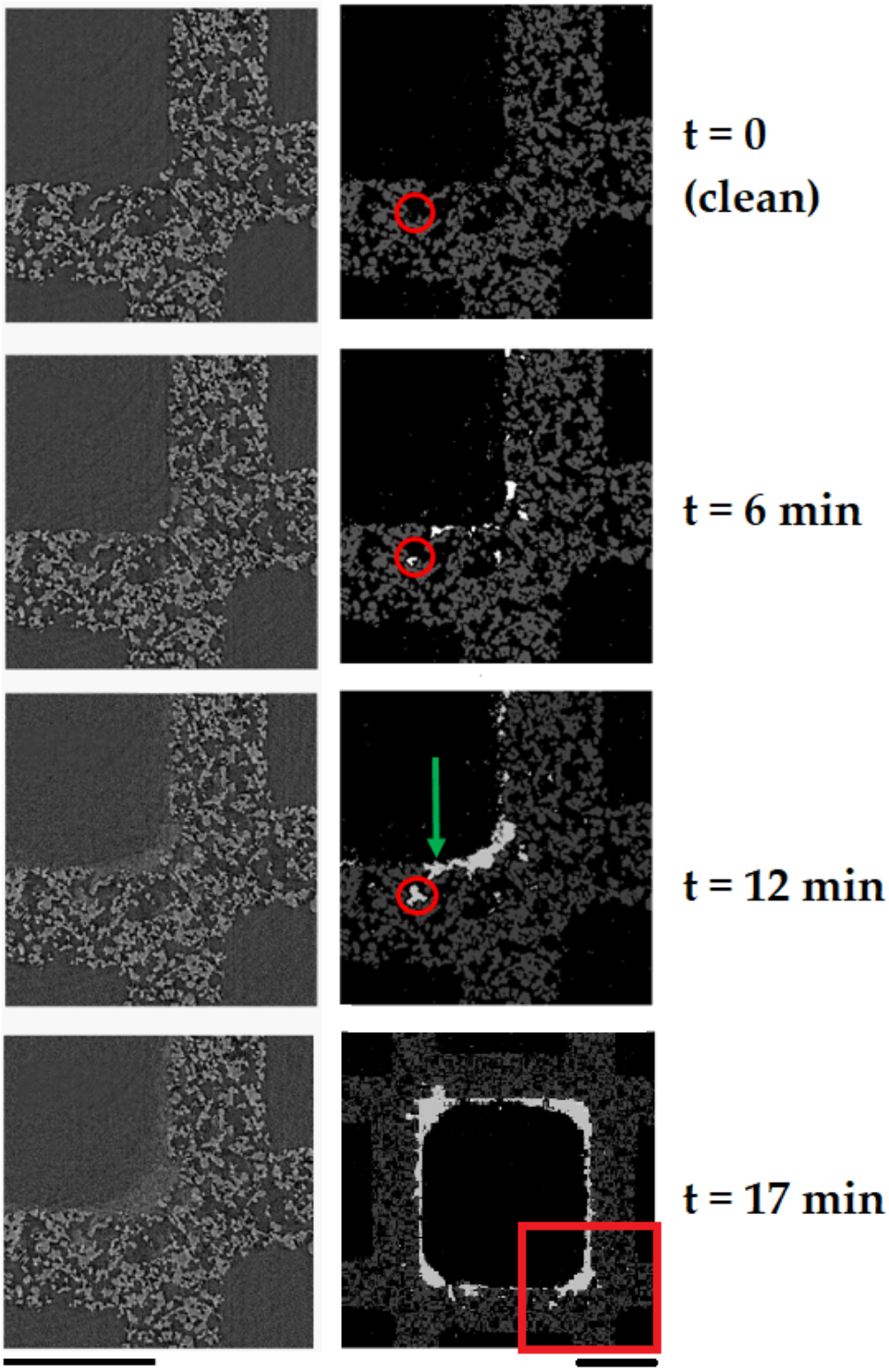

FIGURE 4.1: Comparison of greyscale micro-CT virtual slices (left column) and corresponding segmented slices (right column). Slices are 8 mm from the top (upstream) inlet of the sample. TiO_2 aerosol deposits are white, the filter segment is grey and the pore and background segments are black. The red circle tracks a pore filling event that occurred during the time series. The green arrow indicates a pore blocking event caused by the growing cake layer. The final image indicates the position of the previous slices within the channel. Scale bars = 500 μm.

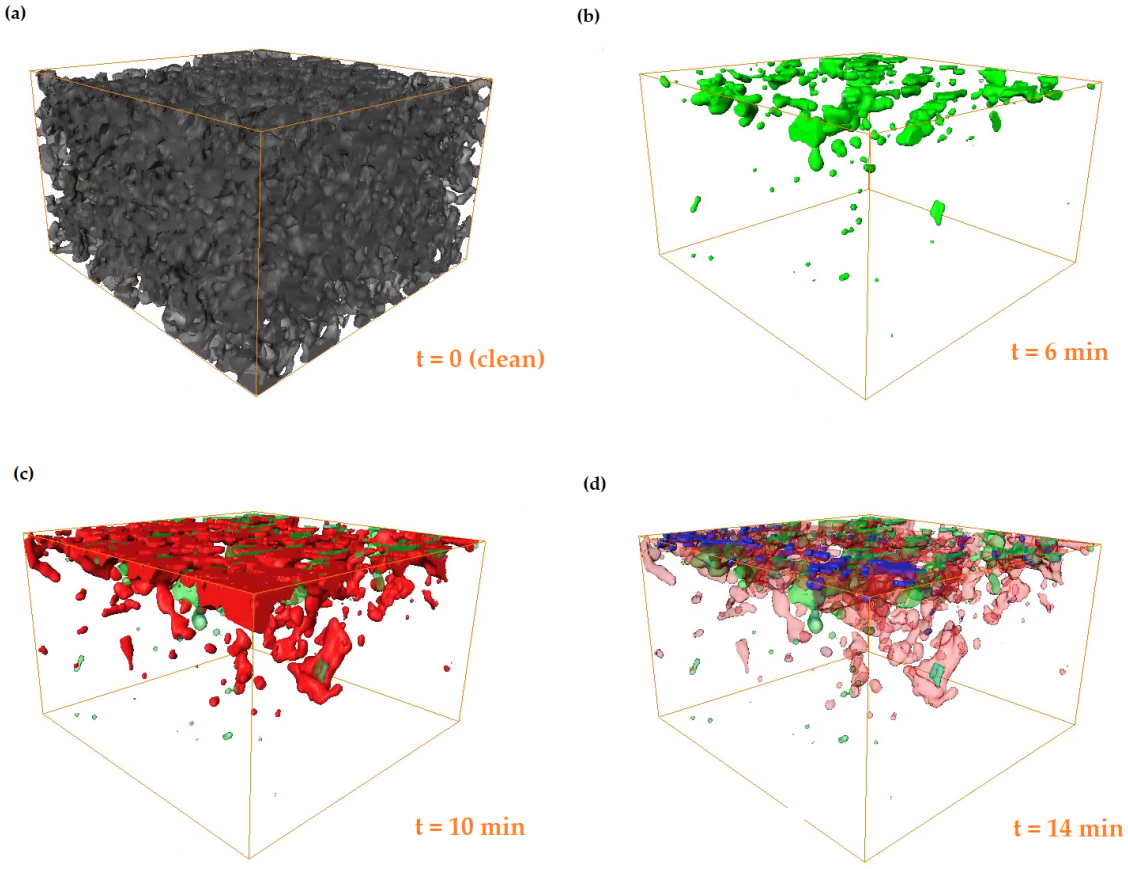

FIGURE 4.2: 480 × 480 × 295 μm (300 × 300 × 184 pixels) micro-CT volume showing TiO_2 deposits in the pore space at different times during the filtration, the aerosol flow is from top to bottom. (**a**) t = 0 (showing the rendered filter phase only, shaded in grey), (**b**) 6 min (green), (**c**) 10 min (red) and (**d**) 14 min (blue).

This analysis was extended into 3D in figure 4.2. In figure 4.2 we show how the location of deposition changed with time during the filtration. The volumes encompass the inlet channel surface (top surface in figure 4.2) of the wall to the outlet channel surface (bottom). From this volumetric perspective it becomes possible to visualise the transition in filtration regimes, i.e. from deep bed filtration through to cake filtration. In figure 4.2.b, after 6 minutes of loading, we see deposition occurring in the deep bed of the filter (rendered in green) and that the deposit is yet to block all the surface pores of the filter. Therefore in 4.2.c, after 10 minutes of loading, we see that deposition continued in the deep bed (rendered in red), however, the surface pores are now almost completely blocked by the deposit. As a result, in figure 4.2.d, after 14 minutes of loading, no deep bed deposition has occurred and we have transitioned into the cake filtration regime with deposition (rendered in blue) only near the surface. This qualitative analysis of visualisation is useful, however for a more accurate understanding of the filtration quantification is required.

4.2.2 Quantifying Filtration

A Representative Elementary Volume (REV) is a volume large enough to be statistically representative of a material property and is often used in porous materials research (Costanza-Robinson, Estabrook, and Fouhey, 2011; Shah et al., 2017; Al-Raoush and Willson, 2005; Ozelim Luan Carlos de and Cavalcante André, 2018). We perform a REV analysis for porosity, this is shown in 4.3.b. In order to calculate REV we use an edited version of the porespy (an open source python toolkit for quantitative analysis of porous media images) REV function (Gostick et al., 2019). The porespy function randomly samples cubic subvolumes from a volume and calculates the porosity within each subvolume. However, because of the large aspect ratio of the wall volume used, see figure 4.3.a, the largest cubic volume was 184^3 px (295^3 μm) which was smaller than the REV. Therefore we edited the function to continue sampling rectangular volumes once the maximum size in an axis had been hit by cubic volumes, this is plotted in 4.3.b. In the preceding analysis we use $184\times600\times600$ px volumes, this volume is plotted on the figure 4.3.b as a green vertical line. At this volume the calculated porosity in the subvolumes had converged to 0.60, meaning this volume was an REV.

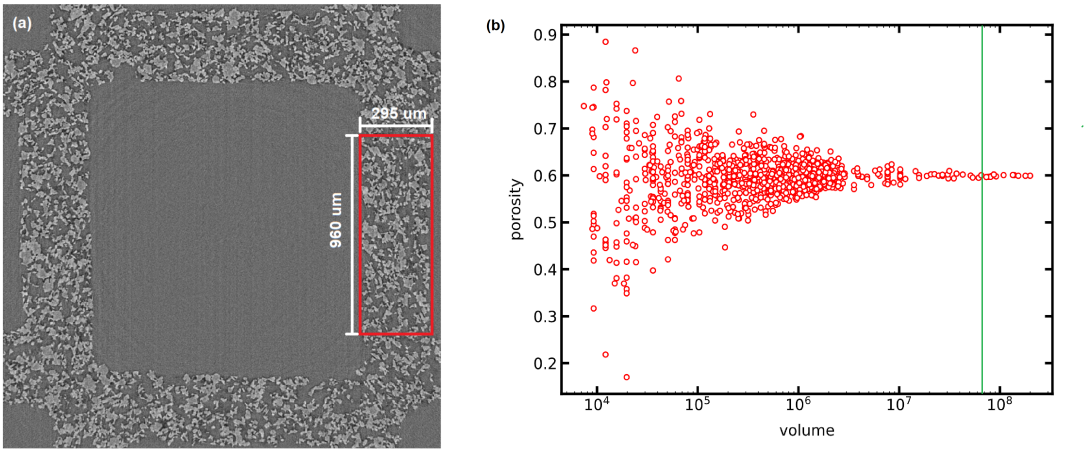

FIGURE 4.3: REV analysis;(a) A micro-CT slice showing a the cross section of a volume used for REV determination in red, (b) REV plot, the REV used in the preceding analysis is shown in green.

$$N = \frac{\delta\sigma}{\delta t} = \frac{V_2 - V_1}{(t_2 - t_1).REV} \tag{4.1}$$

We then calculated the REV porosity in all 18 time steps in the data set in order to quantify the change in deep bed porosity due to TiO_2 deposit in a statistically valid manner. The REV changes from an initial clean porosity of 0.60 to a porosity of 0.56 after 20 minutes of loading. The REV can also be used to calculate the filtration rate expressed as the rate of change of specific deposit volume with time, see equation 4.1; Where N is the filtration rate, σ is specific deposit volume, t is filtration time (the time elapsed since the start of the filtration), $V_{1,2}$ is the volume of deposit in a representative volume at $t_{1,2}$, and REV is the volume in a REV. The peak deep bed filtration rate occurs between 5–6 min, this then decreases until 10 minutes after which the deep bed filtration rate tends towards zero. This is indicative of the three filtration regimes; deep bed filtration, mixed or transition filtration, and cake filtration. The maximum filtration rate of 4 $\mu m^3.mm^{-3}.min^{-1}$ occurs between 5–6 minutes, this is in-line with theory were we would have expected filtration rate to be highest at the beginning of the filtration. However, there does appear to be lag between the start of the filtration, measured as the time where the aerosol rig is turned on, and the start of the filtration in the volume analysed. This is almost certainly due to apparatus fault where the SAG was not properly aerosolising the powder on the dosing ring at the start of the experiment. The deep bed filtration rate then decreases between

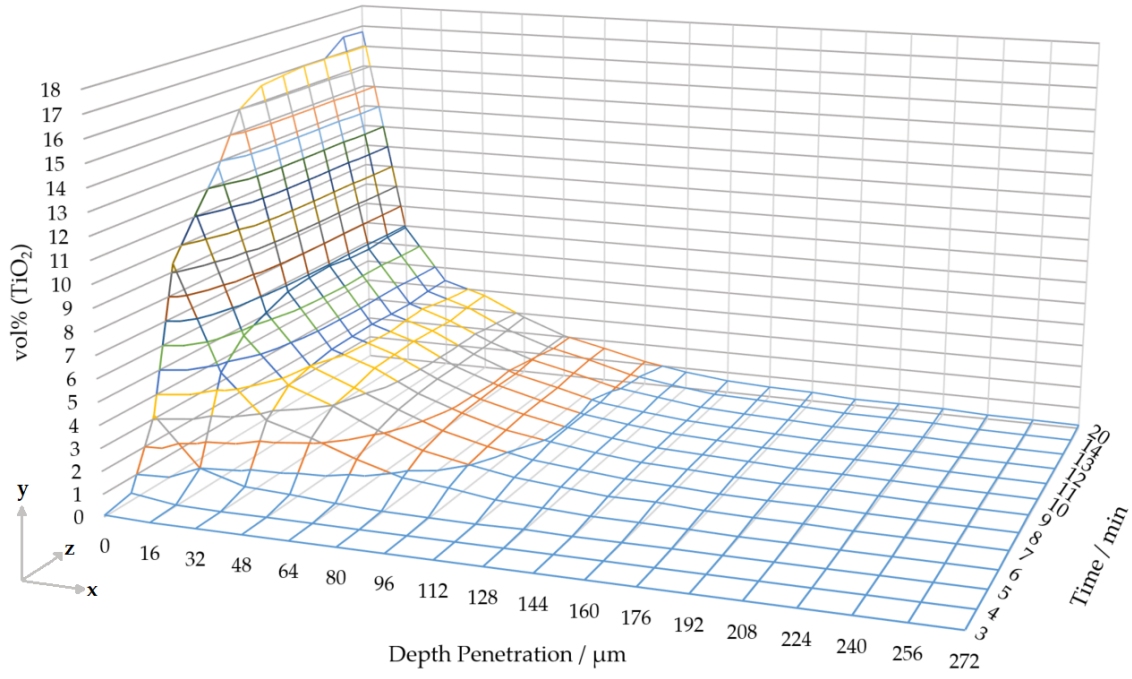

FIGURE 4.4: Concentration of TiO_2 deposits (y-axis) against penetration depth (x-axis) and time (z-axis) for porosity in a representative volume during continuous filtration. The volume was divided into 16 μm wide sub-volumes along the width of the filter wall and TiO_2 volumes calculated from within each of these sub-volumes in the time series, these are expressed as volume percentages in the figure.

6–10 minutes, again this is in-line with theory where this is due to mixed behaviour during the transition regime, i.e. some cake filtration occurs lowering the deep bed filtration rate. This mixed behavior is observed in the 3D visualisation with this technique, see figure 4.2.c, were we observe deep bed deposits but also the formation of a thick deposit layer on the surface pores. Finally, the deep bed filtration rate tends towards zero after 10 minutes during the deep bed filtration regime (again in-line with expectations) with the exception of a jump in filtration rate between 13–14 minutes. This may be due to the build up of pressure causing the re-entrainment of deposit. After this jump the filtration rate returns to ~ 0 $\mu m^3.mm^{-3}.min^{-1}$ until the end of the filtration. This pattern can be observed for different filter depths in figure 4.4 (where filtration rate is the gradient, $\frac{\delta y}{\delta z}$).

We also quantify penetration depth from the REV. The $960 \times 960 \times 295$ μm ($600 \times 600 \times 184$ voxels) REV was divided into 18 sections, each with a shape of $960 \times 960 \times 16$ μm ($600 \times 600 \times 10$ voxels) width-wise. Thus, each sub-volume within the

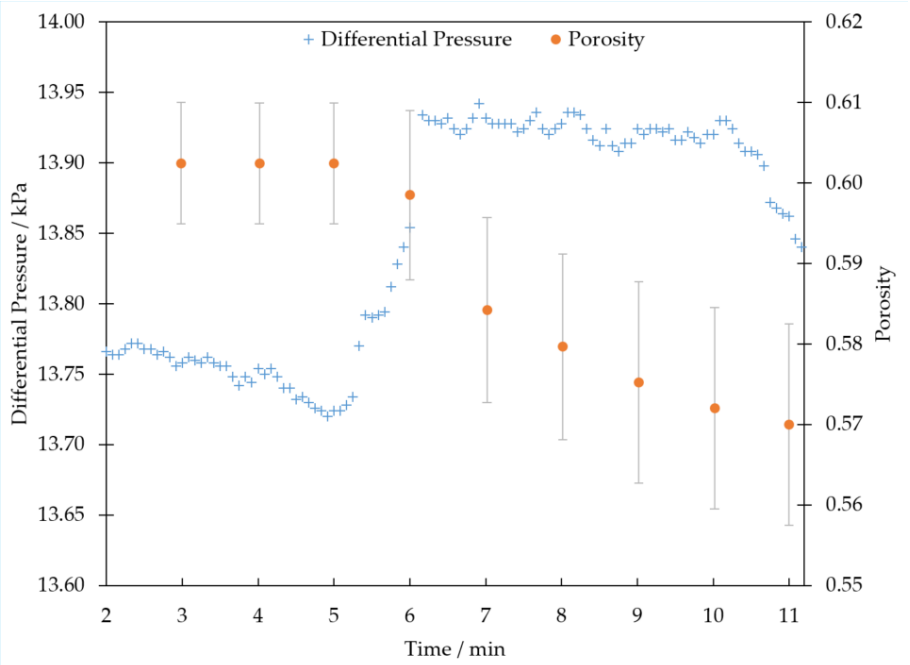

FIGURE 4.5: Plot of porosity and the pressure difference between the filter sample inlet and outlet against time during an in-situ filtration. Each porosity data plot represents the point in the time series where a tomography scan was finished (∼1 per minute), each porosity value is calculated from a representative volume as discussed above.

REV had a width of 16 μm (10 pixels) in the through wall flow direction (the final subvolume, the outlet channel side, had a width of 14 pixels). We calculated the volume percentage of TiO_2 in each sub-volume with a pixel count of the deposit segment and divided this by the volume of the sub-volume. This was done to all the time steps in the dataset, as shown in figure 4.4. A depth of zero in figure 4.4 is the inlet surface; therefore, we considered the build-up of deposit in the deep bed. Figure 4.4 shows that the concentration of deposit decays with distance from the inlet channel surface. This decaying profile with depth is similar throughout the filtration. From figure 4.4 we can also see that filtration rate plateaus earlier deeper in the filter wall. For example, filtration rate plateaus at 10 minutes for inlet surface pores (penetration = 0 μm), 9 minutes at a depth of 16 μm, and 7 minutes at a depth of 32 μm.

The pressure drop across the filter channel sample is plotted in figure 4.5. After 5 minutes of loading, the pressure drop through the filter increases sharply, from $\sim$ 13.75 kPa to $\sim$ 13.93 kPa, correlating exactly with the start of the deep bed pore

filling resolved by the time resolved XCT. Thus, in Figure 4.5, the representative volume porosity value drops just as the pressure loss spikes, showing good correlation between the pressure reading and image-based porosity plot. A sensitivity analysis was performed for the filter and deposit thresholds, plotted as error bars in figure 4.5. By applying a threshold one graylevel above and below the actual threshold values results in a porosity value that is higher (for thresholds $+1$ graylevel) or lower (for thresholds -1 graylevel) than the calculated value, see figure 4.5.

4.3 Summary

This work demonstrated time resolved pore scale 4D microscopy of filtration for the first time. Here we demonstrated the technique on a SiC DPF filter sample. These filters are designed to carry higher loads of deposit compared to GPFs, both in the deep bed and as a caking layer. This is because during in-operando DPF filtration the high soot concentration in the exhaust quickly deposit in the filter, and the DPF filtration then relies on the rapid build up of deposit to achieve high filtration efficiency. The higher soot loads made the deposit easier to resolve and therefore ideal for this proof of concept study.

The non-destructive nature of XCT means that operational samples can be used to achieve time resolved imaging of filtration. This combined with sufficient resolution means that we were able to resolve specific pore filling and blocking events in the filter as they occurred during the filtration. We demonstrated good agreement with literature and theory (see Choi and Lee, 2013, & Tien and Brenner, 2013), by clearly resolving the three filtration regimes with the technique; deep bed filtration, transition or mixed filtration, and cake filtration. Furthermore, the imaging and simultaneous pressure readings were in good agreement, as the images showed a sharp decrease in porosity at the same time as an increase in pressure drop was measured. We demonstrated that this method can be used to measure filtration rates and deposit profiles in statistically relevant sub-volumes of the filter. This method is an improvement over literature experimental methods for particulate filtration in terms of quantifiable results, statistical relevance, and its ability to achieve time resolved studies.

Blank Page.

Chapter 5

Multiscale Time Resolved Microscopy of Aerosol Filtration in GPFs

5.1 Introduction

Backpressures across GPFs are higher compared to DPFs due to higher flow rates, temperatures and lower filter permeability. Furthermore, GDI fuel efficiency is more sensitive to backpressure than diesel engines (Awad et al., 2020). The lower permeability of GPFs is in order to achieve higher clean filtration efficiency. This is because, unlike in DPFs which mostly operate at high soot loads (where high filtration efficiency is achieved with cake filtration), GPFs operate at much lower loads and rely on deep bed filtration. Understanding the distribution of deposits in the deep bed pores along the length of a channel is useful for manufacturers so that they can design better soot management strategies that will keep deposit levels at their optimum level for good filtration efficiency and backpressure. Studies have modelled the deposition of soot along the channel of GPFs and DPFs with 1D and 3D CFD models (Gong et al., 2018b; Lee and Lee, 2013; Hayashi and Kubo, 2008). For DPFs the findings of these models in regard to soot deposition profiles along the channel length have been validated experimentally by SEM (Bensaid et al., 2009; Bensaid, Marchisio, and Fino, 2010). These studies axially cut filter samples along the length of the channel and measure the soot cake thickness from channel cross sections at

each cut with SEM. This method is effective for DPFs operating at relatively higher loads which rely on soot cake filtration, however this method does not extend to GPFs, which run at lower soot loads in the deep bed filtration regime. To measure soot deposition profiles in GPFs a method that can resolve deep bed deposits is required.

5.1.1 Method

The experimental method and image processing method are described in detail in section 3.2 & 3.2.5. In this chapter we extend the '4D In-situ Microscopy of Aerosol Filtration' method, see section 3.1 and Chapter 4, to analyse GPF samples at the channel scale. The method relied on 'stitching' together tomograms that spanned the length of a 3 cm long channel sample in order to achieve channel scale resolution whilst still resolving the deposition on the pore scale and in the deep bed. During the experiment a nanopowder was flowed through an operational filter, flow was stopped, the filter was scanned with synchrotron XCT at I13-2, and then flow was resumed. This was repeated thereby creating a time resolved dataset. This allowed us to experimentally determine the deposition profile of a soot like nanopowder along a particulate filter channel at different times during a filtration. ZnO nanoparticles (ZNP) at an aerosol particle concentration of 14×10^7 n/cc, and with the aerosol size distribution shown in figure 3.8, was developed to mimic engine soot which has similar particle and aerodynamic size distributions (Harris and Maricq, 2001; Khalek, Bougher, and Jetter, 2010; Maricq et al., 2000). Thus, the ZNP will have similar flow behaviour to soot particles during filtration. It is important to note that the ZNP is not a good model for ash particles which are much larger and heavier than both soot and the ZNP used in this experiment. This experiment was carried out for coated and uncoated GPF samples. By studying both samples with the same flow conditions we were able to analyse the effect of washcoating on filtration performance.

A quantitative analysis required segmentation as achieved by the 'multiscale and time lapse image processing' workflow described in section 3.2.5. This workflow included standard data reduction, cleaning, and filtering steps (*see section 3.2.5*). The workflow then relied on two image registration steps. The first of these we call

'stitching'. During stitching a series of overlapping tomograms that cover the entire length of the 3 cm long GPF mini-channels were accurately stitched together into one continuous image, see figures 3.9 & 3.13. This was achieved using the image registration tools freely available in SimpleITK's python image processing library. We applied a series of three exhaustive optimisation to solve the registration on the overlapping subvolumes of the tomograms. The first searches a large coarse 3D grid for the best optimised registration according to the Mattes mutual information metric. Starting from the best transform from the previous exhaustive optimisation, the second then repeats the same method but searches a smaller and finer grid. Finally, the third optimisation can then search a very fine grid with 1 px steps to find the ideal transform (3D translation transform) for the registration. Applying this transform will 'stitch' together two tomograms into a continuous volume. This is repeated for all 8 vertically aligned tomograms in the 'zeroth' or 'clean' (acquired before any ZNP deposition) time-step to create a continuous image of the 3 cm long mini-channel.

The second type of registration we call 'temporal' registration. The temporal registration registered volumes of the ZNP loaded filter from later time steps in the experiment onto the stitched together image of the 'zeroth' or 'clean' filter. Again we used SimpleITK. Similarly to the 'stitching' registration the first step was to apply a coarse exhaustive optimisation. It was important to find a good transform from this step so that the registration was robust and could be applied in a script to the entire dataset. Otherwise, during the next step of the registration, an erroneous local minimum transform maybe be output. This next step was to apply a gradient decent optimiser as described in section 3.2.5, page 123. This gradient descent optimised method is more computationally efficient and is required since the volumes being registered are larger than in the 'stitching' step where only overlapping subvolumes needed to be included in the registration. From this method we find the best 3D Euler transform for the registration based on the mean squares metric. By applying this registration to the time resolved data we achieve both 'temporal' registration but also the 'stitching' registration in the deposit loaded volumes since we were registering onto the already stitched together 'zeroth' data.

The fully registered dataset can now be segmented. A mask of the filter phase of the clean 'zeroth' volume is obtained from the global thresholds followed by binary dilation and erosion to smooth and fill holes in the filter segment. This zeroth filter mask is then applied to the 'deposit loaded' volumes such that the remaining high gray level pixels are deposit. The deposit was then segmented using a series of thresholds as described in section 3.2.5, pages 124 - 126. In brief the deposit pixels are segmented if they have an intensity eight levels higher compared to the corresponding pixel in the 'zeroth' clean unloaded tomogram and has an intensity greater than 97. Some of these deposit pixels will be false-positive for deposit segmentation due to unavoidable error when masking the filter segment, i.e. some pixels are included as deposit when they are actually filter pixels missed by the zeroth filter mask. The false-positive pixels were then removed by a series of dilations and erosions as described on page 126, section 3.2.5.

The accuracy of this method was determined by qualitatively comparing the segmentation to the original XCT grayscale slice images. Figures 5.1 & 5.2 show XCT grayscale slices of the bare and coated deposit loaded samples compared to their corresponding segmented slices. This allows for qualitative assessment of the accuracy of the segmentation methods. The slices show that the segmentation was accurate for the filter and deposit phases, studying the in-set regions in figures 5.1 & 5.2 we can see that the deposit was well segmented on the surface of the filter walls and in the deep bed of the filter by comparing the XCT graylevel slice and segmented images.

The catalyst phase was segmented by the U-net machine learning method, as described in detail in section 3.2.5, pages 127 - 131. Figure 5.2 also shows the washcoat segmentation in yellow. From a qualitative evaluation it appears to be an acceptable estimate of on-wall washcoat thickness (by comparing 5.2 a & b). The accuracy of the segmentation in the regions where there is observable separation between the washcoat and filter phases, such as the the top and bottom of the wall segment shown in figure 5.2, shows good accuracy. However it was impossible to segment any in-wall washcoat that may have been present in the sample. As a result it is important to be aware that this segmentation cannot be used to quantify the volume concentration

of washcoat in different parts of the sample. Furthermore, some over segmentation of washcoating is consistently observable in parts of the sample with low coating thickness. This over segmentation re-iterates that this segmentation should not be used for quantifying the volume or thickness of washcoat. However, the confidence in the segmentation is acceptable for coarsely comparing the relative distribution of washcoat along the length of the channel, especially as this varies significantly. Thus, we are able to infer what regions of the channel have relatively high or low levels of washcoating, as in figure 5.10.

5.2 Results

5.2.1 Visualisation

Figures 5.3 & 5.4 show the build up of deposit in the bare and coated filters samples respectively. They show the filter in its clean state (0 s), then after the first loading step of 10 s, and then after 30 s loading intervals (40 s, 70 s, 100s). We again (as in chapter 4) demonstrate in figures 5.3 & 5.4 the pore scale resolution of this technique by being able to resolve the build up of deposit in the deep bed pores overtime. Again, similarly as to chapter 4, in both the bare and coated sample, we can see that deposition starts predominately in the deep bed during the deep bed filtration regime. These deep bed deposits then build up until the filtration transitions towards cake filtration where deposition starts to occur on the wall surfaces. This can be seen in figures 5.3, 5.4, where some surface regions are unfilled and corresponding deep bed regions are filled, this is a result of filtration starting in the deep bed. For the GPF case we are less interested in the cake filtration regime, therefore we stop the filtration earlier compared to the chapter 4 DPF case. As a result of stopping the filtration before we observe full cake filtration there are some surface pores that do not become filled with deposit as was observed in chapter 4.

Figures 5.5 & 5.6 show the build up of deposit in 3D volume renderings of filter sub-volumes overtime (10, 20, 30, 40, 70, 100 seconds of loading) for both samples. The colour map used for the deposit in these figures is based on the graylevel value of the deposit. The graylevel value is assumed to be a qualitative measure for the

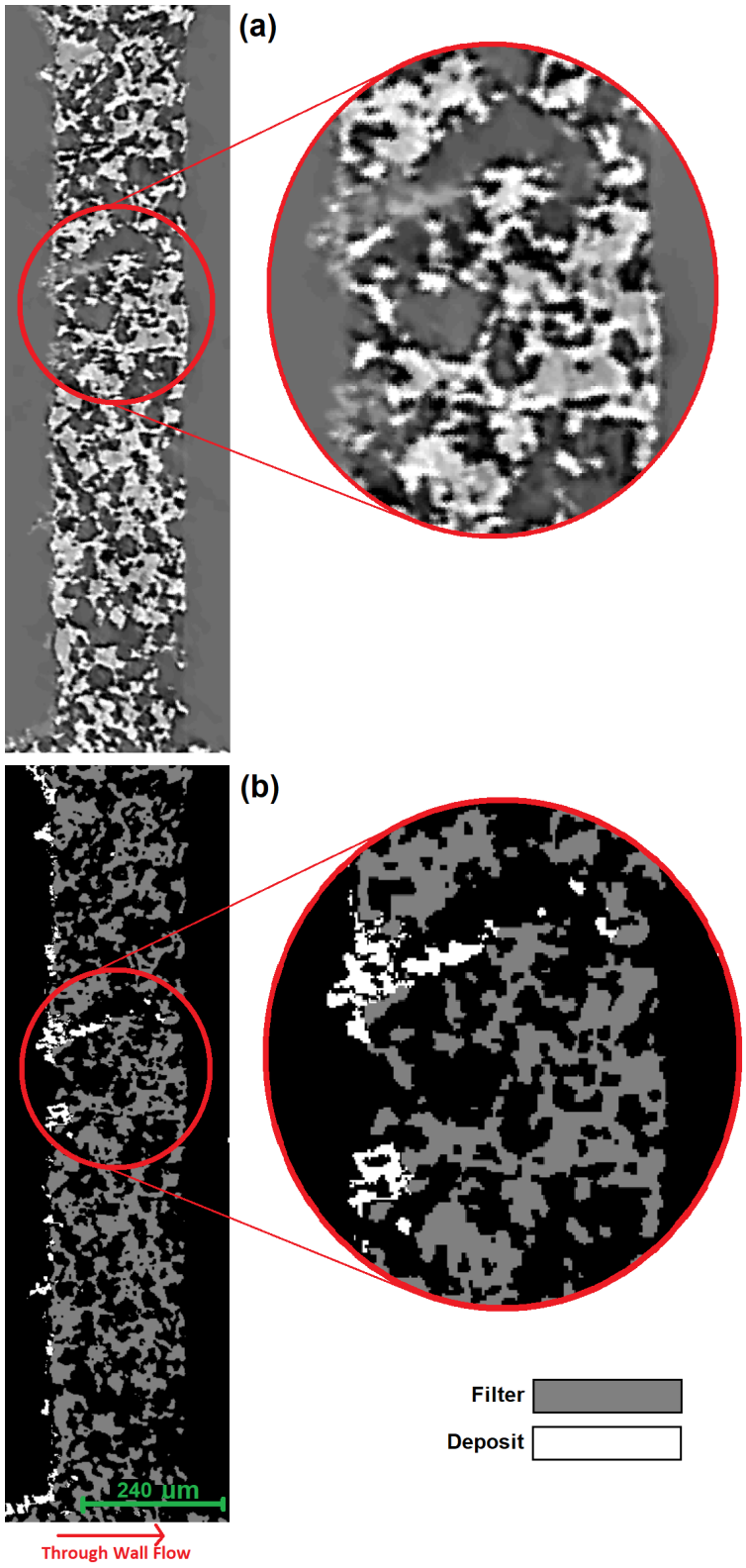

FIGURE 5.1: Comparison of grayscale XCT slice (with NLM filter) and corresponding segmented grayscale slice of the bare sample: (a) grayscale XCT slice (b) grayscale segmented slice. The slices show a cross-section of filter wall perpendicular to the flow direction with through wall flow from left to right. Comparison of the two images allows for qualitative evaluation of the segmentation accuracy.

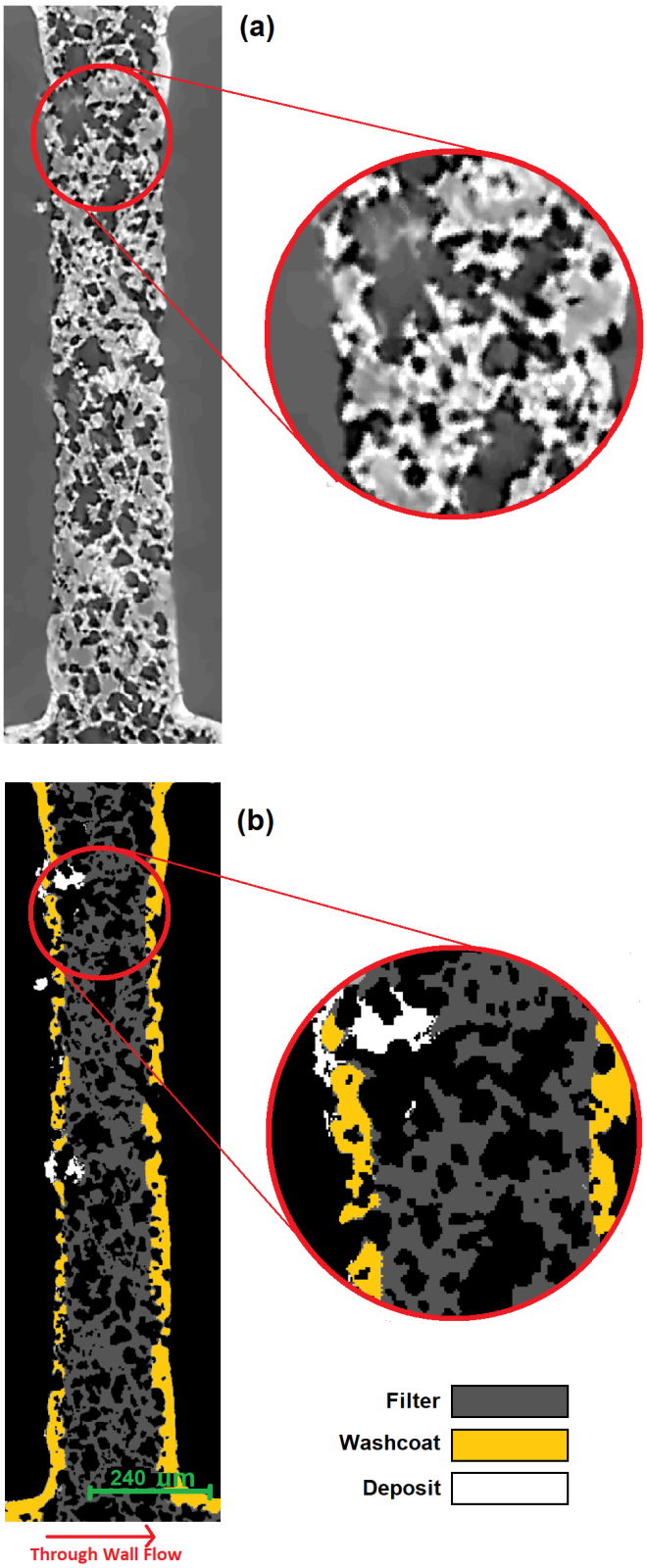

FIGURE 5.2: Comparison of grayscale XCT slice (with NLM filter) and corresponding segmented grayscale slice of the catalyst coated sample: (a) grayscale XCT slice (b) grayscale segmented slice. The slices show a cross-section of filter wall perpendicular to the flow direction with through wall flow from left to right. Comparison of the two images allows for qualitative evaluation of the segmentation accuracy.

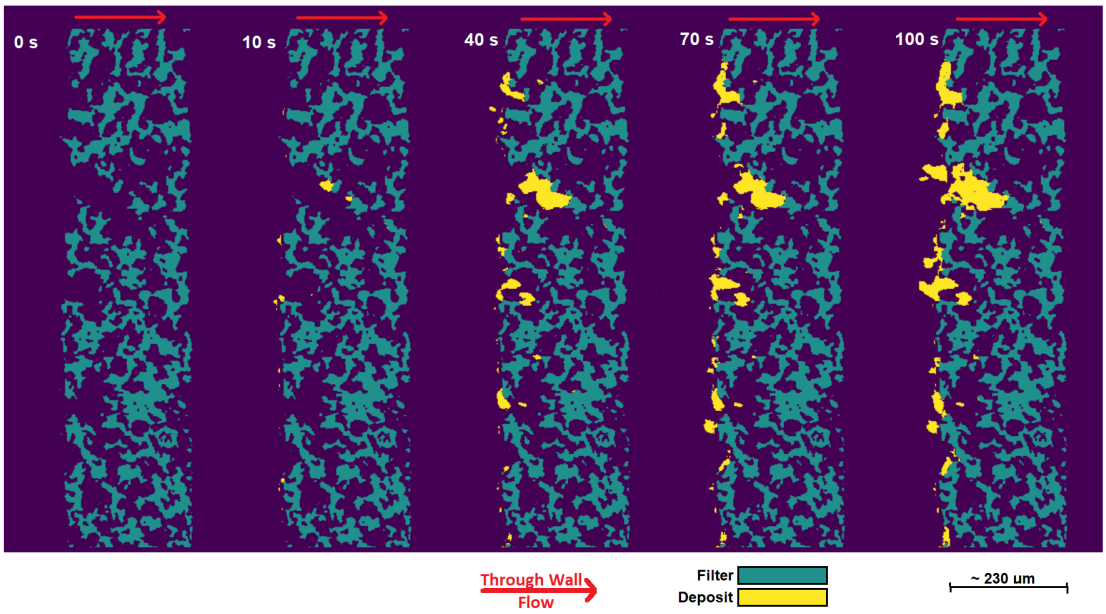

FIGURE 5.3: Segmented slices of the bare data-set showing the build-up of deposit at the back of the channel at 0, 10, 40, 70, 100 seconds of loading. Red arrows indicate through wall flow from the inlet surface to outlet surface (left to right as oriented in the figure).

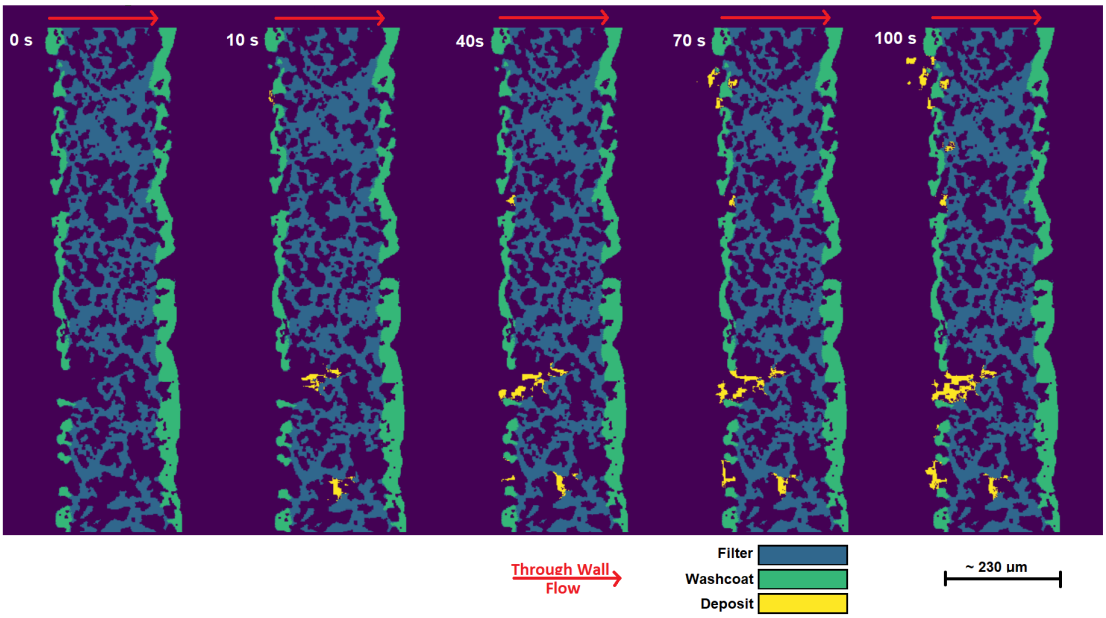

FIGURE 5.4: Segmented slices of the coated data-set showing the build-up of deposit at the back of the channel at 0, 10, 40, 70, 100 seconds of loading. Red arrows indicate through wall flow from the inlet surface to outlet surface (left to right as oriented in the figure).

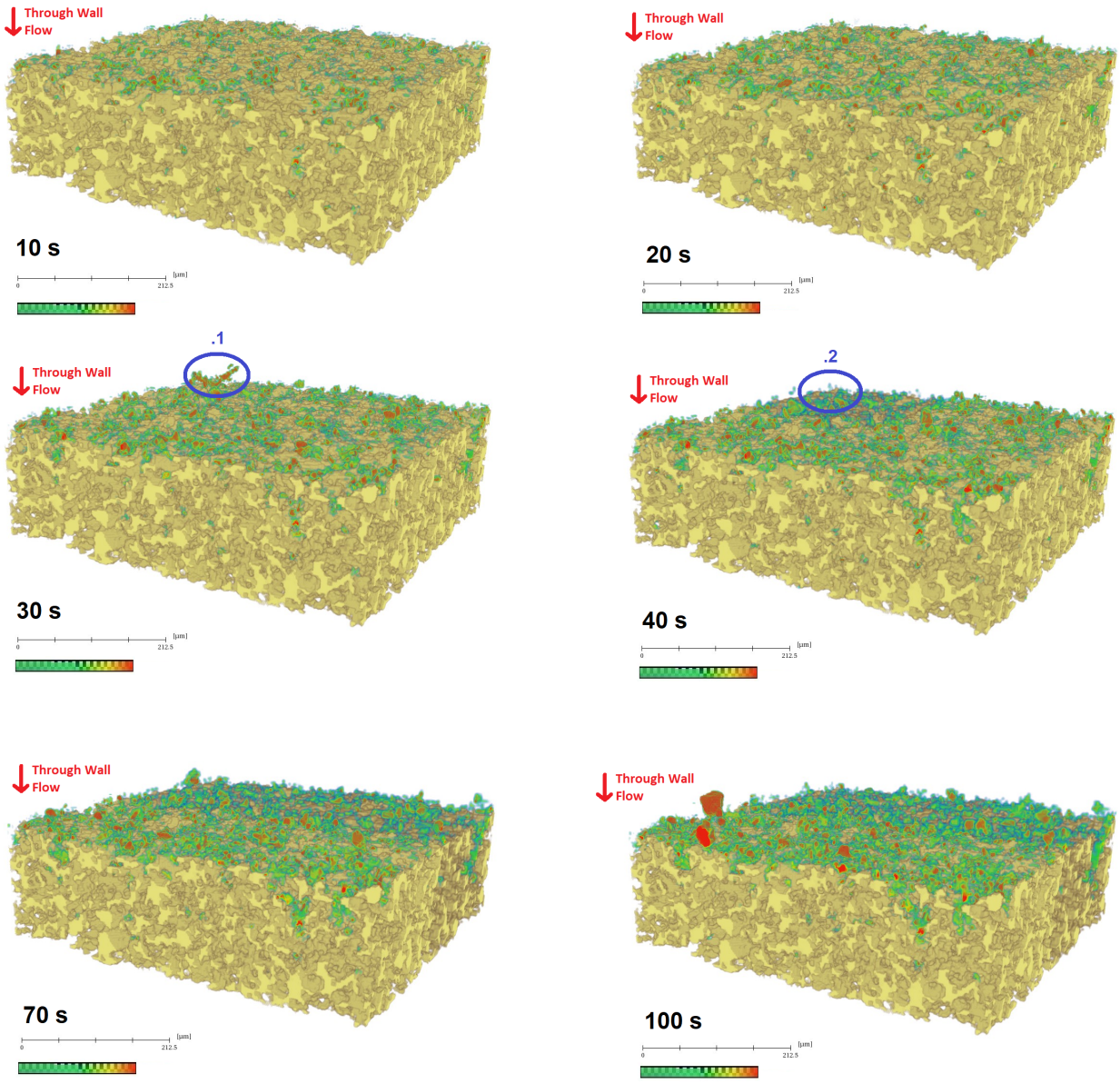

FIGURE 5.5: Time lapse volume rendering of segmented XCT data showing the build up of deposit at 10, 20, 30, 40, 70 and 100 seconds on an uncoated GPF. Scale bars = 213 pixels = 347 μm. The deposits are rendered in the physics.col map according to their graylevel, see legend were colour map range is from 0 -25. The filter is rendered in yellow. Blue ovals show a site before (.1) and after (.2) a re-entrainment event.

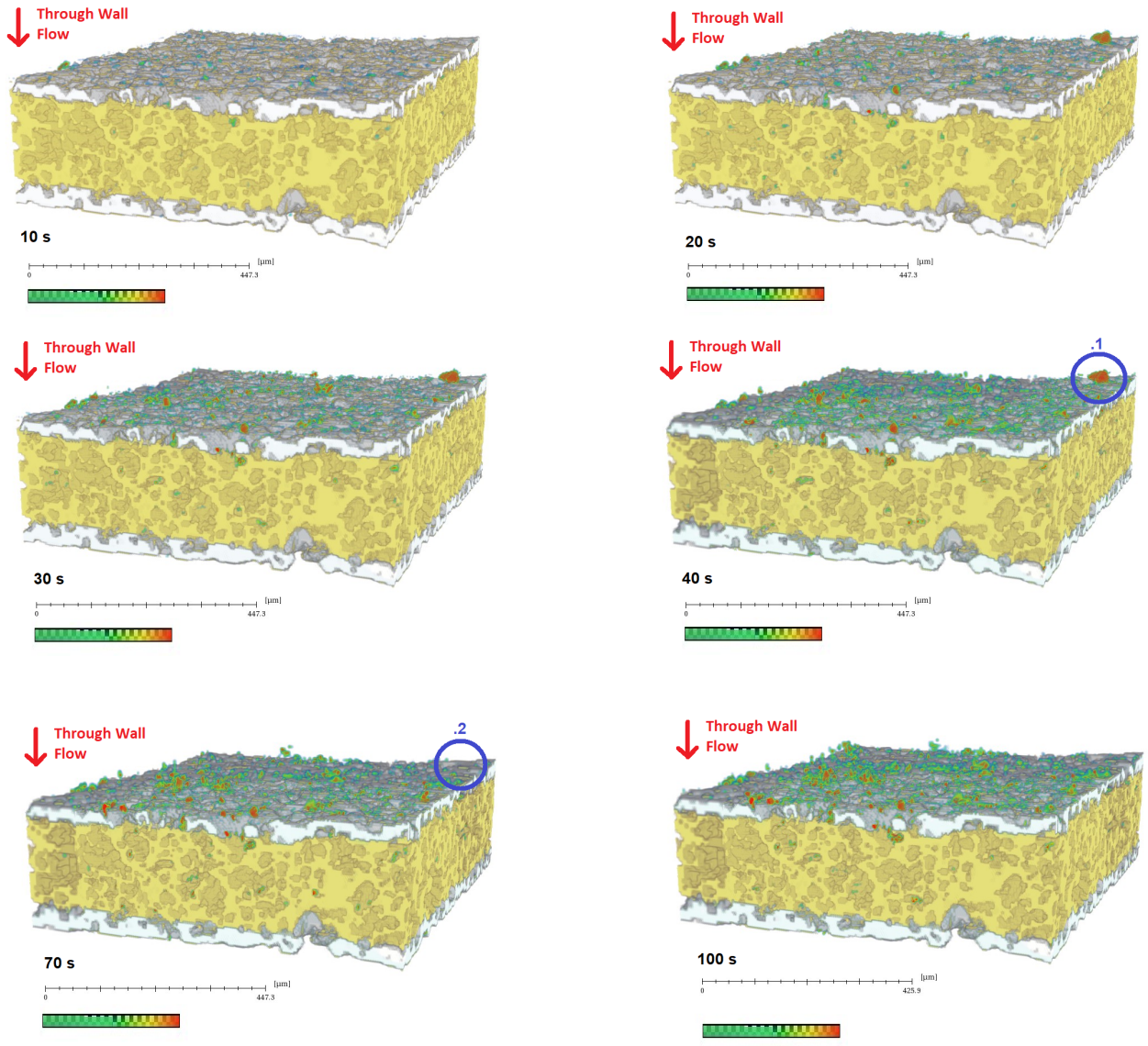

FIGURE 5.6: Time lapse volume rendering of segmented XCT data showing the build up of deposit at 10, 20, 30, 40, 70 and 100 seconds on an coated GPF. Scale bars $\sim$ 450 μm. The deposits are rendered in the physics.col map according to their graylevel, see legend were colour map range is from 0 - 25. The filter is rendered in yellow and the coating in white. Blue ovals show a site before (.1) and after (.2) a re-entrainment event.

relative density of the deposits in the filter, where red represents higher density and blue/green lower density. Again the build up of deposit as described above for figures 5.3 & 5.4 can be observed on the visible surfaces of the rendering in figures 5.5 & 5.6. An interesting phenomena observable in figures 5.5 & 5.6 is the re-entrainment of deposit from the surface of the filter. Re-entrainment is a phenomenon in filtration where deposit in the filter are picked up by the flow and moved from the original deposition site. The blue ovals (labelled .1 and .2) in the figures show were re-entrainment has occurred for deposit on the surface of the filter wall. In oval .1 in both samples we see a dense deposit (rendered in red) and then in oval .2 in the subsequent time lapse volume the deposit has moved. This can be confidently identified as re-entrainment rather than segmentation error because the deposits had a high gray level and therefore was classified as deposit with high certainty.

5.2.2 Quantifying Multiscale Filtration

Channel Scale Deposition Profile

In figures 5.8 & 5.9 we show how the volume fraction of deposit in the deep bed and on the walls of the filter changes along the length of the 3 cm sample channel for both samples. This is achieved by counting the amount of deposit voxels in 600 slice wide bins along the length of channel, and dividing by the volume of the channel. The volume of the channel is calculated by using the utility masks shown in figure 3.14.b-c, in section 3.2.5. By summing the 'walls mask' and 'channel mask' we calculated the channel volume, shown in red in figure 5.7 below. This allowed us to quantify how the volume fraction of deposit changes along the channel using these 600 px wide (975 μm) bins.

We can see that the deposit distribution is not homogeneous along the length of the channel. Deposit volume fraction is highest at the back of the filter in figure 5.8, shown by a large jump between 26 mm to 29 mm at the end of the channel in figure 5.8. This is due to the deposit plug. The deposit plug forms due to large heavy particles with greater inertia travelling down the length of the channel and impacting the the blocked end of the channel. These particles are able to do this because the inertia of the particles mean that they are able to resist gaseous flow

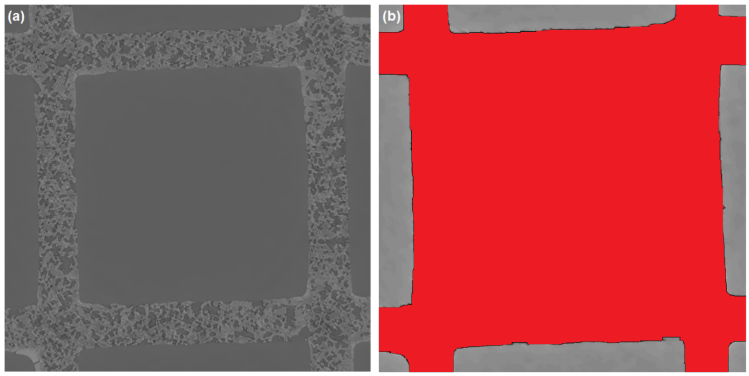

FIGURE 5.7: Figure showing (a) an XCT grayscale slice of a GPF crossection, (b) the same crossection with a mask of the 'central channel' in red. The mask was used to calculate the volume of the 'central channel' for volume fraction calculations

through the walls of the filter. The deposit plug fills the entire central channel of the filter, rather than just filling pores and depositing on wall surfaces, hence the large jump in deposit volume fraction from $\sim 0.03 - 0.6$ for the final filter state (T6 in figure 5.8).

In the bare sample, figure 5.8, deposit concentration is lowest in the centre of the channel length at around 15 - 19 mm, resulting in a characteristic 'U' shaped curve. This is in-line with expectations as we would assume that the through wall flow rate is lowest in the centre of the channel, therefore we would expect lower deposition in these regions, as shown by Gong et al., 2018b; Bensaid et al., 2009; Bensaid, Marchisio, and Fino, 2010. We observe increased loading as we move away from this deposit fraction minimum towards the deposit plug. Similarly to the deposit plug, this preferential loading seems partly due to the larger particles in the aerosol travelling further down the channel and depositing. We observe large agglomerated particles in images of these regions. Additionally, deposition would have increased near the back of the filter due to higher through-wall flow rates (Gong et al., 2018b; Bensaid et al., 2009; Bensaid, Marchisio, and Fino, 2010). Through wall flow rates increases because the blocked channel end blocks axial flow, this causes an increase in pressure near the blocked channel end, this pressure pushes the aerosol through the porous walls of the filter, increasing the filtration rate in that region. Finally, in figure 5.8, we can also see increased loading as we move from the deposit minimum towards the top (or inlet) of the filter. This is also due to the high through wall flow

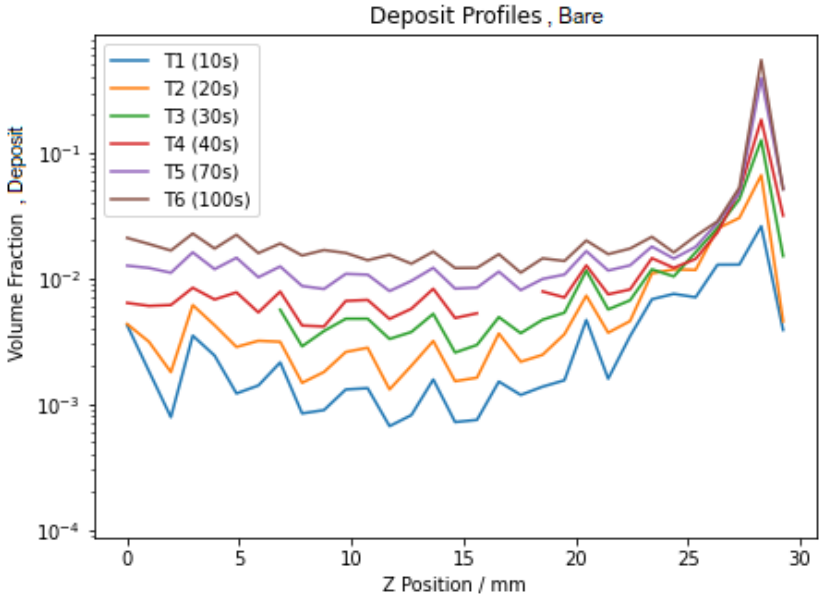

FIGURE 5.8: The distribution of deposit along the length (Z position) of a 3 cm long bare sample channel after different loading times. This is achieved by summing the amount of deposit in 600 slice wide bins along the length of channel, and dividing by the volume of the channel. The volume of the channel is calculated from the mask shown in figure 5.7. * In T3 between $\sim$ 1 - 6 mm there were movement artefacts in the images, these are not included. * T5 between $\sim$ 16 - 19 mm the images were poorly registered and therefore not included

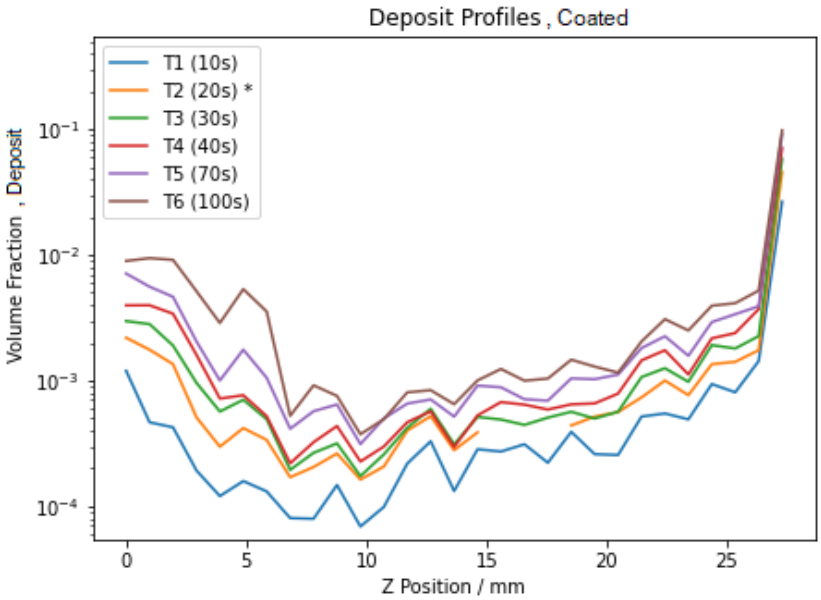

FIGURE 5.9: The distribution of deposit along the length (Z position) of a 3 cm long coated sample channel after different loading times. This is achieved by summing the volume of deposit in 600 slice wide bins along the length of channel, and dividing by the volume of the channel. The volume of the channel is calculated from the mask shown in figure 5.7. * T2 between $\sim$ 16 - 19 mm the images were poorly registered and therefore not included

rates of the exhaust stream as it enters the channel, caused by high pressure near the channel inlet (Gong et al., 2018b; Bensaid et al., 2009; Bensaid, Marchisio, and Fino, 2010).

As time progresses we observe that the 'U' shape becomes less pronounced. Again this is in-line with modeling literature, as shown in Gong et al., 2018b. This happens because deposits reduce through wall permeability, thereby reducing through wall flow rate. Thus, regions at the top and bottom of the channel that had high clean state filtration rates will observe decreasing filtration rates overtime. This has the effect of evening out this characteristic 'U' shape, see figure 5.8.

In figure 5.9, the coated sample, we see a similar pattern but with a more accentuated 'U' shape resulting from preferential front loading, less loading in the channel centre, and a sharp peak in deposit concentration at the back of the filter due to build up of a deposit plug (as discussed above). Since the experimental procedure was identical for both samples we can assume this accentuation is due to the washcoat. The washcoat blocks pores at the surface of the filter walls thereby increasing the pressure drop across the filter, as shown in figure 5.2. In figure 5.11 we can see that the pressure drop with coating is almost twice as high compared to the bare sample (a clean pressure drop of 614 Pa for the coated compared to 317 Pa for the uncoated filter sample).

Another noticeable difference between the bare and coated deposit profiles appears to be that the deposit fraction minimum occurs much earlier in the coated sample, at $\sim$ 10 mm, compared to $\sim$ 15 - 19 mm in the bare sample. This may be due to the non-homogenous distribution of washcoat along the length of the channel. In figure 5.10 we show the distribution of the catalyst phase volume fraction along the channel length. This was calculated by summing the catalyst phase (as segmented by U-net, see section 3.2.5) from 300 slice wide sections and dividing by the channel volume as described above. There is a clear step down in coating volume fraction at 15 mm from a maximum of $\sim$ 0.080 to a minimum of $\sim$ 0.050. The deposit minimum in the coated sample occurs within the high coating volume fraction region. This is likely due to the lower permeability of the coated wall, resulting in less through wall flow rates and therefore lower filtration rates in this region. In the coated sample we

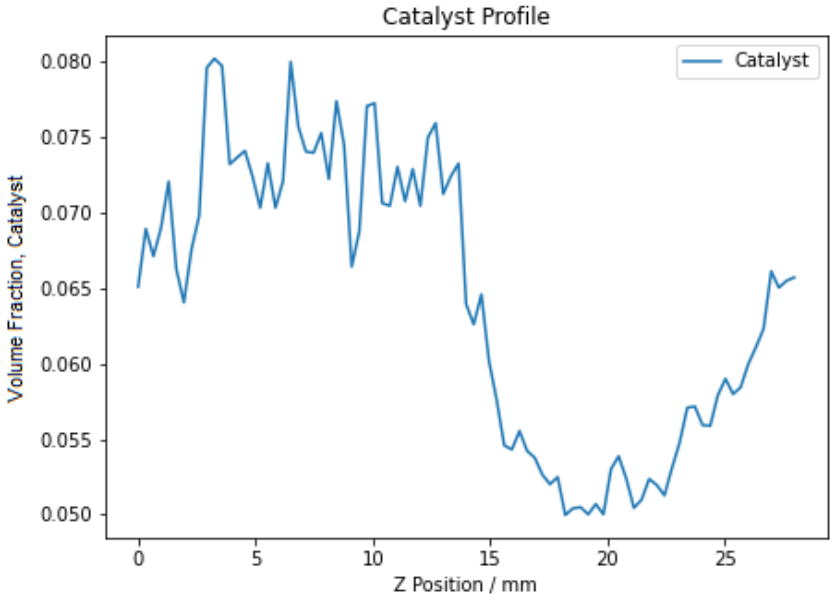

FIGURE 5.10: The distribution of catalyst washcoat along the length (z-axis) of a 3 cm long bare sample channel. This was calculated by summing the catalyst phase (as segmented by U-net, see section 3.2.5) from 300 slice wide sections and dividing by the channel volume. The volume of the channel is calculated from the mask shown in figure 5.7.

believe that the accentuated 'U' shape is caused by the higher pressure in the coated sample causing larger differences in the through wall flow rate along the channel, thereby accentuating this 'U' shaped distribution.

This analysis of deposit volume fraction distribution, figures 5.8 & 5.9, demonstrates the capability of this method to resolve deposit on the pore scale and analyse its distribution on the channel scale along the entire length of the channel.

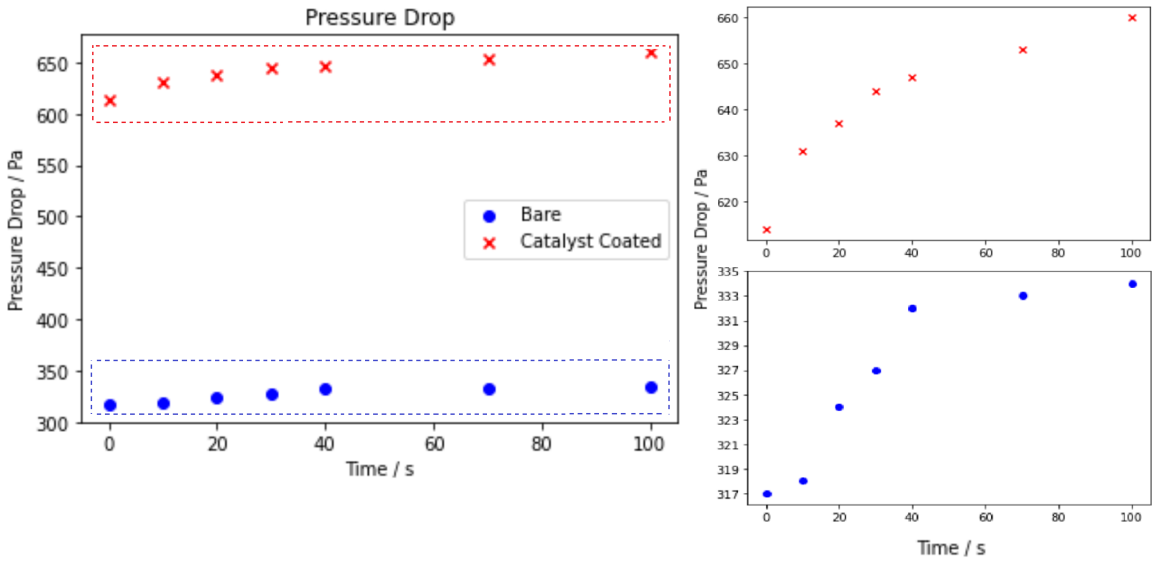

FIGURE 5.11: Pressure drop measured across the bare and coated filter samples during the experiment.

Representative Elementary Volumes

For further analysis of the samples we reduce the computational requirements for analysis by extracting a series of representative volumes evenly distributed along the length of the channel. In order to do so we calculate the representative elementary volume using an edited version of the porespy function, as described in section 4.2.2. In figure 5.12 we show the REV analysis for bare and coated GPF samples. In figure 5.12.a we show that the REV porosity of the bare sample is a 6×10^7 px volume (illustrated by the green vertical line in the figure). The REV volume is where the randomly generated volumes converge, in this case to a porosity of 0.62. However, for the coated sample we find that the porosity REV analysis doesn't converge, see 5.12.b. This is because the catalyst washcoat, which effects the porosity of the filter wall, varies too much on similar length scales to the REV. Therefore we select the same REV value for the catalyst as for the bare sample for comparability. We analyse 5 REVs evenly distributed along the channels at 0, 6.5, 13, 19.5, & 26 mm. These REVs have a size of 750 $\times$ 600 $\times$ 275 px (z, y, x) for the bare samples and 750 $\times$ 600 $\times$ 365 px for the coated sample. This difference in the x dimension between the coated and bare sample is extra channel space, therefore the REV (calculated from inside the filter wall only) in both cases is 750 px $\times$600 px $\times$ *wall thickness*. By reducing the

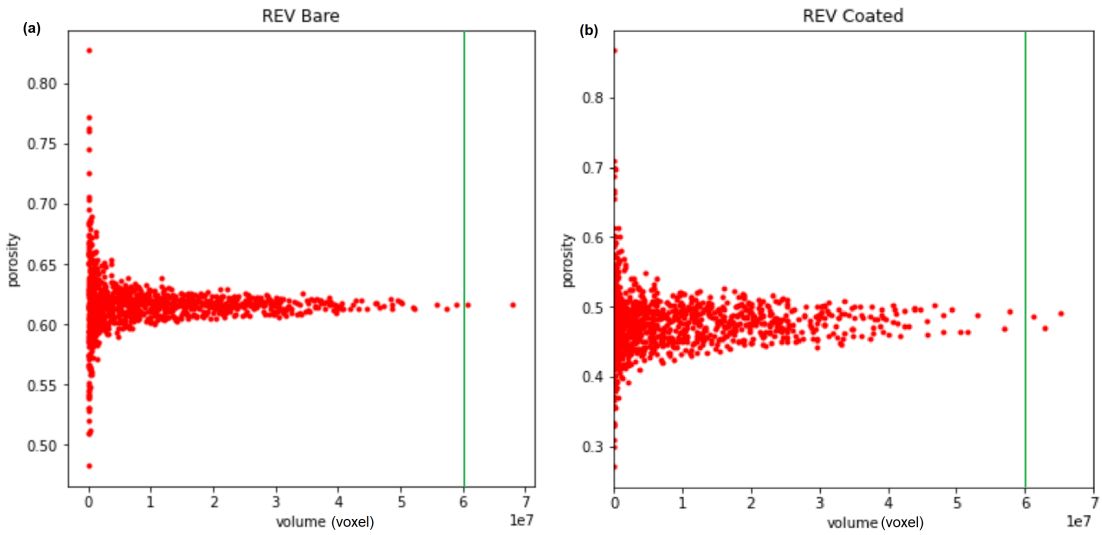

FIGURE 5.12: REV analysis for; (a) the bare sample, and (b) the coated sample.

data set to a series of REVs we reduce its size to 0.3% of its full size.

In-wall Deposit Penetration

An attribute of this experimental method is the ability to extract spatial information about the deposit on both channel and pore scales. Of interest is how far into the filter wall deposits penetrate at different positions along the length of the channel. In order to achieve this deposit pixels need to be labelled with their position in the channel wall. One of the methods for achieving this is shown in figure 5.13. First we calculated the distance transform from the inlet channel (shown in gray in figure 5.13.b) for the interior of the filter wall. The product of this distance transform and the deposit masks created a volume where every deposit voxel has a value equal to its depth in the the filter wall. Similarly, by calculating the distance transform from the filter wall into the inlet channel we can label the height of the on-wall deposit as it builds up on the channel surface.

As in chapter 4 (figure 4.4), this allows us to calculate the penetration depth of deposit, we plot this for T6 (100s loading) for both samples, as in figure 5.14.a,b. However, this method extends the analysis from chapter 4 by examining the penetration profiles at different position along the length of the channel (z positions). This was achieved with the series of 5 representative volumes that span the channel z-axis at

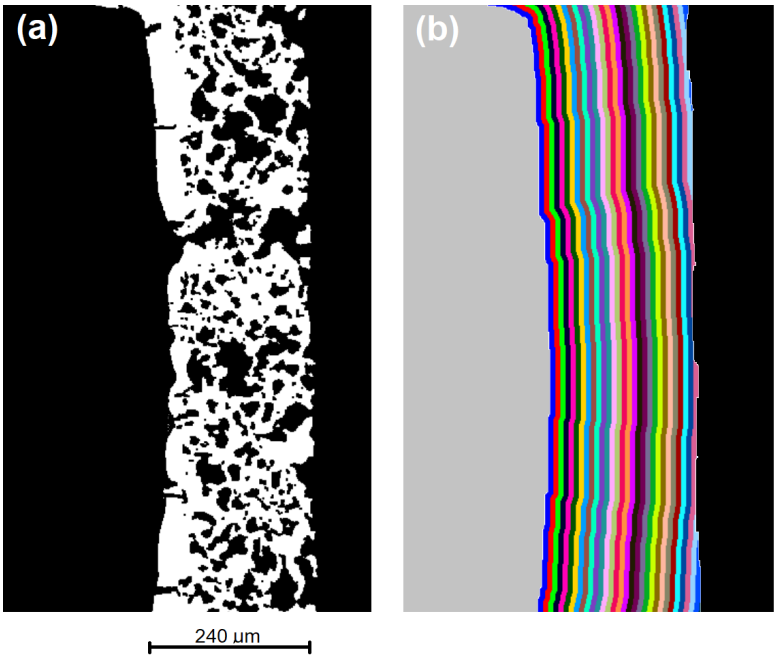

FIGURE 5.13: Distance transform calculated for a coated wall section: (a) A cross section of the filter mask, (b) Distance transform calculated from the inlet channel (gray), for the inside of the wall of the filter. Each colour band is 5 px (∼8 μm) wide, and separated by its distance from the inlet channel.

0 mm, 6.5 mm, 13 mm, 19.5 mm, & 26 mm. In figure 5.14.a,b these REV penetration plots are coloured blue, orange, green, red, & purple respectively. In figure 5.14.a,b the '*X position*' refers to the position of the deposit on the x-axis, where, as shown in figure 5.14.c, the origin is at the surface of the filter wall, the positive x direction is towards the inlet channel, and the negative x direction is into the filter wall. Thus deep bed deposits will have a negative value, and deposit at the top of a tall surface agglomerate will have a large positive value.

In figure 5.14.a we see that the amount of on-wall and surface pore deposit decreases as we we move down the length of the channel in the bare sample. We also observe that the penetration depth increases as we move towards the back of the filter in the bare filter sample. We calculate that the mean penetration depth for deep bed deposit (excluding on-wall deposit) also increases from front to back for the bare sample; from 16 μm at 0 mm (z-position), through 20 μm at 13 mm, to 31 μm at 26 mm. We suggest this is because more penetrating particles are able to travel further down filter channel before being filtered by deep bed filtration, as a result of this, as

we look further down the channel these particles are able to penetrate deeper into the filter wall before being deposited. The previous observation of less penetration at the top of the filter corroborates this as it suggest that at the front of the filter less penetrating particles penetrate less into the filter walls and therefore quickly build up near the wall surface. In figure 5.14.b, the coated sample, this pattern of increasing penetration depth with z position is not observable, this is partly due to the low loads in the centre of the channel (the same 'U' shaped deposition profile as shown in figure 5.9). However, we have found that the ratio of in-wall to on-wall deposit increases as you move down the coated channel; from 0.31 at 0 mm (z-position), through 0.52 at 13 mm, to 1.25 at 26 mm.

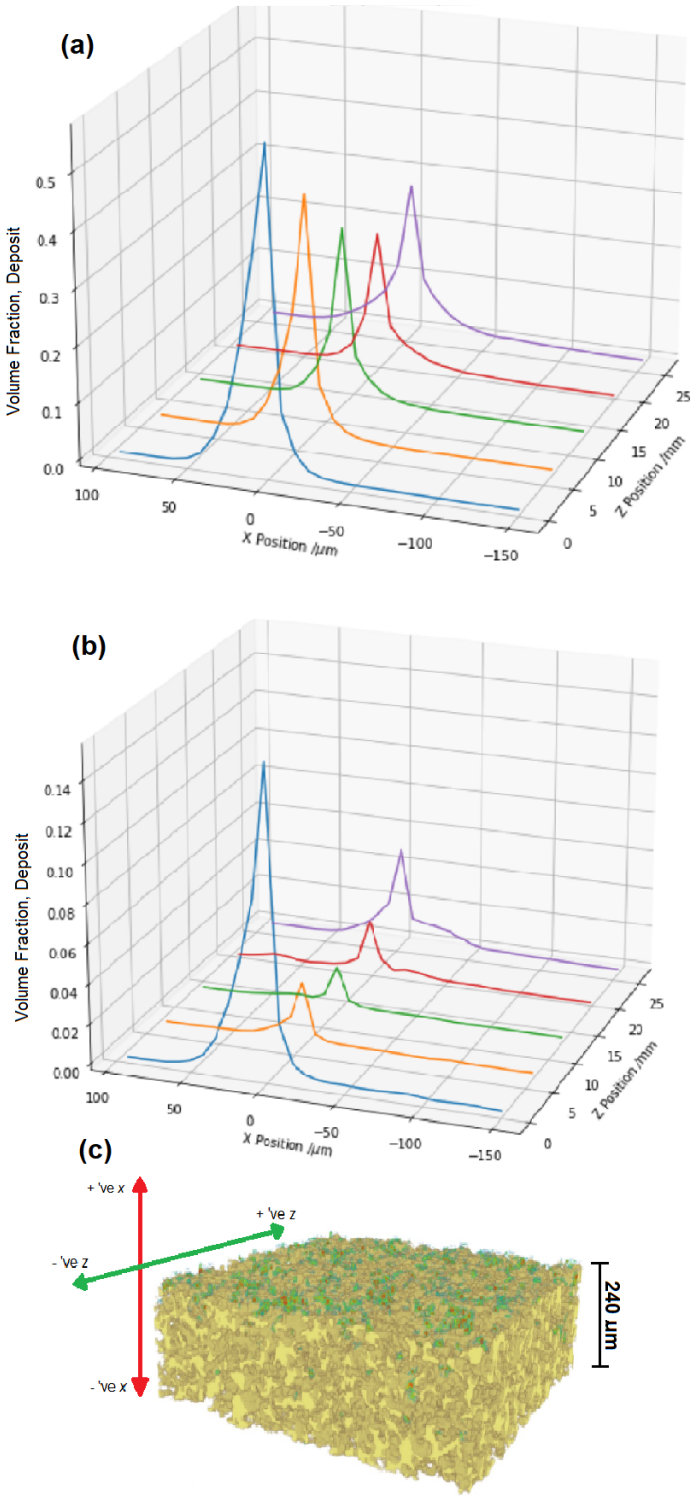

FIGURE 5.14: Plots showing the distribution of deposit along the *X axis* (describes on-wall height above the wall surface and in-wall depth below the wall surface) at 5 different positions along the *Z axis* (0, 6.5, 13, 19.5, 26 mm) which describes position along the length of the filter channel; (a) for the bare sample at T6 (100s loading), (b) for the coated sample at T6 (100s loading). (c) shows the definition of the axes. The negative x direction is into the filter wall and the positive x direction is height above the wall surface. The surface of the filter wall is by definition at 0 on the x-axis. The z direction describes the length along the filter channel. Positive Z is towards the back of the filter (downstream) and the top of the filter is defined as 0 on the z-axis.

Pore Network

Another method for extracting spatial information on deposit from this method is to extract a pore network via instance segmentation with a watershed algorithm (SNOW). Extracting a pore network results in a labelled image where each individual pore is separated with a unique label via an instance segmentation. From this image it is then possible to extract characteristics for each unique pore, such as; volume, equivalent diameter, and sphericity. Once these characteristics have been extracted it is possible to then map these characteristic values back onto the labelled image. For example, in figure 5.15, we extract the pore diameter characteristic and map it back onto the image so that each unique pore is labelled by its diameter. We used the the SNOW algorithm from porespy for network extraction (Gostick, 2017; Gostick et al., 2019). SNOW is an acronym for Sub-Network of an Over-segmented Watershed. The algorithm utilises a marker-based watershed segmentation algorithm to separate the image into pore regions. The key advantage of using SNOW over other watershed algorithms (like that described in section 2.1.8 (Bradski, 2000)) is that it finds a set of initial markers in the image that prevent the watershed algorithm from over-segmenting the pores by removing 'spurious peaks and saddles' from distance transforms of the pore space (Gostick, 2017).

By using the SNOW algorithm we extracted the pore network from all the representative volumes in both samples. Before applying the SNOW algorithm any disconnected porosity was removed from the image of the pore space. The extracted network is shown in figure 5.15.b. From the network we then extract the diameter characteristic for each pore. The diameter was calculated as that of the largest sphere that could fit in the pore volume. This was found by taking the maximum of the distance transform of the separated pore region in isolation. This allowed us to to calculate pore diameter distribution (calculated over all 5 representative volumes) for both samples. These are plotted in blue in figure 5.16.a.b. This diameter value for each pore was then mapped back onto the image such that each unique pore was labelled with its diameter, see 5.15.b. We then mask this image with the deposit mask, the result of this is an image where every non-zero voxel is a deposit voxel labelled with the diameter of the pore it deposited in. This was carried out for

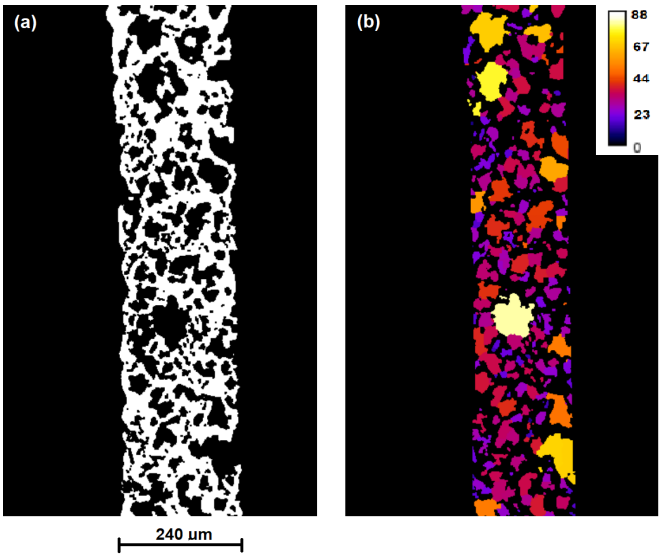

FIGURE 5.15: Pore network extraction via instance segmentation with SNOW algorithm; (a) A z-slice of a labelled mask of the pore space from which the pore network was extracted, (b) the labelled pore space where the label values are the diameter of the sphere that would fit within the pore volume. Colour map legend = 0 - 88 μm.

the T6 (100 s loading) time step over all the representative volumes in both samples. The histogram of this image is shown in red in 5.16.a.b. Thus, we show show how deposit is distributed over different pore volumes.

In figure 5.16 we can see that (for both samples) the deposit peak is shifted to the right compared to the pore diameter distribution peak. This is most clear in figure 5.16.a, which shows the pore diameter distribution (blue) and the distribution of deposits across the range of pore diameters (red) in a bare GPF sample. The red histogram shows two distinct peaks, the first at $\sim$ 50 μm diameter, and the second at $\sim$ 80 μm diameter. If each pore contributed equally to the filtration rate, independent of size, we would expect the shape of the red deposit distribution histogram to approximately match that of the blue pore diameter distribution histogram. However the blue pore diameter distribution has only a single peak at $\sim$ 35 μm diameter. This shows that the larger pores hold more deposit. This result may be expected for a number of reasons;

1. The volume of smaller pores limits the volume of deposit that can be held.

2. Large pores are able to carry more deposit as a result of their larger volume.

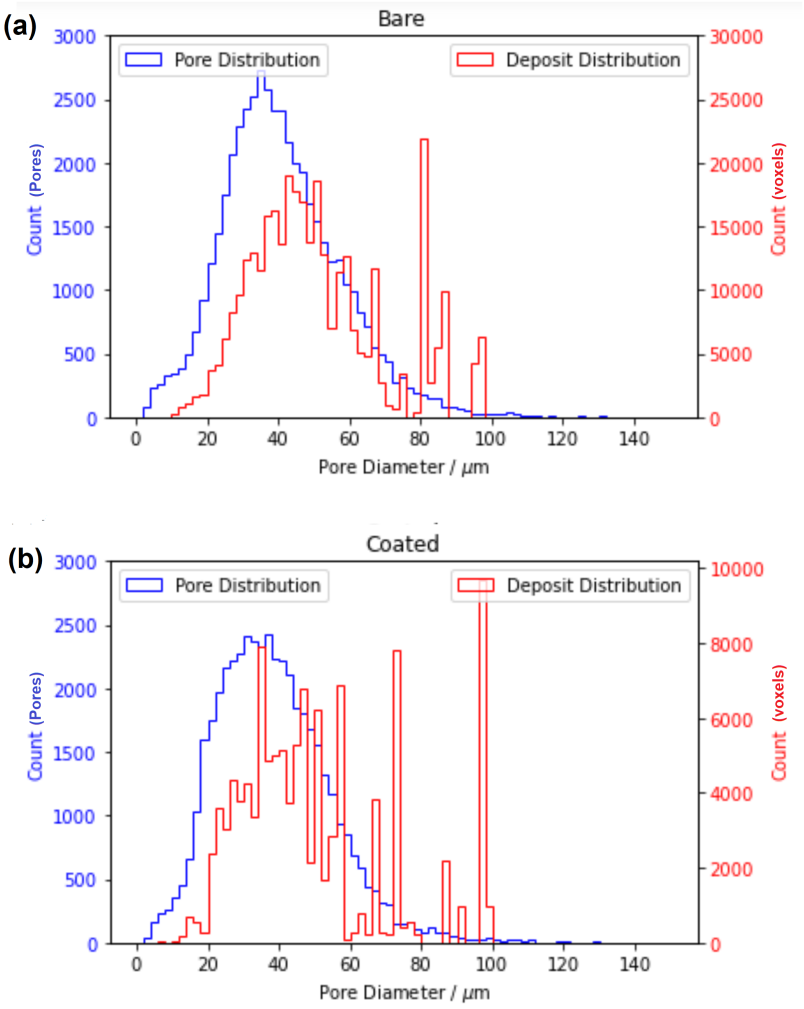

FIGURE 5.16: Comparison of the pore diameter distribution (blue) and the distribution of deposit across the range of pore diameters (red), for (a) the bare sample (T6, 100s loading) and (b) the coated sample (T6, 100s loading).

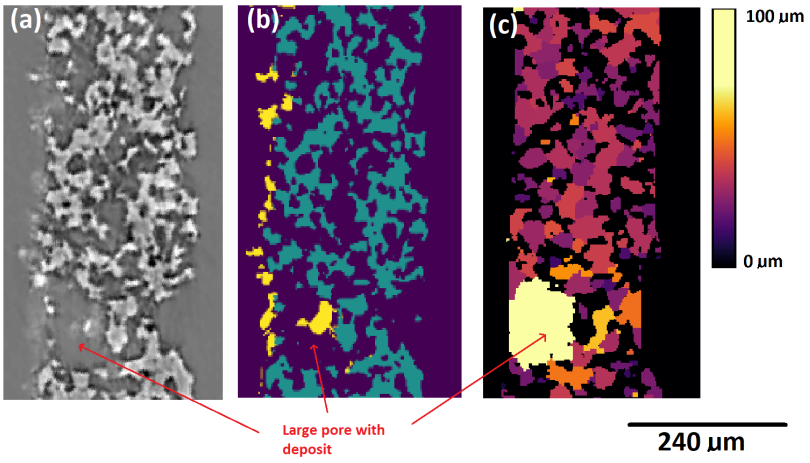

FIGURE 5.17: Example showing how a larger pore (96 μm diameter) is preferentially filled, (a) a grayscale XCT slice (T6 100 s loading), (b) the corresponding segmented image where the filter is green and the deposit is yellow, (c) corresponding image where each pore has been separated and labelled with its equivalent diameter

3. Smaller pores may restrict flow and therefore experience lower aerosol flow

4. Large pores create permeable flow paths with higher aerosol flow rates, resulting in higher filtration rates (even at low filtration efficiencies).

In figure 5.16.a,b, we observe that a small number of large outlying pores carry a significant fraction of total deposit. In figure 5.17 we show an example of such a pore located just below the inlet surface of the filter wall. We suggest that these large pores may capture deposit as described in bullet point 4 above. They create highly permeable flow paths that bypass the surrounding tighter porous network of the filter, thereby capturing a significant proportion of the deposit but also potentially lowering the overall filtration efficiency of the device, termed 'leakers' by Joshi and Johnson, 2018. Which is to say, the pores that experience the highest filtration rate (defined as the rate at which a pore captures deposit), may be the pores with the lowest filtration efficiency (defined as the fraction of aerosol successfully captured from the aerosol that flowed through the pore). Thus, it may be considered that these large outlying pores have a negative effect on desired performance.

The importance of the pore size distribution on the performance of particulate filters has been previously modelled and is understood to be a key factor in performance (Yang and Strzelec, 2019; Gong et al., 2018b; Joshi and Johnson, 2018). Yang

and Strzelec, 2019, use modelling to find the ideal pore size distribution for particulate filters. Gong et al., 2018b, show the importance of including a realistic pore size distributions in CFD models, showing that assuming monodisperse pores is an over-simplification when modeling GPFs. Our method provides a useful method for validating the performance of filters in terms of pore size distribution.

5.3 Summary

In this chapter we demonstrated a method for resolving deposition during a filtration in 4D for the pore and channel scale of a wall flow filter. This was demonstrated for two GPF samples, one bare and one coated by a catalyst washcoat. We demonstrated how a number of useful filtration characteristics can be extracted from this in-situ method. First we demonstrated how this method can be used to plot the deposit distribution along the length of the filter channel (for deposit in and on the filter wall). This method was able to do so by resolving deposits on the pore scale and extending this to the channel scale in order to resolve the distribution along the channel. From this we found that the deposit distribution for both samples created a 'U' shaped distribution where deposition had been favoured at the front and the back of filter. This is in good alignment with modelling literature that predicts this 'U' shape (Gong et al., 2018b; Lee and Lee, 2013; Hayashi and Kubo, 2008). In doing this we show the potential for this technique for validating models of both pore scale and channel scale flow in particulate filters. We also showed this 'U' shape was more accentuated in the the coated sample compared to the bare sample. We suggest the accentuation in the coated example is due to the higher pressures caused by the coating creating larger pressure gradients, thereby exaggerating the variation in through wall flow rate along the length of the channel.

We were also able to extract pore scale information about the deposits. By plotting distance maps along the x-axis, we were able to label each deposit voxel with its depth in the filter wall (x-axis). From this we were able to discern how deposits in the bare sample penetrated further into the wall as we moved along the length of the channel. We also saw in both samples that a larger proportion of the deposit at the front of the channel was due to on-wall deposits whilst at the back of the filter

a larger proportion was due to in-wall deposits (after 100 s of loading). Further pore scale information on the deposits was achieved by labelling the deposits with the diameter of the pore they deposited in. This allowed us to see which pores where capturing the most deposit. We found that in general larger diameter pores were favoured. A few very large pores contributed a significant proportion of the deposit captured by the filter. We suggest these pores may create favourable flow paths through the filter which result in this build up within them, however such flow paths may reduce the overall filtration efficiency of the device, such pores are termed 'leakers' in Joshi and Johnson, 2018. Using this method we can investigate the performance of different pore sizes during a filtration, which has been shown to be an important factor in device performance in literature (Yang and Strzelec, 2019; Gong et al., 2018b).

5.3.1 Outlook

In future work it may be possible to improve upon this method to study filtration in pre-aged ash loaded samples. The complex morphology introduced by the ash layer makes the study of filtration via experimental methods like this attractive. Furthermore, the interaction of ash and soot in-operando during filtration and regeneration is still of great interest to industry (Lambert et al., 2016; Joshi and Johnson, 2018). For example, there is ongoing interest in how a small concentration of ash (2 -3 g/L) can improve filtration efficiency with relatively little backpressure penalty, thereby improving the quality factor of the filter (Shao et al., 2016; Lambert et al., 2017; Hua et al., 2018). This preferable soot loaded pressure drop with ash loading may be because the ash prevents the soot from depositing in the deep bed, where it has a greater effect on backpressure (Shimoda et al., 2012). 4D tomography methods such as is demonstrated here may offer an opportunity to study this aspect of the ash loaded GPF system, however, many challenges will need to be overcome to achieve this. During the beamtime at I13-2 we also performed this experimental method on pre-aged ash loaded (20 g/L) samples. We did not include this data in the analysis above as quantification of the data proved too challenging. Firstly, there is no contrast between the pre-aged ash and the ZNP deposited in the sample during the experiment, see figure A.2. In the non-aged bare and coated examples the lack of

contrast between the deposit and filter was not an issues due to the filter phase remaining stationary during the experiments run-time. As a result we could mask out the filter phase so that the remaining high intensity pixels in the image belonged to the deposit phase. However, in the pre-aged ash loaded samples the ash layer is not stationary and is often re-entrained, see figure A.2, as a result this segmentation method is ineffective. Finally, the resolution is likely too low. The ZNP likely deposits in the sub-micron pores between ash particles, making accurate segmentation by our micro-CT method impossible. In future work, it may be possible, utilising methods such as nano-CT or correlative tomography, to overcome these contrast and resolution issues.

This chapter demonstrated how 4D time resolved XCT can resolve deposits on the pore and channel scale of particulate filters. Such a technique could be used in future work to validate models of filtration both on the pore scale, such as those from Yang et al., 2009, Belot et al., 2020, and Plachá et al., 2020, and on the channel scale, such as from Gong et al., 2018b, Lee and Lee, 2013, and Hayashi and Kubo, 2008. For example, in figure A.3, we present ongoing work from a collaboration with University of Chemistry and Technology, Prague, where we compare our experimental results (taken from a small sub-volume of this dataset) to their models of soot filtration. A similar experimental method could be easily extended to include various flow rates, particle size distributions, and filter designs to test the accuracy of model predictions under a range of different conditions. Manufacturers can have higher confidence in the results from such validated models, thus potentially reducing the burden of prototype testing during the design stage.

Chapter 6

X-ray Ptychotomography and XRF-CT of Automotive Ash

6.1 Introduction

Particulate matter from automotive sources can vary significantly in both chemical composition and structure. It is this which determines its toxicity to humans in the urban environment, its potential for climate forcing, and, of interest to this study, its role in effecting the operating conditions of automotive exhausts (Brown et al., 2013; Bond et al., 2013; Wang et al., 2020). In this study we imaged ash PM deposits removed from GPFs in 3D with sufficient resolution to resolve primary particles, the structure of agglomerates of primary particles, and the internal structures of individual particles. This was combined with 3D elemental mapping that provides a way to infer the origins of specific ash species. This nano-CT was achieved with X-ray Ptychotomography (XPT) and correlated X-ray Fluorescence Tomography (XRF-CT) at the I13-1 beamline at Diamond Light Source as described in section 3.3.

Ash in this automotive context refers to incombustible PM species that build up in the exhaust during use. Unlike organic and carbonaceous PM species, ash cannot be burnt off, or regenerated, and therefore builds up in the GPF during use until eventually it needs to be manually removed. Ash can effect the performance of filters in countless ways. For example, the build up of ash layers increases the backpressure across the filter. This increased backpressure then lowers the fuel efficiency of the engine as the pistons have to push against this pressure. Thus porosity and in-situ

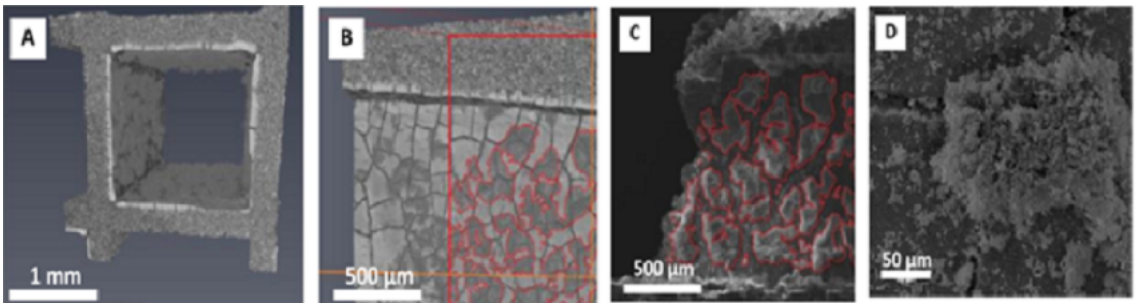

FIGURE 6.1: **(a)** XCT volume rendering (grayscale) of the inlet channel of a pre-aged ash loaded GPF, **(b)** XCT volume rendering of the inlet channel surface with the ash layer outlined in red, **(c)** the same ash layers were identified via a correlative method with SEM, **(d)** Higher magnification SEM showing a large ash pile

ash density are of interest as these are directly related to the ash layer permeability. Alternatively, ash can sometimes aide performance, studies have shown that small amounts of ash can improve the quality factor of the filter (the quality factor of a filter optimises for high filtration efficiency and low pressure drop, see equation 2.11) by acting as an extra layer of filtration that produces relatively little backpressure (Lambert et al., 2017; Hua et al., 2018). The chemistry of ash can also effect performance, studies have shown that ash can poison the catalyst in washcoated GPFs (Seong et al., 2019; Panchal et al., 2021), and a study from Choi and Seong, 2016, has shown that Ca species in ash can catalyse the regeneration of carbonaceous soot.

Also of interest is the behaviour of ash at high temperatures. At elevated temperatures ash primary particles will grow, sinter together, and coalesce. This increases the ash density and decreases the total volume of ash agglomerates (Sappok, Kamp, and Wong, 2012; Ishizawa et al., 2009; Wang et al., 2020). Wang et al., 2020, in their review of automotive ash literature, suggest that this phenomena could be used as an ash management strategy as the densified ash has been shown to lower backpressure and, due to its lower volume, improve the deposit storage capability of the filter. However uncontrolled exposure to high temperatures can be problematic. Ash - substrate sintering or wetting can block the catalyst washcoat and field-returned filter samples show a clear relationship between problematic samples and sintered ash content (Wang et al., 2020).

Ash morphology is important for many of the phenomena discussed above. Therefore in previous work we have attempted to resolve the extended structure of ash agglomerates in 3D. We found that it was possible to achieve acceptable contrast using XCT. In figure 6.1.a,b we show that ash was resolved by synchrotron XCT at low magnifications and verify this with correlative SEM, see figure 6.1. However, we found that the resolution of XCT and Transmission X-ray Microscopy (TXM) was limiting for the study of ash as we could not resolve the finer structures observed with SEM. Furthermore, in a previous beamtime we have attempted to collect this high resolution data using ptychography and XPT but failed due to beamline faults, as described in section 3.3.2 and figure A.1. Similarly, literature studies have used high resolution XCT and TXM to image ash structures, these also do not resolve fine structures such as internal porosity and primary particles (Kamp et al., 2017).

SEM and TEM have appropriate spatial resolution but cannot typically resolve 3D structure. However, 3D structure can be resolved with SEM serial sectioning techniques such as FIB SEM (Echlin et al., 2020). Many literature studies have employed FIB SEM to image cross sections in post-mortem analysis of ash laden samples (Kamp, Sappok, and Wong, 2012; Custer et al., 2016; Kamp, Sappok, and Wong, 2013). By removing material from the sample the FIB SEM technique brings previously obscured features to the surface to be analysed. The internal porosity of automotive ash particles was first observed using this technique (Kamp, Sappok, and Wong, 2012). Resin infiltration is often required for FIB SEM serial sectioning to create 3D reconstructions (Varambhia et al., 2022; Echlin et al., 2020). The resin stabilises the friable ash agglomerates, thereby preventing movement artefacts. Furthermore, it can improve segmentation of the dataset by removing background signal, thereby acquiring information predominantly from the exposed surface, thereby acquiring higher fidelity slices (Sabharwal et al., 2017). Resin infiltration also creates a flat surface for milling. FIB SEM serial sectioning is a powerful tool for analysing ash structures in 3D at high resolution. However, it is by its nature a destructive technique. This means that the same site cannot be re-examined once it has been studied with FIB SEM. Therefore, the FIB SEM technique is most applicable to post-mortem samples.

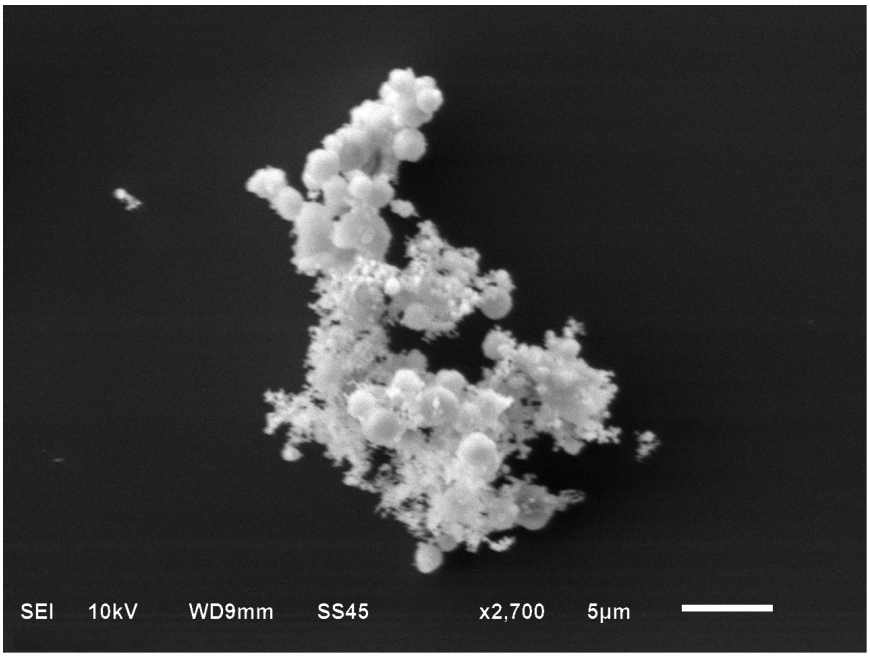

FIGURE 6.2: SEM secondary electron image (SEI) of an ash agglomerate.

In this work we present a novel combined synchrotron XPT and XRF-CT method to resolve the extended structure of ash agglomerates in 3D at comparable resolutions to FIB SEM serial sectioning. This is compared to FIB SEM serial sectioning, SEM, and SEM EDX. The XPT & XRF-CT technique allows us to quantify physical characteristics, such as particle size distribution, external porosity, and internal porosity. Such characteristics are important for understanding the effects of ash on GPF operation described above. XPT in this context is a semi-destructive technique, after imaging the sample is still intact, however a small ash sample has to be removed from an aged monolith before imaging.

6.1.1 Method

This method is described in detail in section 3.3. The ash in this study is from pre-aged washcoated cordierite GPF monoliths, provided by Johnson Matthey (JM). These samples underwent accelerated aging to simulate the aging process of GPFs during their operational lifetime in an exhaust system. The aging process loaded the GPFs with ash. A modified furnace burner, fueled by propane and ignited by spark plugs,

was used. The burner's flame was directed into a combustion chamber where lubricant oil (zinc dialkyldithiophosphate (ZDDP) with calcium additive) was injected. The burned oil released ash into the exhaust stream. The aging process followed a rich-lean cycle with a temperature ramp-up to 950°C at a rate of 5°C per minute, followed by a 16-hour hold at that temperature. The gas flow parameters were adjusted during the process, see section 3.3.1. The samples used in this experiment had a 20 g/l ash loading and were all coated GPFs.

The ash was removed from these pre-aged samples for imaging. In order to remove the ash an inlet channel section is cut from the monolith and one wall of the channel is removed with a sharp scalpel, exposing the ash deposited in the channel. During the removal of the wall, damage to the washcoat and cordierite occurs, this can lead to fragments of washcoat and cordierite in the sampled ash. Ash from the exposed channel is then carefully and gently picked up on a tip of a pair of tweezers. The ash was then deposited onto conductive SiN TEM membranes. An SEM secondary electron image of an ex-situ ash agglomerate on a SiN membrane is shown in figure 6.2. Alternatively, a wooden pick with a small amount dried epoxy on the tip was used to pick up ash from the exposed channel so that the ash settled on the head of the pick. The wooden pick was preferred to a metallic pin to prevent fluorescence from the pin head obscuring the XRF peaks of metallic elements of interest in the sample. By removing the ash from the GPF channel there is a risk of damaging the ash. Care is taken to make sure the ash is disturbed as little as possible as it is transferred to the TEM membrane or wooden pick. We believe this sample preparation method is necessary for nano-CT compared to literature methods were large amounts of ash is coarsely removed from the monolith. For example, ash is blown out of the monolith by removing the plugs at the bottom of the channels and then collected (McGeehan et al., 2005; McGeehan et al., 2009; Konstandopoulos et al., 2000) or gently shaken out of the monolith (Merkel, Cutler, and Warren, 2001).

For imaging a monochromatic 9.7 keV beam was developed by the I13-1 beamline at Diamond Light Source. We use different scan parameters for the different sample designs (described in section 3.3) resulting in different pixel sizes. This was partly due to the high aspect ratio of the membrane sample limiting the number of angles

TABLE 6.1: Correlated XPT and XRF-CT Imaging parameters. For full details of imaging parameters see sections 3.3.4 - 3.3.5.

	Beam Energy	**Number of X Step**	**Number of Y Step**	**Step Distance**	**Number of Angles**	**Angular Range**	**Reconst -ruction**	**Pixel Size**
XPT of Wooden Pick Mounted Sample	9.7 KeV	100	50	0.5 μm	500	180°	FBP	45.3 nm
XPT of SiN Membrane Sample	9.7 KeV	100	55	0.25 μm	500	146°	SART	22.6 nm
XRF-CT of Wooden Pick Mounted Sample	9.7 KeV	100	40	0.5 μm	70	180°	SART	0.5 μm
XRF-CT of SiN membrane Sample	9.7 KeV	100	55	0.25 μm	70	146°	SART	0.25 μm

from which acquisition was possible. Imaging parameters for different samples are shown in Table 6.1.

After acquisition the XPT images were smoothed with a NLM filter. We also performed SEM and SEM EDX on the membrane sample studied during the beamtime, see section 3.3.6. We used the JEOL JSM-6610LV described in section 2.4. FIB SEM serial sectioning of a comparable resin infiltrated and ash loaded GPF sample was performed on a a ZEISS Crossbeam 550 microscope and reconstructed with the ATLAS 5 software (*by Dr Gareth Hatton of Johnson Matthey plc.*) and then smoothed with a NLM filter.

6.2 Results

6.2.1 Chemical Speciation of Ash

In figure 6.3.a,c, from FIB SEM serial sectioning, and figure 6.3.b,d, from XPT, we can see how both techniques have resolved similar structures in the ash agglomerates. In both cases we observe large spherical particles which include internal porosity. At lower magnification in figure 6.2, a SEM secondary electron image, and figure 6.4.a, an XPT tomogram volume rendering, we observe two different particle morphologies. There are the large spherical porous particles and smaller particles that form a fine dendritic structure around the larger particles.

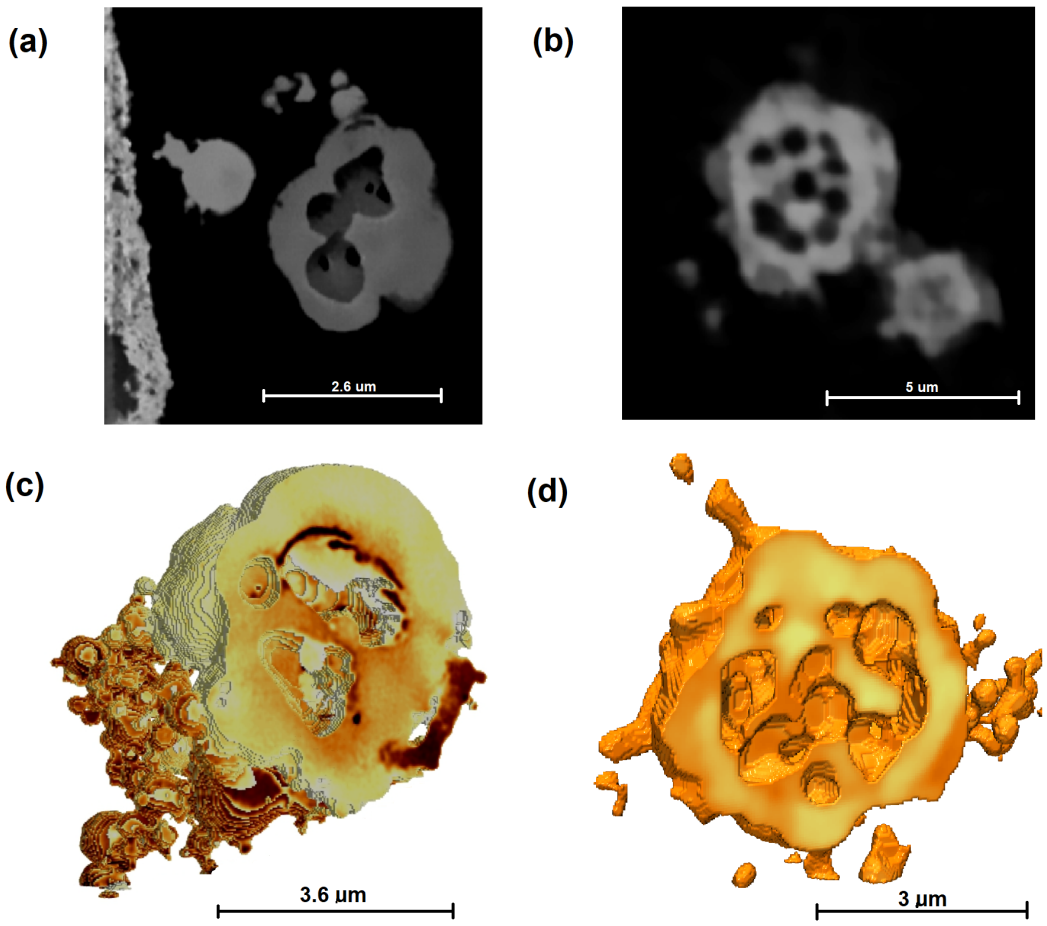

FIGURE 6.3: Comparison of FIB SEM and XPT of ash primary particles after NLM smoothing; (a) a FIB SEM slice, (b) an XPT slice, (c) a FIB SEM volume rendering, (d) an XPT volume rendering

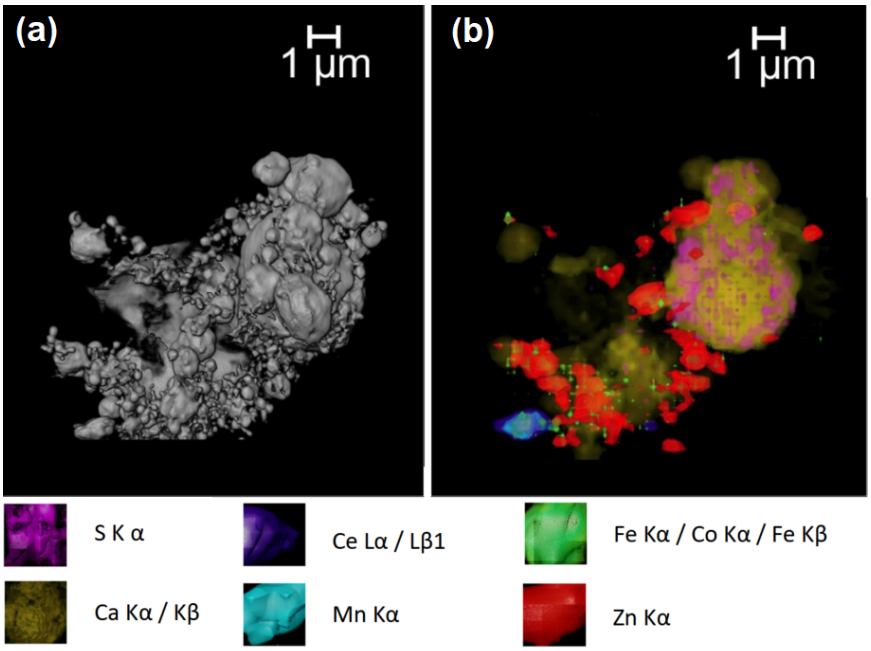

FIGURE 6.4: Shows (a) an XPT 3D rendering of an ash agglomerate, (b) XRF-CT 3D rendering of the same agglomerate, where; S Kα is rendered magenta, Ce Lα/Lβ1 is rendered purple, Fe Kα/Co Kα/Fe Kβ is rendered green, Ca Kα/Kβ is rendered yellow, Mn Kα is rendered turquoise and Zn Kα is rendered in red.

Figure 6.6 shows the spectra obtained from four different regions centered on ash agglomerates obtained with XRF and SEM EDX. By matching the peaks in the spectra to characteristic x-ray energies we can then create maps of elemental composition. In figure 6.4.a we show a 3D XPT rendering of the agglomerate and in figure 6.4.b we show the correlated 3D XRF-CT map. Similarly, in figure 6.5, we have correlated 2D XPT and XRF-CT images. By comparing the correlated images we can see how different particle morphologies in the XPT correlate with characteristic x-rays detected with XRF-CT. We find that the large particles described above correlate with the Ca Kα/Kβ signal (rendered in yellow). We also see that S Kα signal clusters around these large particles, this is particularly visible in figure 6.4.b where the sulphur signal rendered in magenta is around the large particle on the right of the image. This is corroborated with the SEM EDX shown in figure 6.7.b,c. Here the Ca Kα/Kβ map (yellow) and the S Kα map (magenta) show a positive correlation. Furthermore by comparing the position of the signal in the map to the SEI image of the agglomerate

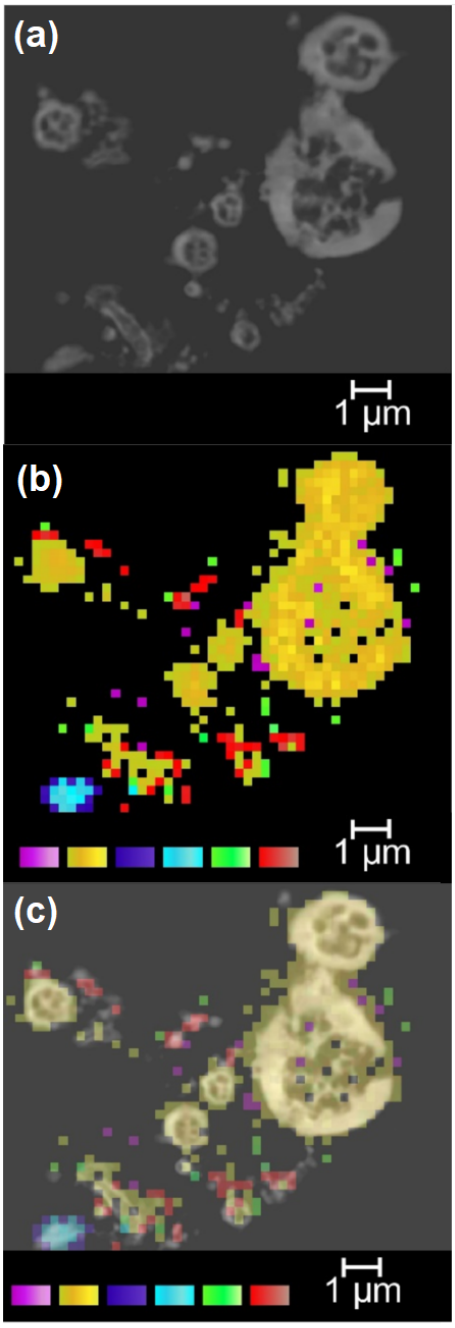

FIGURE 6.5: Shows (a) a 2D slice through XPT data showing the structure of an ash agglomerate and the internal structure of ash particles, (b) a 2D slice through the XRF-CT data, (c) the XRF-CT data overlayed onto the XPT data. Where; S Kα is rendered magenta, Ce Lα/Lβ1 is rendered purple, Fe Kα/Co Kα/Fe Kβ is rendered green, Ca Kα/Kβ is rendered yellow, Mn Kα is rendered turquoise and Zn Kα is rendered in red.

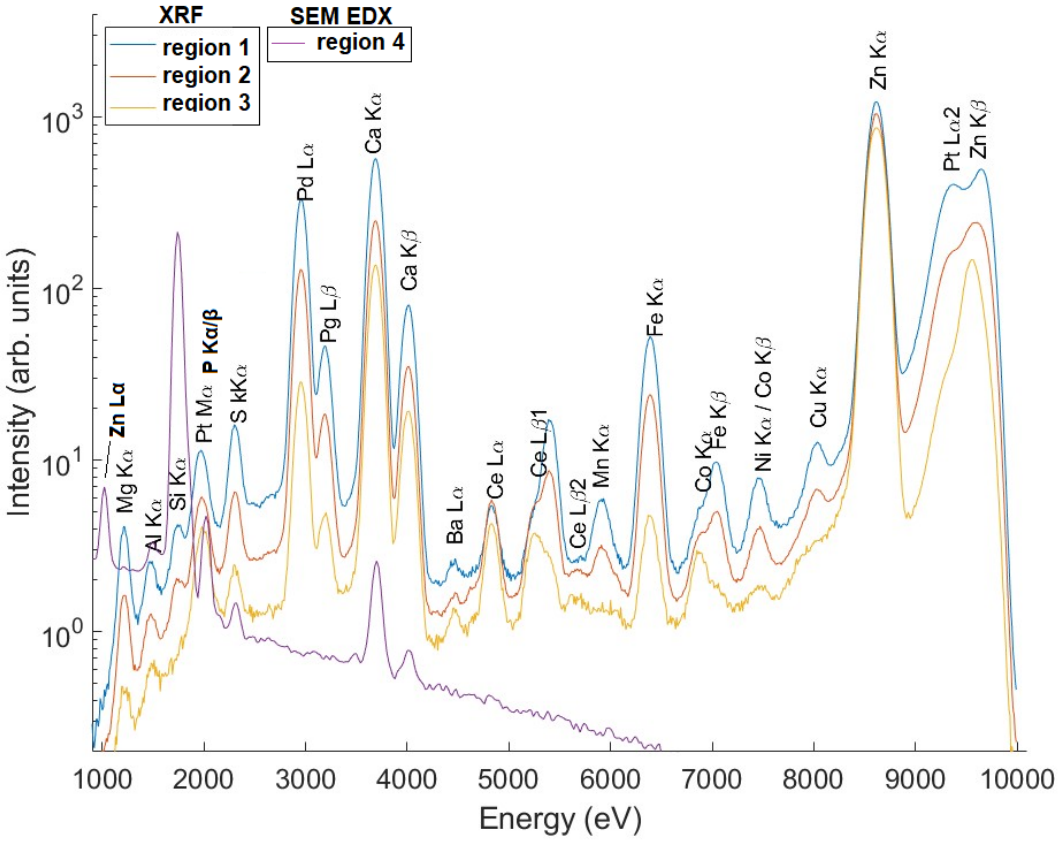

FIGURE 6.6: XRF and SEM EDX spectrum from 4 different regions centered on ash agglomerates. Regions 1,2,4 are membrane samples. Region 3 was ash mounted on the head of a pick. All ash was removed from a catalyst washcoated GPF channel, hence the Pt, Pd, & Mn peaks that are not typically associated with ash. XRF spectrum were integrated from all projections and locations in the fluorescence tomography scans. Similarly the SEM EDX spectrum is integrated from the EDX map presented in figure 6.7.

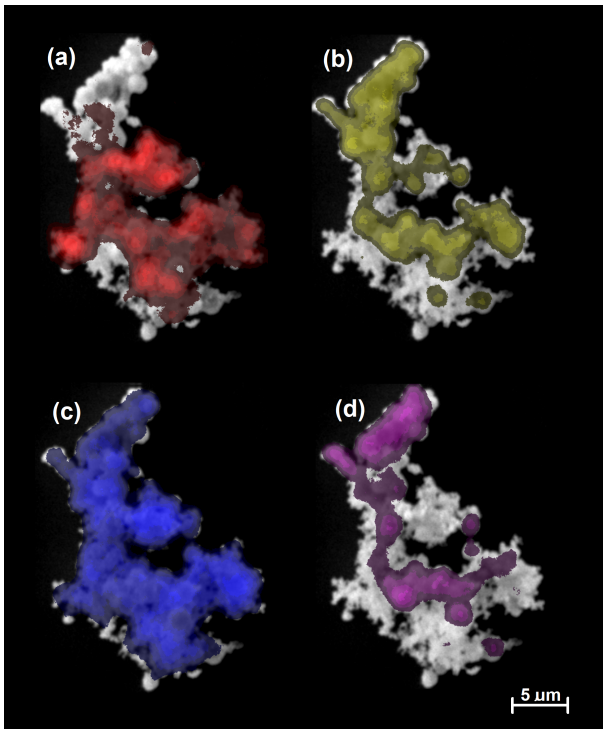

FIGURE 6.7: SEM SEI images of the same ash agglomerate from figure 6.2 overlayed with SEM EDX maps; (a) with the EDX map for Zn Lα overlayed in red, (b) Ca Kα/Kβ in yellow, (c) P Kα in blue, and (d) S Kα in magenta.

(figure 6.2), we see that they correlate with the position of the large particles. However, we observe that some of the large particles at the bottom of the agglomerate are not in the Ca Kα/Kβ or S Kα maps. This is because the sample is not ideal for EDX due to the height of the agglomerate, as a result we have north - south shadowing that blocks signal from the bottom of the image.

The smaller dendritic particles predominantly correlate with the Zn Kα signal rendered in red in figure 6.4.b. Again this is in agreement with the SEM EDX, see figure 6.7.a. Here we see that the Zn Kα EDX map is most intense for these smaller particles away from the large spherical Ca particles. The XRF-CT data also shows that some of the small particles correlate with Fe Kα/Kβ/Co Kα peaks, rendered in green. Finally, the XRF CT data resolves a particle (at the bottom left of figure 6.4.a,b) which correlates with Ce Lα/Lβ1 and Mn Kα peaks, rendered in purple and turquoise. From this XRF signal we can deduce that this particle is not an ash particle but is from the GPF washcoat. Similarly, the Pt and Pd peaks observable in figure 6.6 are associated

with this washcoat particle. These washcoat particles are present in the ash agglomerate as a results of damaging the washcoat when cutting open the coated GPF to remove the ash.

These findings are in agreement with the literature on the chemical speciation of automotive ash, as discussed in section 2.6.3 (see figure 2.24). Such literature has traced the origins of the the elemental species in automotive ash (Wang et al., 2020; Morcfos, Ayyappan, and Harris, 2011). The Zn, Ca species come from the burning of zinc dialkyldithiophosphate (ZDDP) lubricant oil, in which Ca is a common additive as a detergent. From literature studies of ash we can assume these zinc particles are zinc phosphates, such as $Zn_3(PO_4)_2$. Similarly we assume that the Ca particles are predominantly formed of $CaSO_4$. The XRF-CT in this work does not resolve any P peaks in the samples, which are introduced by burning ZDDP lubricant oil, however the SEM EDX does resolve the P Kα peak. Finally, the Fe Kα/Kβ/Co Kα peaks in the XRF-CT should be assumed to be from Fe nanoparticles that form due to wear from upstream components.

6.2.2 Physical Properties of Ash

Moving forward with the analysis we will investigate the physical characteristics of ash obtained from analysing the 3D XPT data. As shown in figure 6.3 the XPT and FIB SEM serial sectioning resolve similar features in ash. The FIB SEM is able to achieve higher spatial resolution, however because the resin does not penetrate the interior pores of the ash particles, quantification of this porosity can be challenging. This is because signal from the background of the pore is detected, therefore including out of plane information, thereby introducing artefacts into 3D reconstructions from serial FIB SEM. However, such artefacts are unlikely to be insurmountable.

In order to quantify physical characteristics of the agglomerate and particles within we segment the XPT data into background/pores and particles segments. For this analysis we are using the pick mounted sample that was reconstructed with FBP. The reconstructed data was smoothed with a 2D (z-slice wise) NLM algorithm. Once smoothed the data was then histogram matched, such that the histograms fell within the same range across the entire dataset. This was achieved by matching each slices

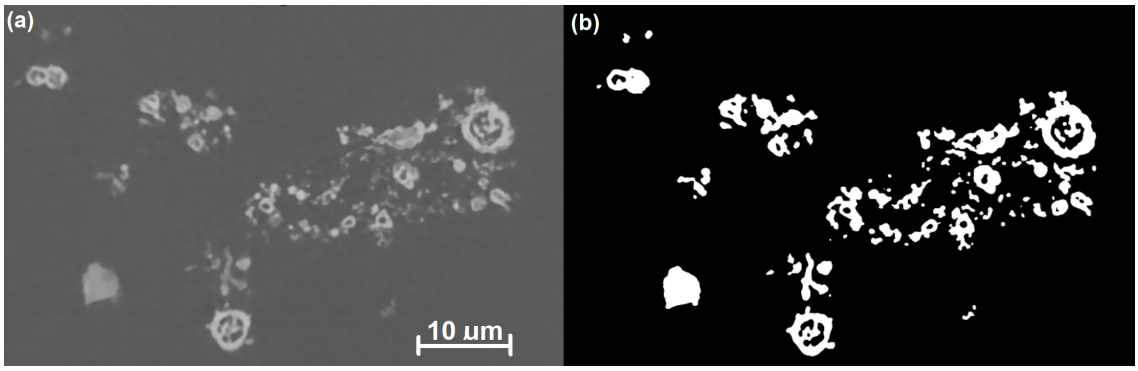

FIGURE 6.8: Comparison of the grayscale and segmented images; (a) grayscale slice XPT slice of the ash agglomerate, (b) the same slice after segmentation

peak intensity (background) to the global average peak intensity. A challenge with segmenting this data set was that the small dendritic particles had relatively low pixel values compared to the large spherical particles, see figure 6.8.a. By selecting a global threshold value that picked these small particles we would also erroneously pick the internal porosity of the large particles. In order to achieve a segmentation that picked the low intensity particles and preserved internal porosity of the large particles we used the following method; (1) We select a global threshold (volume > 110) that includes the low pixel value particles, (2) We select a second threshold (volume > 140) that preserves the internal porosity of the large particles but misses the low pixel value particles, (3) we use the porespy 'fill blind pores' function to calculate a mask of the internal pores from the second thresholded image, (4) we then mask out the internal pores in the first thresholded image so that low intensity particles are included and internal porosity is preserved. The result of this segmentation is shown in figure 6.8.

We can now calculate characteristics of interest for the ash agglomerates from this segmentation, such as; external porosity, internal porosity and packing density. In order to calculate the external porosity and packing density we first have to define a bounding volume for the agglomerate. This is because the agglomerate only fills a fraction of the volume of the image, therefore calculating over the entire image would result in a massively over estimated porosity and underestimated packing density. We define two different bounding volumes. This was because we notice

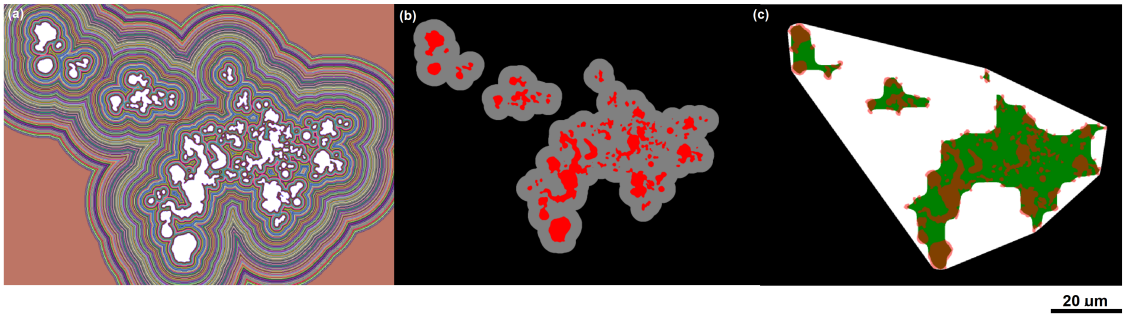

FIGURE 6.9: Ash bounding volumes; (a) the distance transform used to calculate the bounding volume of the densely packed clusters (in a XPT slice), each colour band represents a different distance from the nearest particle and white represents the particles (with internal porosity filled), (b) the bounding volume in gray is the thresholded distance map before the erosion operation and the particles (with internal porosity filled) is in red, (c) the final bounding volumes where the white volume is the bounding volume calculated by the convex hull method, the green volume is the bounding volume calculated from the distance map and defines the densely packed region of ash, and the ash particles are shown in red.

that the porosity is not homogeneous throughout the sample, instead it is characterised by clusters of high packing density separated by voids (a volume rendering of the entire field of view is shown in figure 6.10). The first is a bounding volume for the densely packed regions of ash, and can be used to calculate the porosity within clusters. This bounding volume is shown in green in figure 6.9.c. This was calculated via a distance transform from the particles segmentation image as shown in figure 6.9.a. We then threshold this distance transform (volume < 50) as shown in gray in 6.9.b. This was then finally eroded by a disk of diameter 50 px to create the bounding volume. As shown in figure 6.9.c, in green, the volume includes only the regions of the image where the ash is densely packed inside clusters such that we are a calculating the porosity pertaining to the space between the close packed particles. The second bounding volume was calculated via the convex hull method. This volume is shown in white in figure 6.9.c. This volume bounds the entire ash sample and from it we can calculate the porosity of the entire sample, including the voids between these densely packed clusters.

The external porosity is calculated by the bounding volume minus the filled particles volume divided by the bounding volume. We calculate that the external porosity is

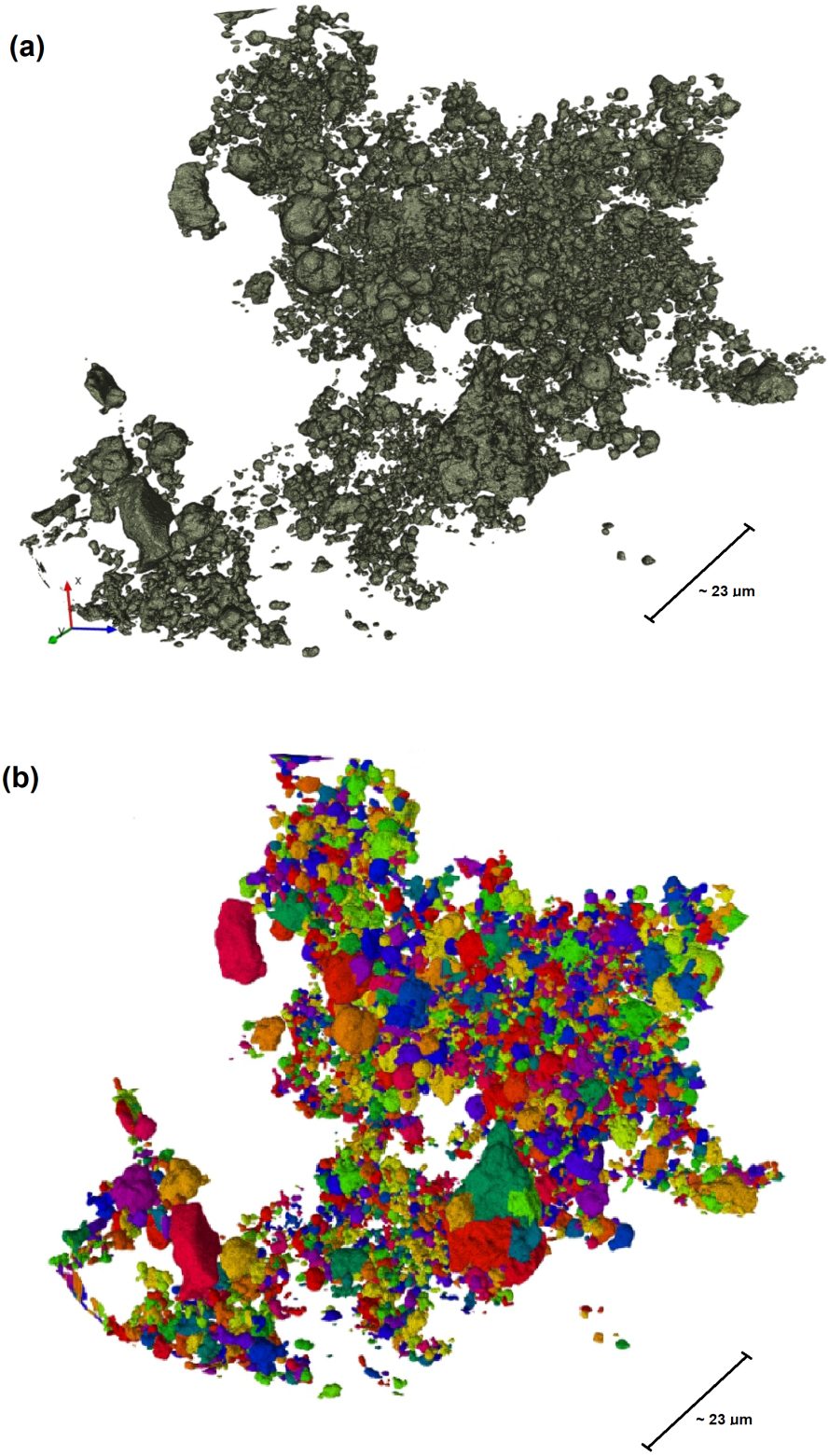

FIGURE 6.10: (a) Volume rendering of ash showing the entire field of view, (b) volume rendering showing particle separation

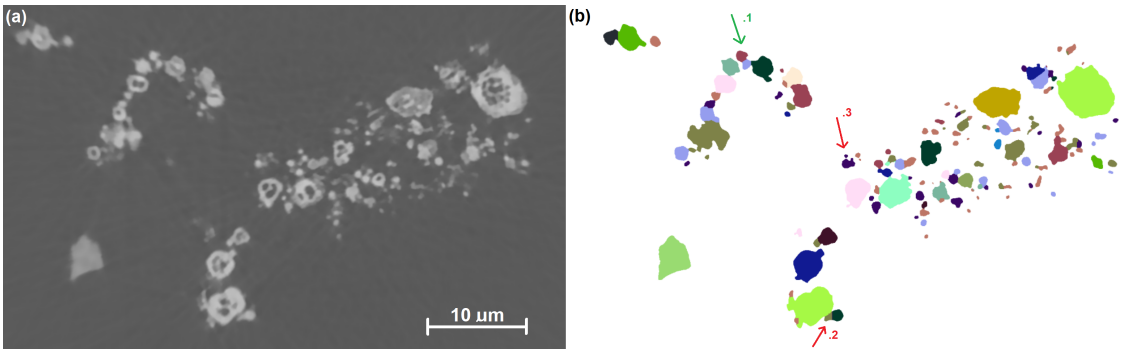

FIGURE 6.11: Particle separation; (a) grayscale XPT slice of the ash agglomerate, (b) the same slice with the particles segmented and separated such that each particle has a unique pixel value. Arrow .1 shows an example of good particle separation, whilst arrows .2 & .3 show erroneous separation.

57% (2.s.f) in the dense packed clusters (calculated from the bounding volume defined by the distance transform method above) and 88% (2.s.f) in the whole sample (bound by the convex hull).

Calculating the packing density requires separating the particles from one another using instance segmentation via a watershed algorithm. We use the SNOW algorithm. This is shown in figure 6.11. By separating all the particles we can count all the particles within the bounding volume in order to calculate the packing density. We find the segmentation in figure 6.11 acceptable, however it does contain errors. The arrow.1 (green) in figure 6.11 shows a series of particles that have been well segmented, whilst the the red arrows show erroneous segmentation. Arrow.2 shows a large non-spherical particle that is erroneously separated into two regions. Whilst arrow.3 shows two small spherical particles that have failed to be separated. When applying this segmentation we have a trade off between these two errors. We found when selecting the radius of the maximum filter kernel choosing a larger radius will reduce errors like arrow .2 but increase errors like arrow .3. By counting the number of regions in the segmented image and dividing by the volume of the bounding region we calculated the packing density to be 0.27 μm^{-3} (2.s.f) in the densely packed clusters and 0.061 μm^{-3} (2.s.f) in the whole sample volume.

From the separated particles segmentation we can also plot the particle size distribution as shown in figure 6.12. In figure 6.12.a we plot the number distribution (counts

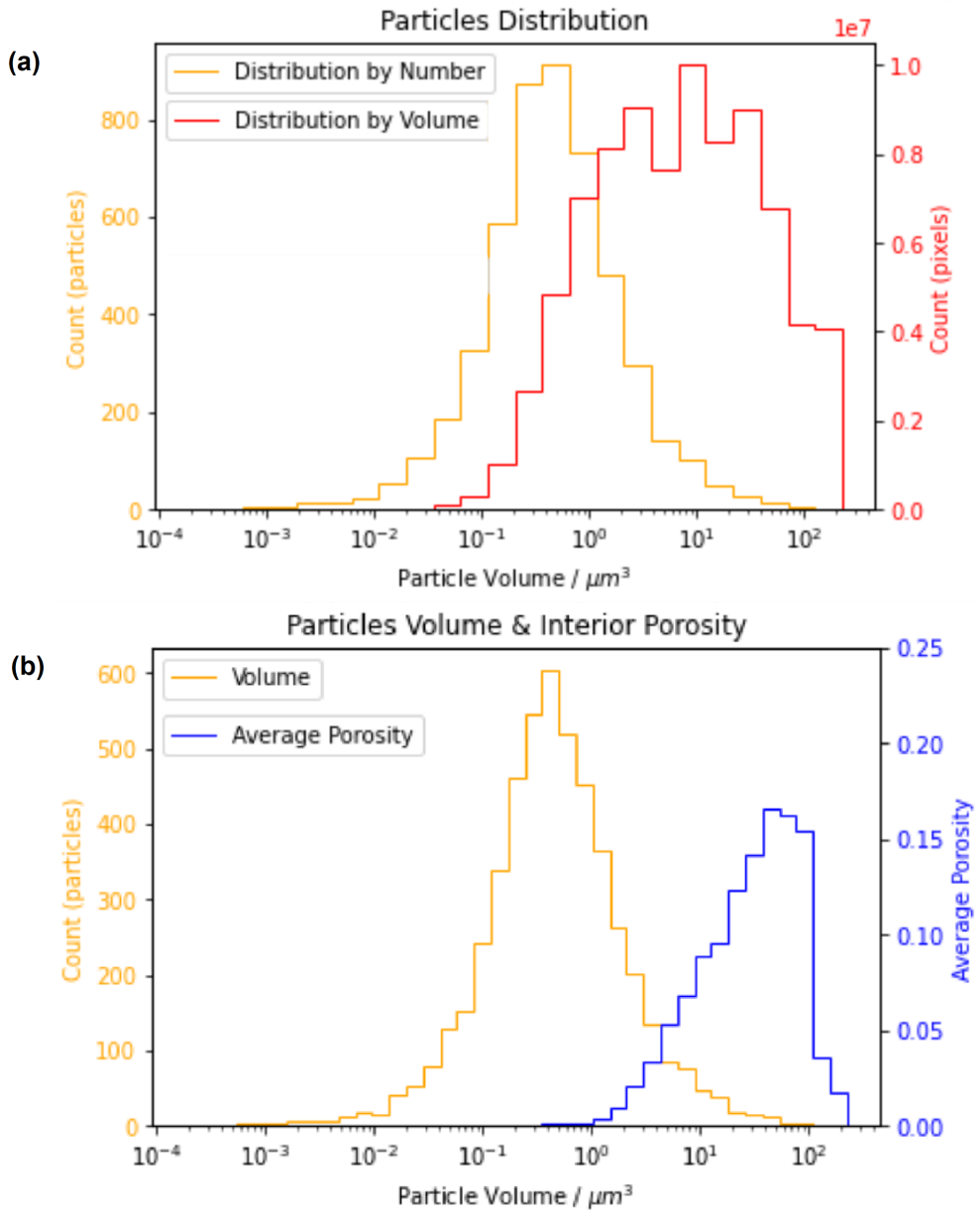

FIGURE 6.12: (a) A comparison of the particle distribution by number (of particles) in orange and the particle distribution by volume (calculated by a pixel-wise count) in red. (b) The particles volume distribution in the ash sample by number (orange) and the average porosity for particles at each particle size bin (blue)

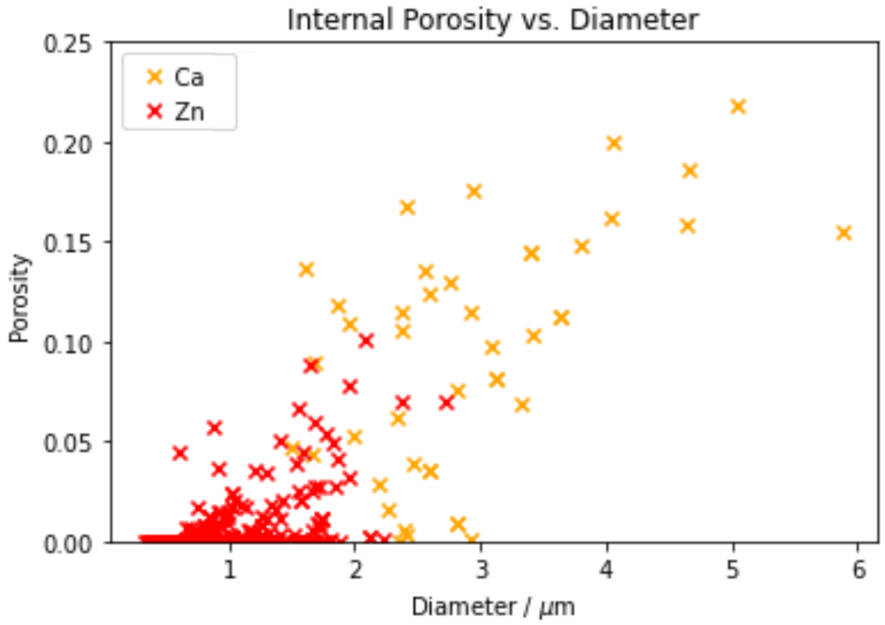

FIGURE 6.13: A scatter plot showing the relationship between porosity and diameter for separated particles. The Ca particles are plotted in orange and the Zn in red.

TABLE 6.2: Physical Characteristics of Ash: *External porosity* and *packing density* are calculated from two different bounding volumes, the 'loose pack' bounding volume considers the voids between close packed regions which are exclusively considered in the 'close pack' bounding volume. *Internal porosity* is the internal porosity of the Ca, Zn or All Particles as a semented volume, whilst the *mean internal porosity* is the mean porosity calculated from a set of individual particles. Mode and mean particle diameters and volumes are calculated on a *by number* basis (counting particles) or *by volume* basis (counting pixels).

Table 6.2: Physical Characteristics of Ash		
	Loose Pack	**Close Pack**
External Porosity	88%	57%
Packing Density	0.061 μm^{-3}	0.27 μm^{-3}
	Ca	**Zn**
Internal Porosity (*All Particles = 5.3%*)	12%	1.5%
Mean Internal Porosity (*All Particles = 0.46%*)	8.2%	0.54%
Mean Diameter	2.76μm	1.22μm
	Min	**Max**
Diameter Distribution	0.10 μm	7.6 μm
Volume Distribution	1.3×10^{-3} μm^3	228 μm^3
	Mode	**Mean**
Particle Diameter by Volume	1.2 μm	2.8 μm
Particle Diameter by Number	0.35 μm	1.1 μm
Particle Volume by Volume	6.9 μm^3	26 μm^3
Particle Volume by Number	0.35 μm^3	1.55 μm^3

by particle) in orange. By number the mode volume is at 0.35 μm^3 (2.s.f.) and the mode diameter is at 0.35 μm (2.s.f.). We plot the volume distribution (counts by pixel) in red. By volume the mode volume is at 6.9 μm^3 (2.s.f.) and the mode diameter is at 1.2 μm (2.s.f.). Figure 6.12.b shows that the particles that have the highest porosity are the largest particles, we calculated that the particles that contribute the most internal porosity are those with a volume of 30 μm^3 (2.s.f.).

This is corroborated by the plot in figure 6.13. This scatter plot shows that larger particles tend to have higher internal porosity. Furthermore by overlaying the XRF-CT data onto the separated particles segmentation we show that these larger porous particles are Ca particles, whilst the smaller particles are Zn, confirming what we suspected from our qualitative evaluation of the correlated XPT and XRF-CT images. A visualisation of this internal porosity in two large ash particles is shown in figure 6.14. The separation of different species was achieved by applying a threshold to the XRF-CT to segment the images into Ca or Zn segments. This was a high threshold that missed some particles with low signal, however the particles that are selected by this method can be identified as Ca or Zn with a higher degree of certainty. These segmentations were then registered onto the XPT data so that we could identify, from the separated particles segmentation, particles by their speciation. These particles, were then plotted as Ca (orange) and Zn (red) as shown in figure 6.13. Finally, we calculate that the average particle diameter for the Ca is 2.76 μm and the average porosity is 8.2%, whilst the zinc particles are 1.22 μm and 0.54% respectively. The physical characteristics of ash calculated by this method are summarised in table 6.2.

6.2.3 Discussion

Particle Size Distribution:

The particle size and porosity of ash are characteristics of interest because they have been shown to be closely related to ash permeability, filtration efficiency enhancement, and the interaction of ash with the catalyst coating (Wang et al., 2020). Various studies have measured the particle size distribution of ash using different methods (see table 6.3). However, the particle size distributions given range from 0.1 - 0.5

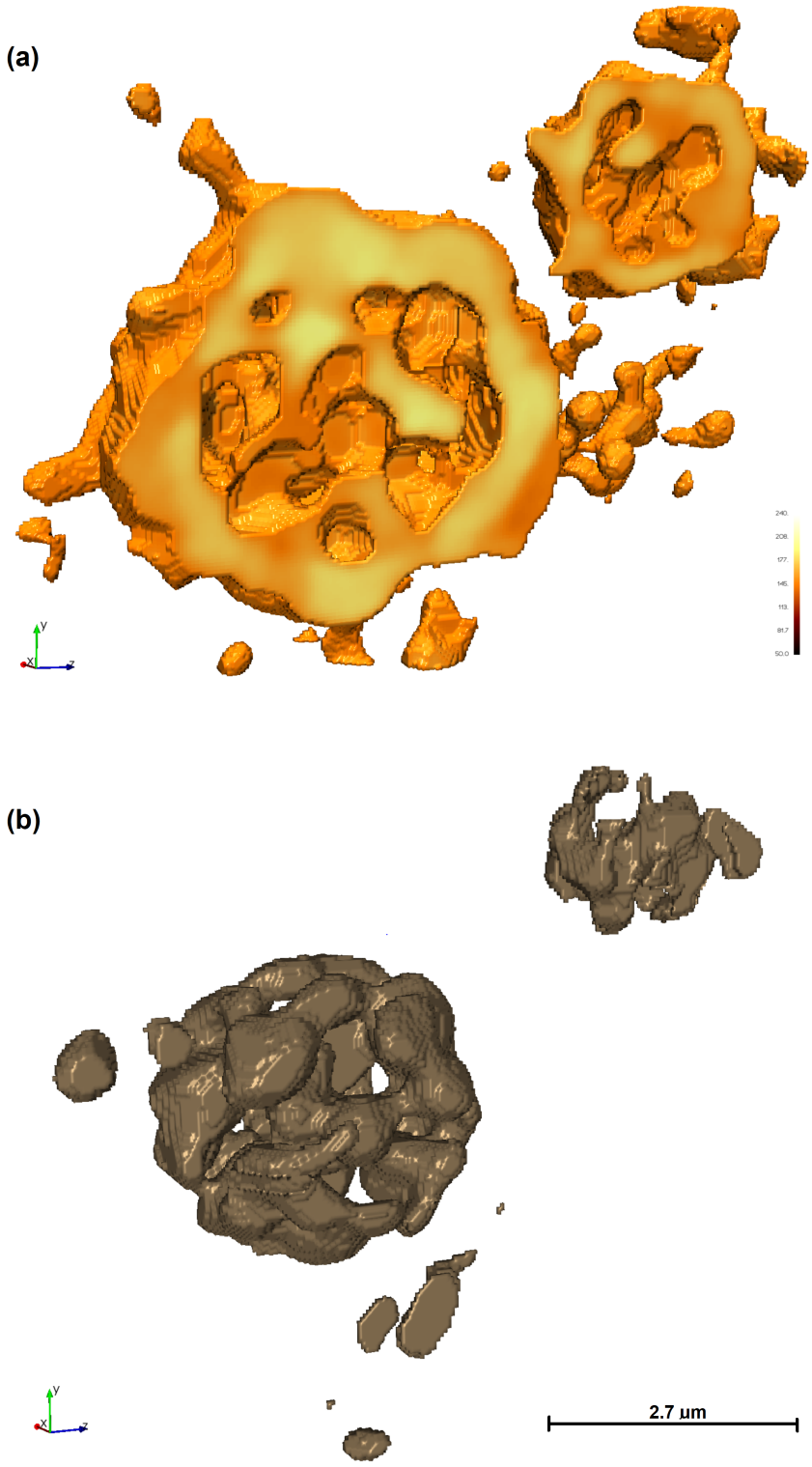

FIGURE 6.14: Volume rendering showing the structure of ash particles, (a) rendering two large Ca particles sliced so that the internal porosity is visible, (b) rendering the internal pores of the same ash particles (not sliced).

μm (Merkel, Cutler, and Warren, 2001), to 2.4 - 37.6 μm (Young et al., 2004). This lack of consensus is largely due to different definitions of 'particle' and the range of methods and resolutions used to measure the particle size distribution.

McGeehan et al., 2005, and Chiou, 2013, use a light scattering technique. The method works by suspending the particles in a solution and then passing the suspension through a light source as a fine dilute stream of particles. The degree of light obscuration and scattering is then used to determine the size of the particles. When computing diameters from this approach the particles are assumed to be spheres (Chiou, 2013). Both Chiou and McGeehan show a single peak for the particle size distribution by number but a bi-modal distribution by volume, although, this bi-modal peak is more obscured in Chiou, 2013. McGeehan et al., 2005, compare this data to SEM micrographs and conclude that the bi-modal peak with larger particles (averaging 20 μm) is due to this technique measuring large agglomerations of many sub-micron particles. Zarvalis, Lorentzou, and Konstandopoulos, 2009, use an aerosol sizer to measure the aerodynamic diameter distribution of aerosolised ash. Although aerodynamic diameter is useful when considering transport phenomena, a draw back of this technique is that it is not a direct measure of spatial diameter. Finally, the most common technique according to Wang et al., 2020, is image analysis of SEM micrographs. SEM is useful for capturing the detailed geometry of particles, however quantifying particle size distribution of ash particles can be a challenge. In order for accurate particle sizing with SEM a sample should ideally have a relatively tight particle size distribution and the particles should be deposited in a single flat layer. However, ash particles sizes range from < 100 nm to 10's of μm, furthermore, due to the propensity for ash particles to sinter together in the high temperatures of the exhaust during regeneration, ash tends to form branch-like, non-spherical, 3D (not flat) morphologies. The XPT method for determining particle size distribution has many advantages. Similarly to SEM, as an image based method XPT is able to capture the detailed geometry of the sample at comparable resolutions, however XPT is able to do so in 3D. This allows XPT to capture particle volumes as well as particle diameters. This is inherently advantageous for irregularly shaped objects like ash which may contain significant out of plane features missed in 2D.

TABLE 6.3: Literature Values for ash porosity, size (mean or distribution) and permeability. Source: Adapted from Wang et al., 2020.

Source	**Porosity**	**Particle Size (μm)**	**Permeability (m^2)**	**Method**
Konstandopoulos et al., 2000	-	0.5-10	2.8-7.4×10^{-14}	**Particle Size:** Light Scattering Sizing, Aerosol Sizing, SEM. **Permeability:** Empirical Model
Merkel, Cutler, and Warren, 2001	83%	0.1-0.5	-	**Porosity:** Estimation based on gravimetric measurement and assumed density & fraction of ash species. **Particle Size:** SEM
Young et al., 2004	85%	2.4–37.6	5×10^{-12}	-
McGeehan et al., 2005; McGeehan et al., 2009	90%	0.1-10	-	**Porosity:** Estimation based on gravimetric measurement and assumed density & fraction of ash species. **Particle Size:** Light Scattering Sizing, SEM.
Sonntag and Eilts, 2016	-	0.3-30	-	**Particle Size:** Aerosol Sizing (SMPS)
Zarvalis, Lorentzou, and Konstandopoulos, 2009	-	0.5-10	1.8-2.3×10^{-14}	**Particle Size:** Light Scattering Sizing, Aerosol Sizing, SEM. **Permeability:** Empirical Model
Chiou, 2013	91-95%	0.97 - 1.39 (Mean Diameter)	-	**Pososity:** SEM. **Particle Size:** Light Scattering Sizing.
Sappok et al., 2009	90-95%	-	2.8-7.7×10^{-14}	**Porosity:** Estimation based on gravimetric measurement and assumed density & fraction of ash species. **Permeability:** Empirical Model.
Our Work	89%	0.1-7.6	-	Nano-CT (XPT)

In this work we report a particle size distribution (by number) of 0.1 - 7.6 μm with a mode of 0.35 μm. This is generally aligned with literature which broadly reports that the majority of particles are less than 1 μm with a long tail of fewer very large particles, see table 6.3 (Wang et al., 2020). McGeehan et al., 2005, report on a bimodal distribution (by volume) using a laser light scattering technique. The second larger peak constituted particles that were agglomerates of sub-micron particles (McGeehan et al., 2005). Other than this bi-modal peak, our results are in good agreement. McGeehan et al., 2005, report that the mode particle size by number is around 0.4 μm. The range of particles sizes reported was 0.1 - > 10 μm. Whilst one could argue that not considering the agglomerates as particles is more consistent when considering the microstructure of ash, it is clear that the bimodal distribution is representative of the natural structure of ash on larger length scales. This is to say, both approaches have merits.

Porosity:

We calculate the total porosity to be 89% from the 'loose pack' convex hull method. This is similar to the values from Chiou, 2013, McGeehan et al., 2005 and Sappok et al., 2009, see table 6.3. On the other hand the 'close pack' method is not well aligned with the literature values. We identify two methods in the literature for calculating porosity. Chiou, 2013, use SEM to image a cross section of an ash layer embedded in resin. From this they segment the image into ash and void in order to calculate porosity. Other studies estimate the porosity from the in-situ density of ash (measured gravimetrically), the intrinsic densities of the various compounds that constitute ash, and the measured ash composition from XRD (Merkel, Cutler, and Warren, 2001; McGeehan et al., 2005; Sappok et al., 2009).

External & Internal Porosity:

For the first time, we are able to separate the porosity of ash into external and internal porosity. This internal porosity is disconnected from the external porosity. Therefore the internal porosity should not be considered relevant porosity to ash permeability and filtration efficiency enhancement which are concerned with flow through the 'external porosity' of ash layers in filters. We calculate that the external porosity is 88% (2.s.f) in the whole sample (bound by the convex hull 'loose pack'). However,

the internal porosity of the particles was calculated to be 5.3%, thus the internal or disconnected porosity of the sample is just 0.6%. In a relatively porous ash layer including or excluding this porosity is unlikely to make a significant difference to calculations of permeability and will likely be within existing error. However, it is worth noting that as the porosity of the ash layers decreases, as it does during in-operando ageing, where many high temperature regenerations lead to denser ash layers (Wang et al., 2020), the inclusion of these pores may become more significant. For example, if we calculate the volume fraction for internal pores in the close pack region this comes out be 2.4%. Such a condition was observed in Sappok, Kamp, and Wong, 2012, where during heating from 650 °C to 1000 °C particle sizes grew by approximately one order of magnitude and the porosity decreased from 96% to < 40%. In such a scenario being able to discriminate between internal and external porosity may be critical.

Particle Size, Growth, & Internal Porosity:

We find that the internal porosity is not evenly distributed among the different kinds of particles. In figure 6.12 we show that the high volume particles have a higher internal porosity. By comparing the mean internal porosity (blue) in figure 6.12.b to both the particle volume distribution by number (orange) and volume (red), we can see this is the case. Furthermore in figure 6.13 we provide the chemical dimension with the correlated XRF-CT. Here we see that there is a clear trend for Ca particles being large and, as for the trend discussed above, more porous. In table 6.3 we state the mean porosity and diameter of the Ca and Zn species in the sample. This trend for the Ca particles may be indicative of their growth mechanism. We suggest that at high temperatures the calcium particles (predominantly $CaSO_4$) become malleable and trapped gas in the internal pores applies an outward pressure causing particle growth. This may explain the observed positive correlation between diameter and internal porosity, see figure 6.13. This aligns with literature which finds that, in general, with increasing temperature the primary ash particle sizes also increase (Sappok, Kamp, and Wong, 2012; Wang et al., 2020). This effect is important because this has been shown to increases the ash density, which in-turn decreases the ash (external) porosity and the total volume of larger ash structures. This phenomena

has been shown to greatly effect aged filter performance (Sappok, Kamp, and Wong, 2012; Ishizawa et al., 2009; Wang et al., 2020). We speculate that if this positive correlation between internal porosity and diameter holds during such a densification as observed by Sappok, Kamp, and Wong, 2012, that a significant proportion of the total porosity may be internal and therefore disconnected. This reiterates that in some scenarios discriminating between internal and external porosity may be critical, and also demonstrates how nano-CT and by extension XPT could be a useful technique for studying ash sintering during heating.

Other Considerations:

The use of XPT for characterisation of ash has many advantages beyond being able to calculate porosity, packing density, and particle size distribution from a single technique. Image analysis of XPT data can extract a range of other characteristics too, for example, sphericity, surface area and aspect ratios can all easily be extracted from the data on a particle by particle basis. Furthermore, the value of high quality 3D visualisations of microstructures should not be understated when it comes to improving qualitative understanding of the sample, for example see figures 6.4, 6.10, 6.14. In these visualisations we are able to resolve finer structures of different particle, such as large spherical Ca species and their internal porosity, as well as the smaller dendritic Zn species.

6.3 Summary & Outlook

This study presents the successful utilisation of nano-CT, specifically XPT and correlated XRF-CT, to achieve unprecedented resolution and quantification of structures within automotive ash in 3D. This marks the first time that such techniques have been applied to analyse and identify the chemistry-related structures of various ash particles observed in these XPT images. To validate these methods, FIB SEM serial sectioning, SEM, and SEM EDX were employed.

By implementing instance segmentation to distinguish particles in the XPT dataset, important characteristics were quantified, including particle size distribution, average particle sizes, and porosity. These results exhibited strong agreement with

values reported in existing literature obtained through alternative methods. By utilising the XRF-CT data, information regarding the variations in physical characteristics between Ca and Zn particles in the ash was obtained for the first time. This demonstrates the ability of this technique to discriminate between different species in the ash, something that previous literature studies has not been able to achieve in a quantitative fashion.

Furthermore, this study achieved the separation and quantification of internal and external porosity in ash, for the first time in literature. Previous methods relied on gravimetric measurements and theoretical ash species densities to calculate porosity, lacking the ability to differentiate between internal and external porosity. This information is particularly significant when calculating permeability, as only connected external porosity influences the permeability of the ash layer. Our findings revealed an internal porosity of 0.6% (total volume fraction) compared to 88% external porosity. Thus, we conclude, that in similar ash samples, the inclusion or exclusion of internal pores in permeability calculations is unlikely to significantly impact accuracy. However, in denser ash subjected to high temperatures, internal porosity may become more influential (Sappok, Kamp, and Wong, 2012; Wang et al., 2020).

Nano-CT, as demonstrated in this study, offers the ability to examine the intricate structures of automotive ash in three dimensions, with impressive pixel resolutions of 22.6 - 45.3 nm. Future research could explore the application of nano-CT, both in laboratory and synchrotron settings, to investigate how ash formed at different temperatures, and from different formulations, differ from one another ex-situ. This study establishes a workflow for quantitatively analysing physical properties derived from nano-CT data of ash, with the aim of encouraging other researchers in the field to adopt this technique. Finally, we suggest that in future work, with carefully designed sample configurations, it may be feasible to observe particle growth and sintering of ash removed from the filter on a primary particle scale, with sufficient resolution to identify changes in internal porosity, see section 7.1.

Chapter 7

Conclusion

Particulate filters remain an important topic for study. Currently, when measured by life expectancy loss, exposure to PM causes the greatest loss of human life globally; PM pollution reduces average life expectancy by 2.2 years, first-hand cigarette smoke by 1.9 years, alcohol use by 8 months, HIV/AIDS by 4 months, malaria by 3 months, and conflict and terrorism by 9 days (Lelieveld et al., 2020; Greenstone, Hasenkopf, and Lee, 2022). Although alternative powertrains will hopefully replace the ICE in the future and dramatically reduce urban air pollution, the phase in period is expected to take 15 - 20 years in developed countries due to barriers to entry (Olivetti et al., 2017; Berkeley, Jarvis, and Jones, 2018). As a stop gap, it is important to make sure that the current and next generation of vehicles on the road are clean, without sacrificing fuel efficiency.

In this project we developed X-ray microscopy methods for the study of particulate filters. Since filtration fundamentally deals with how volumes change with time (Tien and Brenner, 2013), time lapse XCT is a useful, yet novel, technique. In sections 3.1 & 3.2 we present methods that use time lapse XCT to study soot-like nano-aerosol filtration in particulate filters. The methods presented in these chapters required the development of a bespoke aerosol flow rig and data processing pipelines. The aerosol flow rig was designed for in-situ imaging as aerosol was flowed through operational particulate filter samples. In-line flow meters and manometers were installed. The flow rig, 3D printed sample holder, and filter sample successfully met design requirements of remaining operational whilst rotating for tomography and

minimising unnecessary beam attenuation. Data processing pipelines were developed to segment the data for quantification and post-processing. This was challenging due to the large size of some of the data sets and overlapping grey levels for some phases of interest, see section 3.2.5.

In chapter 4 we demonstrated that by using pink beam radiation at I13-2 it is possible to continuously image TiO2 nanopowder as it deposits in the pores of a filter over time. The spatial and temporal resolution was enough to resolve pore scale blocking events. This allowed us to observe the transition of the filter from deep bed filtration, through transition filtration, and into the cake filtration regime. By resolving deep bed filtration we were able to see how the porosity of the filter wall changed during the filtration and we were able to track deposit concentration with depth during the filtration, as shown in our paper (Jones et al., 2020). This was the first time that deep bed filtration had been imaged in 4D. In chapter 5 we present results from work that extended this method so that the entire length of a 3 cm long 'mini-channel' was imaged in 4D. This allowed deposit concentration profiles to be measured both into the filter wall, as in chapter 4, and also along the length of the particulate filter channel. From this we found that the deposit distribution for both samples created a 'U' shaped distribution where deposition had been favoured at the front and the back of filter. This is in good alignment with modelling literature that predicts this 'U' shape (Gong et al., 2018b; Lee and Lee, 2013; Hayashi and Kubo, 2008). Additionally, by separating the pores using an instance segmentation and labelling each pore with its diameter, we showed that a small number of large pores contained a significant proportion of the deposit.

Understanding how particles deposit in the filter during a filtration is important as deposits change the microstructure of the filter which effects filtration efficiency and pressure drop. High filtration efficiencies result in cleaner emission from the exhaust, however this often comes at the cost of higher pressure drops, which ultimately lower the fuel efficiency of the engine. When designing new particulate filters and catalyst coatings for filters it is useful to understand how changes in design effect performance. Manufacturers use models to lead design, for example simulating filtration through filters with different pore size distributions to determine

the most effective distribution (Yang and Strzelec, 2019), but also to test designs, for example simulating flow through an XCT volume to observe predicted filtration performance (Kočí et al., 2019). Prototypes are then tested on aerosol flow rigs to accurately determine filtration efficiency and backpressure characteristics. Prototypes are also rapidly aged and analysed post-mortem. This prototype testing and redesign cycle can often be a very time consuming part of product development, slowing the rate at which effective filters can get to market.

Time lapse XCT of filtration in particulate filters could improve this. Firstly, during prototype testing, the time lapse XCT method could be used to create a more data rich analysis of prototype performance. Hypothetically, this may lead to better inferences about device performance, thus requiring fewer redesign iterations during product development. Secondly, the time lapse XCT method could be used to validate models of filtration in particulate filters. Manufacturers can place higher confidence in such validated models. Again this can reduce the burden of prototype testing as manufacturers can rely more on testing and redesigning digital prototypes, a comparatively rapid process. This work has proven valuable to our industrial sponsors Johnson Matthey, who have since procured a SAG410/U machine and implemented these methods into their work.

In this project we also demonstrate the applicability of XPT and correlated XRF-CT to the study of automotive ash. This ash can effect the operation of filters in myriad ways (Lambert et al., 2017; Hua et al., 2018; Panchal et al., 2021), therefore understanding its structure is of importance (Wang et al., 2020). In chapter 6 we demonstrated how this method can resolve the fine structure of automotive lubricant oil ash. We resolved the internal porosity of ash, and quantified this internal porosity for the first time in the literature (as far as the author is aware). By overlaying the correlated XRF-CT maps onto the XPT we were able to infer the chemistry of individual ash particles. For example this allowed us to calculate that the internal porosity was 12% for Ca species and 1.5% for Zn species. Furthermore, by using an instance segmentation to separate primary particles we showed that there is a positive correlation between particle diameter and particle internal porosity. We

suggested that this is indicative of the particle growth mechanism at elevated temperatures. Growth mechanisms in ash are important as they could elucidate the mechanisms by which ash particles sinter together during high temperature events in the particulate filters during use. Sintered ash can effect filter performance as it can lower ash related pressure drop, but also block the catalyst coating and lead to problematic ash plugs (Wang et al., 2020). Due to XPT being a non-destructive imaging technique, future work may look to observe the sintering of ash particles with time resolved XPT, as discussed in section 7.1. Finally, we suggest that quantitative nano-CT methods, such as XPT, have been under utilised by researchers in this area. In chapter 6 we demonstrated a workflow for quantitatively analysing the physical properties derived from nano-CT data of ash, with the hope that other researchers will adopt this technique to study automotive ash.

In conclusion, this project has developed advanced X-ray microscopy experimental methods (time lapse XCT and XPT methods) and demonstrated how these can impact particulate filter research. Future work applying these techniques can now extend the methods demonstrated here to validate models of soot filtration and resolve ash sintering mechanisms, as discussed in the next section.

7.1 Future Work

Future work on time lapse XCT of filtration in particulate filters could improve the method with a view towards model validation. An important aspect of model validation is particle size distribution. In this work we used an off line Cambustion DMS500 aerodynamic particle sizer, see section 3.2.3. However, future versions of the method may want to install an in-line particle sizer, such as a scanning mobility particle sizer (SMPS), so that upstream and downstream aerosol particle size distribution and concentrations can be measured live as the experiment proceeds. This will allow the experimentalist to measure dynamic changes in filtration efficiency as the experiment proceeds. Additionally, an upstream filter can be installed into the flow rig, this can be used to remove large agglomerated particles from the aerosol and could be used to create a tight size distribution when using a fine graded filter. Future experiments may extend the scope to include multiple different flow rates

and particle size distributions in order to determine the effect on the sample filter performance and deposit distribution profiles.

Future work on XPT of ash structures could also be impactful. Due to the non destructive nature of the technique it would be possible to resolve the fine structure of the ash in 3D before and after being subjected to elevated temperatures in a furnace. A stop - start imaging method where the sample is imaged, then removed from the beamline to be heated in a furnace, and then re-imaged would likely be the simplest method. The key challenges here would be sample design because the ash would need to stay put between image acquisitions so that the same particles could be imaged after the heating cycle. Additionally, the scope of the experiment reported in chapter 6 could be simply extended to a range of other ash species. For example, ash from single additive lubricants (e.g. Ca, Zn) and other fully formulated oils (e.g. CJ4, ZDDP) could be studied and compared.

END

Blank Page.

Appendix A

Supplementary Information

A.1 Unsuccessful Ptychotomography Beamtime Projections

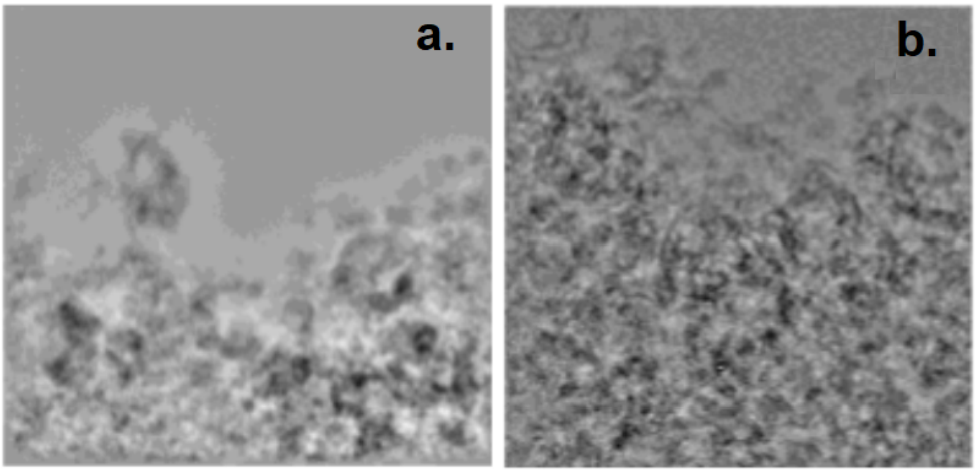

FIGURE A.1: (a,b) Grayscale ptychography projections from an unsuccessful XPT beamtime. The beamtime failed due to issues with the rotation stage and files saving improperly due to beamline faults. However, we were able improve our sample preparation for the next beamtime as a result of our time on beam.

A.2 Multiscale Time Resolved Microscopy of Aerosol Filtration in Ash Loaded GPFs

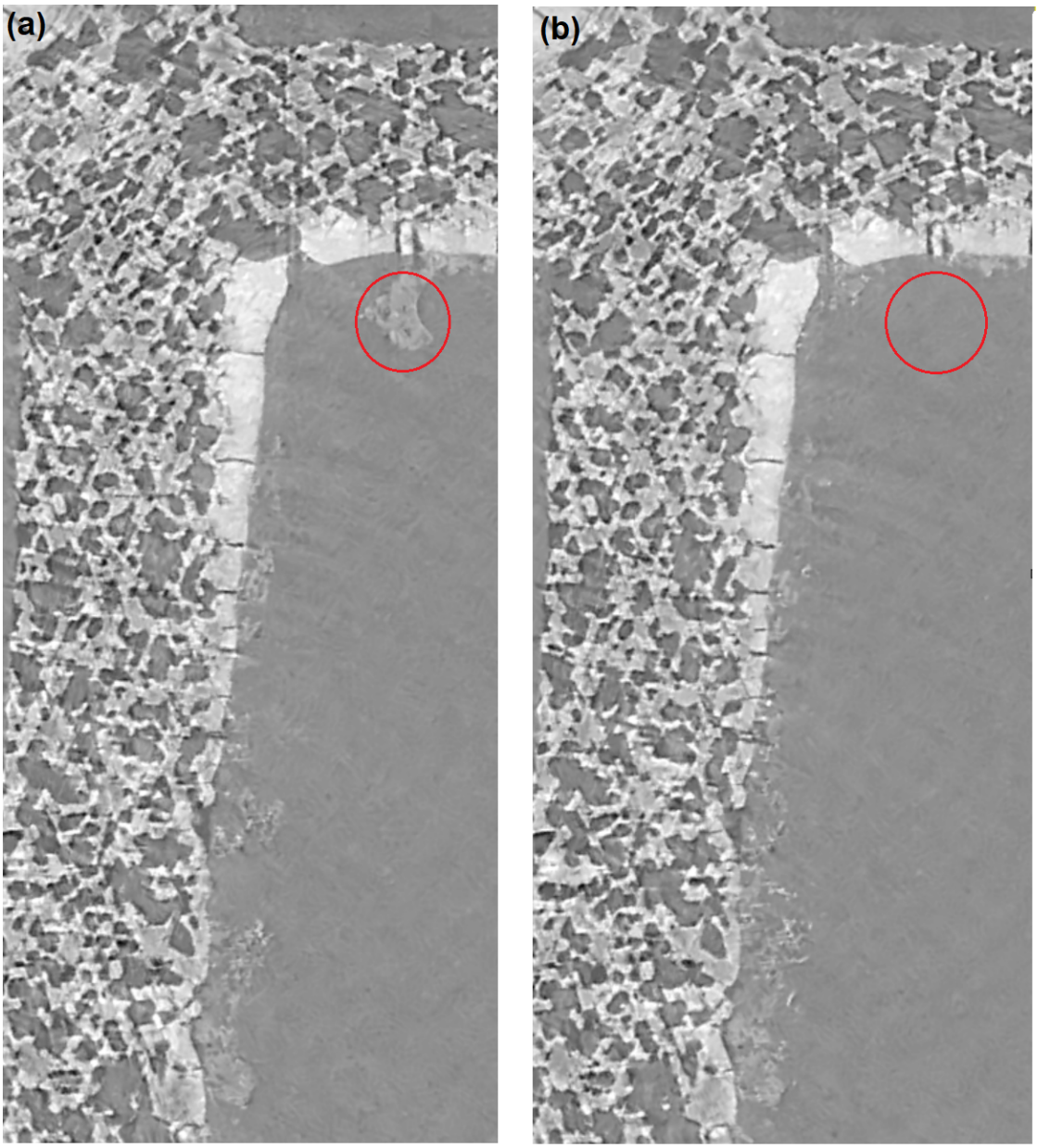

FIGURE A.2: ZNP deposition in pre-aged ash loaded samples. We were not able to separate the ash and ZNP deposits because of the lack of contrast between the phases and the movement of the ash layer during the experiment. (a) XCT slice showing the initial ash loading state after 0 s of ZNP loading, (b) XCT slice showing Ash and ZNP loading after 40 s of ZNP loading. Note that the large ash agglomerate indicated in red was re-entrained (moved) during the experiment.

A.3 Model Verification - Collaboration with University of Chemistry and Technology, Prague

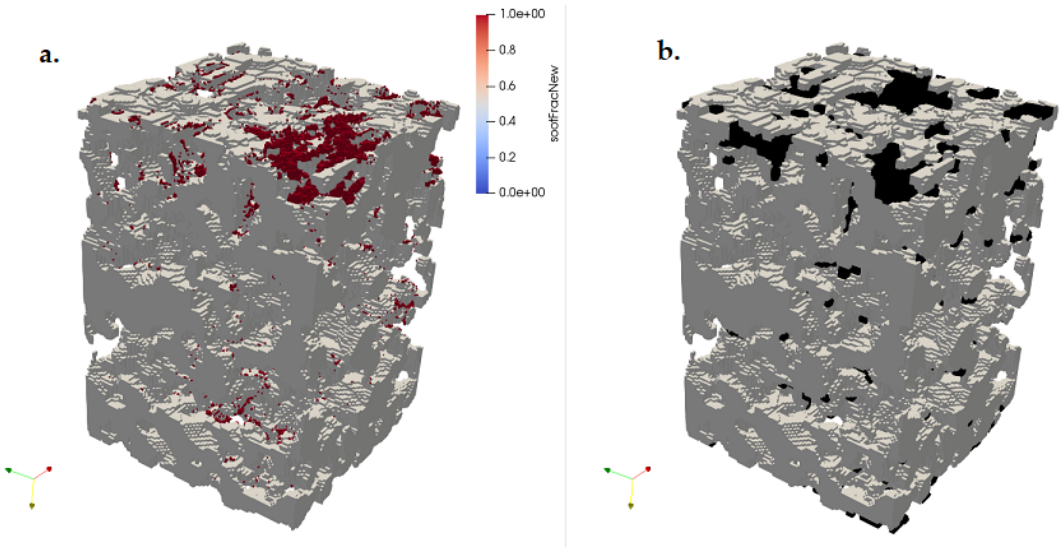

FIGURE A.3: Model Validation. Initial results using our data shows acceptable correlation between our experiment and modelling results. This work is the result of an ongoing collaboration with a group from University of Chemistry and Technology, Prague. The modelling was carried out by Petr Koci and Marie Placha of University of Chemistry and Technology, Prague. **(a)** Modelling Visualisation, **(b)** Microscopy Visualisation.

Blank Page.

Bibliography

Ahmed, OMH and Yushou Song (2018). "A review of common beam hardening correction methods for industrial computed tomography". In: *Sains Malaysiana* 47.9, pp. 1883 –1890. URL: http://dx.doi.org/10.17576/jsm-2018-4708-29.

Al-Raoush, R. I. and C. S. Willson (2005). "Extraction of physically realistic pore network properties from three-dimensional synchrotron X-ray microtomography images of unconsolidated porous media systems". In: *Journal of Hydrology* 300.1, pp. 44–64. ISSN: 0022-1694. DOI: https://doi.org/10.1016/j.jhydrol.2004.05.005. URL: http://www.sciencedirect.com/science/article/pii/S0022169404002355.

Albertin, Fauzia et al. (2019). "X-Ray Computed Tomography In Situ: An Opportunity for Museums and Restoration Laboratories". In: *Heritage* 2.3, pp. 2028–2038. ISSN: 2571-9408. DOI: 10.3390/heritage2030122. URL: https://www.mdpi.com/2571-9408/2/3/122.

Alkidas, Alex C. (2007). "Combustion advancements in gasoline engines". In: *Energy Conversion and Management* 48.11. 19th International Conference on Efficiency, Cost, Optimization, Simulation and Environmental Impact of Energy Systems, pp. 2751–2761. ISSN: 0196-8904. DOI: https://doi.org/10.1016/j.enconman.2007.07.027. URL: https://www.sciencedirect.com/science/article/pii/S0196890407002221.

Alsop, K. et al. (2021). "Accurate prediction of saw blade thicknesses from false start measurements". In: *Forensic Science International* 318, p. 110602. ISSN: 0379-0738. DOI: https://doi.org/10.1016/j.forsciint.2020.110602. URL: https://www.sciencedirect.com/science/article/pii/S0379073820304643.

Amirante, Riccardo et al. (2017). "Effects of lubricant oil on particulate emissions from port-fuel and direct-injection spark-ignition engines". In: *International Journal of Engine Research* 18.5-6, pp. 606–620. DOI: 10.1177/1468087417706602. eprint:

https://doi.org/10.1177/1468087417706602. URL: https://doi.org/10.1177/1468087417706602.

Atwood, R. C. et al. (2015). "A high-throughput system for high-quality tomographic reconstruction of large datasets at Diamond Light Source". In: *Philos Trans A Math Phys Eng Sci* 373.2043. ISSN: 1471-2962 (Electronic) 1364-503X (Linking). DOI: 10.1098/rsta.2014.0398. URL: https://www.ncbi.nlm.nih.gov/pubmed/25939626.

Awad, Omar I et al. (2020). "Particulate emissions from gasoline direct injection engines: A review of how current emission regulations are being met by automobile manufacturers". In: *Science of the Total Environment* 718, p. 137302.

Bagi, Sujay and Carl Justin Kamp (2022). "Implications of Hydrated Ash on Filtration Efficiency and Performance of Particulate Filters (DPF, GPF, and SCRF)—a Perspective". In: *Emission Control Science and Technology*, pp. 1–5.

Baiker-Sørensen, Martin et al. (2020). "Interpol review of shoe and tool marks 2016-2019". In: *Forensic Science International: Synergy* 2, pp. 521–539. ISSN: 2589-871X. DOI: https://doi.org/10.1016/j.fsisyn.2020.01.016. URL: https://www.sciencedirect.com/science/article/pii/S2589871X20300164.

Belot, Igor et al. (2020). "Numerical investigation of the impact of washcoat distribution on the filtration performance of gasoline particulate filters". In: *Chemical Engineering Science* 221, p. 115656. ISSN: 0009-2509. DOI: https://doi.org/10.1016/j.ces.2020.115656. URL: http://www.sciencedirect.com/science/article/pii/S0009250920301883.

Bensaid, S. et al. (2009). "Experimental investigation of soot deposition in diesel particulate filters". In: *Catalysis Today* 147. 3rd International Conference on Structured Catalysts and Reactors, ICOSCAR-3, Ischia, Italy, 27-30 September 2009, S295–S300. ISSN: 0920-5861. DOI: https://doi.org/10.1016/j.cattod.2009.07.039. URL: https://www.sciencedirect.com/science/article/pii/S0920586109003733.

Bensaid, Samir, Daniele L. Marchisio, and Debora Fino (2010). "Numerical simulation of soot filtration and combustion within diesel particulate filters". In: *Chemical Engineering Science* 65.1. 20th International Symposium in Chemical Reaction Engineering—Green Chemical Reaction Engineering for a Sustainable Future, pp. 357–363. ISSN: 0009-2509. DOI: https://doi.org/10.1016/j.ces.2009.06.051. URL: https://www.sciencedirect.com/science/article/pii/S0009250909004473.

Berkeley, Nigel, David Jarvis, and Andrew Jones (2018). "Analysing the take up of battery electric vehicles: An investigation of barriers amongst drivers in the UK". In: *Transportation Research Part D: Transport and Environment* 63, pp. 466–481. ISSN: 1361-9209. DOI: https://doi.org/10.1016/j.trd.2018.06.016. URL: https://www.sciencedirect.com/science/article/pii/S1361920917301001.

Bilderback, Donald H, Pascal Elleaume, and Edgar Weckert (2005). "Review of third and next generation synchrotron light sources". In: *Journal of Physics B: Atomic, Molecular and Optical Physics* 38.9, S773–S797. DOI: 10.1088/0953-4075/38/9/022. URL: https://doi.org/10.1088/0953-4075/38/9/022.

Blažek, Miroslav et al. (2021). "Washcoating of catalytic particulate filters studied by time-resolved X–ray tomography". In: *Chemical Engineering Journal* 409, p. 128057.

Bodey, A J and C Rau (2017). "Launch of the I13-2 data beamline at the Diamond Light Source synchrotron". In: *Journal of Physics: Conference Series* 849, p. 012038. DOI: 10.1088/1742-6596/849/1/012038. URL: https://doi.org/10.1088/1742-6596/849/1/012038.

Bond, Tami C et al. (2013). "Bounding the role of black carbon in the climate system: A scientific assessment". In: *Journal of geophysical research: Atmospheres* 118.11, pp. 5380–5552.

Brabant, L. et al. (2012). "A novel beam hardening correction method requiring no prior knowledge, incorporated in an iterative reconstruction algorithm". In: *NDT & E International* 51, pp. 68–73. ISSN: 0963-8695. DOI: https://doi.org/10.1016/j.ndteint.2012.07.002. URL: https://www.sciencedirect.com/science/article/pii/S096386951200093X.

Bradski, G. (2000). "The OpenCV Library". In: *Dr. Dobb's Journal of Software Tools*.

Brown, James S. et al. (2013). "Thoracic and respirable particle definitions for human health risk assessment". In: *Particle and Fibre Toxicology* 12.10. DOI: 10.1186/1743-8977-10-12. URL: https://doi.org/10.1186/1743-8977-10-12.

Buades, A., B. Coll, and J.-M. Morel (2005). "A non-local algorithm for image denoising". In: *2005 IEEE Computer Society Conference on Computer Vision and Pattern Recognition (CVPR'05)*. Vol. 2, 60–65 vol. 2. DOI: 10.1109/CVPR.2005.38.

Burnett, TL et al. (2014). "Correlative tomography". In: *Scientific reports* 4.1, p. 4711.

Chao, Weilun et al. (2005). "Soft x-ray microscopy at a spatial resolution better than 15nm". In: *Nature* 435, pp. 1210–1213. ISSN: 1476-4687.

Chen, Bo et al. (2013). "Three-dimensional structure analysis and percolation properties of a barrier marine coating". In: *Scientific reports* 3.1, pp. 1–5.

Chiou, Casey Casey Jianzhi (2013). "Individual and synergistic effects of lubricant additive (Ca, Mg, Zn) combinations on ash characteristics and DPF performance". PhD thesis. Massachusetts Institute of Technology.

Choi, Seungmok and Kyeong Lee (2013). "Detailed Investigation of Filtration and Regeneration Processes in a Diesel Particulate Filter System". In: *Proceedings of the FISITA 2012 World Automotive Congress*. Lecture Notes in Electrical Engineering. Chap. Chapter 63, pp. 811–823. ISBN: 978-3-642-33840-3 978-3-642-33841-0. DOI: 10.1007/978-3-642-33841-0_63.

Choi, Seungmok and Heeje Seong (2016). "Lube oil-dependent ash chemistry on soot oxidation reactivity in a gasoline direct-injection engine". In: *Combustion and Flame* 174, pp. 68–76.

Cnudde, V. and M. N. Boone (2013). "High-resolution X-ray computed tomography in geosciences: A review of the current technology and applications". In: *Earth-Science Reviews* 123, pp. 1–17. ISSN: 0012-8252. DOI: https://doi.org/10.1016/j.earscirev.2013.04.003. URL: http://www.sciencedirect.com/science/article/pii/S001282521300069X.

Coban, S.B. et al. (2015). "When do the iterative reconstruction methods become worth the effort?" In: *MIMS EPrint 2015.47. UK: Manchester Institute for Mathematical Sciences, The University of Manchester, 2015*. ISSN: 1749-9097.

Costanza-Robinson, Molly S., Benjamin D. Estabrook, and David F. Fouhey (2011). "Representative elementary volume estimation for porosity, moisture saturation, and air-water interfacial areas in unsaturated porous media: Data quality implications". In: *Water Resources Research* 47.7. ISSN: 0043-1397. DOI: 10.1029/2010WR009655. URL: https://doi.org/10.1029/2010WR009655.

Custer, Nicholas et al. (2016). "Lubricant-derived ash impact on gasoline particulate filter performance". In: *SAE International Journal of Engines* 9.3, pp. 1604–1614.

Davis, G. R. and J. C. Elliott (2006). "Artefacts in X-ray microtomography of materials". In: *Materials Science and Technology* 22.9, pp. 1011–1018. DOI: 10.1179/

174328406X114117. eprint: https://doi.org/10.1179/174328406X114117. URL: https://doi.org/10.1179/174328406X114117.

Dobson, K. J. et al. (2016). "4-D imaging of sub-second dynamics in pore-scale processes using real-time synchrotron X-ray tomography". In: *Solid Earth* 7.4, pp. 1059–1073. DOI: 10.5194/se-7-1059-2016. URL: https://se.copernicus.org/articles/7/1059/2016/.

Dremel, Kilian et al. (2014). "Beam hardening correction in x-ray computed tomography: A comparison of two iterative model-based reconstruction methods". In: *11th European Conference on Non-Destructive Testing (ECNDT 2014), Prague 2014, Oct 6-11 (ECNDT 2014)*. URL: https://www.ndt.net/events/ECNDT2014/app/content/Paper/576_Dremel_Rev1.pdf.

Du, Wenjia et al. (2021). "Microstructure analysis and image-based modelling of face masks for COVID-19 virus protection". In: *Communications Materials*, p. 69. DOI: 10.1038/s43246-021-00160-z. URL: https://doi.org/10.1038/s43246-021-00160-z.

du Plessis, Anton, Ina Yadroitsava, and Igor Yadroitsev (2020). "Effects of defects on mechanical properties in metal additive manufacturing: A review focusing on X-ray tomography insights". In: *Materials and Design* 187, p. 108385. ISSN: 0264-1275. DOI: https://doi.org/10.1016/j.matdes.2019.108385. URL: https://www.sciencedirect.com/science/article/pii/S0264127519308238.

Echlin, McLean P. et al. (2020). "Serial sectioning in the SEM for three dimensional materials science". In: *Current Opinion in Solid State and Materials Science* 24.2, p. 100817. ISSN: 1359-0286. DOI: https://doi.org/10.1016/j.cossms.2020.100817. URL: https://www.sciencedirect.com/science/article/pii/S1359028620300152.

Einstein, A. (1905). "Über einen die Erzeugung und Verwandlung des Lichtes betreffenden heuristischen Gesichtspunkt". In: *Annalen der Physik* 322.6, pp. 132–148. DOI: https://doi.org/10.1002/andp.19053220607. eprint: https://onlinelibrary.wiley.com/doi/pdf/10.1002/andp.19053220607. URL: https://onlinelibrary.wiley.com/doi/abs/10.1002/andp.19053220607.

Fanis, A De et al. (2013). "Fast X-ray imaging at beamline I13L at Diamond Light Source". In: *Journal of Physics: Conference Series* 425.19, p. 192014. DOI: 10.1088/

1742-6596/425/19/192014. URL: https://doi.org/10.1088/1742-6596/425/19/192014.

Faulkner, Helen Mary Louise and JM Rodenburg (2004). "Movable aperture lensless transmission microscopy: a novel phase retrieval algorithm". In: *Physical review letters* 93.2, p. 023903.

Ferreira, Talita R, Nathaly L Archilha, and Luiz F Pires (2022). "An analysis of three XCT-based methods to determine the intrinsic permeability of soil aggregates". In: *Journal of Hydrology* 612, p. 128024.

Fienup, James R (1978). "Reconstruction of an object from the modulus of its Fourier transform". In: *Optics letters* 3.1, pp. 27–29.

Fuchs, T., M. Kachelriess, and W.A. Kalender (2000). "Direct comparison of a xenon and a solid-state CT detector system: measurements under working conditions". In: *IEEE Transactions on Medical Imaging* 19.9, pp. 941–948. DOI: 10.1109/42.887841.

Garcea, S.C., Y. Wang, and P.J. Withers (2018). "X-ray computed tomography of polymer composites". In: *Composites Science and Technology* 156, pp. 305–319. ISSN: 0266-3538. DOI: https://doi.org/10.1016/j.compscitech.2017.10.023. URL: https://www.sciencedirect.com/science/article/pii/S0266353817312460.

Ghosh, Sandeep et al. (2021). "CrackWeb: A modified U-Net based segmentation architecture for crack detection". In: *IOP Conference Series: Materials Science and Engineering*. Vol. 1080. 1. IOP Publishing, p. 012002.

Giammar, Daniel et al. (2018). *Impact of Microstructure on the Containment and Migration of CO2 in Fractured Basalts*. Tech. rep. Washington Univ., St. Louis, MO (United States).

Gong, Jian et al. (2018a). "Importance of filter's microstructure in dynamic filtration modeling of gasoline particulate filters (GPFs): Inhomogeneous porosity and pore size distribution". In: *Chemical Engineering Journal* 338, pp. 15–26. ISSN: 1385-8947. DOI: https://doi.org/10.1016/j.cej.2018.01.006. URL: https://www.sciencedirect.com/science/article/pii/S1385894718300068.

– (2018b). "Importance of filter's microstructure in dynamic filtration modeling of gasoline particulate filters (GPFs): Inhomogeneous porosity and pore size distribution". In: *Chemical Engineering Journal* 338, pp. 15–26. ISSN: 1385-8947. DOI:

https://doi.org/10.1016/j.cej.2018.01.006. URL: https://www.sciencedirect.com/science/article/pii/S1385894718300068.

Gostick, Jeff T (2017). "Versatile and efficient pore network extraction method using marker-based watershed segmentation". In: *Physical Review E* 96.2, p. 023307.

Gostick, Jeff T et al. (2019). "PoreSpy: A python toolkit for quantitative analysis of porous media images". In: *Journal of Open Source Software* 4.37, p. 1296.

Grangeat, Pierre (1991). "Mathematical framework of cone beam 3D reconstruction via the first derivative of the radon transform". In: *Mathematical Methods in Tomography*. Ed. by Gabor T. Herman, Alfred K. Louis, and Frank Natterer. Berlin, Heidelberg: Springer Berlin Heidelberg, pp. 66–97. ISBN: 978-3-540-46615-4.

Greenstone, M, C Hasenkopf, and K Lee (2022). "Air Quality Life Index 2022". In: eprint: https://aqli.epic.uchicago.edu/wp-content/uploads/2022/06/AQLI_2022_Report-Global.pdf.

Gudla, Visweswara Chakravarthy et al. (2020). "Environmentally induced crack (EIC) initiation, propagation, and failure: A 3D in-situ time-lapse study of AA5083 H131". In: *Corrosion Science* 174, p. 108834. ISSN: 0010-938X. DOI: https://doi.org/10.1016/j.corsci.2020.108834. URL: https://www.sciencedirect.com/science/article/pii/S0010938X20301049.

Guizar-Sicairos, M and P Thibault (2021). "Ptychography: A solution to the phase problem". In: *Physics Today* 12 (9), p. 42. DOI: doi:10.1063/PT.3.4835.

Guizar-Sicairos, Manuel and James R Fienup (2008). "Phase retrieval with transverse translation diversity: a nonlinear optimization approach". In: *Optics express* 16.10, pp. 7264–7278.

Harris, Stephen J and M Matti Maricq (2001). "Signature size distributions for diesel and gasoline engine exhaust particulate matter". In: *Journal of Aerosol Science* 32.6, pp. 749–764.

Hayashi, Hidemitsu and Shuichi Kubo (2008). "Computer simulation study on filtration of soot particles in diesel particulate filter". In: *Computers & Mathematics with Applications* 55.7. Mesoscopic Methods in Engineering and Science, pp. 1450–1460. ISSN: 0898-1221. DOI: https://doi.org/10.1016/j.camwa.2007.08.012. URL: https://www.sciencedirect.com/science/article/pii/S0898122107006396.

Heinzl, C., A. Amirkhanov, and J. Kastner (2018). *Processing, Analysis and Visualization of CT Data. In: Carmignato S., Dewulf W., Leach R. (eds) Industrial X-Ray Computed Tomography*. Springer. URL: https://doi.org/10.1007/978-3-319-59573-3_4.

Herman., Gabor T. (1980). *Fundamentals of Computerized Tomography: Image Reconstruction from Projections*. Springer London. ISBN: 978-1-84628-723-7. URL: https://doi.org/10.1007/978-1-84628-723-7.

HMGOV (1956). *Clean Air Act*. Chap. 52. URL: http://www.legislation.gov.uk/ukpga/Eliz2/4-5/52/enacted.

Holler, Mirko et al. (2019). "Three-dimensional imaging of integrated circuits with macro-to nanoscale zoom". In: *Nature Electronics* 2.10, pp. 464–470.

Hsieh, Jiang et al. (2013). "Recent Advances in CT Image Reconstruction". English. In: *Current Radiology Reports* 1.1, pp. 39–51. DOI: 10.1007/s40134-012-0003-7.

Hua, Lun et al. (2018). "Effect of ash on gasoline particulate filter using an accelerated ash loading method". In.

Hubbel, JH. (1969). "NIST: Photon Cross Sections, Attenuation Coefficients, and Energy Absorption Coefficients from 10 keV to 100 GeV". In: URL: https://apps.dtic.mil/sti/citations/ADD095298.

IARC (2012). *IARC: Diesel engines exhaust carcinogenic*. URL: https://www.iarc.fr/en/media-centre/pr/2012/pdfs/pr213_E.pdf.

Ishizawa, T et al. (2009). "Investigation into ash loading and its relationship to DPF regeneration method". In: *SAE international journal of commercial vehicles* 2.2009-01-2882, pp. 164–175.

Ito, Yoshitaka et al. (2015). "Next generation of ceramic wall flow gasoline particulate filter with integrated three way catalyst". In.

Jacobson, Mark Z. (2012). *Air Pollution and Global Warming: History, Science, and Solutions*. 2nd ed. Cambridge University Press. DOI: 10.1017/CBO9781139109444.

Jeol (2022). *Glossary of SEM terms*. https://www.jeol.co.jp/en/words/semterms/. Accessed: 2022-10-08.

Johnson, T. F. et al. (2021). "High-resolution imaging of depth filter structures using X-ray computed tomography". In: *Journal of Materials Science* 56.27, pp. 15313–

15326. ISSN: 1573-4803. DOI: 10.1007/s10853-021-06238-w. URL: https://doi.org/10.1007/s10853-021-06238-w.

Jones, Matthew P. et al. (2020). "4D In-Situ Microscopy of Aerosol Filtration in a Wall Flow Filter". In: *Materials* 13.24, p. 5676. ISSN: 1996-1944. DOI: 10.3390/ma13245676. URL: https://www.mdpi.com/1996-1944/13/24/5676.

Joshi, Ameya (2017). "Progress and Outlook on Gasoline Vehicle Aftertreatment Systems". In: *Johnson Matthey Technol. Rev.* 61.4, pp. 311–325. DOI: https://doi.org/10.1595/205651317X696306.

Joshi, Ameya and Timothy V Johnson (2018). "Gasoline particulate filters—A review". In: *Emission Control Science and Technology* 4.4, pp. 219–239.

Jørgensen, J. S. et al. (2021). "Core Imaging Library - Part I: A Versatile Python Framework for Tomographic Imaging". In: *Philosophical Transactions of the Royal Society A: Mathematical, Physical and Engineering Sciences* 2204, p. 379. DOI: doi:10.1098/rsta.2020.0192.

Kamp, Carl J, Alexander G Sappok, and Victor W Wong (2013). "Automotive Catalysis Aging: A Novel Approach for the Direct Observation of Interfacial and Sub-Surface Chemical and Structural Properties Relevant to Catalyst Aging and Functionality". In: *MRS Online Proceedings Library* 1641.1, pp. 1–6.

Kamp, Carl Justin, Alexander Sappok, and Victor Wong (2012). "Soot and Ash Deposition Characteristics at the Catalyst-Substrate Interface and Intra-Layer Interactions in Aged Diesel Particulate Filters Illustrated using Focused Ion Beam (FIB) Milling". In: *SAE International Journal of Fuels and Lubricants* 5.2, pp. 696–710. ISSN: 19463952, 19463960. URL: www.jstor.org/stable/26272701.

Kamp, Carl Justin et al. (2017). "Ash Permeability Determination in the Diesel Particulate Filter from Ultra-High Resolution 3D X-Ray Imaging and Image-Based Direct Numerical Simulations". In: *SAE International Journal of Fuels and Lubricants* 10.2, pp. 608–618. ISSN: 19463952, 19463960. URL: www.jstor.org/stable/26274140.

Karnati, Venkateswarlu, Mithun Uliyar, and Sumit Dey (2009). "Fast Non-Local algorithm for image denoising". In: *2009 16th IEEE International Conference on Image Processing (ICIP)*, pp. 3873–3876. DOI: 10.1109/ICIP.2009.5414044.

Khalek, Imad A, Thomas Bougher, and Jeff J Jetter (2010). "Particle emissions from a 2009 gasoline direct injection engine using different commercially available fuels". In: *SAE International Journal of Fuels and Lubricants* 3.2, pp. 623–637.

Konstandopoulos, A., E. Skaperdas, and M. Masoudi (2002). "Microstructural Properties of soot deposits in diesel particulate traps". In: *SAE 2002-0101015*.

Konstandopoulos, Athanasios G. et al. (2000). "Fundamental Studies of Diesel Particulate Filters: Transient Loading, Regeneration and Aging". In: *SAE Transactions* 109, pp. 683–705. ISSN: 0096736X, 25771531. URL: www.jstor.org/stable/44745878.

Konstandopoulos, Athanasios G et al. (2006). "A multi-reactor assembly for screening of diesel particulate filters". In.

Kočí, Petr et al. (2019). "3D reconstruction and pore-scale modeling of coated catalytic filters for automotive exhaust gas aftertreatment". In: *Catalysis Today* 320, pp. 165–174. ISSN: 09205861. DOI: 10.1016/j.cattod.2017.12.025.

Kuppili, Venkata Sree Charan (2019). "X-ray far-field ptychotomography at I13-1 diamond light source". PhD thesis. UCL (University College London).

Kyle, J. Richard and Richard A. Ketcham (2015). "Application of high resolution X-ray computed tomography to mineral deposit origin, evaluation, and processing". In: *Ore Geology Reviews* 65. Applications of Modern Analytical Techniques in the Study of Mineral Deposits, pp. 821–839. ISSN: 0169-1368. DOI: https://doi.org/10.1016/j.oregeorev.2014.09.034. URL: https://www.sciencedirect.com/science/article/pii/S0169136814002492.

Lambert, Christine K et al. (2016). "Analysis of high mileage gasoline exhaust particle filters". In: *SAE International Journal of Engines* 9.2, pp. 1296–1304.

Lambert, Christine K et al. (2017). "Analysis of ash in low mileage, rapid aged, and high mileage gasoline exhaust particle filters". In: *SAE International Journal of Engines* 10.4, pp. 1595–1603.

Landis, Eric N. and Denis T. Keane (2010). "X-ray microtomography". In: *Materials Characterization* 61.12, pp. 1305–1316. ISSN: 1044-5803. DOI: https://doi.org/10.1016/j.matchar.2010.09.012. URL: https://www.sciencedirect.com/science/article/pii/S1044580310002706.

Lee, Hoon and Kyeong O Lee (2013). "Development of a 3-D model for analyzing the effects of channel geometry on filtration characteristics in particulate filter system". In: *SAE paper*, pp. 01–1583.

Lelieveld, Jos et al. (Mar. 2020). "Loss of life expectancy from air pollution compared to other risk factors: a worldwide perspective". In: *Cardiovascular Research* 116.11, pp. 1910–1917. ISSN: 0008-6363. DOI: 10.1093/cvr/cvaa025. eprint: https://academic.oup.com/cardiovascres/article-pdf/116/11/1910/33723418/cvaa025.pdf. URL: https://doi.org/10.1093/cvr/cvaa025.

Leo, WIlliam R. (1994). *Techniques for Nuclear and Particle Physics Experiments: A How-to Approach (2nd Edition)*. Springer-Verlag Berlin Heidelberg. ISBN: 978-3-540-57280-0. DOI: 10.1007/978-3-642-57920-2.

Li, Jiang et al. (2017). "Optical and Scintillation Properties of Ce3+-Doped LuAG and YAG Transparent Ceramics: A Comparative Study". In: *Journal of the American Ceramic Society* 100.1, pp. 150–156. DOI: https://doi.org/10.1111/jace.14461. eprint: https://ceramics.onlinelibrary.wiley.com/doi/pdf/10.1111/jace.14461. URL: https://ceramics.onlinelibrary.wiley.com/doi/abs/10.1111/jace.14461.

Liu, Xiaobo et al. (2020). "Ore image segmentation method using U-Net and Res_Unet convolutional networks". In: *RSC advances* 10.16, pp. 9396–9406.

Maiden, Andrew M and John M Rodenburg (2009). "An improved ptychographical phase retrieval algorithm for diffractive imaging". In: *Ultramicroscopy* 109.10, pp. 1256–1262.

Man, B. De et al. (2001). "An iterative maximum-likelihood polychromatic algorithm for CT". In: *IEEE Trans, on Med. Imaging* 20.10, pp. 999–1008.

Maricq, M Matti, Joseph J Szente, and Ken Jahr (2012). "The impact of ethanol fuel blends on PM emissions from a light-duty GDI vehicle". In: *Aerosol Science and Technology* 46.5, pp. 576–583.

Maricq, M Matti et al. (2000). "Sooting tendencies in an air-forced direct injection spark-ignition (DISI) engine". In: *SAE transactions*, pp. 169–175.

McGeehan, James et al. (2009). "Analysis of DPF incombustible materials from volvo trucks using DPF-SCR-Urea with API CJ-4 and API CI-4 PLUS oils". In: *SAE International Journal of Fuels and Lubricants* 2.1, pp. 762–780.

McGeehan, James A et al. (2005). "On The Road to 2010 Emissions: Fieid Test Results and Analysis with DPF-SCR System and Ultra Low Sulfur Diesel Fuel". In: *SAE transactions*, pp. 1308–1322.

Merkel, Gregory A, WA Cutler, and Christopher J Warren (2001). "Thermal durability of wall-flow ceramic diesel particulate filters". In: *SAE Transactions*, pp. 168–182.

Miao, Jianwei et al. (1999). "Extending the methodology of X-ray crystallography to allow imaging of micrometre-sized non-crystalline specimens". In: *Nature* 400.6742, pp. 342–344.

Moldovan, Mariella et al. (2003). "Impact of ageing on the distribution of platinum group elements and catalyst poisoning elements in automobile catalysts". In: *Surface and Interface Analysis: An International Journal devoted to the development and application of techniques for the analysis of surfaces, interfaces and thin films* 35.4, pp. 354–359.

Morcfos, Michelle, Ponnaiyan Ayyappan, and Thomas Harris (2011). *Characterization of DPF ash for development of DPF regeneration control and ash cleaning requirements*. Tech. rep. SAE Technical Paper.

Nakayama, Hiroki et al. (2019). "Development of GPF Using Micro-CT Measurement and Numerical Analytical Technique". In: *Topics in Catalysis* 62.1, pp. 419–425.

Nusslin, Fridjof (2020). "Wilhelm Conrad Rontgen: The scientist and his discovery". In: *European Journal of Medical Phyics* 79, pp. 65 –68.

O'Driscoll, Rosalind et al. (2018). "Real world CO2 and NOx emissions from 149 Euro 5 and 6 diesel, gasoline and hybrid passenger cars". In: *Science of The Total Environment* 621, pp. 282–290. ISSN: 0048-9697. DOI: https://doi.org/10.1016/j.scitotenv.2017.11.271. URL: https://www.sciencedirect.com/science/article/pii/S0048969717333296.

Olivetti, Elsa A. et al. (2017). "Lithium-Ion Battery Supply Chain Considerations: Analysis of Potential Bottlenecks in Critical Metals". In: *Joule* 1.2, pp. 229–243. ISSN: 2542-4351. DOI: https://doi.org/10.1016/j.joule.2017.08.019. URL: https://www.sciencedirect.com/science/article/pii/S2542435117300442.

Otsu, N. (1979). "A threshold selection method from gray-level histograms". In: *IEEE Trans Syst Man Cybern* 9.1, pp. 62 –66. DOI: doi:10.1109/TSMC.1979.4310076. URL: http://ieeexplore.ieee.org/stamp/stamp.jsp?tp=&arnumber=4310076&isnumber=4310064.

Ozelim Luan Carlos de, S. M. and L. B. Cavalcante André (2018). "Representative Elementary Volume Determination for Permeability and Porosity Using Numerical Three-Dimensional Experiments in Microtomography Data". In: *International Journal of Geomechanics* 18.2, p. 04017154. DOI: 10.1061/(ASCE)GM.1943-5622.0001060. URL: https://doi.org/10.1061/(ASCE)GM.1943-5622.0001060.

Panchal, Monik et al. (2021). "Operando XAFS investigation on the effect of ash deposition on three-way catalyst used in gasoline particulate filters and the effect of the manufacturing process on the catalytic activity". In: *Journal of Physics: Condensed Matter* 33.28, p. 284001.

Parker, G.R. et al. (2021). "4D micro-scale, phase-contrast X-ray imaging and computed tomography of HMX-based polymer-bonded explosives during thermal runaway". In: *Combustion and Flame* 226, pp. 478–489. ISSN: 0010-2180. DOI: https://doi.org/10.1016/j.combustflame.2020.12.025. URL: https://www.sciencedirect.com/science/article/pii/S0010218020305745.

Paz-Garcia, J.M. et al. (2016). "4D analysis of the microstructural evolution of Si-based electrodes during lithiation: Time-lapse X-ray imaging and digital volume correlation". In: *Journal of Power Sources* 320, pp. 196–203. ISSN: 0378-7753. DOI: https://doi.org/10.1016/j.jpowsour.2016.04.076. URL: https://www.sciencedirect.com/science/article/pii/S0378775316304396.

Pfeiffer, Franz (2018). "X-ray ptychography". In: *Nature Photonics* 12.1, pp. 9–17. DOI: https://doi.org/10.1038/s41566-017-0072-5.

Plachá, Marie et al. (2020). "Pore-scale filtration model for coated catalytic filters in automotive exhaust gas aftertreatment". In: *Chemical Engineering Science* 226. ISSN: 00092509. DOI: 10.1016/j.ces.2020.115854.

Price, Stephen WT et al. (2022). "μ-CT Investigation into the Impact of a Fuel-Borne Catalyst Additive on the Filtration Efficiency and Backpressure of Gasoline Particulate Filters". In: *SAE International Journal of Fuels and Lubricants* 15.2.

Raaschou-Nielsen, Ole et al. (2013). "Air pollution and lung cancer incidence in 17 European cohorts: prospective analyses from the European Study of Cohorts for Air Pollution Effects (ESCAPE)." In: *The Lancet. Oncology* 14.9, 813–822. URL: https://doi.org/10.1016/S1470-2045(13)70279-1.

Rau, C. et al. (2016). "Imaging in real and reciprocal space at the Diamond beamline I13". In: *AIP Conference Proceedings* 1696.1, p. 020047. DOI: 10.1063/1.4937541. URL: https://aip.scitation.org/doi/abs/10.1063/1.4937541.

Rau, Christoph et al. (2011). "Coherent imaging at the Diamond beamline I13". In: *physica status solidi (a)* 208.11, pp. 2522–2525.

Ronneberger, Olaf, Philipp Fischer, and Thomas Brox (2015). "U-net: Convolutional networks for biomedical image segmentation". In: *International Conference on Medical image computing and computer-assisted intervention*. Springer, pp. 234–241.

Rutty, G.N. et al. (2013). "The role of micro-computed tomography in forensic investigations". In: *Forensic Science International* 225.1. Postmortem Imaging, pp. 60–66. ISSN: 0379-0738. DOI: https://doi.org/10.1016/j.forsciint.2012.10.030. URL: https://www.sciencedirect.com/science/article/pii/S0379073812004847.

Sabharwal, Mayank et al. (2017). "Improving FIB-SEM Reconstructions by Using Epoxy Resin Embedding". In: *ECS Transactions* 77.11, p. 1337. DOI: 10.1149/07711.1337ecst. URL: https://dx.doi.org/10.1149/07711.1337ecst.

Sappok, Alexander, Carl Kamp, and Victor Wong (2012). "Sensitivity analysis of ash packing and distribution in diesel particulate filters to transient changes in exhaust conditions". In: *SAE International Journal of Fuels and Lubricants* 5.2, pp. 733–750.

Sappok, Alexander et al. (2009). "Characteristics and effects of ash accumulation on diesel particulate filter performance: Rapidly aged and field aged results". In.

Sappok, Alexander G and Victor W Wong (2007). *Detailed chemical and physical characterization of ash species in diesel exhaust entering aftertreatment systems*. Tech. rep. SAE Technical Paper.

Sappok, Alexander Georg (2009). "The nature of lubricant-derived ash-related emissions and their impact on diesel aftertreatment system performance". PhD thesis. Massachusetts Institute of Technology.

Schwartz, Jonathan et al. (2019). "Removing stripes, scratches, and curtaining with nonrecoverable compressed sensing". In: *Microscopy and Microanalysis* 25.3, pp. 705–710.

Segel, E. et al. (1987). "A linearization beam-hardening correction method for x-ray computed tomographic imaging of structural ceramics." In: *Review of Progress in Quantitative Nondestructive Evaluation* 0, pp. 411–419.

Seong, Heeje et al. (2019). "Deactivation of three-way catalysts coated within gasoline particulate filters by engine-oil-derived chemicals". In: *Industrial & Engineering Chemistry Research* 58.25, pp. 10724–10736.

Shah, S. M. et al. (2017). "Convex hull approach for determining rock representative elementary volume for multiple petrophysical parameters using pore-scale imaging and Lattice–Boltzmann modelling". In: *Advances in Water Resources* 104, pp. 65–75. ISSN: 0309-1708. DOI: https://doi.org/10.1016/j.advwatres.2017.03.008. URL: http://www.sciencedirect.com/science/article/pii/S0309170817302373.

Shamsolmoali, Pourya et al. (2019). "A novel deep structure U-Net for sea-land segmentation in remote sensing images". In: *IEEE Journal of Selected Topics in Applied Earth Observations and Remote Sensing* 12.9, pp. 3219–3232.

Shao, Huifang et al. (2016). "Effect of lubricant oil properties on the performance of gasoline particulate filter (GPF)". In: *SAE International Journal of Fuels and Lubricants* 9.3, pp. 650–658.

Shimoda, Takehide et al. (2012). "Potential of a low pressure drop filter concept for direct injection gasoline engines to reduce particulate number emission". In.

Sonntag, Fabian and Peter Eilts (2016). "Evaluation of accelerated ash loading procedures for diesel particulate filters". In.

Stewart, Mark and David Rector (2004). "A Mechanistic Model for Particle Deposition in Diesel Particluate Filters Using the Lattice-Boltzmann Technique". In: *28th International Conference on Advanced Ceramics and Composites A: Ceramic Engineering and Science Proceedings*, pp. 437–446. ISSN: 9780470291184. DOI: doi:10.1002/9780470291184.ch6310.1002/9780470291184.ch63. URL: https://doi.org/10.1002/9780470291184.ch63.

Tang, Chao-Sheng et al. (2019). "Three-dimensional characterization of desiccation cracking behavior of compacted clayey soil using X-ray computed tomography". In: *Engineering Geology* 255, pp. 1–10. ISSN: 0013-7952. DOI: https://doi.org/10.1016/j.enggeo.2019.04.014. URL: https://www.sciencedirect.com/science/article/pii/S0013795218321136.

Tariq, Farid et al. (2018). "Uncovering the mechanisms of electrolyte permeation in porous electrodes for redox flow batteries through real time in situ 3D imaging". In: *Sustainable Energy & Fuels* 2.9, pp. 2068–2080.

Thibault, Pierre and Manuel Guizar-Sicairos (2012). "Maximum-likelihood refinement for coherent diffractive imaging". In: *New Journal of Physics* 14.6, p. 063004.

Thibault, Pierre et al. (2009). "Probe retrieval in ptychographic coherent diffractive imaging". In: *Ultramicroscopy* 109.4, pp. 338–343.

Thompson, A and R Leach (2017). *Introduction to Industrial X-ray Computed Tomography. In: Carmignato S., Dewulf W., Leach R. (eds) Industrial X-Ray Computed Tomography*. Springer. URL: https://doi.org/10.1007/978-3-319-59573-3_1.

Tien, C. and H. Brenner (2013). *Granular Filtration of Aerosols and Hydrosols: Butterworths Series in Chemical Engineering*. Elsevier Science. ISBN: 9781483162423. URL: https://books.google.co.uk/books?id=MeMgBQAAQBAJ.

Twigg, Martyn V et al. (2004). "The effect of phosphorus and boron lubricant oil additives on catalyst and engine durability". In: *SAE transactions*, pp. 948–959.

UN (2017). *Sustainable Mobility for All. 2017. Global Mobility Report 2017: Tracking Sector Performance.* URL: https://sdgs.un.org/sites/default/files/publications/2643Global_Mobility_Report_2017.pdf.

Varambhia, Aakash et al. (2022). "Combining State of the Art Opensource and Proprietary Machine Learning Technologies to Build a Data Analysis Pipeline for Gasoline Particulate Filters using X-ray Microscopy, Focused Ion Beam-Scanning Electron Microscopy and Transmission Electron Microscopy". In: *Johnson Matthey Technology Review*.

Vavřík, D. et al. (2017). "Laboratory based study of dynamical processes by 4D X-ray CT with sub-second temporal resolution". In: *Journal of Instrumentation* 12.02, pp. C02010–C02010. DOI: 10.1088/1748-0221/12/02/c02010. URL: https://doi.org/10.1088/1748-0221/12/02/c02010.

Villarraga-Gómez, Herminso and Stuart T. Smith (2020). "Effect of the number of projections on dimensional measurements with X-ray computed tomography". In: *Precision Engineering* 66, pp. 445–456. ISSN: 0141-6359. DOI: https://doi.org/10.1016/j.precisioneng.2020.08.006. URL: https://www.sciencedirect.com/science/article/pii/S0141635920302944.

Vlachos, Nickolas D. and Athanasios G. Konstandopoulos (2006). "Digital Materials Methods for DPF Development". In: *SAE Transactions* 115, pp. 79–89. ISSN: 0096736X, 25771531. URL: www.jstor.org/stable/44687470.

Vo, Nghia T, Robert C Atwood, and Michael Drakopoulos (2015). "Radial lens distortion correction with sub-pixel accuracy for X-ray micro-tomography". In: *Optics express* 23.25, pp. 32859–32868.

– (2018). "Superior techniques for eliminating ring artifacts in X-ray micro-tomography". In: *Optics express* 26.22, pp. 28396–28412.

Václavík, Marek et al. (2017). "Structure characterisation of catalytic particulate filters for automotive exhaust gas aftertreatment". In: *Materials Characterization* 134, pp. 311–318. ISSN: 10445803. DOI: 10.1016/j.matchar.2017.11.011.

Wagner, UH et al. (2012). "Ultra-high performance mirror systems for the imaging and coherence beamline I13 at the Diamond Light Source". In: *AIP Conference Proceedings*. Vol. 1437. 1. American Institute of Physics, pp. 9–14.

Walt, Stéfan van der et al. (June 2014). "scikit-image: image processing in Python". In: *PeerJ* 2, e453. ISSN: 2167-8359. DOI: 10.7717/peerj.453. URL: https://doi.org/10.7717/peerj.453.

Walton, Heather et al. (2015). *Understanding the Health Impacts of Air Pollution in London*. URL: https://www.london.gov.uk/sites/default/files/hiainlondon_kingsreport_14072015_final.pdf.

Wang, Yujun et al. (2020). "The origin, transport, and evolution of ash in engine particulate filters". In: *Applied Energy* 263, p. 114631.

WHO (2021). "WHO Air Quality Guidelines; Particulate Matter (PM2.5 and PM10), Ozone, Nitrogen Dioxide, Sulfur Dioxide, Carbon Monoxide". In: eprint: https://www.who.int/publications/i/item/9789240034228.

Willis, R. D. and T L. Conner (2003). "GUIDELINES FOR THE APPLICATION OF SEM/EDX ANALYTICAL TECHNIQUES FOR FINE AND COARSE PM SAMPLES." In: *U.S. Environmental Protection Agency, Washington, DC*. EPA/600/R-02/070 (NTIS PB2004-100988).

Willmott, Philip (2019). "Introduction". In: *An Introduction to Synchrotron Radiation*. John Wiley & Sons, Ltd. Chap. 1, pp. 1–18. ISBN: 9781119280453. DOI: https://doi.org/10.1002/9781119280453.ch1. eprint: https://onlinelibrary.wiley.com/doi/pdf/10.1002/9781119280453.ch1. URL: https://onlinelibrary.wiley.com/doi/abs/10.1002/9781119280453.ch1.

Wilson, P. et al. (2017). "Utilizing X-ray computed tomography for heritage conservation: The case of Megalosaurus bucklandii". In: pp. 1–5. DOI: 10.1109/I2MTC.2017.7969983.

Wu, Kaige et al. (2019). "A Comparative Study of Localized Corrosion and Stress Corrosion Cracking of 13Cr Martensitic Stainless Steel Using Acoustic Emission and X-ray Computed Tomography". In: *Materials* 12.16. ISSN: 1996-1944. URL: https://www.mdpi.com/1996-1944/12/16/2569.

Yamamoto, Kazuhiro and Kazuki Yamauchi (2013). "Numerical simulation of continuously regenerating diesel particulate filter". In: *Proceedings of the Combustion Institute* 34.2, pp. 3083–3090. ISSN: 15407489. DOI: 10.1016/j.proci.2012.06.117.

Yamamoto, Kazuhiro et al. (2006). "Lattice Boltzmann simulation on porous structure and soot accumulation". In: *Mathematics and Computers in Simulation* 72.2-6, pp. 257–263. ISSN: 03784754. DOI: 10.1016/j.matcom.2006.05.021.

Yanagida, Takayuki and Yutaka Fujimoto (2014). "Evaluations of pure zinc sulfide crystal scintillator". In: *Japanese Journal of Applied Physics* 53.3, p. 032601. DOI: 10.7567/jjap.53.032601. URL: https://doi.org/10.7567/jjap.53.032601.

Yang, Juan et al. (2009). "Single wall diesel particulate filter (DPF) filtration efficiency studies using laboratory generated particles". In: *Chemical Engineering Science* 64.8, pp. 1625–1634. ISSN: 00092509. DOI: 10.1016/j.ces.2008.12.011.

Yang, Lin et al. (2015). "In-situ tracking of water transport in cement paste using X-ray computed tomography combined with CsCl enhancing". In: *Materials Letters* 160, pp. 381–383. ISSN: 0167-577X. DOI: https://doi.org/10.1016/j.matlet.

2015.08.011. URL: https://www.sciencedirect.com/science/article/pii/S0167577X15303669.

Yang, Pengze and Andrea Strzelec (2019). "Numerical study of pore size and distribution effects on gasoline particulate filter performance". In: *SAE International Journal of Engines* 12.5, pp. 489–508.

Young, Dianna M et al. (2004). "Ash storage concept for diesel particulate filters". In.

Zarvalis, Dimitrios, Souzana Lorentzou, and Athanasios G Konstandopoulos (2009). "A methodology for the fast evaluation of the effect of ash aging on the diesel particulate filter performance". In.

Zhang, Guangjian et al. (2020). "Experimental investigation of internal two-phase flow structures and dynamics of quasi-stable sheet cavitation by fast synchrotron x-ray imaging". In: *Physics of Fluids* 32.11, p. 113310.

Zhu, Xiaohui et al. (2016). "Measuring spectroscopy and magnetism of extracted and intracellular magnetosomes using soft X-ray ptychography". In: *Proceedings of the National Academy of Sciences* 113.51, E8219–E8227.

Ziesche, Ralf F et al. (2020). "4D imaging of lithium-batteries using correlative neutron and X-ray tomography with a virtual unrolling technique". In: *Nature communications* 11.1, p. 777.

Zwanenburg, E A, M A Williams, and J M Warnett (2021). "Review of high-speed imaging with lab-based x-ray computed tomography". In: *Measurement Science and Technology* 33.1, p. 012003. DOI: 10.1088/1361-6501/ac354a. URL: https://doi.org/10.1088/1361-6501/ac354a.